

**SYNTHESIS AND CHARACTERIZATION
OF NEW HETEROCYCLE-BASED
DISCOTIC MESOGENS FOR
OPTOELECTRONIC APPLICATIONS**

Thesis

Submitted in partial fulfillment of the requirements for the degree of

DOCTOR OF PHILOSOPHY

By

VINAYAKUMARA D. R.



DEPARTMENT OF CHEMISTRY

NATIONAL INSTITUTE OF TECHNOLOGY KARNATAKA

SURATHKAL, MANGALORE - 575 025

July, 2019

DECLARATION

By the Ph.D. Research Scholar

I hereby declare that the Research Thesis entitled “**Synthesis and characterization of new heterocycle-based discotic mesogens for optoelectronic applications**” which is being submitted to the **National Institute of Technology Karnataka, Surathkal** in partial fulfillment of the requirements for the award of the **Degree of Doctor of Philosophy in Chemistry** *is a bonafide report of the research work carried out by me.* The material contained in this Research Thesis has not been submitted to any University or Institution for the award of any degree.

Vinayakumara D. R.

Reg. No. 148044CY14F07

Department of Chemistry

Place: NITK - Surathkal

Date:

CERTIFICATE

This is to *certify* that the Research Thesis entitled “**Synthesis and characterization of new heterocycle-based discotic mesogens for optoelectronic applications**” submitted by Mr. Vinayakumara D. R. (Register Number: **148044CY14F07**) as the record of the research work carried out by him *is accepted as the Research Thesis submission* in partial fulfillment of the requirements for the award of degree of Doctor of Philosophy.

Prof. A. Vasudeva Adhikari

Research Guide

Date:

Chairman - DRPC

Date:

DEDICATED TO MY

BELOVED PARENTS

ACKNOWLEDGEMENTS

I wish to express profound sense of gratitude to my honoured research supervisor **Dr. Airody Vasudeva Adhikari**, Professor-HAG, Department of Chemistry. He constantly encouraged and inspired me with his intensive research capability at every stage of my research. Without his serious involvement, thoughtfulness and patience, it would have been difficult for me to complete this endeavour successfully. It was an invaluable experience to work with him and to learn so many things from him both as a scientist and as a human being. It has been a great pleasure and I really cherished working with him.

I sincerely thank **Prof. K. Umamaheshwar Rao**, Director, NITK and **Prof. Swapan Bhattacharya**, former Director, NITK for providing necessary facilities to carry out this research work. I express my earnest thanks to the RPAC members, Prof. D. Krishna Bhat, Chemistry Department and Prof. M. N. Sathyanarayana, Physics Department, NITK for insightful comments and constructive criticism towards the improvement of research quality.

My special thanks to **Prof. Sandeep Kumar**, SCM group, Raman Research Institute, Bangalore for extending the laboratory facility to carry out synthesis and liquid crystalline studies. I am very grateful to him for his valuable and inspiring guidance throughout my stay in RRI.

I am also thankful to Prof. A. N. Shetty, Prof. A. C. Hegde, Prof. B. R. Bhat, Prof. A. M. Isloor, Dr. Udaya Kumar D., Dr. D. R. Trivedi, Dr. S. S. Mal, Dr. P. B. Beneesh, Dr. Saikat D. and Dr. Debashree C., Department of Chemistry for their constant support and encouragement. I also wish to extend my gratitude to all non-teaching staff in the Department of Chemistry.

I would like to thank my colleagues Dr. Praveen Naik, Mr. Naveen Chandra P., Ms. Rajalakshmi K., Ms. Kavya S. Keremane and Mr. Madhukara Acharya for their constant support, encouragement and company.

I am grateful to my close friends Swamynathan K., Manjunath Kaddipujar and Dr. Pramod Tadapatri for their invaluable help during the course of this work. Also, I am indebted to my friends Dr. H. T. Srinivas, Dr. Anup Pandith, Irlasivakumar, Marichandran and Prakashiah B. G. for their support and help during my research work.

I extend my sincere thanks to all the research scholars of the Chemistry Department for their constant help and support.

Mere words are not enough to express my gratitude to my family, father Mr. Revanna D., mother Mrs. Susheelamma, brother Mr. Vishwas K. R. and my beloved wife *Mrs. Shruti B. R.* for being a constant source of affectionate encouragement and help throughout my research work. I have greatly benefited by their valuable suggestions, thought-provoking advices and prayers. Also, I admit all my family members and friends for their love and constant support. Finally, I thank the God almighty for strengthening me during hardships to successfully complete this endeavour.

Vinayakumara D. R.

ABSTRACT

Organic π -conjugated molecules are gaining significant attention because of their substantial capability of producing low-cost, eco-friendly, flexible and large-area plastic electronics. Certainly, discotic liquid crystals (DLCs) are renowned soft self-assembled one-dimensional (1-D) organic nanostructures as they possess robust co-facial π - π stacking in the longer columnar axis, which provides a significant channel for effective anisotropic charge mobility. These LC materials are recognized to possess superior potential to be utilized as active semiconducting layers in organic electronic devices in comparison to the organic single crystals or amorphous polymers in terms of several aspects. At present, a significant number of researchers are keenly working on this class of materials for their applications in future optoelectronic devices. In this context, it was planned to design, synthesize optically dynamic unconventional discotic molecules based on various heterocyclic moieties (**HT**₁₋₃₅) and to study the structure-property relationships. Also, it was contemplated to employ the selected LC materials in optoelectronic devices and to evaluate their performance.

Based on the thorough literature survey, six series of molecules, *i.e.* **Series-1** to **6** carrying important heterocycles appended with variety of substituted aryl motifs were designed by following different designing strategies. They were successfully synthesized using appropriate synthetic protocols and their chemical structures were confirmed by means of routine spectral techniques. Further, their liquid crystalline properties were investigated by set of standard methods. Most of the newly prepared materials were found to be rich in mesomorphism, dominated with columnar (Col) self-assembly. Furthermore, they were subjected to detailed photophysical as well as electrochemical characterizations and the obtained optoelectronic results were corroborated with theoretical simulations (DFT). Majority of them were shown to be superior light absorption and emitting materials. Finally, the columnar LC materials owning essential properties were employed as emissive layer in the fabrication of multi-layer OLED devices; the attained results were promising. Conclusively, by improving the molecular design, prospective DLCs with plausible applications in molecular electronics, can be achieved.

Keywords: Self-assembly, DLCs, Optoelectronics, OLED, Heterocycles.

CONTENTS

CHAPTER 1: GENERAL INTRODUCTION

1.1	INTRODUCTION TO LIQUID CRYSTALS	1
1.2	CLASSIFICATION OF LIQUID CRYSTALS	2
1.2.1	Lyotropic LCs	3
1.2.2	Thermotropic LCs	3
1.3	DISCOTIC LIQUID CRYSTALS	6
1.3.1	Mesophases of DLCs	7
1.4	IDENTIFICATION AND CHARACTERISATION OF MESOPHASES	8
1.5	STRUCTURES OF DISCOTIC MESOGENS	11
1.5.1	Heterocycle-based discotics	12
1.6	DLCs AS ORGANIC SEMICONDUCTORS	13
1.6.1	Luminescent DLCs	14
1.6.2	DLCs in organic light emitting diodes (OLEDs)	15
1.7	BROAD OBJECTIVES	17
1.8	THESIS STRUCTURE	18

CHAPTER 2: LITERATURE REVIEW, SCOPE AND OBJECTIVES OF THE PRESENT WORK

2.1	INTRODUCTION	19
2.2	LITERATURE SURVEY	20
2.3	OVERVIEW OF LITERATURE SURVEY	33
2.4	SCOPE AND OBJECTIVES	34

CHAPTER 3: SYNTHESIS AND STRUCTURAL CHARACTERIZATION OF NEW HETEROCYCLIC SYSTEMS

3.1	INTRODUCTION	37
-----	--------------	----

3.2	EXPERIMENTAL	38
3.2.1	Materials and methods	38
3.2.2	Design and synthesis of HT₁₋₇ (Series-1)	38
3.2.2.1	Results and discussion	40
3.2.2.2	Experimental procedures	43
3.2.3	Design and synthesis of HT₈₋₁₀ (Series-2)	49
3.2.3.1	Results and discussion	51
3.2.3.2	Experimental procedures	53
3.2.4	Design and synthesis of HT₁₁₋₂₀ (Series-3)	55
3.2.4.1	Results and discussion	57
3.2.4.2	Experimental procedures	60
3.2.5	Design and synthesis of HT₂₁₋₂₆ (Series-4)	67
3.2.5.1	Results and discussion	68
3.2.5.2	Experimental procedures	70
3.2.6	Design and synthesis of HT₂₇₋₃₁ (Series-5)	73
3.2.6.1	Results and discussion	75
3.2.6.2	Experimental procedures	78
3.2.7	Design and synthesis of HT₃₂₋₃₅ (Series-6)	81
3.2.7.1	Results and discussion	83
3.2.7.2	Experimental procedures	85
3.3	CONCLUSIONS	88
CHAPTER 4: MESOMORPHIC, OPTOELECTRONIC AND ELECTROCHEMICAL STUDIES		
4.1	INTRODUCTION	89
4.2	MESOMORPHIC STUDIES	89
4.2.1	Experimental methods	90

4.2.2	Results and discussion	90
4.2.2.1	Mesomorphic behaviour of HT₁₋₇ (Series-1)	90
4.2.2.2	Mesomorphic behaviour of HT₈₋₁₀ (Series-2)	102
4.2.2.3	Mesomorphic behaviour of HT₁₁₋₂₀ (Series-3)	107
4.2.2.4	Mesomorphic behaviour of HT₂₁₋₂₆ (Series-4)	115
4.2.2.5	Mesomorphic behaviour of HT₂₇₋₃₁ (Series-5)	120
4.2.2.6	Mesomorphic behaviour of HT₃₂₋₃₅ (Series-6)	128
4.3	PHOTOPHYSICAL STUDIES	137
4.3.1	Experimental methods	137
4.3.2	Results and discussion	138
4.3.2.1	Optical properties of HT₁₋₄ (Series-1)	138
4.3.2.2	Optical properties of HT₈₋₁₀ (Series-2)	140
4.3.2.3	Optical properties of HT₁₁₋₂₀ (Series-3)	143
4.3.2.4	Optical properties of HT₂₁₋₂₆ (Series-4)	152
4.3.2.5	Optical properties of HT₃₂₋₃₅ (Series-6)	153
4.4	ELECTROCHEMICAL STUDIES	157
4.4.1	Experimental methods	157
4.4.2	Results and discussion	157
4.4.2.1	Electrochemical properties of HT₁₋₄ (Series-1)	157
4.4.2.2	Electrochemical properties of HT₈₋₁₀ (Series-2)	158
4.4.2.3	Electrochemical properties of HT₁₁₋₁₃ (Series-3)	159
4.4.2.4	Electrochemical properties of HT₂₃ (Series-4)	160
4.5	THEORETICAL INVESTIGATION	161
4.5.1.	Simulations	161
4.5.2.	Results and discussion	161
4.5.2.1	Molecular modelling of HT₁₋₄ (Series-1)	162

4.5.2.2	Molecular modelling of HT₈₋₁₀ (Series-2)	163
4.5.2.3	Molecular modelling of HT₁₁₋₂₀ (Series-3)	163
4.5.2.4	Molecular modelling of HT₁₁₋₂₀ (Series-4)	166
4.5.2.5	Molecular modelling of HT₃₂₋₃₅ (Series-6)	166
4.6	CONCLUSIONS	167
CHAPTER 5: OLED DEVICE FABRICATION STUDIES		
5.1.	INTRODUCTION	169
5.2.	MATERIALS AND METHODS	170
5.3.	EXPERIMENTAL	170
5.4.	RESULTS AND DISCUSSION	171
5.4.1	OLED device performance of HT₂ (Series-1)	171
5.4.2	OLED device performance of HT₁₂ (Series-3)	174
5.5	CONCLUSION	176
CHAPTER 6: SUMMARY AND CONCLUSIONS		
6.1	SUMMARY	177
6.2	CONCLUSIONS	178
6.3	SCOPE FOR FUTURE WORK	180
	REFERENCES	181
	LIST OF PUBLICATIONS	195
	CIRCULULUM VITAE	197

LIST OF FIGURES

Fig 1.1	Structure of cholesteryl benzoate and its thermal behaviour	01
Fig 1.2	Molecular ordering in different states of matter	02
Fig 1.3	Classification of liquid crystals	03
Fig 1.4	Schematic representation of a calamitic LC where $l \gg b$	04
Fig 1.5	General template for banana-shaped liquid crystals	05
Fig 1.6	Chemical structure of first DLC	06
Fig 1.7	Self-assembly of discotic molecules into columnar phase	06
Fig 1.8	Structures of various nematic phases exhibited by discotic mesogens	07
Fig 1.9	Schematic representations of main types of 2-D lattices of columnar phases	08
Fig 1.10	Schlieren texture of nematic phase and mosaic pattern of columnar phase	09
Fig 1.11	A typical DSC plot of a liquid crystal	10
Fig 1.12	A typical X-ray diffraction pattern of a Col _h phase	10
Fig 1.13	Structures of some known heterocyclic discotic cores	11
Fig 1.14	Some of the heterocyclic discotic cores	13
Fig 1.15	Schematic of energy and charge migration in DLCs	14
Fig 1.16	Schematic of working principle of multi-layer OLED	16
Fig 1.17	Commonly used components of OLED fabrication	16
Fig 3.1	Design of new D-A-D configured molecules HT ₁₋₇ of Series-1	39
Fig 3.2	FTIR (ATR) spectrum of HT ₁	41
Fig 3.3	¹ H NMR spectrum of HT ₁ recorded in CDCl ₃	42
Fig 3.4	¹³ C NMR spectra of HT ₁ recorded in CDCl ₃	42
Fig 3.5	MALDI-TOF spectrum of HT ₁	43
Fig 3.6	Design of new star-shaped molecules HT ₈₋₁₀ of Series-2	49
Fig 3.7	FTIR spectrum of HT ₁₀	51
Fig 3.8	¹ H NMR spectrum of HT ₁₀ recorded in CDCl ₃	52
Fig 3.9	¹³ C NMR spectrum of HT ₁₀ recorded in CDCl ₃	52
Fig 3.10	MALDI-TOF spectrum of HT ₁₀	53

Fig 3.11	Design of D-A-D' structured molecules HT ₁₁₋₂₀ of Series-3	56
Fig 3.12	FTIR spectrum of HT ₁₁	58
Fig 3.13	¹ H NMR spectrum of HT ₁₁ recorded in CDCl ₃	59
Fig 3.14	¹³ C NMR spectrum of HT ₁₁ recorded in CDCl ₃	59
Fig 3.15	MALDI-TOF spectrum of HT ₁₁	60
Fig 3.16	Design of wedge-shaped molecules HT ₂₁₋₂₆ of Series-4	67
Fig 3.17	FTIR spectrum of HT ₂₃	69
Fig 3.18	¹ H-NMR spectrum of HT ₂₃ recorded in CDCl ₃	69
Fig 3.19	¹³ C-NMR spectrum of HT ₂₃ recorded in CDCl ₃	70
Fig 3.20	Design of tapered and wedge molecules HT ₂₇₋₃₁ of Series-5	73
Fig 3.21	FTIR spectrum of HT ₂₇	75
Fig 3.22	¹ H-NMR spectrum of HT ₂₇ recorded in CDCl ₃	76
Fig 3.23	¹³ C-NMR spectrum of HT ₂₇ recorded in CDCl ₃	76
Fig 3.24	FTIR spectrum of HT ₃₀	77
Fig 3.25	¹ H-NMR spectrum of HT ₃₀ recorded in CDCl ₃	77
Fig 3.26	¹³ C-NMR spectrum of HT ₃₀ recorded in CDCl ₃	78
Fig 3.27	Design of D-A-D' configured complexes HT ₃₂₋₃₅ of Series-6	81
Fig 3.28	FTIR spectrum of HT ₃₂	83
Fig 3.29	¹ H-NMR spectrum of HT ₃₂ recorded in CDCl ₃	84
Fig 3.30	¹³ C-NMR spectrum of HT ₃₂ recorded in CDCl ₃	84
Fig 4.1	POM images of HT ₁ : (a) at 150 °C and (b) 30 °C; (c) DSC thermogram of HT ₁ ; (d) XRD profile obtained for Col _{ob} phase for the compound HT ₁ at 144 °C	92
Fig 4.2	(a) DSC thermogram of HT ₂ ; POM images of HT ₂ at (b) 141 °C and (c) 120 °C captured on cooling; XRD profiles obtained for HT ₂ at (d) 120 °C and (e) 142 °C; (f) plot of temperature <i>v/s</i> layer spacing and the peak intensity of (10) peak	94
Fig 4.3	(a) DSC thermogram of HT ₃ ; POM images of HT ₃ captured on slow cooling from I state at (b) 135 °C and (b) 100 °C; XRD profiles obtained for the compound HT ₃ at (d) 110 °C and (e)	97

	130 °C; (f) variation of FWHM of the aromatic stacking peak as a function of temperature	
Fig 4.4	(a) DFT based energy-minimized structure of HT₂ ; (b) energy-minimized structure of HT₂ showing chemical functional descriptors (CFDs); (c) energy-minimized structure of H-bonded dimer for HT₂	100
Fig 4.5	Schematic demonstration of the self-assembly of HT₂ in ordered and disordered columnar hexagonal mesophase	101
Fig 4.6	DSC thermograms of compounds: (a) HT₈ ; (b) HT₉ ; (b) HT₁₀	102
Fig 4.7	Polarized optical micrographs of the compounds: HT₈ at (a) 44 °C and (b) 30 °C; HT₉ at (c) 35 °C and (d) 25 °C; HT₁₀ at (e) 27 °C and (f) 20 °C	103
Fig 4.8	XRD spectra obtained for HT₈ : (a) at 35 °C and (b) at 24 °C	104
Fig 4.9	Schematic model for Col _h self-assembly of CPBz8	106
Fig 4.10	DSC thermograms: (a) HT₁₁ ; (b) HT₁₂ ; (c) HT₁₃ (d) HT₁₄ ; (e) HT₁₅ ; (f) HT₁₆ ; (g) HT₁₇ ; (h) HT₁₈ ; (i) HT₁₉ ; (j) HT₂₀	108
Fig 4.11	Optical images captured for HT₁₁₋₁₃ under cross-POM: (a) at 90 °C and (b) at 60 °C for HT₁₁ ; (c) at 124 °C and (d) at 30 °C for HT₁₂ ; (e) at 80 °C and (f) at 30 °C for HT₁₃	110
Fig 4.12	XRD patterns obtained for HT₁₁ at various temperatures (a) in the higher temperature mesophase and (b) the lower temperature mesophase ranges	111
Fig 4.13	Schematic model showing the energy-minimized structure of HT₁₂ and its self-assembly in Col _h and Col _r phases with plausible H-bonding	114
Fig 4.14	(a) DSC thermogram obtained for HT₂₃ ; POM textures observed: (b) at 65 °C and (c) at 25 °C	116
Fig 4.15	XRD spectra for Col _h phase of HT₂₃ : (a) at 55 and (b) at 25 °C	117
Fig 4.16	Supramolecular disc of HT₂₃	118
Fig 4.17	A model for self-assembly of HT₂₃ for Col _h	119
Fig 4.18	DSC thermograms of (a) HT₂₇ and (b) HT₂₈	121

Fig 4.19	Microphotographs of HT₂₇ (a) 85 °C and (b) 77 °C; textures of HT₂₈ obtained at (c) 98 °C and (d) 25 °C	121
Fig 4.20	XRD pattern obtained for HT₂₈ at various temperatures	124
Fig 4.21	Schematic illustration of SmA mesophase structure of HT₂₈	124
Fig 4.22	DSC traces of HT₃₀ : (a) first scan and (b) second cycle; POM textures of HT₃₀ captured at (c) at 120 °C and (d) 111 °C	125
Fig 4.23	XRD patterns of HT₃₀ at (a) 123 °C and (b) 125 °C	126
Fig 4.24	H-bond driven supramolecular disc of HT₃₀	126
Fig 4.25	Schematic of columnar hexagonal self-assembly of HT₃₀	128
Fig 4.26	POM texture of 20b at (a) 137 °C and (b) 85 °C; (c) DSC thermogram of 20b ; (d) XRD pattern of 20b	130
Fig 4.27	(a) DSC thermogram of 20c ; POM texture of 20c captured at (b) 145 °C and (c) 25 °C; (d) DSC thermogram of 20d ; POM texture of 20d at (e) 150 °C and (f) 70 °C	131
Fig 4.28	(a) XRD pattern obtained for Col _h phase of 20c and (b) Col _{h1} and Col _{h2} phases of 20d at various temperatures	131
Fig 4.29	(a) DSC thermogram of HT₃₄ ; POM texture of HT₃₄ captured at (b) 30 °C and (c) 25 °C; (d) DSC thermogram of HT₃₅ ; POM texture of HT₃₅ at (e) 83 °C and (f) 60 °C	134
Fig 4.30	XRD pattern obtained for (a) Col _h phase of HT₃₄ ; XRD traces recorded within (b) lower and (c) high-temperature mesophase ranges of HT₃₅	135
Fig 4.31	Schematic illustration of phase transition of HT₃₅	136
Fig 4.32	(a) UV-visible absorption spectra of HT₁₋₄ ; (b) PL spectra; (c) Fluorescence decay profile and (d) the emission hue.	139
Fig 4.33	(a) Absorbance and (b) PL spectra of HT₁ in various solvents	139
Fig 4.34	(a) Fluorescence spectra of spin-coated thin films of samples; (b) the emission hue of same thin films and (c) powder samples	140
Fig 4.35	(a) Absorption spectra in DCM solution (b) Emission spectra of same solution (c) Logarithmic time-resolved fluorescence decay profiles of HT₈₋₁₀ mesogens (d) Emission hue of solutions	141

Fig 4.36	Absorption and (b) Emission spectra of HT₈ in different solvents; (c) Lippert-Mataga plot and (d) Stokes shift <i>vs</i> E _T (30)	142
Fig 4.37	(a) PL spectra of spin-coated thin films; (b) emission hue of the same thin films and (c) LCs in bulk under the light of 365 nm	143
Fig 4.38	Absorption and emission spectra of HT₁₁₋₁₃ in DCM	144
Fig 4.39	(a) PL decay profiles obtained for DCM solution and (b) their emission hue; (c) PL spectra obtained for thin films and (d) their emission hue	145
Fig 4.40	(a) Absorption and (b) emission spectra of HT₁₁ recorded in solvents of varied polarity	145
Fig 4.41	(a) UV-Visible absorption spectra, (b) emission spectra and (c) emission hue; (d) fluorescence life-time traces of lumenogens	148
Fig 4.42	(a) Emission hue of thin films and (b) Emission profile HT₁₄₋₂₀	149
Fig 4.43	Normalized electronic absorption spectra for (a) CP1 (b) CP3 (c) CP4 and (d) CP7 in solvents of different polarity index	150
Fig 4.44	Normalized emission spectra for (a) HT₁₄ (b) HT₁₆ (c) HT₁₇ and (d) HT₂₀ ; (e) solvents of different polarity index Lippert-Mataga and (d) Stokes shift <i>vs</i> E _T (30) correlation plots	151
Fig 4.45	(a) UV-Visible absorption and (b) PL spectra of HT₂₁₋₂₆	152
Fig 4.46	(a) UV-Visible absorption; (b) PL spectra in different solvents and (c) corresponding Lippert-Mataga plot of HT₂₃	153
Fig 4.47	(a) UV-Visible absorption and (b) PL spectra of HT₃₂₋₃₅ of solution; (c) thin film photoluminescence spectra of HT₃₂₋₃₅	154
Fig 4.48	Cyclic voltammograms of LCs HT₁₋₄	158
Fig 4.49	Cyclic voltammograms of HT₈₋₁₀	159
Fig 4.50	Cyclic voltammograms of HT₁₁₋₁₃	159
Fig 4.51	Cyclic voltammograms of HT₁₁₋₁₃	160
Fig 4.52	(a) HOMO, LUMO and band gap energies; (b) MEPs of HT₂	162
Fig 4.53	DFT based electrostatic potential map and FMOs of HT₈ ,	163
Fig 4.54	Simulated optimized geometry, HOMOs and LUMOs of the model structure of HT₁₁₋₁₄	164

Fig 4.55	Energy minimized structures of HT ₁₄₋₂₀ and electron density distributions of their HOMO and LUMO orbitals	165
Fig 4.56	HOMO and LUMO orbitals of HT ₂₃	166
Fig 4.57	(a) Optimized structures of HT ₃₂₋₃₅ and (b) their side view	167
Fig 4.58	Electronic distributions in the FMOs of HT ₃₂₋₃₅	167
Fig 5.1	Energy-level diagram of the materials used and schematic of the different OLED architectures of Devices A-D	173
Fig 5.2	(a) J-V-L characteristics; (b) PL spectra of PVK, HT ₂ , PVK:10 wt% HT ₂ thin films and EL spectra of Device D ; (c) EL spectra of Device D at different bias voltages and (d) chromaticity diagram of the OLEDs	173
Fig 5.3	Figure 5.3 (a) Schematic of the different OLED architectures (b) Energy-level diagram, of OLED Devices E-G . (c) J-V-L characteristics. (d) EL spectra of Device G at different bias voltages	176

LIST OF TABLES

Table 4.1	Phase transition temperatures and corresponding enthalpies of HT₁₋₇	91
Table 4.1	XRD characterization data of HT₁ at 144 °C	93
Table 4.3	XRD characterization data of HT₂₋₄ at different temperatures	98
Table 4.4	Phase transition temperatures and corresponding enthalpies of HT₈₋₁₀	103
Table 4.5	XRD characterization data of HT₈₋₁₀ at different temperatures	105
Table 4.6	Phase transition temperatures and corresponding enthalpies of HT₁₁₋₂₀	109
Table 4.7	XRD characterizations data of HT₁₁₋₁₃ at different temperatures	112
Table 4.8	Phase temperatures and corresponding enthalpy changes of HT₂₁₋₂₆	116
Table 4.9	XRD characterization data of HT₂₃ at different temperatures	118
Table 4.10	Phase transitions and corresponding enthalpy changes of HT₂₇₋₃₁	122
Table 4.11	XRD characterization data of HT₂₈ at different temperatures	123
Table 4.12	XRD characterization data of HT₃₀ at different temperatures	127
Table 4.13	Phase temperatures and enthalpy changes of 20a-b	129
Table 4.14	XRD characterization data of 20b-d	132
Table 4.15	Phase temperatures and the energy changes HT₃₂₋₃₅	133
Table 4.16	XRD characterization data of HT₃₂₋₃₅ at different temperatures	136
Table 4.17	Optical characterization data of new heterocyclic derivatives	155
Table 4.18	Solvatochromic data of selected new heterocyclic derivatives	156
Table 4.19	Electrochemical data new LC materials	160
Table 5.1	Electroluminescent data of newly fabricated OLEDs	175

ABBREVIATIONS

A	: Acceptor
Alq ₃	: Tris(8-hydroxyquinoline) aluminium
ATR	: Attenuated total reflectance
BCP	: Bathocuprene
CFD	: Chemical functional descriptors
CLC	: Columnar liquid crystal
Col _h	: Columnar hexagonal
Col _r	: Columnar rectangular
Col _{ob}	: Columnar oblique
Cr	: Crystalline phase
CV	: Cyclic voltametry
D	: Donor
DCM	: Dichloromethane
DFT	: Density functional theory
DLC	: Discotic liquid crystal
DSC	: Differential scanning calorimetry
ETM	: Electron transporting material
FMO	: Frontier molecular orbital
FTIR	: Fourier transfer infrared
HBM	: Hole blocking material
HOMO	: Highest occupied molecular orbital
HT	: Heterocycle
I	: Isotropic phase
ICT	: Intramolecular charge transfer
ITO	: Indium tin oxide
LC	: Liquid crystal
MEP	: Molecular electrostatic potential map
N	: Nematic phase
N _D	: Nematic discotic phase
NMR	: Nuclear magnetic resonance

LUMO	:	Lowest occupied molecular orbital
OPV	:	Organic photovoltaic cell
OLED	:	Organic light emitting diode
OFET	:	Organic field effective transistor
POM	:	Polarised optical microscope
PEDOT-	:	Poly(3,4-ethylenedioxythiophene)-poly(styrenesulfonate)
PSS		
PXRD	:	Powder X-ray diffraction
PL	:	Photoluminescence
QY	:	Quantum yield
T _m	:	Melting temperature
T _c	:	Clearing temperature
TOF	:	Time of flight
UV	:	Ultraviolet
XRD	:	X-ray diffraction

GENERAL INTRODUCTION

Abstract

Chapter 1 deals with a brief introduction to liquid crystals and their classifications. Also, it covers the description on various mesophases of discotic liquid crystals and a concise account on different techniques used for the mesophase characterization. Further, it includes the structural aspects and important physical features of the DLCs. Finally, the chapter ends with highlights on application of DLCs in organic light emitting diodes.

1.1 INTRODUCTION TO LIQUID CRYSTALS

Liquid crystalline state is a serendipitous discovery by an Austrian botanist Friedrich Reinitzer and German physicist Otto Lehman in 1888 (Reinitzer 1888, 1989). When working on functions of cholesterol, Friedrich Reinitzer noticed two melting points in one of the synthesized cholesterol derivatives, *i.e.* cholesteryl benzoate (**Fig 1.1**). The solid material seemed to melt at 145.5 °C into a cloudy liquid. On further heating, he observed that, the cloudiness suddenly disappeared at 178.8 °C to a clear transparent liquid. Further, Otto Lehman studied this compound under hot-stage polarizing optical microscopy and he convinced that, the cloudy liquid was a thermodynamically distinct phase with a unique molecular order. Then, he introduced the terms ‘flüssige Krystalle’ (fluid crystals), ‘fliessende Krystalle’ (flowing crystals), and ‘krystallinische Flüssigkeiten’ (crystal fluids), to denote this intermediate phase (Lehmann 1889). Since after this discovery, the immense efforts have been made by a large number of scientific communities all-over the world to understand the basics of this state. As a result, the triggering molecules responsible for this state of matter are identified as liquid crystals (LCs).

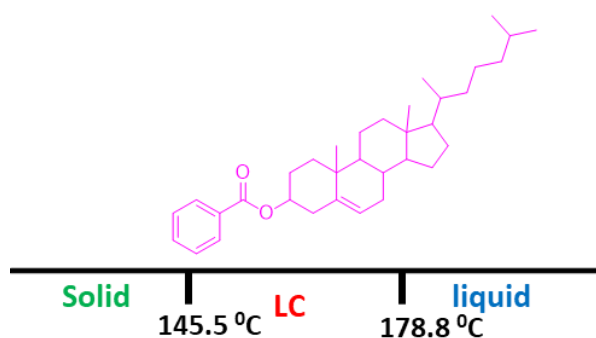


Figure 1.1 Structure of cholesteryl benzoate and its thermal behaviour

LC state is an intermediate state between classical crystalline and liquid state. Because of this reason, it is referred as “mesophase” (*mesos* = between) and the constituent molecules as “mesogens”. In mesophase, the molecules have long-range positional order as the molecules orient in perfect crystalline solid, and also possess movement like in liquids as schematically represented in **Fig 1.2**. Later, this new state of matter was eventually accepted as fourth state of matter along with solid, liquid and gaseous states. Liquid crystalline phase can be generated by a broad range of compounds. Typically, the molecules possessing rigid central part appended with soft flexible chains will induce mesogenic behaviour. Depending on their structural feature and kind of inter- and intramolecular interactions (π - π interactions, Coulombic forces, hydrogen bonds, or ionic interactions, dipole-dipole interaction, etc.) involved, various liquid crystalline phases, say nematic, columnar, smectic etc. can be obtained. In LC state, molecules possess considerable order in diverse arrangements with an additional important property, *i.e.* fluidity which results anisotropic physical properties to molecular state as shown in **Fig 1.2**. This unusual property has led to their widespread applications in various fields. Liquid crystal molecules may be purely either organic in nature or organometallics having metal complexed with suitable organic ligands or inorganic central core carrying saturated alkyl chains.

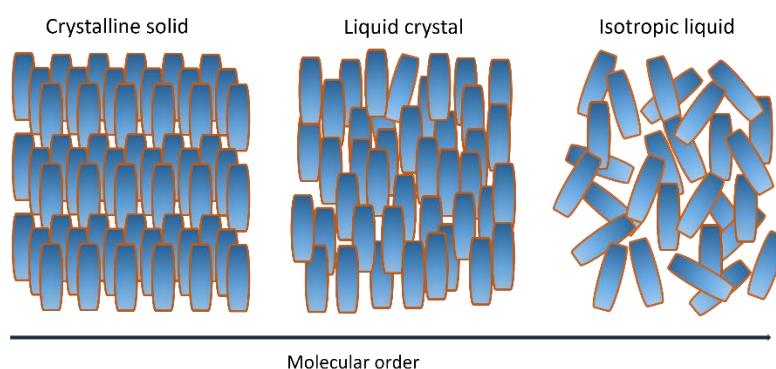


Figure 1.2 Molecular ordering in different states of matter

1.2 CLASSIFICATION OF LIQUID CRYSTALS

There are several ways of classifying liquid crystals. Firstly, liquid crystals are broadly classified as monomeric or oligomeric and polymeric liquid crystals, depending on the molar mass of the constituent molecules. Secondly, depending on how the liquid crystalline phase has been achieved whether by adding a solvent or by varying the

temperature, LCs are divided into lyotropic and thermotropic, respectively. **Fig 1.3** summarizes the broad classification of liquid crystals.

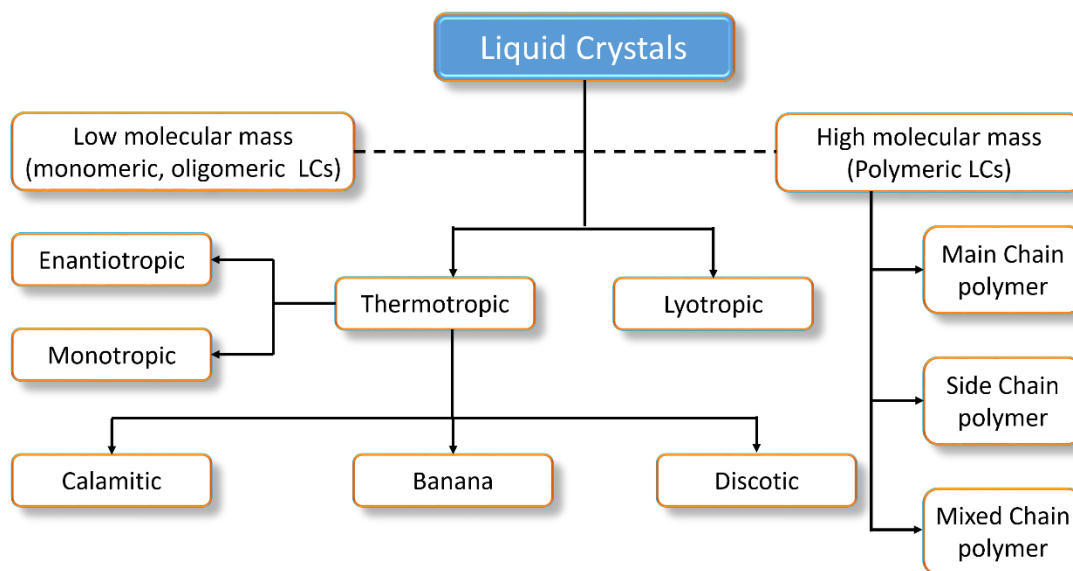


Figure 1.3 Classification of liquid crystals

1.2.1 Lyotropic LCs

In lyotropic LCs, mesophase is generated upon addition of solvent, usually polar solvents like water and alcohol. Typically, a material composed of amphiphilic molecules owing distinct parts of contrasting character, *i.e.* a hydrophilic polar “head” and a hydrophobic nonpolar “tail” is known to show lyotropic LC phases. On addition of solvent to this kind of materials, the lattice forces between the molecules in the crystal will be relaxed. In these materials, by varying the type of solvent, concentration and temperature, different types of mesophases can be obtained. Typical examples of lyotropic liquid crystals are soaps in water, various phospholipids, polypeptides *etc.*

1.2.2 Thermotropic LCs

When the mesophases are obtained in the transitions between the solid and liquid phases, then they are regarded as thermotropic liquid crystals. This mesophase can be obtained either by heating a solid material or by cooling an isotropic liquid. Such phases are called enantiotropic, if thermodynamically stable mesophases are obtained on heating the solid phase as well on cooling the isotropic liquid. If the mesophase is obtained only while cooling the isotropic liquid, then it is called monotropic phase, which is a metastable mesophase. The essential requirement for a molecule to be a

thermotropic liquid crystal is presence of a structure consisting of a central core (often aromatic) and a flexible peripheral moiety (generally aliphatic chains). Moreover, along with the geometric anisotropy, interaction anisotropy and nano segregation are the driving parameters for mesophase formation. As the present study focusses mainly on thermotropic LC materials, only such class of compounds have been emphasized in the following section.

Further, depending on the geometrical shape of the molecules, thermotropic LCs are classified as rod-like (calamitics), bent-core (banana) and disc-like (discotic). These liquid crystals show different phases like nematic, smectic, columnar, helical, B phases *etc.* based on the arrangement of molecules in the liquid crystalline phase.

Calamitic LCs:

Calamitic or rod shape liquid crystals were the first thermotropic mesogens to be discovered. Normally, they possess simple rod-shaped geometry. Structurally these molecules have elongated shapes, *i.e.* the length (l) is significantly greater than the breadth (b) of the molecule, as depicted in **Fig 1.4**.

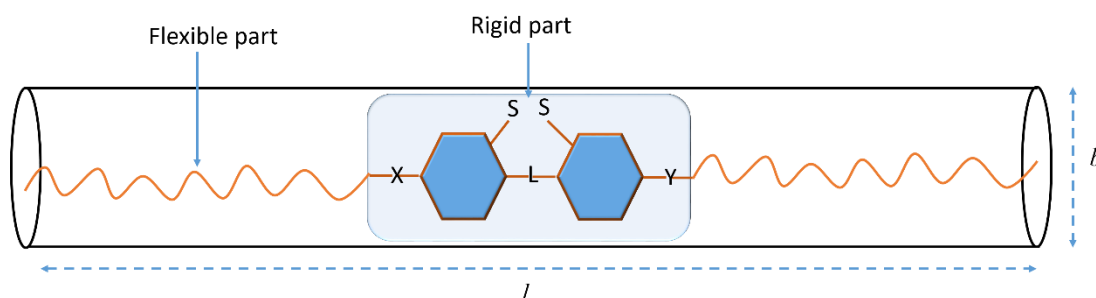


Figure 1.4 Schematic representation of a calamitic LC where $l \gg b$

The combination of shape anisotropy, interaction anisotropy and incompatibility of chemical groups in calamitics leads to the formation of more than one mesophase. A typical rod shape LC molecule contains one or more aromatic/alicyclic rings attached directly or *via* some linking groups. Most of them possess hydrocarbon chains and lateral substituents as well. A typical chemical structure of these molecules is represented by the general template as given in **Fig 1.4** where the rings are attached *via* linking groups L and lateral substituents S which are responsible to modify the mesophase morphology and physical properties of calamitic

liquid crystals (groups such as $-X$, $-\text{NO}_2$, $-\text{CH}_3$, $-\text{OCH}_3$, $-\text{CN}$ etc.); the central core moiety is attached to flexible hydrocarbon chains *via* linking groups X and Y.

Banana LCs:

Mesomorphic behaviour was also observed in banana-shaped molecules. This investigation opened up an immense research in the LC field. Till now, several bent-shaped LCs have been synthesized and characterized. Typically, bent-shaped liquid crystalline molecules are composed of three units, *viz.* an angular central core, two linear rigid arms and terminal chains as shown in **Fig 1.5**. These structures represent a new sub-class of thermotropic liquid crystals, which can display not only classical nematic and or smectic phase(s), but also novel types of smectic-like phases called ‘B’ phases and are numbered according to their chronological discovery, from B_1 to the most recent B_8 , where the symbol B stands for banana or bent- or bow-shaped mesogens.

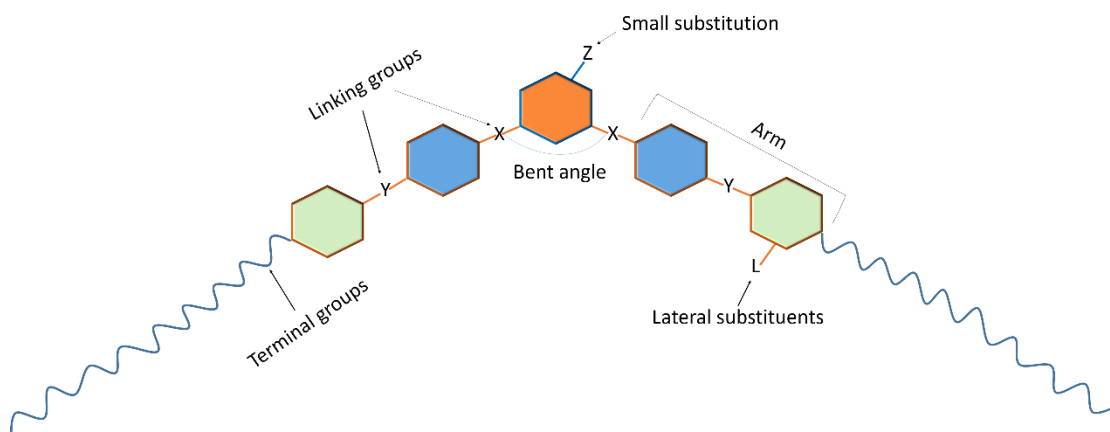


Figure 1.5 General template for banana-shaped liquid crystal

Discotic LCs:

In 1977, Prof. S. Chandrashekar and his colleagues at Raman Research Institute investigated the mesophase formed by relatively simple plate-like or disc-shaped molecules, as depicted in **Fig 1.6** (Chandrasekhar et al. 1977). They elucidated that, the synthesized plate molecules stack into columns that form hexagonal arrangement. This exciting invention is one of the milestone discoveries of Indian research and it opens up a new area in the fascinating liquid crystal research. Since the present work mainly

deals with the study of DLCs, a detailed account of them has been given in the following sections.

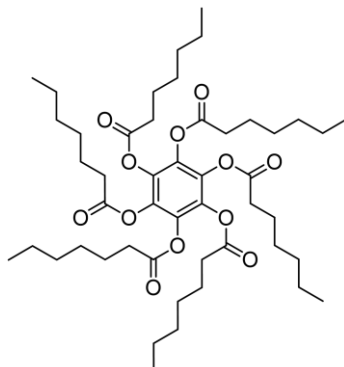


Figure 1.6 Chemical structure of first DLC

1.3 DISCOTIC LIQUID CRYSTALS

Generally, discotic mesogens consist of plate-like rigid aromatic core which is appended with number of flexible saturated alkyl chains at the periphery. This structural feature imparts soft-nature to the molecules, there by the molecules arrange into different orientations. Evidently, the properly designed disc-like molecules (primary structure) undergoes self-stack into one on the other to form secondary one-dimensional columnar structures, which in turn self-organizes into various two-dimensional architectures (tertiary structure), as indicated in **Fig 1.7**. The main motivation for such self-assembly is the significant intermolecular π - π interactions which hold the discotic molecules in an ordered arrangement. In addition to this, other non-covalent interactions like H-bonding, Coulombic attraction, metal complexation, van der Waals force and charge transfer process experienced by the molecules render the columnar structures as a thermodynamically stable mesophase.

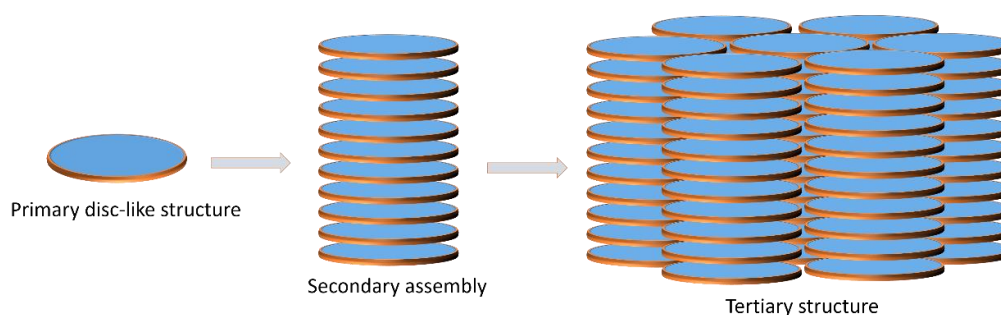


Figure 1.7 Self-assembly of discotic molecules into columnar phase

Since the current research work is centred on the synthesis and investigations of new discotic liquid crystals, the different mesophases formed by such class of LCs are discussed in the following section.

1.3.1 Mesophases of DLCs

Depending on shape, size of the central core unit, nature of peripheral chains and connecting groups between alkyl chains and discotic core, there are variety of packing arrangements of discotic mesogens in the liquid crystalline phases. There are two major types of mesophases found in disc-like molecules, *i.e.* nematic, and columnar. Columnar phases are the most common mesophases, while other phases are rarely observed. Few discotic mesogens are known to exhibit more than one mesophase.

Nematic phases of discotic mesogens:

In discotic nematic phase, the molecules have translational and rotational movements around their axis, although they tend to orient themselves in a preferential direction along their director (**Fig 1.8a**). The chiral nematic phase, also known as a cholesteric phase, displays a helical arrangement where alignment between stacks gets rotated from each other to produce a long-range chirality of the stacks (**Fig 8b**). As depicted in **Fig 1.8c**, the nematic columnar phase is characterized by a columnar stacking of the molecules, however these columns do not form two dimensional (2D) lattice structures. Also, they display a positional short-range order and an orientational long-range order. In discotic nematic lateral phases, the disc-shaped molecules aggregate into large disc-shaped superstructures and these aggregates show a typical nematic arrangement as shown in **Fig 1.8d**.

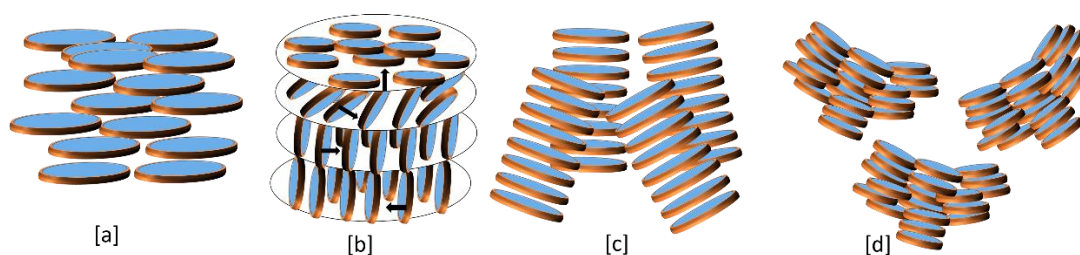


Figure 1.8 Structures of various nematic phases exhibited by discotic mesogens: (a) Discotic nematic (b) Chiral nematic (c) Columnar nematic and (d) Nematic lateral

Columnar mesophases of discotics:

Discotic columnar mesophases originate from self-stacking of molecules one on top of the other forming 1-D columnar assembly and these columns are further organized into various two-dimensional lattices. Here, the molecules arrange themselves either periodically or disordered fashion within the columnar axis. Consequently, depending on the dynamics of the discotic molecules along the columnar axis and the symmetry parameters, columns can adopt different 2D lattice structures like columnar hexagonal (Col_h), columnar rectangular (Col_r), columnar oblique (Col_{ob}), columnar square (tetragonal) (Col_{tet}) *etc.* **Fig 1.9** illustrates the schematic representations of hexagonal, tetragonal, oblique, and rectangular columnar mesophases.

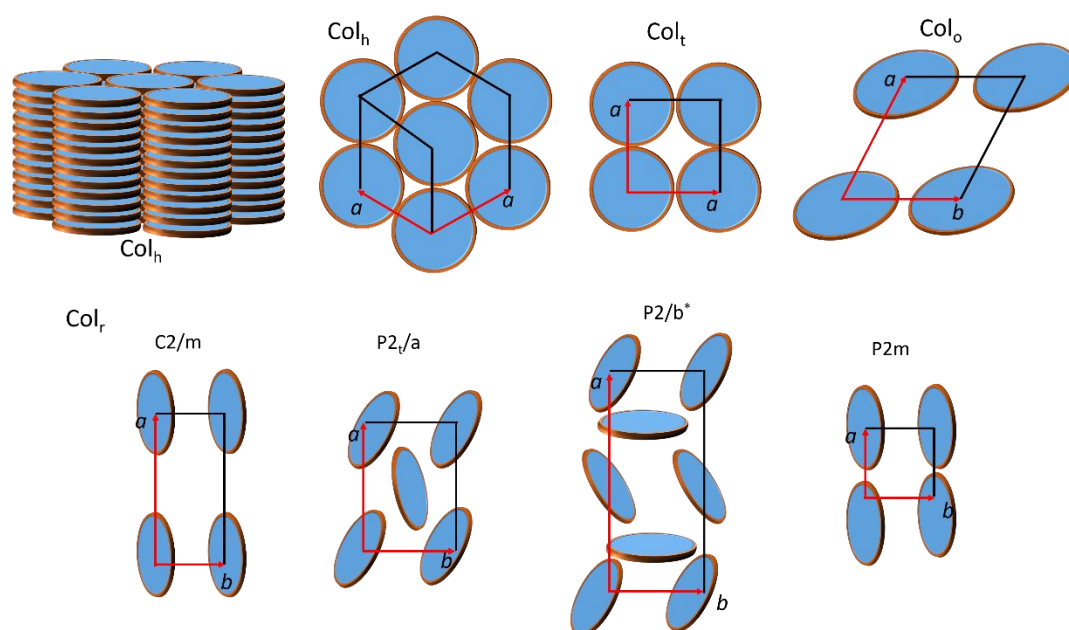


Figure 1.9 Schematic representations of main types of 2-D lattices of columnar phases, showing commonly observed plane groups of Col_r (Kumar, 2011)

1.4 IDENTIFICATION AND CHARACTERISATION OF MESOPHASES

A combination of techniques is to be employed for the complete characterization of mesophases exhibited by any LC material. Commonly, a triumvirate of hot stage Polarized Optical Microscope (POM), Differential Scanning Calorimetry (DSC) and temperature variable X-Ray Diffraction (XRD) techniques

have been extensively used for the identification as well as characterization of mesophase morphology. These methods have been discussed briefly in the following section.

Polarized Optical Microscope (POM):

Polarized Optical Microscopy (POM) is an optical analytical technique which is being used to study order and fluidity of LC phases. Generally, the molecules in LC states align along one or two orthogonal axes and disordered along the rest of axes. Because of this, molecules tend to be highly anisotropic, which makes LC state to be optically birefringent. Thus, on incident of plane polarized light LC material displays birefringent texture. Therefore, occurrence of fluidic birefringence is the typical indication of LC property. Since the birefringence is dependent on ordering of the molecular components, the obtained textures can also provide the type of morphology in mesophase. Hence, the various LC phases with different molecular organizations have representative optical textures. For instance, the nematic and columnar phases show characteristic textures, as depicted in **Fig 1.10**.

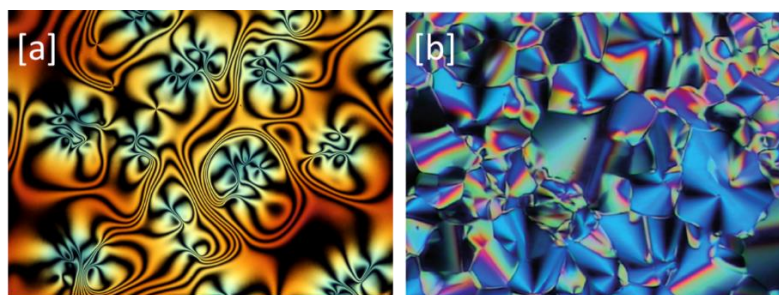


Figure 1.10 (a) Schlieren texture of nematic and (b) mosaic pattern of Col phases

Differential Scanning Calorimetry (DSC):

Differential scanning calorimetry (DSC) is an important thermo-analytical technique that is used for the measurements of the transition temperatures in materials. In case of LCs, it can precisely measure all the transitions between crystalline, liquid crystalline and isotropic phases. An illustrative DSC trace of an LC material is depicted in **Fig 1.11**. The area beneath the DSC peak is the enthalpy of transition (ΔH) which is the difference in energies of the material before and after the measured transition. Typically, enthalpy change for crystalline to a mesophase transformation (melting temperature, T_m) is in the range of 20-100 kJmol^{-1} , while the ΔH for mesophase to

isotropic liquid phase (clearing temperature, T_c) is below 10 kJmol^{-1} . There would be more than one peak between T_m and T_c , if the material exhibits poly-mesomorphism and the ΔH for such transitions will be in the range of $2\text{-}10 \text{ kJmol}^{-1}$. These thermodynamic parameters of an LC material provide valuable information regarding number of mesophases and the extent of molecular order in the particular mesophase as well as the glass transition temperature of the material.

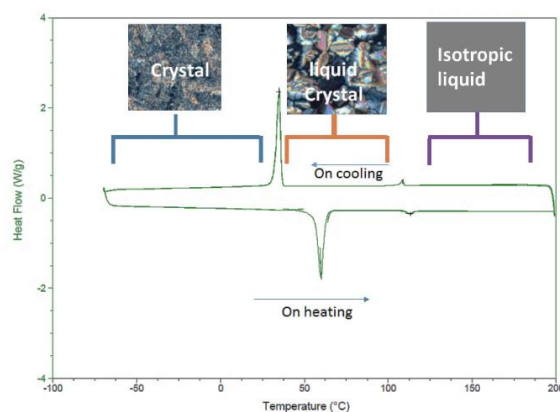


Figure 1.11 A typical DSC plot of an LC material

X-ray diffraction technique (XRD):

X-ray diffraction technique is an ultimate tool to characterize the mesophase symmetry of liquid crystalline materials for which a well-equipped X-ray diffraction instrument is necessary. It works on the basis of Bragg's law; it is easy to estimate the positioning of the molecules in mesomorphism and hence structure of mesophase. For instance, X-ray diffraction pattern of a columnar hexagonal mesomorphology would give reflections in the ratio of $1:1/\sqrt{3}:1/2:1/\sqrt{7}$ in the lower angle region and broad reflections in the wide angle region due to fluidic nature of alkyl chains as well as core-core interactions (**Fig 1.12**).

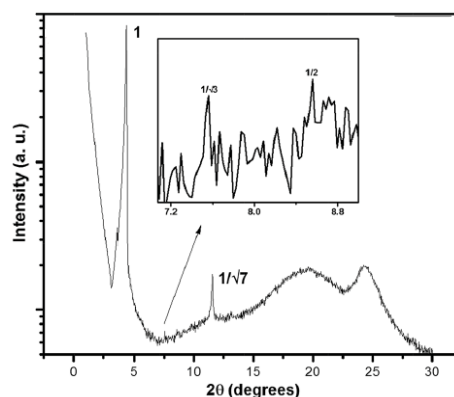


Figure 1.12 A typical X-ray diffraction pattern of a Col_h phase

1.5 STRUCTURES OF DISCOTIC MESOGENS

Ever since the discovery of DLCs, widespread efforts have been made both by chemists and physicist to understand the structure-LC property relationships of discotics. Structurally, a typical discotic mesogen composes of a rigid core surrounded by 3-12 saturated fluidic alkyl chains with more than three carbon units at the periphery. These aliphatic chains are attached to central core either directly or through some linking groups like ether/thioether, ester, amide, alkylene alkenylene *etc.* as schematically displayed in **Fig 1.13**. A slight change in any one of the above mentioned parameters results in the alternation of mesophase property. For example, varying in length of peripheral chains by a single carbon unit would lead to change in mesophase structure; however, this structural modification cannot alter the optoelectronic properties of the mesophase. It is well-established that, the only way to tune the electro-optics of mesophase is by tailoring the central-rigid core moiety. Therefore, constructing the various discs is a matter of interesting area to achieve the functional DLCs in virtue of their widespread application ranging from biomedical to electronics (Kumar 2011).

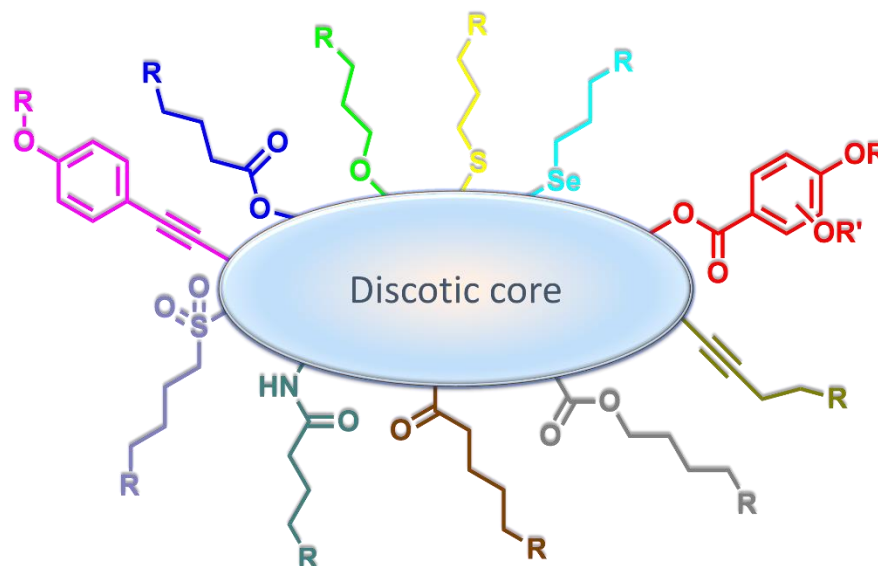


Figure 1.13 General template of discotic liquid crystals

Recently, non-discoidal, unsymmetrical, and non-aromatic cores with suitable substituents are also proven to exhibit discotic mesophase. By tuning such discrete central core moieties, it is possible to synthesize the new DLCs with improved material properties. Further, certain discotic cores capable of forming the hydrogen bonding play

an important role in formation mesophase. Generally, there are two possible ways for construction of supramolecular LCs through H-bonding interactions, one is the step-wise assembly of disc-like entities which would organize into columns (Beltrán et al. 2009; Blanco et al. 2016; Hirschberg et al. 2000; Kleppinger et al. 1995; Suarez et al. 1998; Zhu et al. 2010), whereas in the other case, molecules possessing polar and lipophilic units simultaneously arrange to form a large H-bonding network and 2-D nanoscale segregation without any intermediate step (Fuchs et al. 2002; Maly et al. 2006; Tschierske 2013; Yagai et al. 2011, 2012). Till now, a large number of H-bonding scaffolds with appropriate design have been investigated to obtain columnar mesophases. Among the various class of compounds, carboxylic acids, amides, pyridines, polyalcohols, carbohydrates, oligopeptides, pyrazoles, triazines, melamines *etc.* were widely studied H-bonding motifs. Here, heterocyclic core-systems are of particularly important class because of the several advantageous factors. A detailed account on heterocycle-based DLCs has been given in the following section.

1.5.1 Heterocycle-based discotics

From the last two decades, an extensive work has been progressing to realize the different heterocycle-based DLCs. Normally, electronegative heteroatoms like N, O, S greatly influence the electronic nature of discotics without modifying the structural aspect of the respective carbocyclic analogues due to the stronger polar induction (Roy et al. 2012). Moreover, most of the heterocyclic rings are electron deficient; when they are appended to electron rich groups, their intramolecular dipolar induction often leads to the donor-accepter interaction. The presence of such structures brings about good light absorption and/or emission characteristics for the mesogens, mainly due to push-pull induced intramolecular charge transport behaviour. Further, in D-A architected mesogens, the donor-acceptor interactions predominantly stabilize the self-assembly through extended conjugation. Consequently, this type of highly ordered self-assembled systems with the preserved emission is considered to be potential candidates for optoelectronic applications (Blanco et al. 2016; Yadav et al. 2017).

Heterocycles are the most promising motif for the synthesis of H-bonded LCs as they stabilize the columnar structures by forming stable and specific H-bonds,

imparting lateral and longitudinal dipoles to overall structure (Cheng and Gao 2015). Some of the most studied heterocyclic cores are summarized in **Fig 1.14**.

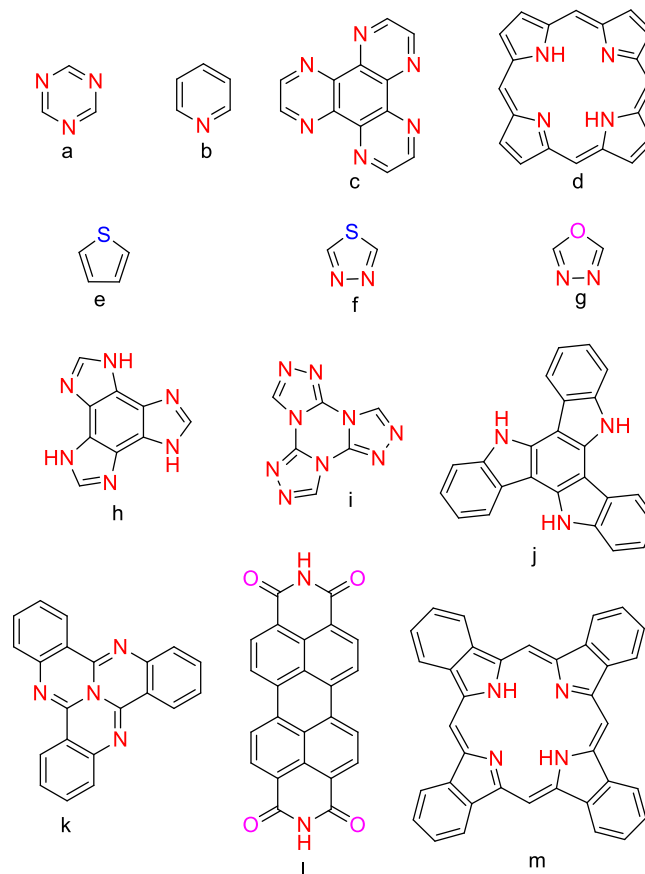


Figure 1.14 Chemical structures of some known heterocyclic discotic cores, a-m

1.6 DLCs AS ORGANIC SEMICONDUCTORS

As discussed earlier, properly designed discotic molecules self-segregate into columnar structures with the intramolecular distance of 3.5-4 Å and intercolumnar spacings of 20-40 Å which depend on the length of alkyl chains attached to discotic core (**Fig 1.15**). This stacking of aromatic cores facilitates the effective π -orbitals overlap of adjacent molecules along the columnar axis. Here, the interaction between the neighbouring columns is several magnitudes less than that within the columns. Consequently, charge migration is expected to be quasi-one-dimensional; the charge carrier mobility along the columns is reported to much more than that between the columns. Interestingly, time-of-flight charge mobility up to about $0.1 \text{ cm}^2\text{V}^{-1}\text{s}^{-1}$ has been realized in columnar mesophases (Kumar 2011). This is due to insulating contiguous of alkyl chains which separate the columns. Because of this reason, DLCs are regarded as soft molecular wires. In addition to their intrinsic charge carrier

behaviour, they possess several advantageous features like inherent anisotropic photoconductivity, controlled molecular order, easy processability, good self-healing, excellent optical absorption, high solubility in wide range of organic solvents, intense fluorescence and great response to various external stimuli. These advantageous factors render DLCs as potential candidates in several commercial applications (Kumar et al. 2017; Kumar 2016).

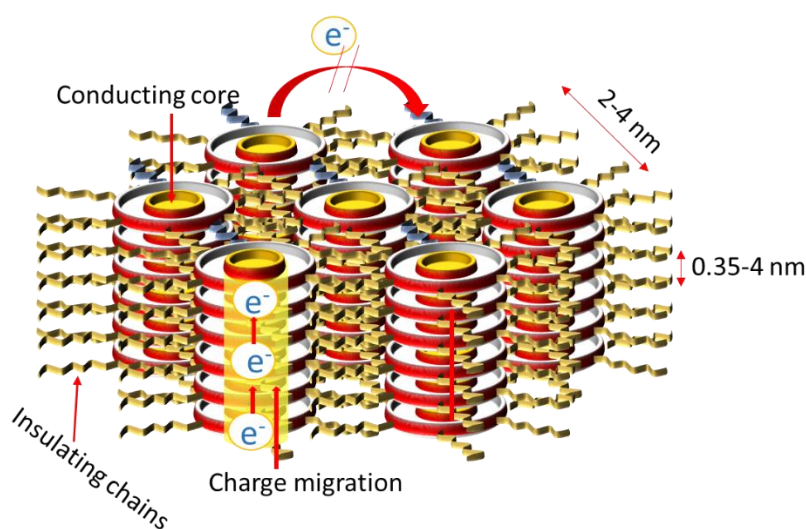


Figure 1.15 Schematic representation of energy and charge migration in DLCs

The DLCs owing afore mentioned features with preserved solid state luminescence are considered to be promising optical materials due to their switchable luminescent behaviour by the external stimuli like temperature, mechanical stress, metal ion, pH *etc.* More importantly, they find applications in flexible OLEDs as active components. The detailed account on fluorescent DLCs is outlined below.

1.6.1 Luminescent DLCs

Recently, fluorescent DLCs are emerged as an important class of light emitting materials in addition to conventional luminescent materials. Since luminescence mechanism is highly sensitive to molecular structure and type of aggregation in their state of matter, slight changes in the molecular structure can significantly alter their emission colour. Consequently, luminescence in DLCs renders them promising fluorescent sensor. Especially, conducting DLCs with preserved solid state luminescence can potentially be employed in the fabrication of OLEDs.

At present, there has been a flurry of work progressing to achieve highly intense fluorescent discotic mesogens. Generally, two approaches have been endeavouring to achieve luminescence at LC state, *i.e.* either by connecting the mesogenic component to a chromophore or incorporating favourable configuration like donor-accepter in the basic design itself. The latter approach is the most successful and extensively used strategy. Therefore, incorporation of electron donor and acceptor units in the core system would yield high fluorescent discotic mesophases. Also, various substituted heterocyclic cores were found to exhibit sufficient emission mainly by the intermolecular charge transport (ICT) ability. However, the principal stacking of discotics into columnar fashion causes notorious fluorescence quenching.

1.6.2 DLCs in organic light emitting diodes (OLEDs)

Since the breakthrough discovery of electroluminescence from organic molecules in 1987 (Tang and VanSlyke 1987), Organic Light Emitting Devices (OLEDs) are considered as a next-generation eco-friendly solid-state lighting technology. This may be because of their advantageous features like low cost, high power efficiency, wide color gamut, ease of fabrication by solution processes, and chance to produce curved thin and flexible devices (Brütting et al. 2013; Buckley 2013; Gaspar and Polikarpov 2015; Kalyani and Dhoble 2012; Tsujimura 2017; Xu et al. 2016). Nevertheless, the current challenges in this area include the development of ideal light emitting device materials, engineering of the device structures and their optimization to get more efficient and long-life devices (Jou et al. 2015).

The common OLEDs are double charge injection devices, requiring the simultaneous supply of both electrons and holes. Typically, OLEDs can be made into three different configurations, *viz.* single, double and multilayer devices. Amid, multilayer device configurations were found to be most efficient. Classically, a multilayer device comprises a sandwich of thin emissive layer between the anode (ITO) appended to organic hole transporting/hole injection layer and cathode (metals like Al, Ca, Ba, Mg) attached to organic electron transporting/electron injection layer (**Fig 1.16**). Drifting the injected electrons from cathode and holes from anode through organic layer under external electric field produces the bound electron-hole pair at chromophoric site. The recombination of these pairs generates the luminescence.

Efficient devices require the matching of energy levels to minimize the barriers for carrier injection and to trap both electron and holes exclusively in the emitter region. More commonly, ultra-thin LiF or CsF layers are used as electron injection components (EIL); PBD (2-(4-biphenyl)-5-(4-*t*-butylphenyl)-1,3,4-oxadiazole), Alq₃ (tris(8-hydroxyquinoline) aluminium TPBI 1,3,5-tris(*N*-phenylbenzimidazol-2-yl)benzene) or BCP (bathocuproine) have been employed as electron transporting materials (ETL); mostly transparent PEDOT-PSS conjugated polymer composite is used as a hole transporting layer (HTL) (**Fig 1.17**).

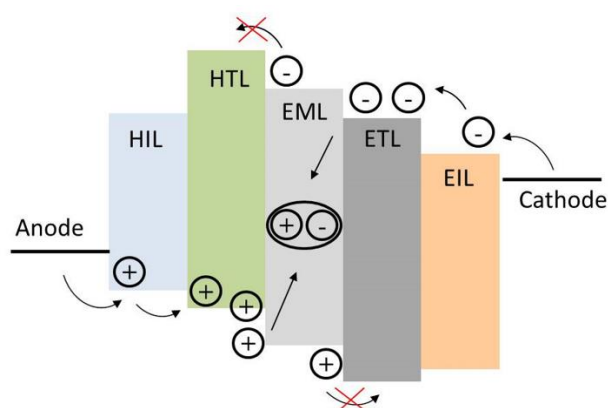


Figure 1.16 Schematic representation of working principle of multi-layer OLED

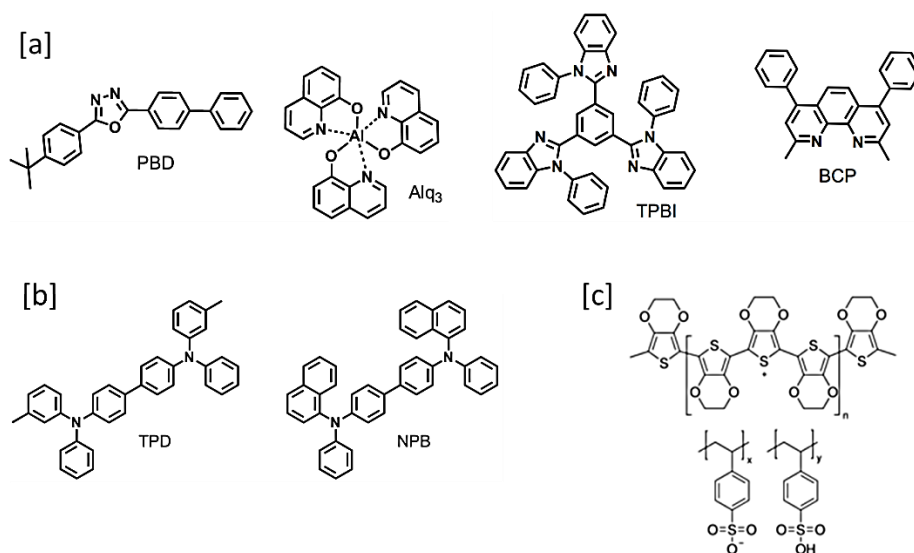


Figure 1.17 Chemical structures of commonly used components in (a) electron transport layer; (b) hole transport layer; (c) hole transporting PEDOT: PSS

Certainly, the emissive layer is a vital component which determines the overall efficiency of the device. Till today, a large variety of luminescent materials has been

developed, so as to improve the device performance (Chen 2004; Chen et al. 2014; Godumala et al. 2016; Kamtekar et al. 2010; Kido and Okamoto 2002; Li et al. 2013; Segura 1998; Yang et al. 2015; Zhu and Yang 2013). Besides a great amount of research in this field, high-performance fluorophores for non-doped OLEDs have not been much explored, as most of the materials do not own good charge transport property with the preserved solid-state emission. In this context, columnar liquid crystals (CLCs) were shown to be better alternatives to the insulating amorphous solids as well as expensive single crystalline fluorophores due to their effective combination of π - π self-stacking with long-range order, self-healing, easy processability, good luminescence ability and intrinsic charge carrier property in the soft condensed state (Bushby and Kawata 2011; Chen et al. 2018; Kaafarani 2010; Kumar 2016; Laschat et al. 2007; O'Neill and Kelly 2011; Sergeyev et al. 2007).

1.7 BROAD OBJECTIVES

From the last two decades, a tremendous research is progressing in the field of organic semiconductors due to their stimulating electronic and optoelectronic properties which enable the development of new exciting electronic devices. A number of different class of organic materials was found to exhibit semiconducting properties including conjugated oligomer, polymers and small π -conjugated molecules. They found extensive applications in field-effect transistors (OFETs), organic light-emitting diodes (OLEDs), organic photovoltaic cells (OPVs) and sensors (Sergeyev et al. 2007). Recently, columnar liquid crystals (CLCs) were emerged as one such kind of semiconducting materials. Besides, CLCs are dominating over other organic semiconductors by owning many more advantageous features. Hence, CLCs can successfully be employed in all above mentioned devices to improve the device performance. Particularly, luminescent discotics have attracted much attention very recently due to their potential suitability in the flexible OLEDs.

In this context, a large number of research groups all around the world are enormously working on design and development of the new CLCs with functional properties. Certainly, achieving the materials possessing the unique combination of LC behaviour with functional properties is not straight forward; it needs a careful design of basic structure. As literature suggests, integrating the properly substituted heterocyclic

system at the core as well as incorporating the donor-accepter conduit is a best way to achieve the luminescence property along with the LC behaviour. After thorough literature survey, it has been thought of designing and synthesizing several new series of D-A configured heterocyclic molecules owing unconventional geometry, with the hope that newly synthesized compounds could show significant functional LC behaviour.

The overall aim of the present work was to design, synthesise and characterize new heterocycle-based molecules. It was also aimed at exploration of their mesomorphic, photophysical and electrochemical properties as a function of structural modifications. Finally, it was intended for designing optoelectronic device structures, *i.e.* OLED by employing the newly synthesized CLCs as emissive component and studying their structure-performance relationship.

1.8 THESIS STRUCTURE

The whole thesis is systematically divided into six chapters. **Chapter 1** outlines a brief introduction to liquid crystals including the classification of LCs, followed by methods used for the LC phase characterization. It also deals with a detailed account on different phases of discotic liquid crystals, their basic material properties and their possible application in OLEDs. **Chapter 2** describes the review of literature survey on design and development of various heterocycle-based liquid crystals. Further, it includes the scope and main objectives of the present research work, arrived at on the basis of the literature review. The experimental protocol for the synthesis of thirty five new heterocyclic derivatives (**HT1-35, Series-1 to 6**) and their complete structural characterization have been elaborated in **Chapter 3**. A detailed investigation of liquid crystalline property of all newly synthesized compounds is included in **Chapter 4**. In addition, it covers in depth photophysical and electrochemical characterization of new compounds. Also, it includes their quantum chemical simulations. **Chapter 5** comprises a detailed OLED device fabrication as well as their performance studies. Finally, **Chapter 6** comprises the summary of the research and important conclusions drawn as well as the outcome of the research work.

LITERATURE REVIEW, SCOPE AND OBJECTIVES OF THE PRESENT WORK

Abstract

This chapter covers an introductory account on heterocyclic discotic mesogens and a review of reported literatures on design, synthesis and material characterizations of various heterocycle-based DLCs owing diverse molecular configurations. Also, it comprises scope and objectives of the present research work, arrived at on the basis of a detailed literature survey.

2.1 INTRODUCTION

Since the consecutive discovery of three main types of thermotropic liquid crystals, a large variety of chemical structures have been designed and synthesized to achieve liquid crystalline property as a function of temperature. Generally, the main backbone of LC materials may be organic, inorganic, organometallic or ionic in nature. As the shape of the molecular structure is one of key parameters in formation of mesophase, it is much essential to maintain the favourable geometry of overall structure. Unlike traditionally acceptable structures, molecules owing some unconventional structures have recently been successfully introduced in achieving the diverse mesomorphism, more importantly to accomplish the functional properties at the mesophase. The known unconventional structural motifs include elongated rod-like, semi-disc, polycatenar, wedge-shaped, taper-shaped, dendrimers and dendrons which were shown to exhibit columnar phases. Consequently, use of normal polycyclic aromatic hydrocarbons in such discrete LCs has been ruled out, instead some relatively small aromatic, heteroaromatic or combination of both should be integrated at the core region while designing DLCs. At present, heterocyclic systems have attracted much attention, as they have not been explored much. Such DLCs would show good *p*-type semiconducting behaviour.

To design the discotic mesogens, a variety of heterocyclic derivatives have been used as core moieties, which include pyridine, thiophene, pyrimidine, oxadiazole, thiodiazole, 1,2,3-triazole, *s*-triazine, pyrazine, quinoxaline, pyrazole, carbazole, imidazole, thiazole, oxazole, tetrazole *etc.* Incorporation of these heterocycles into

conjugated systems leads to a stable mesophase mainly due to donor-accepter interactions (Roy et al. 2012). Further, they are highly attractive and promising scaffolds in view of their prospective optoelectronic properties. Because of their electron deficiency, they exhibit excellent thermal and oxidative stability. Also, they facilitate effective packing and impart admirable luminescence properties when functionalized with appropriate donors (Chen et al. 2014). Such heterocyclic systems are potential candidates for achieving tailor-made LC compounds with essential properties, required in optoelectronics.

The following section provides a brief account on literature reports on various heterocycle-based columnar LCs featuring unconventional molecular geometry. It also covers some interesting literature on closed-type hydrogen bonded CLCs derived from few heterocycles.

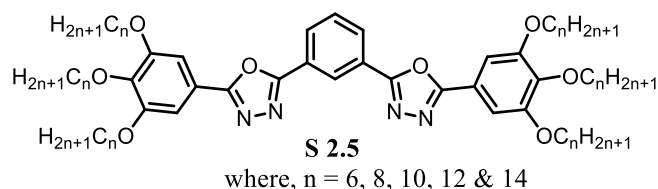
2.2 LITERATURE SURVEY

Hemi-disc shaped CLCs:

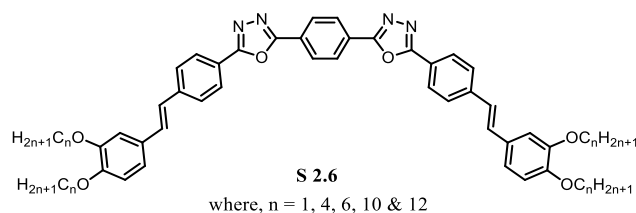
Half-disc configuration is one of the most favourable structural motifs to induce the columnar mesophase. Generally, hemi-discs exhibit columnar structures by pairing up of two molecules to accomplish the complete disc-shape through some strong non-covalent interactions like H-bonding, polarity induction or metal complexation. A number of hemi-disc molecules based on aromatic and/or heteroaromatic systems have been synthesized to achieve columnar mesomorphism. Some of the reported heterocycle-based hemi-disc derivatives are summarised as follows.

Kozhevnikov et al. (2008) synthesized two series of half-disc shaped Pt complexes derived from pyridine, **S 2.1** and **S 2.2**. Among the investigated derivatives, **S 2.1** showed columnar rectangular phase (Col_r), irrespective of the length of peripheral chains, whereas **S 2.2** displayed columnar phase hexagonal (Col_h) by co-miscible of two molecules into a disc. Introduction of a cyclopentene ring was found to stabilize the mesophase strongly when compared to **S 2.1**. They exhibited excellent solid state fluorescence, which was sensitive to method of preparation and tribological stimulation.

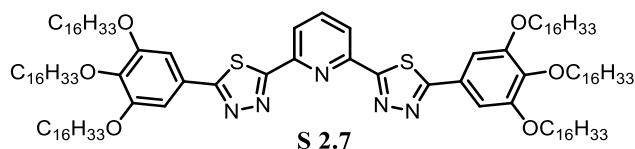
difference in transition temperatures. They featured Col_h mesophase constituting two molecules per each columnar stratum. Further, they were found to emit light in pure blue region.



Sivadas et al. (2014) reported a series of molecules **S 2.6** possessing pseudodiscoidal shape; these compounds displayed columnar phase with hexagonal and oblique lattice. Further, the derivatives with longer alkyl chains exhibited supergelation property in nonpolar solvents showing very high thermal and mechanical stability. Surprisingly, these materials don't possess any H-bonding motif. They showed self-standing gelation ability mainly by means of π -stacking interactions of the constituent molecules.

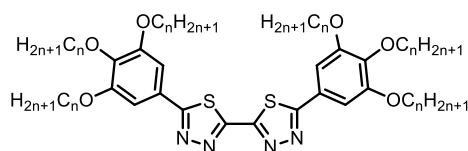


An hexacatenar pyridine-thiadiazole hybrid based compound, **S 2.7** was studied by Pradhan et al. (2016) as columnar liquid crystal. It was shown to self-organize into Col_h and Col_r at room temperature. It displayed super gelating ability with aggregation-induced emission, which was attributed to aromatic π - π interaction. Moreover, this mesogenic compound showed contrasting acidochromic behaviour in solution, LC film and gel states.



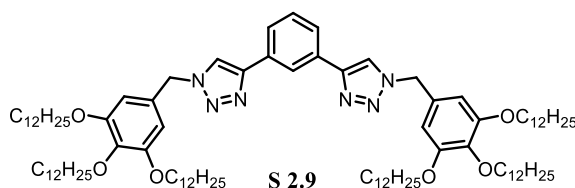
Yadav et al. (2017) synthesized a series of new bis-1,3,4-thiadiazole derivatives with varying alkoxy termini, **S 2.8**. The derivative owing hexyloxy chains exhibited columnar hexagonal mesomorphism at RT. Further studies on their material properties revealed that, this particular derivative demonstrated gelation property in various solvents due to intense π - π interaction and van der Waals attraction experienced by the

saturated alkyl chains. Because of the strong donor-accepter interactions, these materials showed bright blue emission. Also, their electroluminescence ability was investigated.



S 2.8 where, $n = 6, 8 \text{ \& } 10$

In a study Nguyen et al. (2017), a columnar mesogenic material carrying two polar 1,2,3-triazolyl substitutions, S 2.9, was found to exhibit two distinct Col_h phases as function of temperature. Especially, the columnar LC phase possessed by this material displayed a high response to external AC E-field, showing the alignment either perpendicular (homeotropic) or parallel (planar) to ITO substrate. Finally, the authors revealed that, the conductivity of the mesophase after the E-field-assisted alignment was 2.8 times higher than that of the non-aligned one.



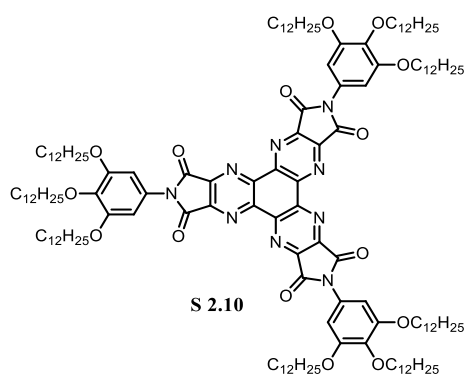
S 2.9

Star-shaped CLCs:

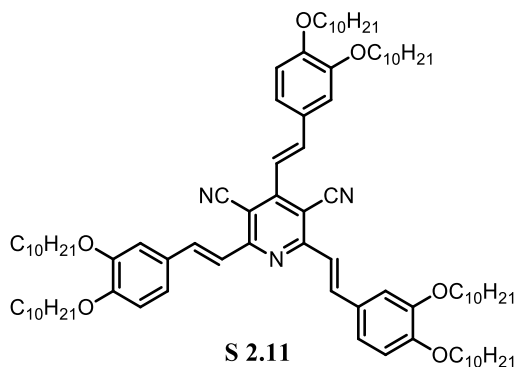
Star-shaped or ‘hekates’ having three-arm mesogens behave differently from conventional rod- and disk-shaped LCs because they have void space between the arms. They are emerging as one of the promising unconventional discotics due to their exceptional compatibility with columnar self-assembly (Detert et al. 2010; Lehmann 2009). Usually, the presence of voids between the arms of the star-shaped mesogens causes lowering of transition temperature with wide mesophase range and hence promotes the advantageous glassy state (Lehmann 2009). Because of their synthetic flexibility, a variety of heterocyclic systems can be introduced in order to achieve functional mesomorphism in hekates. Further, their material characteristics can be tailored by reducing the symmetry using different arms. Consequently, a large number of aromatic and heteroaromatic cores have been employed in the star-shaped designs to accomplish the columnar mesophases along with essential functional properties for

their applications in various devices. Some of the hecates derived from various heterocycles are discussed below:

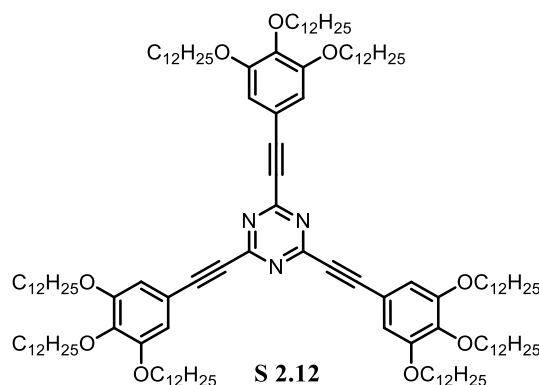
Pieterse et al. (2001) synthesized a star-shaped hexaazatriphenylene discotic mesogen as electron deficient material, **S 2.10**. It showed Col_h mesomorphism and featured photo induced electron transfer ability with poly (3-hexylthiophene) as a donor. Therefore, the above mentioned strategy provides a route to develop similar type of mesogens for the potential use in photovoltaic devices.



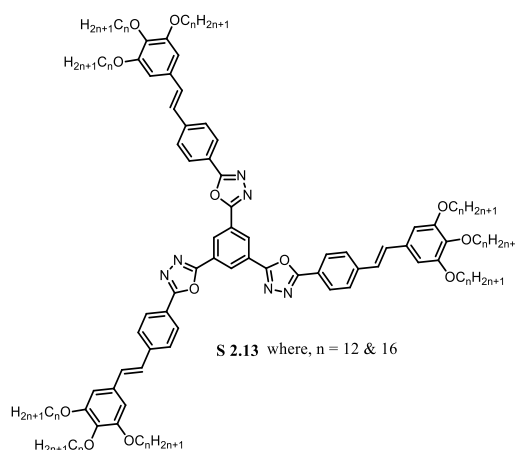
Attias et al. (2002) designed and synthesized a new class of discotics based on 3,5-dicyano-2,4,6-tristyryl core, **S-2.11**. Evidently, it could be self-assembled into 2-D columnar hexagonal by antiparallel arrangement of two molecular units to form disc-shaped dimers. Also, the authors studied the electrochemical and photophysical properties in solution state. The electron affinity of central pyridine ring was further increased by two cyano groups, which favoured the electron injection. This DLC was shown to possess permanent dipole moment, acting perpendicular to the columnar axis in order to favour strong dipolar interaction and consequently, a long-range intracolumnar order appears to offer high carrier mobility.



A C_3 -symmetric discotic molecule with tri-azaheterocycle core, **S 2.12** was synthesized by Pieterse et al. (2003) and they were studied its optoelectronic properties. According to the authors, it segregated into a columnar phase, but they failed to predict the exact symmetry of the Col mesophase. In addition, it showed UV/Vis absorption and emission with considerable solvatochromism.

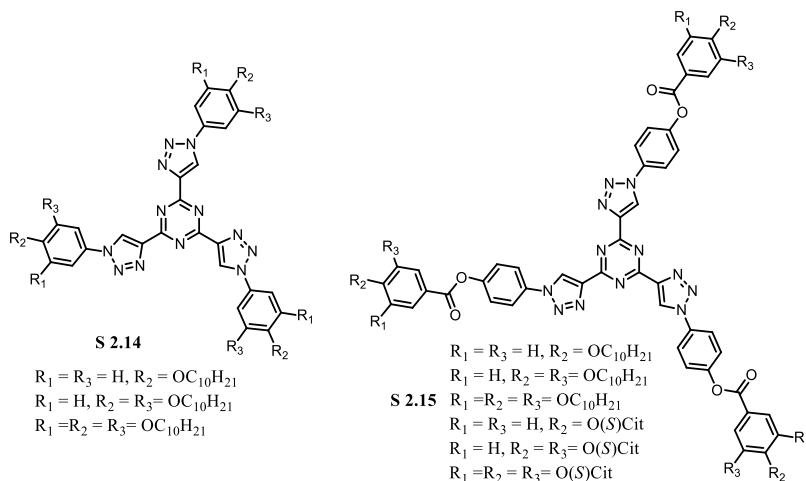


In an attempt to study the octupolar molecules, Varghese et al. (2009) designed and synthesized two oxadiazole derivatives, **2.13**. Both of them exerted Col_h phase and transformed into glassy state without disturbing the columnar order. Further, they exhibited spontaneous concentration dependent hierarchical self-assembly from spheres to fibrous gels and strong discrete fluorescence at various aggregated states.

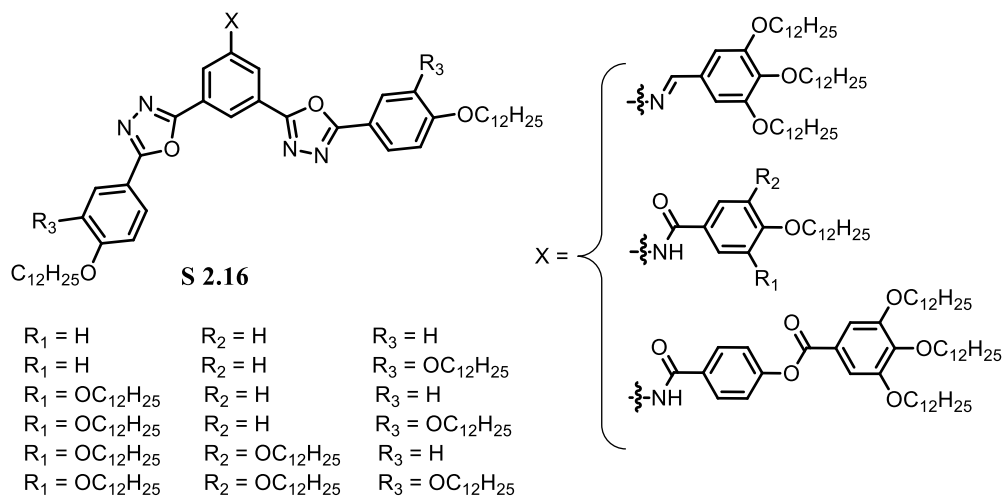


To understand the behaviour of mixed heterocyclic derivatives, Beltrán et al. (2010) prepared a series of compounds based on tris(triazolyl)triazine core, **S 2.14** using “click chemistry” protocol. These materials were found to self-assemble in Col_h phase at room temperature and they were intense blue fluorophores both in solution as well as solid states. Recently, structurally similar compounds (**S 2.15**) with extended arms

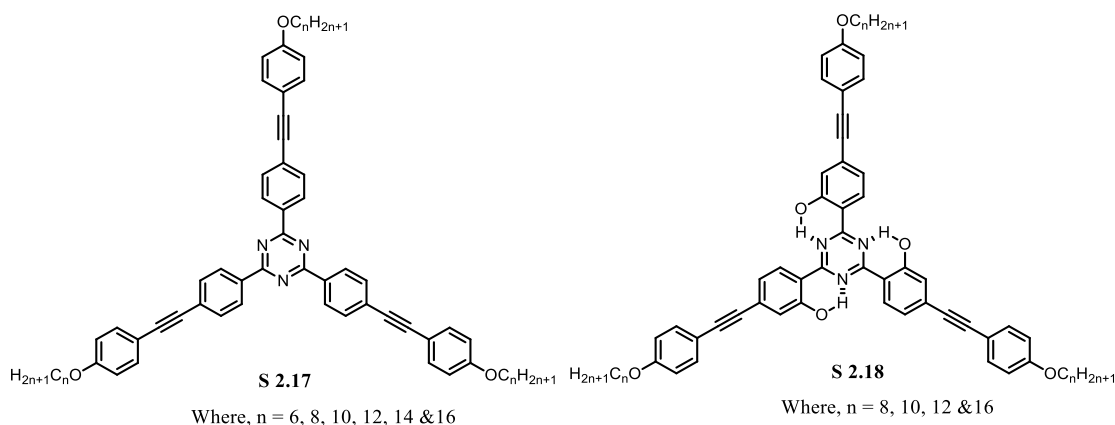
were reported by Beltrán et al. (2012). These compounds exhibited Col_h assembly by adopting the antiparallel alignment of two molecules in polar conformation rather than the C_3 conformation. They also emitted light in blue region with higher quantum yield than that of **S 2.14** series of compounds. Interestingly, all the members of the **S 2.14** featured solvatochromism, but not **S 2.15** derivatives.



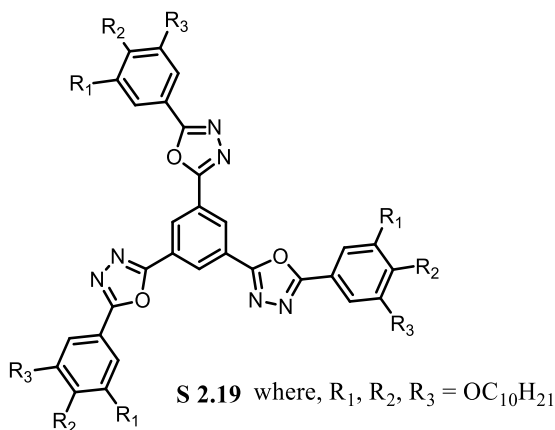
Westphal et al. (2013) synthesized and characterized a series of unsymmetrical star-shaped discotics bearing amide, imine, and ester functionalities with varying peripheral chains (**S 2.16**). The results revealed that, variation in the length and number of linear alkoxy terminals of any of the arms in this design exerted significant changes in their material properties, including mesomorphism, absorption and luminescence. Evidently, most of the members of the series showed Col_h assembly with high fluorescence.



A series of 1,3,5-triazine based LCs (**S 2.17**) synthesized by Lee and Yamamoto (2002) was shown to possess disordered columnar phase with high fluorescence quantum efficiency. Similarly, Jiao et al. (2015) synthesized a series of C_{3h} -symmetric molecules, **S 2.18** by incorporating hydroxyl groups at suitable positions. The OH functionality has involved in strong intramolecular H-bonding with central triazine core, thereby planarizing the core and hence inducing the stable columnar mesophase with hexagonal symmetry.



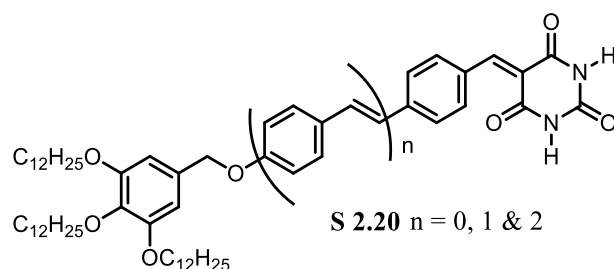
In another report, Pradhan et al. (2016) studied star-shaped molecules based on 2,4,6-triazine central core attached to symmetrically substituted 1,3,4-oxadiazole arms, **S 2.19**. According to the authors, increasing the number of peripheral chains would stabilize the columnar mesomorphism with lowering the isotropization point. Further, they studied their electrochemical and optical properties. Also **S 2.19** was shown to possess blue and green emission with narrow band gap. Surprisingly, the material overcome from tremendous aggregation emission quenching, possibly due to several different diastereomeric conformations in the columnar packing.



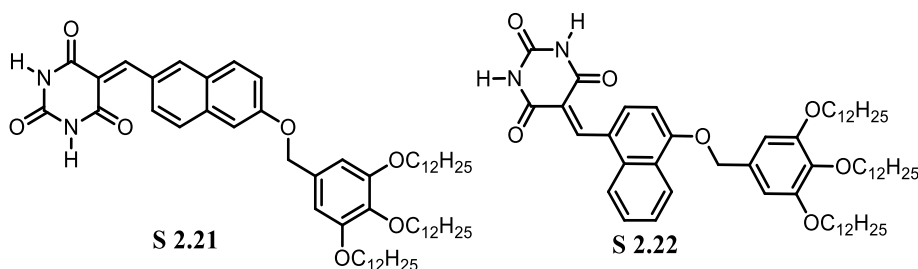
Wedge- and tapered-shaped CLCs:

In the unconventional columnar LCs, wedge and tapered-shaped structures also play an important role. Generally, they show columnar morphology mainly by supramolecular strategy. Usually, the groups at the focal point of the wedge/tapered molecules are responsible for the formations of disc-like architectures conferring the columnar mesophases. Such mesogens derived from heterocycles are rarely explored. A few of them have been highlighted below:

Yagai et al. (2011) studied three wedge-shaped barbituric acid derivatives, which offered supramolecular CLC phases with rectangular structure by the formation of catenation, *i.e.* formation of macrocycles *via* H-bonding. However, in methylcyclohexane solution state, they behaved differently; depending on the number of π -conjugated repeating units, they formed nano-rings of different diameter, *viz.* 25, 36 and 40 nm.

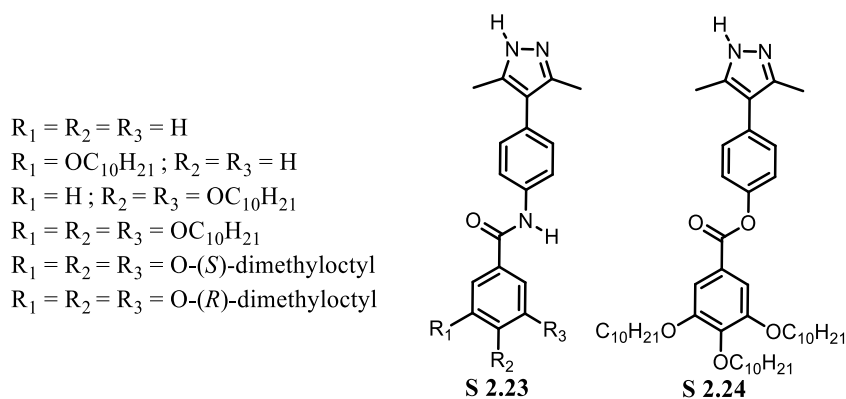


The same group reported a regeoisomeric pair of naphthalene derivatives bearing barbituric acid Yagai et al. (2012). The observed dissimilar thermotropic mesomorphism (S 2.21 and S 2.22 exhibited Col_r and Col_h , respectively) indicated the striking impact of regeoisomrism on LC properties. The compounds also formed nano ring and nano rod structures by hierarchical organization of hexameric rosettes.

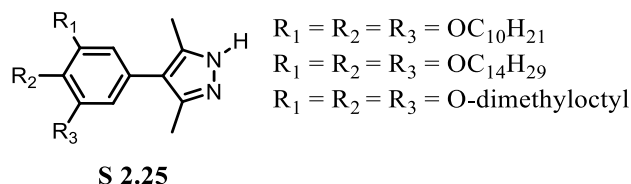


A series of taper-shaped mesogens derived from 4-aryl-1H-pyrazoles, S 2.23 was reported by Moyano et al. (2013). Among the six compounds, the trialkoxy-

substituted derivatives were found to be columnar liquid crystalline *via* the formation of supramolecular aggregates. When the amide functionality was replaced by ester, the resultant material, **S 2.24** showed exactly similar mesomorphism, suggesting that pyrazole ring at the tip plays a deciding role for the formation LC phase in these tapered structures. Further, the authors explored the optical properties of mesogenic materials and found luminescence in the visible region.



On continuing the efforts on pyrazole derivatives, Blanco et al. (2016) synthesized a set of pyrazole compounds, **S 2.25** by adopting Henry and Michael reaction protocol. These compounds exhibited supramolecular CLCs in spite of simple molecular geometry and found to be fluorescent materials with relatively high QY.

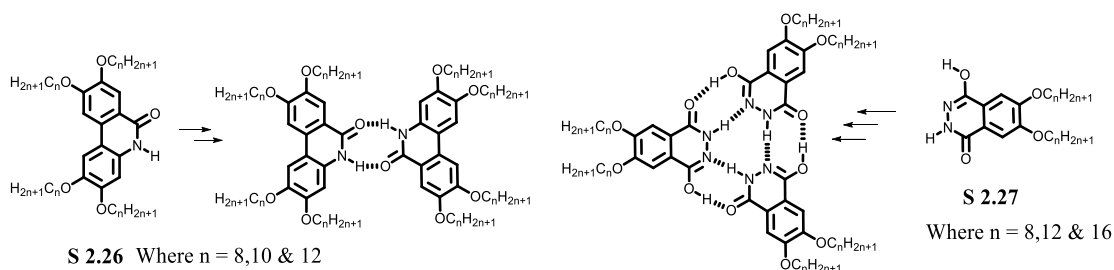


H-bonding CLCs:

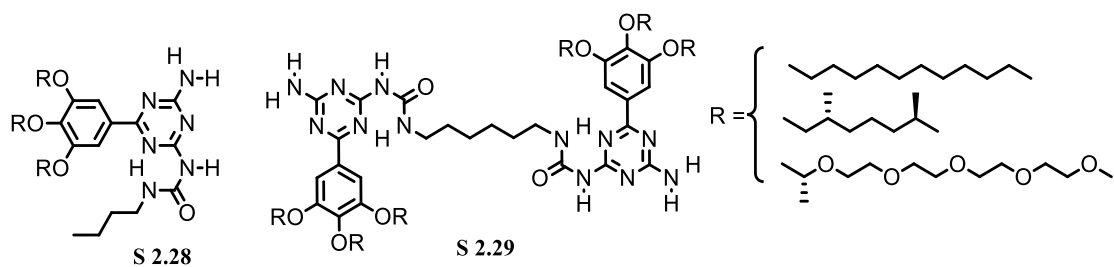
As mentioned earlier, H-bonding induced columnar liquid crystalline materials are one of the fascinating groups of stimuli responsive LCs. In such systems, mesomorphic properties can be tuned by simple tailoring the molecular structures. Till now, a large number of H-bonding scaffolds with appropriate design have been investigated to obtain columnar mesophases. Among the various class of compounds, carboxylic acids, amides, pyridines, polyalcohols, carbohydrates, oligopeptides, pyrazoles, triazines, melamines, *etc.* are widely studied H-bonding motifs. Particularly, heteroaromatic systems capable of forming H-bond are much advantageous as they deliver highly stable and ordered mesophases through well-defined H-bonding

interactions. Some of the H-bonding induced heterocyclic CLCs are discussed in the following paragraphs.

Kleppinger et al. (1995) reported first rational molecular design of a predictable self-assembled disk-like supramolecule, **S 2.26** that forms a columnar mesophase. Here, as α -pyridone molecules have a strong tendency of forming discotic dimers, they self-assembled in columnar hexagonal phase. Similarly, (Suarez et al. 1998) used trimeric strategy in developing a series of properly substituted phthalhydrazides, **S 2.27**. Evidently, these molecules formed supramolecular disk through definite H-bonding network, generating columnar architectures with rectangular and hexagonal fashion.

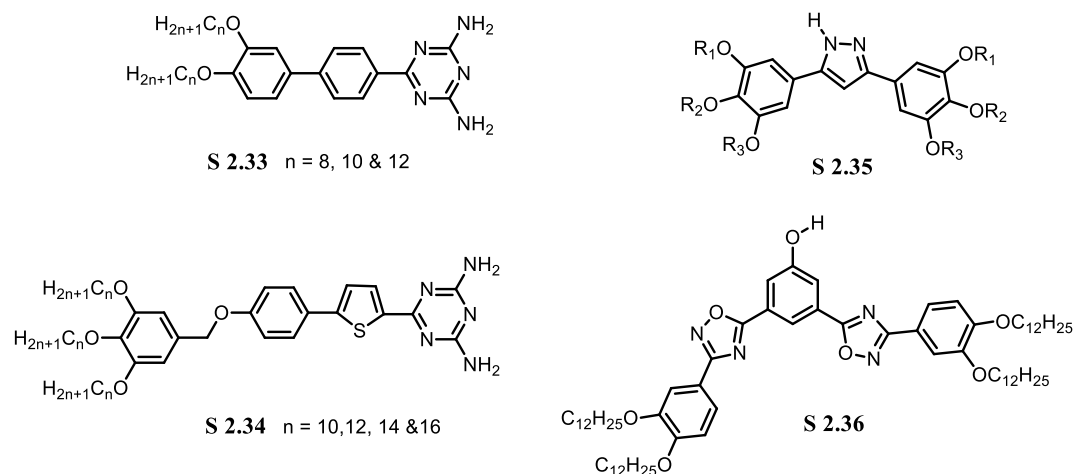


Hirschberg et al. (2000) studied wedge-shaped ureidiotriazine derivatives (**S 2.28**), which were found to form stable Col_h phase by means of disc-like dimers driven through self-complementary quadruple hydrogen bonding. Tethering the two molecules with an appropriate spacer resulted in bifunctional derivatives, **S 2.29**, which also generated columnar mesophases.

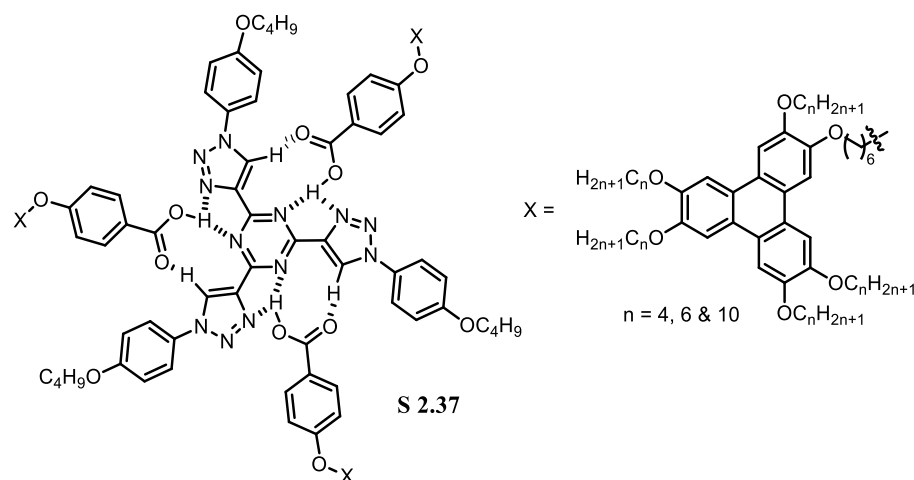


With a different ideology, Lee et al. (2001) prepared a H-bonded complex by coalescing two complementary compounds, *i.e.* benzotri(imidazole) and tri-substituted benzoic acid in 1:3 ratio (**S 2.30**). The yielded complex formed the stable Col phase and the acrylate moiety on the termini of the peripheral chains was found to be photopolymerized to a covalently fixed LC state. On removal of central benzotri(imidazole) core, it generated a nanoporous polymer film containing ordered hexagonal channels.

On the similar lines, a family of hemi-disc shaped 1*H*-pyrazole derivatives, **S 2.35** were synthesized with varying the length, number and type of fluidic chains (chiral and achiral) (Beltrán et al. 2009). As investigated, the pyrazoles assembled into Col_h mesophase by the formation of discotic dimeric units *via* central pyrazole ring and exerted characteristic fluorescence due to the donor-accepter interactions. Likewise, Gallardo et al. (2011) prepared bent-rod shaped 1,2,4-oxadiazoles bearing polar substituents, *viz.* I, NO₂, NH₂, and OH groups, **S 2.36**. These banana-shaped molecules interestingly showed columnar mesomorphism by producing a dimer, trimer, or tetramer inside a single disc, depending on the type of H-bonding groups involved.



Feringán et al. (2016) prepared a series of star-shaped 1:3 hydrogen bonded complexes, **S 2.37** using electron rich hexaalkoxy triphenylene and electron deficient tris(triazolyl)triazine nonmesogenic components. These complexes were emerged into stable coaxial columnar assemblies with remarkable intracolumnar order. The significant intramolecular electronic communication between the donors and acceptor resulted in high ambipolar charge mobility in the complexes.



2.3 OVERVIEW OF LITERATURE SURVEY

Based on the thorough literature survey on discotic liquid crystals derived from various heterocyclic moieties, the following important inferences have been made:

- An excellent synthetic flexibility of the heterocycles compared to aromatics/polyaromatics facilitates preparation of a variety of functional discotics.
- Introducing the heteroaromatics in the core region stabilizes the columnar mesomorphism by the strong intermolecular as well as intracolumnar donor-accepter interactions.
- The heterocyclic motifs allow to access imperative columnar phases by the diverse non-discoidal molecules like star, wedge, tapered, bent and rod-shapes because of their rich mesomorphism.
- The closed type H-bonding ability of heterocycles induces the LC phase in the non-mesogenic systems by the strong intra- and intermolecular H-bonding. Such mesophases were shown to possess highly dynamic response towards the external stimuli.
- The presence of electronegative atoms like O, S and N in heterocycles provides a reduced symmetry, a strong lateral and/or longitudinal polar induction and uneven distribution of the electron density, leading to an intense donor-accepter interaction. These features allow us to tune the photophysical and electronic properties at the mesogenic state.

- The slight variation in D-A interactions in the basic structure of the heterocycle-based mesogens, it is possible to tune the emission colour.
- The electron deficient nature of the aromatic heterocycles imparts the *n*-type semiconducting property to columnar mesophases, which are rarely reported. These materials can be employed in wide variety of optoelectronic devices.
- Overall there is an extensive scope for the proper designing of new molecular structures to achieve the prospective columnar mesomorphism with tuneable optical and electronic properties.

2.4 SCOPE AND OBJECTIVES

In this advanced era, discotic liquid crystalline (DLCs) materials are being successfully employed in the wide range of fields ranging from electronics to biomedical, because of their unique properties (Goodby et al. 2014; Meier et al. 2012; Wang 2016; Wang et al. 2017; Wang and Li 2016, 2018). Especially, tailoring the molecular structures in order to achieve the desirable functional properties in mesomorphic state is important. As discotic liquid crystalline materials possess good prospects for the development of new electro-optical devices like organic field effect transistors (OFETs), organic light emitting diodes (OLEDs) and organic photovoltaic devices (OPVs), design and development of new discotic mesogens will have bright future.

In this context, enormous research activities are progressing in the field of DLCs during last two decades. The literature review reveals that, the discotic materials with coexistence of both good semiconducting properties and absorption or/and emission of light over the broad range of electromagnetic spectrum are limited. In the proposed research work, it has been planned to design new heterocycle-based liquid crystals featuring unconventional molecular geometry by incorporating the donor-accepter configurations in the core system. This intriguing strategy also helps to achieve the long range order, which favours the high charge carrier mobility.

The present work has been aimed to develop the new optimized synthetic routes to offer improved yields for the newly designed heterocyclic mesogens. It was also contemplated to study structure-property relationship of newly synthesized molecules. Effect of core size, linking groups, length of peripheral chains and type of heteroatoms

on their mesomorphic, optical and electrochemical properties would be studied in detail. Further, it has been thought of fabricating optoelectronic devices using new mesogens in order to study their device performance.

Based on above mentioned facts and thorough literature survey, following main objectives have been intended in the present research work.

1. To design and synthesize new heterocyclic derivatives with variety of geometrical configurations capable of forming stable columnar phases
2. To investigate and optimize new synthetic methods to synthesize the newly designed molecules
3. To characterize structurally all intermediates and final compounds by FTIR, $^1\text{H-NMR}$, $^{13}\text{C-NMR}$ and mass spectral techniques followed by elemental analysis
4. To investigate and characterize liquid crystalline properties by using the combination of advanced techniques like Differential Scanning Calorimetry (DSC), Polarized Optical Microscopy (POM) and small angle temperature dependent X-Ray Diffraction (XRD)
5. To study photophysical properties of new compounds by means of UV-Visible and fluorescence spectroscopic techniques
6. To evaluate the electrochemical properties of selected new liquid crystalline compounds by Cyclic Voltammetry (CV) and theoretical simulations (DFT)
7. To carry out preliminary OLED device fabrication studies using selected liquid crystalline materials as an emissive component
8. To study their structure-property correlations

In summary, the heterocyclic derivatives are reviewed to be promising aromatic electron deficient candidates for design of new liquid crystals. They are supposed to play an active role in designing new molecules because of their intense D-A interactions. It is expected that newly designed molecules carrying polar functionalities would show discotic liquid crystalline behaviour over a wide range of temperature. Further, it is hoped that the new molecules would show expected functional properties in their mesophases. Some of the chemical and physical aspects which are essential for the stability of mesophase would be taken care strictly from the point of view of their device fabrications. It is also hoped that the newly investigated liquid crystals may find

applications in other fields like sensors, LCD displays *etc.* The intermediates obtained during the synthesis of target liquid crystals may be useful in the field of medicinal chemistry.

SYNTHESIS AND STRUCTURAL CHARACTERIZATION OF NEW HETEROCYCLIC SYSTEMS

Abstract

This chapter describes molecular design and different synthetic protocols adopted for the synthesis of various heterocyclic derivatives bearing several alkoxy substituted aromatic motifs. Further, it includes structural characterization of the new molecules using spectral techniques.

3.1 INTRODUCTION

Since the discovery of DLCs, ample number of designing strategies and their synthesis have been explored to realise stable columnar mesomorphism. As the recent literatures suggest that, unlike traditional design, a typical columnar mesogen should own the one or more aromatic/heteroaromatic rings surrounded by the saturated chains of optimum lengths, irrespective of shape of the molecules. Generally, there are two widely used protocols for the design, *i.e.* attaching the alkyl chains to polyfunctional core or building the entire molecule by coalescing the alkyl substituted moieties. The latter method is the most accessed strategy because of the lack of availability of suitable polyfunctional aromatic systems. Synthesis of such compounds are often not straightforward, which involves multistep synthesis. As the present work focused on the heterocyclic structures, we mostly built the mesogenic molecule by condensation of one or more alkyl substituted aromatics. Also, the number of synthesis steps have been reduced and optimized to get pure compounds in good yield. In the preparation of LCs, the purification of target materials is most challenging part due to formation of side products having almost same R_f along with target compounds. Therefore, the current work also concentrated on development of purification methods to obtain high pure LC materials.

The following sections cover a detailed account on design and synthesis of six new series of heterocyclic molecules (**HT₁₋₃₅**, **Series-1** to **6**). They also elaborate in depth structural characterization of newly synthesized intermediates and target compounds.

3.2 EXPERIMENTAL

In this section, design, synthesis and characterization of new heterocyclic compounds, *viz.* **HT**₁₋₇ (**Series-1**), **HT**₈₋₁₀ (**Series-2**), **HT**₁₁₋₂₀ (**Series-3**), **HT**₂₁₋₂₆ (**Series-4**), **HT**₂₇₋₃₁ (**Series-5**) and **HT**₃₂₋₃₅ (**Series-6**) have been dealt.

3.2.1 Materials and methods

All the required special chemicals, common organic and inorganic reagents (AR/reagent grade) were purchased from Sigma Aldrich, Merck, Spectrochem and SD's Fine Chem. Ltd. companies and used without any further purifications. All the solvents used to carry out the reactions were analytical grade, they were procured from local companies and dried using standard procedures. The reactions were performed under inert (Ar/N₂) atmosphere and completion of the reaction was monitored by TLC technique. Merck made aluminium sheets coated with silica gel were used for thin layer chromatography (TLC). The synthesized compounds were purified by simple recrystallization and chromatographic separations using silica gel of mesh size 100-200 and 230-400 (Merck made). The chemical structures of new intermediates and final compounds were established by set of techniques. ¹H NMR spectra were recorded on Bruker machine at 500 MHz and ¹³C NMR at 125 MHz using CDCl₃ solvent (Sigma-Aldrich made) and chemical shifts were reported in δ (Hz) related to tetramethylsilane (TMS) as internal standard. FT-IR spectra were obtained by Bruker alpha Fourier transform IR spectrometer using ATR method and only key absorption bands were summarized in wave numbers (cm⁻¹). Elemental analysis was performed on a Carlo-Erba Flash 1112 analyser. Mass spectrometric analysis was carried out using MALDI-TOF mass spectrometer.

3.2.2 Design and synthesis of **HT**₁₋₇ (**Series-1**)

In **Series-1**, flying bird-shaped D-A-D configured molecules (**HT**₁₋₄) carrying electron deficient 3-cyano-2-pyridone as central core substituted by two electron rich dialkoxyphenyl rings at its 4th and 6th positions, were designed keeping in view that, the lactam core is expected to facilitate the formation of disc-like H-bonded dimer. Further, in order to examine the role of H-bonding, similar shaped 2-methoxy-3-cyanopyridine derivatives (**HT**₅₋₇) containing no CONH linkage in the ring with the same substituents have been designed, as pictured in **Fig 3.1**. A series of seven derivatives has been

designed by varying the length of the alkoxy chains attached to both the donors in order to understand the structure-property relationships. Here, presence of donor-acceptor configuration would induce the significant intramolecular charge transport property. Consequently, this feature would result in intense fluorescence and high redox activity.

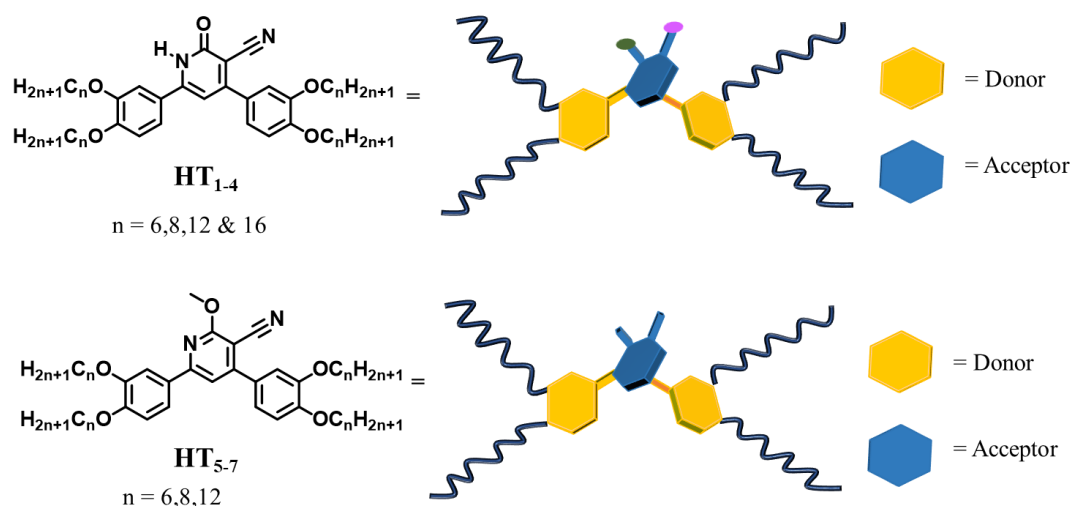
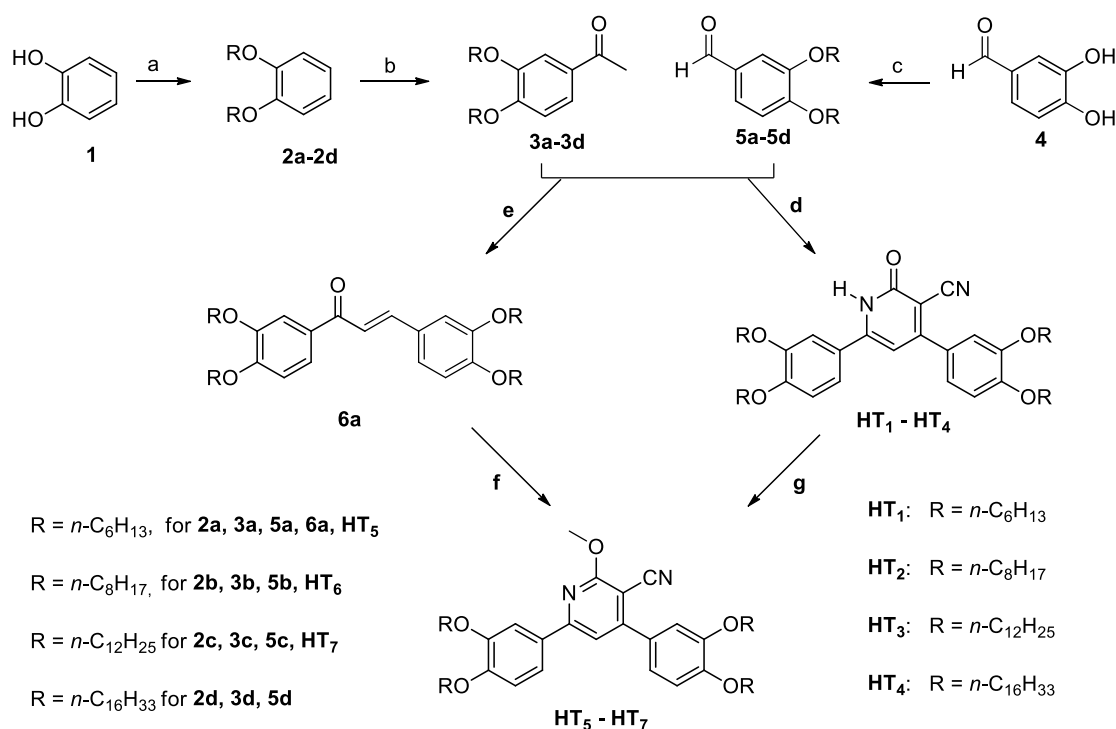


Figure 3.1 Design of new D-A-D configured molecules **HT₁₋₇** of **Series-1**

The synthetic approach for the preparation of newly designed cyanopyridone derivatives is depicted in **Scheme 3.1**. The key intermediates, *viz.* 3,4-dialkoxyacetophenones (**3a-d**) were prepared from catechol (**1**) by adopting Williamson's etherification method (Zhang et al. 2014), followed by Friedel Crafts acylation with acetyl chloride in good yield. Other intermediates 3,4-dialkoxybenzaldehydes (**5a-d**) were synthesized from 3,4-dihydroxybenzaldehyde (**4**) by alkylation using required *n*-alkyl bromides. Then, the precursors **3a-d** were reacted with the intermediates **5a-d** in presence of ethyl cyanoacetate and excess of ammonium acetate, to yield symmetrically substituted compounds **HT₁₋₄**, respectively. While synthesizing these cyanopyridones, precursors **3** and **5** substituted with similar alkoxy chains were used. Further, 2-methoxy-3-cyanopyridine derivatives, **HT₅₋₇** were prepared separately using different synthetic protocols. Here, **HT₁** was synthesized by Claisen-Schmidt condensation of aldehyde **3a** with ketone **5a** to give chalcone followed by cyclization of chalcone with malononitrile in presence of sodium methoxide. Since its yield was poor, an alternate method was used to obtain **HT₁**. In this method, compound **HT₁** was directly alkylated with methyl iodide in presence of a base to form

HT₅ in good yield. The other two compounds **HT**₆₋₇ were synthesized in good yield by the latter method using a similar procedure.



Scheme 3.1 Synthesis pathway for synthesis of **HT**₁₋₇. Reagents and conditions: a) RBr, K₂CO₃, KI, DMF, 70 °C, 70-85 %; b) CH₃COCl, anhydrous AlCl₃, dry DCM, -5-0 °C, 85-92%; c) K₂CO₃, RBr, DMF, 80 °C, 65-85%; d) Ethyl cyanoacetate, AcONH₄, EtOH, 70 °C, 25-40%; e) Aqueous KOH, EtOH, RT, 83 %; f) Malononitrile, NaOMe, MeOH, RT, 40 %; g) MeI, K₂CO₃, DMF, 45 °C, 85-90%

3.2.2.1 Results and discussion

The structures of all new key intermediates and cyanopyridone derivatives of **Series-1** were confirmed by a set of spectral techniques. For instance, FTIR spectrum of **HT**₁ showed prominent stretching bands at 2216 and 1653 cm⁻¹ indicating the presence of cyano and carbonyl groups, respectively (**Fig 3.2**). **Fig 3.3** depicts ¹H-NMR spectrum of **HT**₁ showing a sharp highly down fielded signal at 12.81 ppm and the unique singlet at 6.68 ppm, which confirms the successful construction of cyanopyridone ring by the cyclization reaction. The remaining aromatic protons resonated in between 7.50 and 7.00 ppm, four OCH₂ protons appeared as triplet at 4.10 and protons of hexyloxy chains occurred in between 2.00 and 0.90 ppm. Additionally,

its ^{13}C -NMR spectrum (**Fig 3.4**) showed higher frequency signals at 164 and 160 ppm due to carbonyl carbon and carbon carrying cyano groups, respectively which further confirmed the formation of central cyanopyridone ring. As expected, a number of signals have appeared at down field because of the secondary and tertiary carbons. The characteristic signal occurred at 69.64 ppm is due to OCH_2 group. Further, the base peak at 673.4553 of its MALDI-TOF mass spectrum (**Fig 3.5**) exactly matched with the calculated mass for the molecular formula $\text{C}_{42}\text{H}_{60}\text{N}_2\text{O}_5$. Likewise, structures of all the new compounds were identified and confirmed.

Some selected spectra:

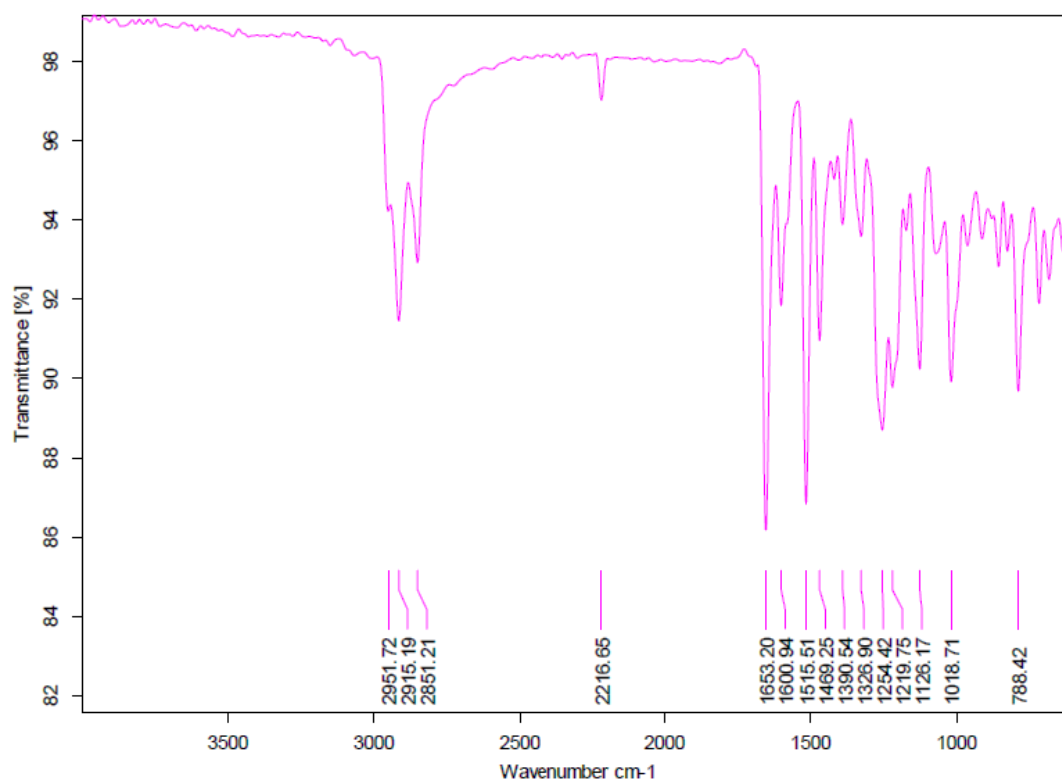


Figure 3.2 FTIR (ATR) spectrum of **HT₁**

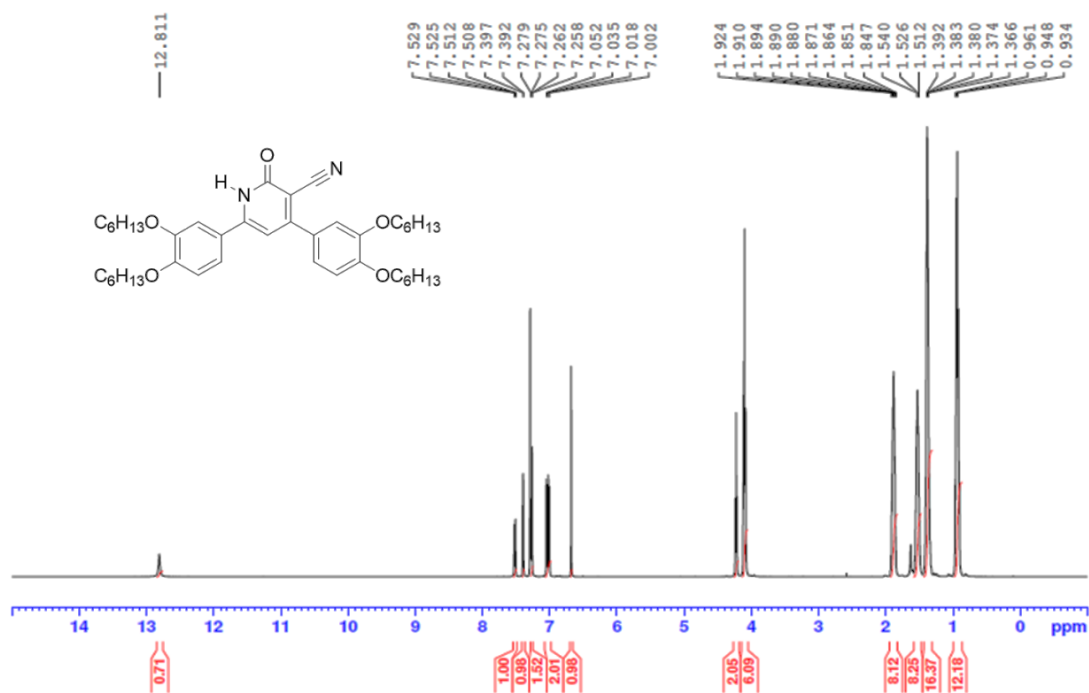


Figure 3.3 ^1H NMR (500 MHz) spectrum of **HT₁** recorded in CDCl_3

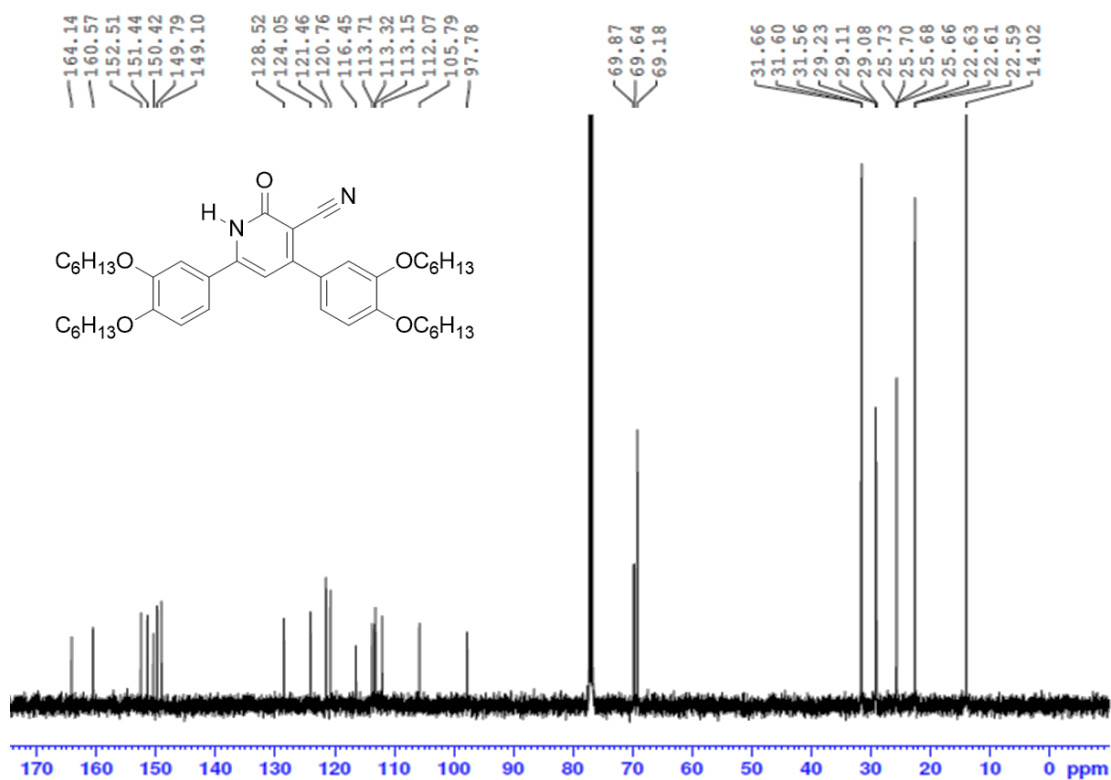


Figure 3.4 ^{13}C NMR (125 MHz) spectrum of **HT₁** recorded in CDCl_3

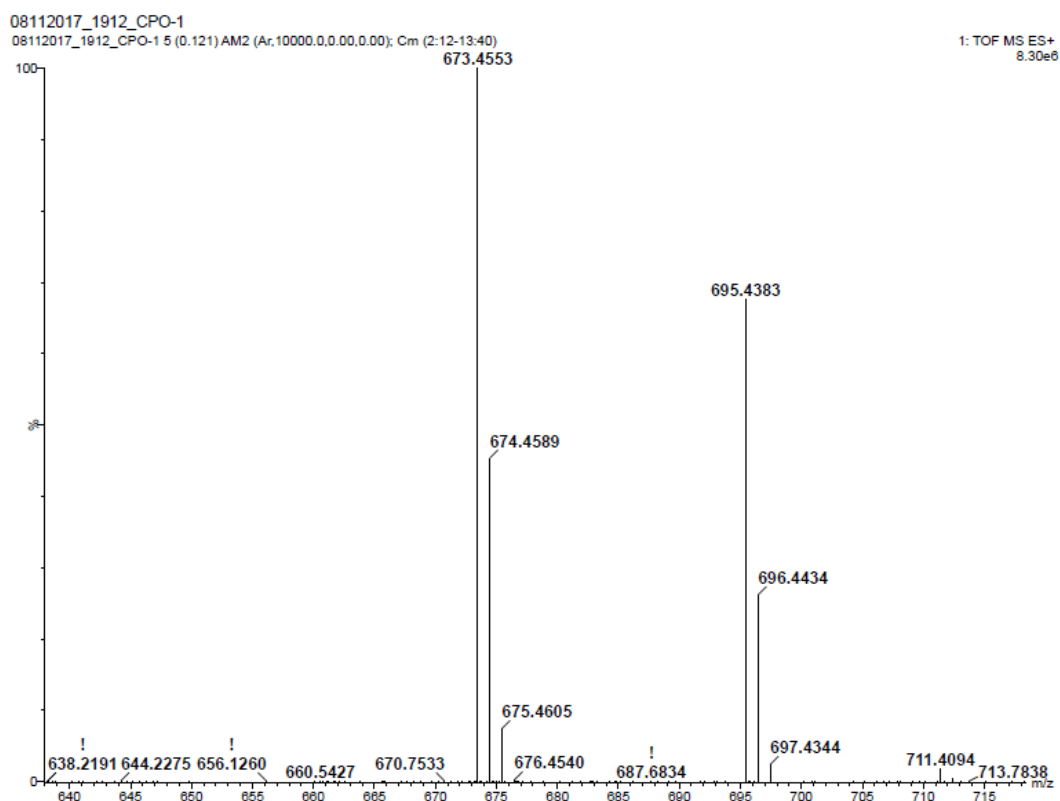


Figure 3.5: MALDI-TOF spectrum of **HT₁**

3.2.2.2 Experimental procedures

In the following section, detailed experimental protocols adopted to synthesize all the intermediates and final heterocyclic derivatives of **Series-1** are discussed. Also, their structural characterization data are included.

General procedure for the synthesis of 1-(3,4-bis(alkoxy)phenyl)ethanone (3a-d)

Under argon atmosphere, the compound 1,2-dihexyloxybenzene **2a** (2g, 7.18 mmol, 1 equiv.) was dissolved in 30 mL of dry DCM and cooled to $-5\text{ }^{\circ}\text{C}$ using NaCl/ice bath. To the stirred reaction mixture, anhydrous AlCl_3 (1 g 7.9 mmol, 1.1 equiv.) was added in small portions. Then, acetyl chloride (0.56 mL, 7.9 mmol, 1.1 equiv.) was added drop-wise and the mixture was stirred at $-5\text{ }^{\circ}\text{C}$. After 30 min, the mixture was warmed to room temperature and continue the stirring for another 30 min. The mixture was poured into 50 mL of ice-cooled water and the separated compound was extracted with DCM (2×50 mL). The combined DCM layers were washed with saturated NaHCO_3 , then with brine and evaporated to dryness. The crude product was recrystallized using methanol to get white solid product **3a**, (Yield, 92 %). FTIR (ATR): ν_{max} in cm^{-1} 2955, 2954, 2928 (Ar C-H), 2857 (Aliph C-H), 1669 (C=O), 1584 (Ar

C=C). ^1H NMR (CDCl_3 , 500 MHz): δ 7.55 (d, 1H, $J = 8.0$ Hz, Ar-H), 7.52 (s, 1H, Ar-H), 6.87 (d, 1H, $J = 8.5$ Hz, Ar-H) 4.06 (m, 4H, $2 \times \text{OCH}_2$), 2.56 (s, 3H, COCH_3), 1.88 – 1.81 (m, 4H, $2 \times \text{O-CH}_2\text{-CH}_2$), 1.49 (m, 4H, $2 \times \text{CH}_2$), 1.36 (m, 8H, $4 \times \text{CH}_2$), 0.92 (t, 6H, $J = 6.5$ Hz, $2 \times \text{CH}_3$). ^{13}C NMR (CDCl_3 , 125 MHz): δ 196.87, 153.52, 148.84, 130.25, 123.18, 112.33, 111.52, 69.11, 31.55, 29.07, 26.20, 25.65, 22.59, 13.99. Elemental Anal. Calcd for $\text{C}_{20}\text{H}_{32}\text{O}_3$ (%): C, 74.96; H, 10.06; Found: C, 74.95, H, 10.08.

The compounds **3b**, **3c** and **3d** were synthesized by adopting similar procedure as described for the synthesis of **3a**.

For **3b**, (Yield, 89 %). IR (ATR): ν_{max} in cm^{-1} 2958, 2952, 2928 (Ar C-H), 2855 (Aliph C-H), 1669 (C=O), 1583 (Ar C=C). ^1H NMR (CDCl_3 , 500 MHz): δ 7.54 (d, 1H, $J = 8.0$ Hz, Ar-H), 7.52 (s, 1H, Ar-H), 6.87 (d, 1H, $J = 8.0$ Hz, Ar-H) 4.06 (m, 4H, $2 \times \text{O-CH}_2$), 2.56 (s, 3H, COCH_3), 1.87-1.83 (m, 4H, $2 \times \text{OCH}_2\text{-CH}_2$), 1.48 (m, 4H, $2 \times \text{CH}_2$), 1.37- 1.30 (m, 16H, $8 \times \text{CH}_2$), 0.89 (t, 6H, $J = 6.5$ Hz, $2 \times \text{CH}_3$). ^{13}C NMR (CDCl_3 , 125 MHz): δ 196.85, 153.53, 148.84, 130.26, 123.18, 112.36, 111.54, 69.17, 31.81, 29.23, 26.20, 26.00, 22.67, 14.09. Elemental Anal. Calcd for $\text{C}_{24}\text{H}_{40}\text{O}_3$ (%): C, 76.55; H, 10.71. Found: C, 76.58; H, 10.61.

For **3c**, (Yield, 90 %). IR (ATR): ν_{max} in cm^{-1} 2958, 2953, 2927 (Ar C-H), 2849 (Aliph C-H), 1666 (C=O), 1590 (Ar C=C). ^1H NMR (CDCl_3 , 500 MHz): δ 7.55 (d, 1H, $J = 8.5$ Hz, Ar-H), 7.52 (s, 1H, Ar-H), 6.87 (d, 1H, $J = 8.5$ Hz, Ar-H) 4.06 (m, 4H, $2 \times \text{OCH}_2$), 2.56 (s, 3H, COCH_3), 1.87 – 1.81 (m, 4H, $2 \times \text{OCH}_2\text{-CH}_2$), 1.48 (m, 4H, $2 \times \text{CH}_2$), 1.33 (m, 32H, $16 \times \text{CH}_2$), 0.89 (t, 6H, $J = 6.5$ Hz, $2 \times \text{CH}_3$). ^{13}C NMR (CDCl_3 , 125 MHz): δ 196.88, 153.54, 148.84, 130.26, 123.18, 112.37, 111.55, 69.13, 30.81, 29.50, 26.20, 26.01, 22.69, 14.11. Elemental Anal. Calcd for $\text{C}_{32}\text{H}_{56}\text{O}_3$ (%): C, 78.63; H, 11.55; O, 9.82. Found: C, 78.63; H, 11.58; O, 9.78.

For **3d**, (Yield, 90 %). IR (ATR): ν_{max} in cm^{-1} 2955, 2951, 2930 (Ar C-H), 2859 (Aliph C-H), 1668 (C=O), 1593 (Ar C=C). ^1H NMR (CDCl_3 , 500 MHz): δ 7.55 (d, 1H, $J = 8.5$ Hz, Ar-H), 7.53 (s, 1H, Ar-H), 6.88 (d, 1H, $J = 8.5$ Hz, Ar-H) 4.06 (m, 4H, $2 \times \text{OCH}_2$), 2.57 (s, 3H, COCH_3), 1.89 – 1.82 (m, 4H, $2 \times \text{OCH}_2\text{-CH}_2$), 1.49 (m, 4H, $2 \times \text{CH}_2$), 1.34 (m, 48H, $24 \times \text{CH}_2$), 0.89 (t, 6H, $J = 6.5$ Hz, $2 \times \text{CH}_3$). ^{13}C NMR (CDCl_3 , 125 MHz): 196.89, 153.54, 148.85, 130.26, 123.18, 112.37, 111.54, 69.14, 31.94,

29.65, 26.22, 25.99, 22.70, 14.12. Elemental Anal. Calcd for C₄₀H₇₂O₃ (%): C, 79.94; H, 12.08. Found: C, 79.86; H, 12.03.

General procedure for the synthesis of 4,6-bis(3,4-dialkoxyphenyl)-2-oxo-1,2-dihydropyridine-3-carbonitriles, HT₁₋₄

An equimolar mixture of 1-(3,4-dihexyloxyphenyl)ethanone **3a** (2 g, 6.24 mmol, 1equiv.) and 3,4-dihexyloxybenzaldehyde **5a** (1.91 g, 6.24 mmol, 1 equiv.) was taken in 50 mL of ethanol. The mixture was warmed to 60 °C to get clear solution. Then, ethyl cyanoacetate (0.8 mL, 6.9 mmol, 1.1 equiv.) and ammonium acetate (7.2 g, 93.6 mmol, 15 equiv.) were added and the mixture was heated to 70 °C for 12 h. After completion of the reaction, the obtained precipitate was filtered and washed with ethanol to obtain yellow solid, **HT₁**. The crude was purified by column chromatography with silica gel of 100-200 mesh using 1:3 pet-ether (60-70°C) and dichloromethane as eluent (Yield, 40 %) IR (ATR): ν_{\max} in cm⁻¹ 2922 (Ar C-H), 2854 (Aliph C-H), 2217 (C≡N), 1653 (C=O), 1600 (Ar C=C). ¹H NMR (CDCl₃, 500 MHz): δ 12.81 (s, 1H, CONH), 7.52 (dd, 1H, *J* = 8.5, 2.0 Hz, Ar-H), 7.39 (d, 1H, *J* = 2.5 Hz, Ar-H), 7.27 (dd, 1H, *J* = 8.0, 2.0 Hz, Ar-H), 7.26 (d, 1H, *J* = 2.0 Hz, Ar-H), 7.04 (d, 1H, *J* = 8.5 Hz, Ar-H), 7.01 (d, 1H, *J* = 8.0 Hz, Ar-H), 6.68 (s, 1H, pyridone-H), 4.22 (t, 2H, *J* = 6.5 Hz, OCH₂), 4.08 (m, 6H, 3×OCH₂), 1.92-1.85 (m, 8H, 4×OCH₂-CH₂), 1.53 (t, 8H, *J* = 7.0 Hz, 4×CH₂), 1.39-1.36 (m, 16H, 8×CH₂), 0.95 (t, 12H, *J* = 6.5 Hz, 4×CH₃). ¹³C NMR (CDCl₃, 125 MHz): δ 164.14, 160.57, 152.51, 151.44, 150.42, 149.79, 149.10, 128.52, 124.05, 121.46, 120.76, 116.45, 113.71, 113.23, 112.07, 105.79, 97.78, 69.56, 31.60, 29.14, 25.69, 22.61, 14.02. Elemental Anal. Calcd for C₄₂H₆₀N₂O₅ (%): C, 74.96; H, 8.99; N, 4.16. Found: C, 74.81; H, 9.261; N, 4.10. HRMS (ESI+) exact mass calculated for C₄₂H₆₀N₂O₅ (M+1): 673.4502, Found: 673.4553.

The compounds **HT₂₋₄** were synthesized by adopting similar procedure as described for the synthesis of **HT₁**.

For **HT₂**, yellow amorphous solid (Yield = 36 %). IR (ATR): ν_{\max} in cm⁻¹ 2915 (Ar C-H), 2851 (Aliph C-H), 2216 (C≡N), 1653 (C=O), 1600 (Ar C=C). ¹H NMR (CDCl₃, 500 MHz): δ 12.95 (s, 1H, CONH), 7.52 (dd, 1H, *J* = 8.5, 2.0 Hz, Ar-H), 7.40 (d, 1H, *J* = 2.0 Hz, Ar-H), 7.28 (dd, 1H, *J* = 8.0 Hz, 2.0 Hz, Ar-H), 7.25 (d, 1H, *J* = 2.0

Hz, Ar-H), 7.04 (d, 1H, $J = 8.5$ Hz, Ar-H), 7.01 (d, 1H, $J = 8.5$ Hz, Ar-H), 6.68 (s, 1H, pyridone-H), 4.22 (t, 2H, $J = 6.5$ Hz, OCH₂), 4.08 (m, 6H, 3×OCH₂), 1.90-1.85 (m, 8H, 4×OCH₂-CH₂), 1.54-1.48 (m, 8H, 4×CH₂) 1.38-1.35 (m, 32H, 16× CH₂), 0.95 (t, 12H, $J = 6.5$ Hz, 4×CH₃). ¹³C NMR (CDCl₃, 125 MHz): δ 164.24, 160.55, 152.51, 151.44, 150.48, 149.78, 149.10, 128.53, 124.05, 121.47, 120.81, 116.47, 113.72, 113.32, 112.14, 105.81, 97.74, 69.57, 31.83, 29.30, 26.00, 22.68, 14.11. Elemental Anal. Calculated for C₅₀H₇₆N₂O₅ (%): C, 76.49; H, 9.76; N, 3.57. Found: C, 76.31; H, 10.364; N, 3.53. HRMS (ESI+) exact mass calculated for C₅₀H₇₆N₂O₅ (M+1): 785.5754, Found: 785.3382.

For **HT**₃, yellow amorphous solid (Yield = 36 %). IR (ATR): ν_{\max} in cm⁻¹ 2951 (Ar C-H), 2851 (Aliph C-H), 2217 (C≡N), 1654 (C=O), 1601 (Ar C=C). ¹H NMR (CDCl₃, 500 MHz): δ 12.60 (s, 1H, CONH), 7.50 (dd, 1H, $J = 8.5, 2.0$ Hz, Ar-H), 7.37 (d, 1H, $J = 2.0$ Hz, Ar-H), 7.28 (dd, 1H, $J = 8.0, 2.0$ Hz, Ar-H), 7.25 (d, 1H, $J = 2.0$ Hz, Ar-H), 7.04 (d, 1H, $J = 8.5$ Hz, Ar-H), 7.01 (d, 1H, $J = 8.0$ Hz, Ar-H), 6.67 (s, 1H, pyridone-H), 4.21 (t, 2H, $J = 6.5$ Hz, OCH₂), 4.09 (m, 6H, 3×OCH₂), 1.87 (t, 8H, $J = 6.5$ Hz, 4×OCH₂-CH₂), 1.54-1.27 (m, 72H, 36×CH₂), 0.90 (m, 12H, 4×CH₃). ¹³C NMR (CDCl₃, 125 MHz): 164.31, 160.53, 152.52, 151.44, 150.52, 149.78, 149.10, 128.54, 124.03, 121.47, 120.85, 116.49, 113.72, 113.23, 112.18, 105.83, 97.69, 69.56, 31.94, 21.45, 26.0, 22.70, 14.12. Elemental Anal. Calculated for C₆₆H₁₀₈N₂O₅ (%): C, 78.52; H, 10.78; N, 2.77. Found: C, 77.46; H, 10.925; N, 3.07. HRMS (ESI+) exact mass calculated for C₆₆H₁₀₈N₂O₅ (M+1): 1009.8258, Found: 1001.0035.

For **HT**₄, yellow amorphous solid (Yield 35 %). IR (ATR): ν_{\max} in cm⁻¹ 2915 (Ar C-H), 2850 (Aliph C-H), 2217 (C≡N), 1656 (C=O), 1602 (Ar C=C). ¹H NMR (CDCl₃, 500 MHz): δ 12.54 (s, 1H, CONH), 7.40 (dd, 1H, $J = 8.5, 2.0$ Hz, Ar-H), 7.28 (d, 1H, $J = 2.0$ Hz, Ar-H), 7.18 (dd, 1H, $J = 8.0, 2.0$ Hz, Ar-H), 7.15 (d, 1H, $J = 2.0$ Hz, Ar-H), 6.93 (d, 1H, $J = 8.5$ Hz, Ar-H), 6.54 (d, 1H, $J = 8.5$ Hz, Ar-H), 6.57 (s, 1H, pyridone-H), 4.11 (t, 2H, $J = 6.5$ Hz, O-CH₂), 4.0 (t, 6H, $J = 6.5$ Hz, 3×OCH₂), 1.78-1.74 (m, 8H, 4×OCH₂-CH₂), 1.41-1.18 (m, 104H, 52×CH₂), 0.80 (m, 12H, 4×CH₃). ¹³C NMR (CDCl₃, 125 MHz): δ 164.02, 160.58, 152.51, 151.47, 150.34, 149.79, 149.11, 124.06, 121.48, 120.69, 116.44, 113.73, 113.22, 112.03, 105.74, 97.81, 69.57, 31.94, 29.43, 26.0, 22.70, 14.12. Elemental Anal. Calculated for C₈₂H₁₄₀N₂O₅ (%): C,

79.81; H, 11.44; N, 2.27. Found: C, 79.56; H, 11.862; N, 2.30. HRMS (ESI+) exact mass calculated for $C_{82}H_{140}N_2O_5$ (M+1): 1234.0762, Found: 1234.2292.

Synthesis of intermediate (E)-1,3-bis(3,4-bis(hexyloxy)phenyl)prop-2-en-1-one (6a)

An equimolar mixture of **3a** (1g, 3.26 mmol, 1 equiv.) and **5a** (1 g, 3.26 mmol, 1 equiv.) was dissolved in ethanol, to which 50% of aqueous KOH (0.64 g, 11.42 mmol, 3.5 equiv.) was added drop-wise. After stirring at room temperature for 5 hours, the resulted greenish yellow precipitate was filtered and washed with ethanol. Finally recrystallization with DCM and methanol offered the title compound as greenish yellow solid (Yield 83 %). IR (ATR): ν_{\max} in cm^{-1} 2951 (Ar C-H), 2923 (Ar C-H), 2857 (Aliph C-H), 1657 (C=O), 1574 (Ar C=C). 1H NMR ($CDCl_3$, 500 MHz): δ 7.75 (d, 1H, $J = 15.5$ Hz, Olefinic-H), 7.66 (d, 1H, $J = 8.0$ Hz, Ar-H), 7.62 (s, 1H, Ar-H), 7.41 (d, 1H, $J = 15.5$ Hz, Olefinic-H), 7.22 (d, 1H, $J = 8.5$ Hz, Ar-H), 7.19 (s, 1H, Ar-H), 6.93 (d, 1H, $J = 8.0$ Hz, Ar-H), 6.90 (d, 1H, $J = 8.5$ Hz, Ar-H), 4.1-4.0 (m, 8H, $4 \times OCH_2$), 1.89-1.85 (m, 8H, $4 \times OCH_2-CH_2$), 1.51 (m, 8H, $4 \times CH_2$), 1.37 (m, 16H, $J = 6.5$ Hz, $8 \times CH_2$), 0.93 (m, 12H, $4 \times CH_3$). ^{13}C NMR ($CDCl_3$, 125 MHz): δ 188.79, 153.33, 151.57, 149.13, 144.12, 131.40, 128.01, 122.90, 69.24, 31.59, 29.15, 25.68, 22.61, 14.02. Elemental Anal. Calculated for $C_{39}H_{60}O_5$ (%): C, 76.93; H, 9.93. Found: C, 76.99; H, 10.95.

Synthesis of HT₅ from chalcone 6a (method-1)

To a suspension of chalcone **6a** (1 g, 1.48 mmol, 1 equiv.) in 20 mL of anhydrous methanol, sodium methoxide (0.83g, 14.87mmol 10 equiv.) was added portion-wise. Malononitrile (0.11 g, 1.63 mmol, 1.1 equiv.) was then added to it and stirred for 10 hrs at ambient temperature. The obtained pale yellow precipitate was filtered and washed repeatedly with methanol. The crude solid was purified by silica gel (100-200 mesh size) column chromatography using 5% ethyl acetate in pet-ether (60-70 °C) as mobile phase to yield **HT₅** as pale white solid (Yield = 40%). IR (ATR): ν_{\max} in cm^{-1} 2917 (Ar C-H), 2848 (Aliph C-H), 2219 (C \equiv N), 1578 (Ar C=C). 1H NMR ($CDCl_3$, 500 MHz): δ 7.7 (s, 1H, Ar-H), 7.67 (d, $J = 8.5$ Hz, 1H, Ar-H), 7.39 (s, 1H, Ar-H), 7.24 (d, $J = 8.5$ Hz, 1H, Ar-H), 7.22 (s, 1H, Ar-H), 7.01 (d, $J = 8.5$ Hz, 1H, Ar-H), 6.97 (d, $J = 8.5$ Hz, 1H, Ar-H), 4.20 (s, 1H, OCH_3), 4.13-4.07 (m, 8H, $4 \times OCH_2$), 1.88 (m, 8H, $4 \times OCH_2-CH_2$), 1.50 (m, 8H, $4 \times CH_2$), 1.38-1.28 (m, 8H, $4 \times CH_2$), 0.925

(m, 12H, 4× CH_3). ^{13}C NMR (CDCl_3 , 125 MHz): δ 165.08, 157.56, 156.21, 151.59, 150.82, 149.17, 130.17, 128.86, 121.41, 120.71, 116.21, 114.02, 113.40, 113.08, 112.54, 91.68, 69.41, 54.38, 31.93, 29.70, 29.60, 29.45, 29.36, 29.24, 26.05, 22.70, 14.12. Elemental Anal. Calculated for $\text{C}_{43}\text{H}_{62}\text{N}_2\text{O}_5$ (%): C, 75.18; H, 9.10; N, 4.08: Found: C, 75.10; H, 9.12; N, 3.98. HRMS (ESI+) exact mass calculated for $\text{C}_{43}\text{H}_{62}\text{N}_2\text{O}_5$ (M+1): 687.4658, Found: 687.4658.

Synthesis of **HT**₅ from cyanopyridone **HT**₁ (method-2)

A mixture of **HT**₁ (0.5 g, 0.821 mmol, 1 equiv.), anhydrous K_2CO_3 (0.17 g, 1.23mmol, 1.5 equiv.) and methyl iodide (0.041 g, 0.98 mmol, 1.1 equiv.) in 15 mL of dry DMF was stirred at 45 °C for overnight. After completion of the reaction, the mixture was poured into ice and obtained precipitate was filtered and washed with water. It was further purified by silica gel (100 -200 mesh size) column chromatography using 5% ethyl acetate in pet-ether as eluents offered white solid (Yield = 90 %). The spectroscopic properties were identical to that of compound obtained by method-1.

The compounds **HT**₆ was prepared as described in method-2 (Yield 88%) IR (ATR): ν_{max} in cm^{-1} 2920 (Ar C-H), 2848 (Aliph C-H), 2218 ($\text{C}\equiv\text{N}$), 1578 (Ar C=C). ^1H NMR (CDCl_3 , 500 MHz): δ 7.7 (s, 1H, Ar-H), 7.67 (d, $J = 8.5$ Hz, 1H, Ar-H), 7.39 (s, 1H, Ar-H), 7.24 (d, $J = 8.5$ Hz, 1H, Ar-H), 7.22 (s, 1H, Ar-H), 7.01 (d, $J = 8.5$ Hz, 1H, Ar-H), 6.97 (d, $J = 8.5$ Hz, 1H, Ar-H), 4.20 (s, 1H, OCH_3), 4.20-4.07 (m, 8H, 4× OCH_2), 1.88 (m, 8H, 4× $\text{OCH}_2\text{-CH}_2$), 1.51 (m, 8H, 4× CH_2), 1.39-1.31 (m, 32H, 16× CH_2), 0.925 (t, 12H, $J = 5.0$ Hz, 4× CH_3). ^{13}C NMR (CDCl_3 , 125 MHz): δ 165.07, 157.55, 156.21, 151.60, 150.83, 149.18, 130.18, 128.86, 121.41, 120.72, 116.20, 114.04, 113.41, 113.10, 112.53, 91.68, 69.33, 54.37, 31.84, 29.34, 26.06, 22.64, 14.11. Elemental Anal. Calculated for $\text{C}_{51}\text{H}_{78}\text{N}_2\text{O}_5$ (%): C, 76.65; H, 9.84; N, 3.51. Found: C, 76.66; H, 9.90; N, 3.52. HRMS (ESI+) exact mass calculated for $\text{C}_{51}\text{H}_{78}\text{N}_2\text{O}$ (M+1): 799.5910, Found: 799.3246.

HT₇ was also synthesized by adopting the method-2 (Yield 85%) IR (ATR): ν_{max} in cm^{-1} 2955 (Ar C-H), 2849 (Aliph C-H), 2223 ($\text{C}\equiv\text{N}$), 1590 (Ar C=C). ^1H NMR (CDCl_3 , 500 MHz): δ 7.6 (s, 1H, Ar-H), 7.57 (d, $J = 8.5$ Hz, 1H, Ar-H), 7.18 (s, 1H, pyridine-H), 7.14 (d, $J = 8.5$ Hz, 1H, Ar-H), 7.12 (s, 1H, Ar-H), 7.91 (d, $J = 8.5$ Hz,

1H, Ar-H), 6.88 (d, $J = 8.5$ Hz, 1H, Ar-H), 4.10 (s, 1H, pyridine-OCH₃), 4.10-3.97 (m, 8H, 4×OCH₂), 1.78 (m, 8H, 4×OCH₂-CH₂), 1.41 (m, 8H, 4×CH₂), 1.39-1.31 (m, 64H, 32×CH₂), 0.80 (m, 12H, 4×CH₃). ¹³C NMR (CDCl₃, 125 MHz): δ 165.08, 157.55, 156.21, 151.61, 150.84, 149.19, 130.18, 128.87, 121.41, 120.71, 116.20, 114.05, 113.42, 113.11, 112.53, 91.69, 69.34, 54.37, 31.94, 29.24, 27.57, 22.71, 14.12. Elemental Anal. Calculated for C₆₇H₁₁₀N₂O₅ (%): C, 78.59; H, 10.90; N, 2.71. HRMS (ESI+) exact mass calculated for C₆₇H₁₁₀N₂O₅ (M+1): 1023.8414, Found: 1023.9621.

3.2.3 Design and synthesis of HT₈₋₁₀ (Series-2)

In **Series-2**, three new unsymmetrical star-shaped molecules (**HT₈₋₁₀**) bearing cyanopyridine central core, substituted with the trialkoxybenzyl group at its 2nd position and two dihexyloxyphenyl rings at its 4th and 6th positions, respectively have been rationally designed. Their representative molecular structures are shown in **Fig 3.6**. In the new design, the presence of highly electron withdrawing cyano functionality further enhances the electron deficiency of pyridine ring, causing a good electron mobility in the mesophase (Attias et al. 2002). One of the arms of the molecule has been changed in order to study the effect of structure-property correlation. It is also expected that, these highly flexible dissimilar arms would facilitate decrease in isotropic temperatures, which is one of the desirables for easy processing of a mesogenic material in the device fabrication process. Further, the presence of donor-acceptor configurations would offer encouraging photophysical properties in the mesomorphic aggregation.

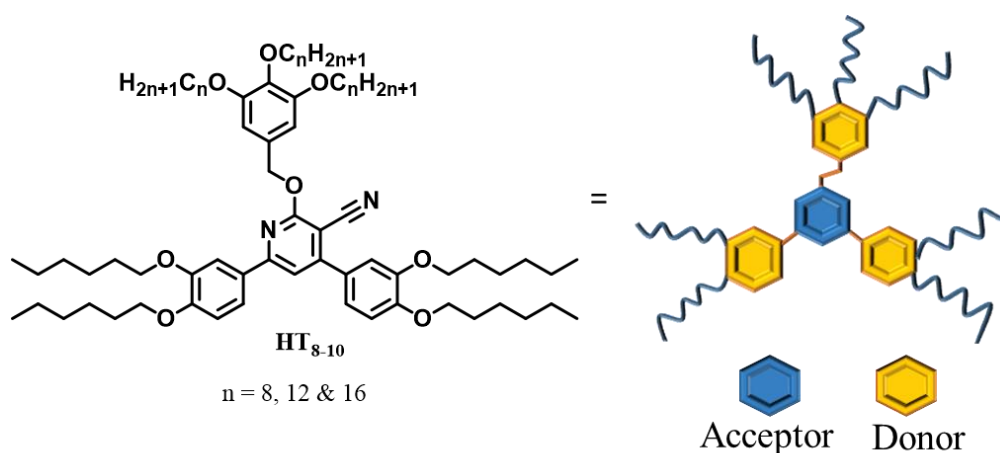
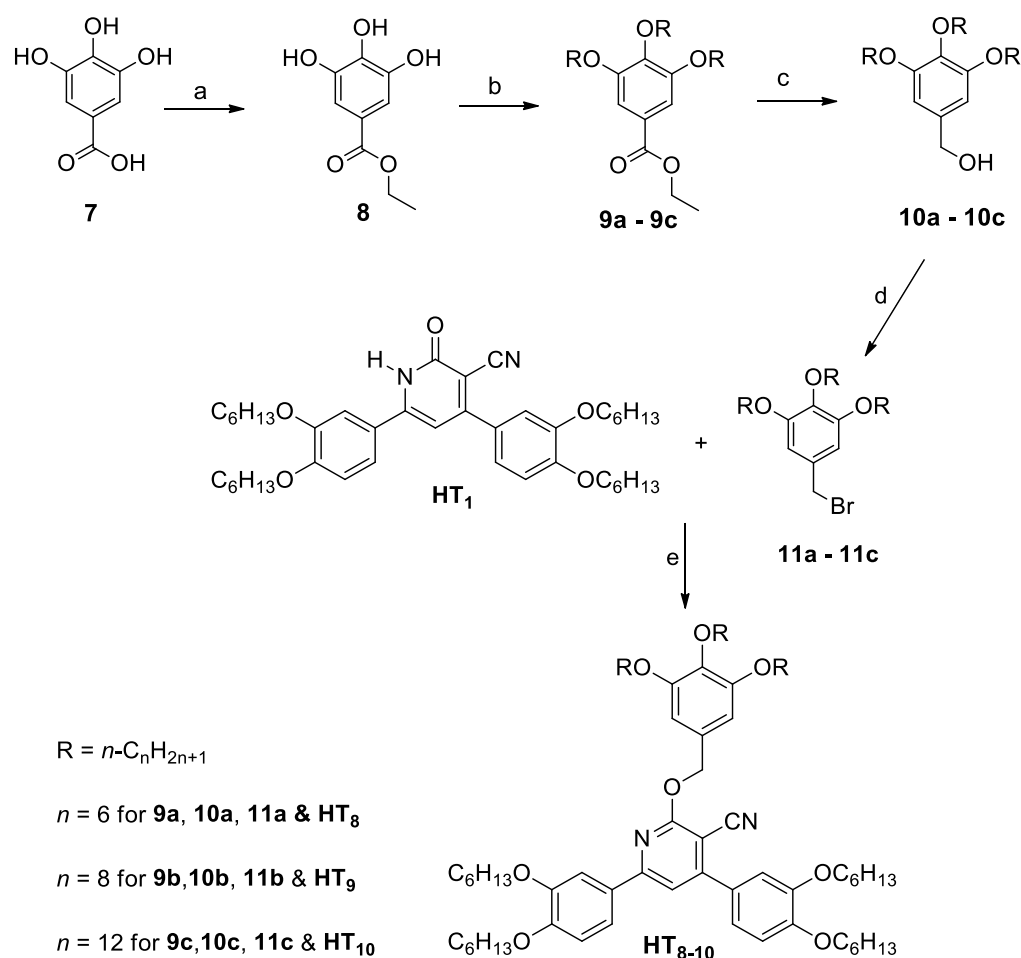


Figure 3.6 Design of new star-shaped discotic molecules **HT₈₋₁₀** of **Series-2**

The synthetic route for the preparation of newly designed hekets is outlined in **Scheme 3.2**. The synthesis of required key-precursor 2-cyanopyridone derivative **HT₁** was discussed in section 3.2.2. The intermediate 3,4,5-trialkoxybenzyl bromides **11a-c** were prepared by employing the reported procedures (Tanabe et al. 2007). Their synthesis involved the acid catalysed esterification of gallic acid (**7**) followed by the alkylation with different *n*-alkylbromide using Williamson's etherification protocol to get ethyl 3,4,5-trialkoxybenzoates **9a-c**. The reduction of esters using LiAlH₄ in dry THF furnished 3,4,5-trialkoxybenzyl alcohols **10a-c**, which on treatment with phosphorus tribromide in DCM at ambient conditions offered key-intermediates **11a-c**. Finally, the simple base catalysed alkylation of compound **HT₁** with different trialkoxybenzyl bromides produced target molecules **HT₈₋₁₀** in good yield.



Scheme 3.2 Synthesis route for preparation of **HT₈₋₁₀**. Reagents and conditions: a) *n*-RBr, anhydrous K₂CO₃, KI, DMF, 80 °C, 12h, 80-89 %; b) LiAlH₄, in dry THF, 0-25 °C, 12h, 90-96 %; c) PBr₃, DCM, 2h, 85-90 %; d) K₂CO₃, DMF, 60 °C, overnight, 60-70 %

3.2.3.1 Results and discussion

The chemical structures of newly synthesized compounds were confirmed by routine spectral techniques. FTIR, $^1\text{H-NMR}$, $^{13}\text{C-NMR}$ and HRMS-TOF spectra of one of the alkyl member *i.e.* **HT**₁₀ are depicted in **Figs 3.7-3.10**, respectively. In FTIR spectrum of **HT**₁₀, absorption band at 2217 cm^{-1} indicated the presence of cyano group of central pyridine core and absence of any absorption in the range of $1650\text{-}1680\text{ cm}^{-1}$ suggested the successful alkylation of pyridone moiety to pyridine. As expected, the set of NMR signals appeared between 8.00 to 6.50 ppm accounts for aromatic protons; a singlet at 5.57 ppm has attributed to benzyloxy protons; unique triplets at 3.90 and 4.10 ppm are due to two distinct OCH_2 ; number of signals in the range of $2.00\text{-}0.90$ ppm are ascribed to primary and secondary protons of saturated alkyl chains. These data confirmed the structure of **HT**₁₀.

In its $^{13}\text{C-NMR}$ spectrum, high frequency resonance at 164.46 ppm is due to tertiary carbon attached to benzyloxy substituent and rest of the down fielded signals are raised by aromatic carbons. The characteristics signal at 73.42 and 69.13 ppm revealed two types of OCH_2 carbons. Both the elemental analysis and mass data unambiguously match with calculated data for $\text{C}_{85}\text{H}_{138}\text{N}_2\text{O}_8$. Similarly, structures of the remaining two final compounds, **HT**₈ and **HT**₉ of the series have been confirmed.

Some selected spectra:

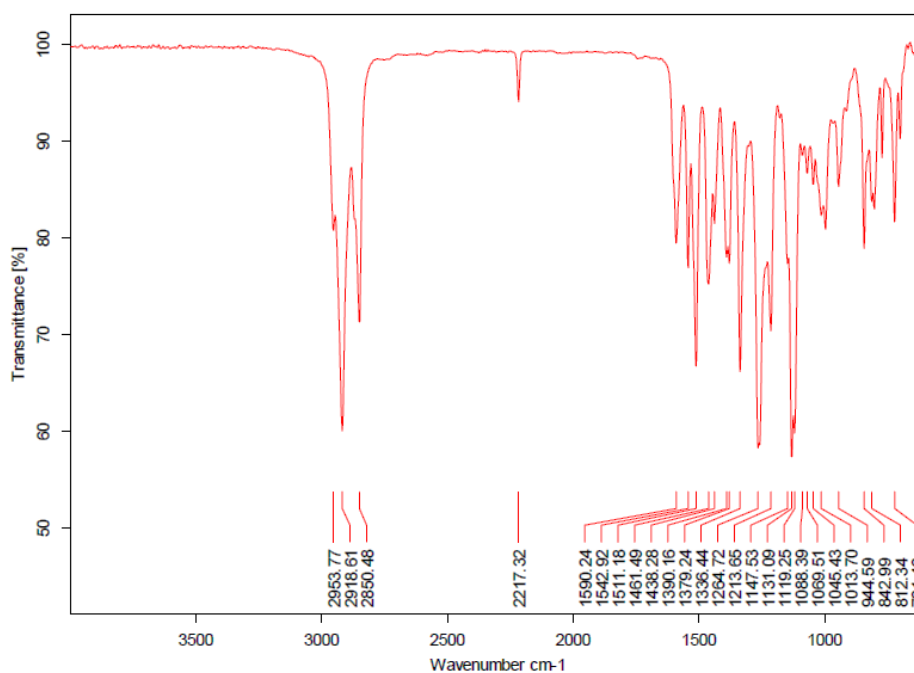


Figure 3.7 FTIR (ATR) spectrum of **HT**₁₀

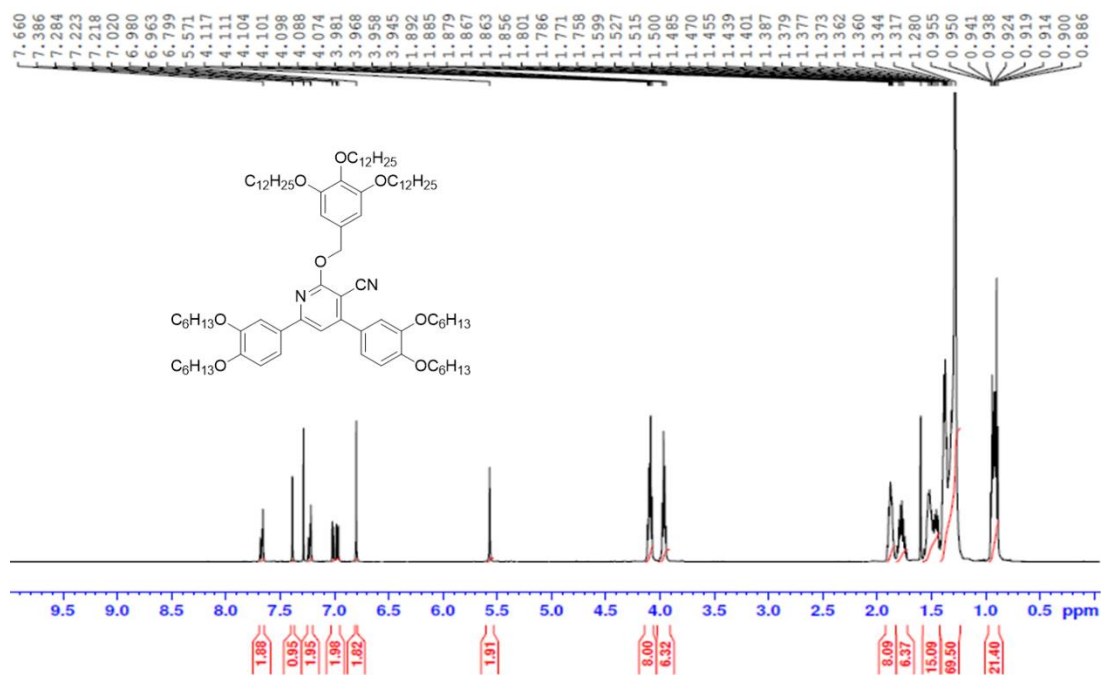


Figure 3.8 ¹H NMR (500 MHz) spectrum of HT₁₀ recorded in CDCl₃

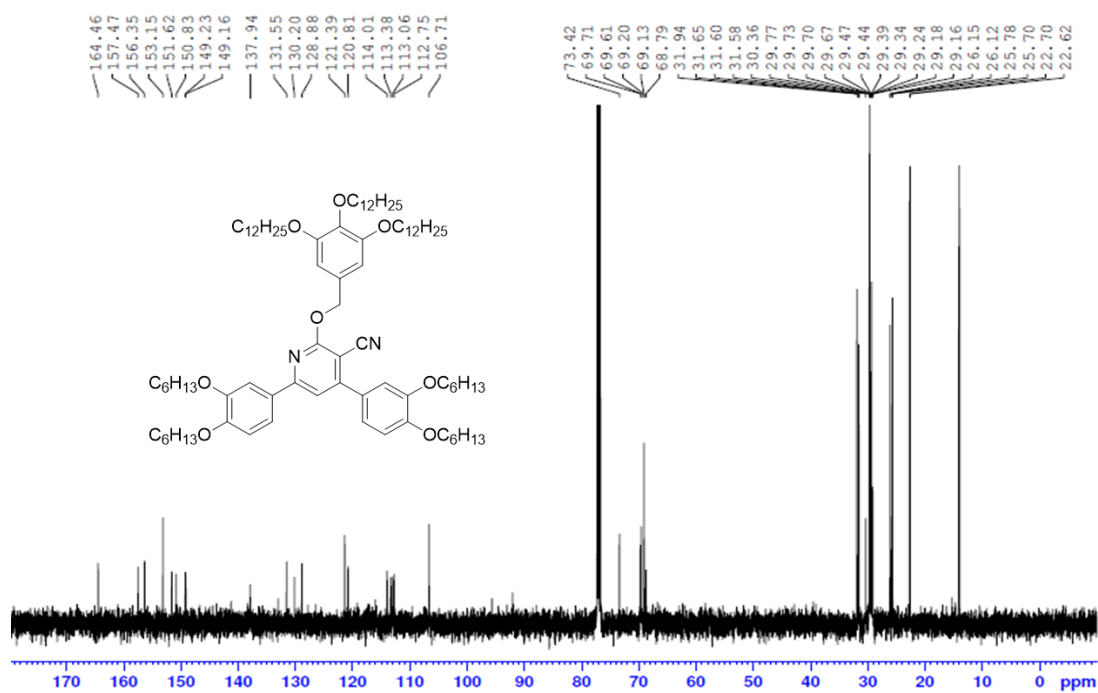


Figure 3.9 ¹³C NMR (125 MHz) spectrum of HT₁₀ recorded in CDCl₃

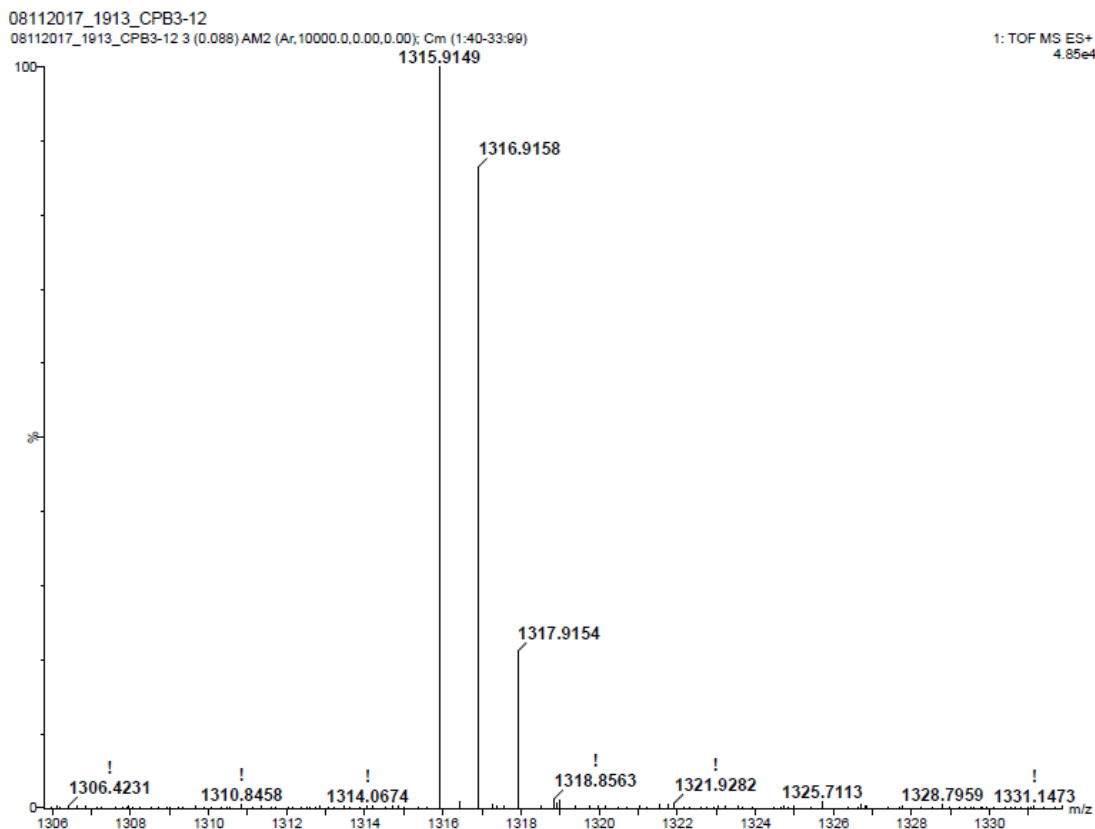


Figure 3.10 MALDI-TOF spectrum of **HT₁₀**

3.2.3.2 Experimental procedures

In the present section, experimental procedures adopted to synthesise star-shaped cyanopyridines (**HT₈₋₁₀**) and their structural characterization have been described.

*General procedure for the synthesis of 4,6-bis(3,4-bis(alkoxy)phenyl)-2-((3,4,5-tris(alkoxy)benzyl)oxy)nicotinonitriles (**HT₈₋₁₀**)*

A mixture of compound **6** (0.3 g, 0.45 mmol, 1 equiv.) and anhydrous K_2CO_3 (0.92 g, 0.67 mmol, 1.5 equiv.) in 15 mL DMF was stirred at room temperature under inert atmosphere for 15 min. Then, trihexyloxybenzyl bromide **11a** (0.23 g, 0.49 mmol, 1.1 equiv.) was added to the mixture and heated to 60 °C for overnight. After completion of the reaction, the reaction mass was added into 50 mL of ice-cold water. The crude product was extracted with dichloromethane (40 mL×2) and the combined organic layers was concentrated. The resulted crude product was purified by silica gel column chromatography (100-200 mesh size) using 3% ethyl acetate in petroleum ether (60-70 °C) as mobile phase to obtain **HT₈** as pure white product (Yield, 70 %). FTIR

(ATR): ν_{\max} in cm^{-1} 2922 (Ar C-H), 2855 (Aliph C-H), 2216 ($\text{C}\equiv\text{N}$) and 1591 (Ar C=C). ^1H NMR (CDCl_3 , 500 MHz): δ 7.68-7.65 (m, 2H, 2 \times Ar-H), 7.38 (s, 1H, pyridine-H), 7.24-7.21 (m, 2H, 2 \times Ar-H), 7.0 (d, 1H, $J = 8.5$ Hz, Ar-H), 6.97 (d, 1H, $J = 8.5$ Hz, Ar-H), 6.79 (s, 2H, 2 \times Ar-H), 5.57 (s, 2H, 2 \times OCH₂-Ar), 4.0 (m, 8H, 4 \times OCH₂), 3.97 (m, 6H, 3 \times OCH₂), 1.88 (m, 8H, 4 \times CH₂), 1.77 (m, 6H, 3 \times CH₂) 1.49-1.28 (m, 42H, 2 \times CH₂), 0.95-0.9 (m, 21H, 7 \times CH₃). ^{13}C NMR (CDCl_3 , 125 MHz): δ 164.46, 157.47, 156.35, 153.15, 151.63, 150.83, 149.23 149.16, 137.93, 131.57, 130.20, 128.88, 121.39, 120.81, 116.04 114.02, 113.39, 113.06, 112.76, 106.71, 92.10, 73.41, 69.71, 69.62, 69.21, 69.12, 69.77, 31.71, 30.228, 29.70, 29.38, 29.24, 29.16, 29.51, 25.73, 25.65, 14.06. Elemental Anal. Calcd (%) for $\text{C}_{42}\text{H}_{60}\text{N}_2\text{O}_5$: C, 74.96; H, 8.99; N, 4.16; O, Found: C, 74.81; H, 9.261; N, 4.10. HRMS (ESI+) exact mass calculated for $\text{C}_{42}\text{H}_{60}\text{N}_2\text{O}_5$ (M+1): 673.4502, Found: 673.1233

The final compounds **HT9-10** were synthesized by adopting similar procedure.

For **HT9**, pale white coloured product (Yield 66%). FTIR (ATR): ν_{\max} in cm^{-1} 2922 (Ar C-H), 2855 (Aliph C-H), 2216 ($\text{C}\equiv\text{N}$) and 1591 (Ar C=C). ^1H NMR (CDCl_3 , 500 MHz): δ 7.68-7.65 (m, 2H, 2 \times Ar-H), 7.38 (s, 1H, pyridine-H), 7.24-7.21 (m, 2H, 2 \times Ar-H), 7.0 (d, 1H, $J = 8.5$ Hz, Ar-H) 6.97 (d, 1H, $J = 8.5$ Hz, Ar-H), 6.80 (s, 2H, 2 \times Ar-H), 5.57 (s, 2H, 2 \times OCH₂-Ar), 4.0 (m, 8H, 4 \times OCH₂), 3.96 (m, 6H, 3 \times OCH₂), 1.87 (m, 8H, 4 \times OCH₂-CH₂), 1.74 (m, 6H, 3 \times CH₂) 1.51-1.27 (m, 54H, 27 \times CH₂), 0.95-0.88 (m, 21H, 7 \times CH₃). ^{13}C NMR (CDCl_3 , 125 MHz): δ 164.45, 157.48, 156.35, 153.14, 151.62, 150.82, 149.24 149.19, 137.94. 131.56, 130.20, 128.87, 121.39, 120.82, 114.0, 113.06, 106.70, 92.09, 73.43, 69.67, 69.04, 31.74, 29.41, 25.74, 25.64, 14.05. Elemental Anal. Calcd (%) for $\text{C}_{73}\text{H}_{114}\text{N}_2\text{O}_8$: C, 76.39; H, 10.01; N, 2.44; O, Found: C, 76.41; H, 10.42; N, 2.29. HRMS (ESI+) exact mass calculated for $\text{C}_{73}\text{H}_{114}\text{N}_2\text{O}_8$ (M+1): 1147.8575, Found: 1147.9898.

For **HT10**, pale white coloured product (Yield 62%). FTIR (ATR): ν_{\max} in cm^{-1} 2922 (Ar C-H), 2846 (Aliph C-H), 2216 ($\text{C}\equiv\text{N}$), 1591 (Ar C=C). ^1H NMR (CDCl_3 , 500 MHz): δ 7.68-7.65 (m, 2H, 2 \times Ar-H), 7.38 (s, 1H, pyridine-H), 7.24-7.21 (m, 2H, 2 \times Ar-H), 7.0 (d, 1H, $J = 8.5$ Hz, Ar-H) 6.97 (d, 1H, $J = 8.5$ Hz, Ar-H), 6.79 (s, 2H, 2 \times Ar-H), 5.57 (s, 2H, 2 \times OCH₂-Ar), 4.10 (m, 8H, 4 \times OCH₂), 3.96 (m, 6H, 3 \times OCH₂), 1.87 (m, 8H, 4 \times OCH₂-CH₂), 1.76 (m, 3H, 2 \times CH₂) 1.51-1.27 (m, 78H, 39 \times CH₂), 0.95-0.88 (m, 21H,

7×CH₃). ¹³C NMR (CDCl₃, 125 MHz): δ 164.46, 157.47, 156.35, 153.15, 151.62, 150.83, 149.23, 149.16, 137.94, 131.55, 130.20, 128.88, 121.39, 120.81, 114.01, 113.38 113.06, 112.75 106.71, 73.42, 69.71, 69.61, 69.20, 69.13, 68.79, 31.94, 31.65, 31.60, 31.58, 30.36, 29.43, 26.15, 26.12, 25.74, 22.66, 14.05. Elemental Anal. Calcd (%) for C₈₅H₁₃₈N₂O₈: C, 77.58; H, 10.57; N, 2.13; Found: C, 77.40; H, 10.64; N, 2.30. HRMS (ESI+) exact mass calculated for C₈₅H₁₃₈N₂O₈ (M+1): 1316.0453, Found: 1315.9982.

3.2.4 Design and synthesis of HT₁₁₋₂₀ (Series-3)

A new class of non-symmetrical D-A-D' structured molecules, **HT₁₁₋₁₃** was rationally designed. In the new design, π -rich 9,10-didodecyloxyphenanthrene and trialkoxybenzene units have been chosen as effective electron donors, while 3-cyanopyridone moiety as an efficient electron acceptor to achieve optimum optoelectronic properties at the liquid crystalline state (**Fig 3.11**). It is expected that, polycyclic aromatic hydrocarbon (PAH) nature of phenanthrene core would possess good self-assembling property with effective π -orbital overlapping, which in turn reduces the inter-columnar spacings resulting in a good charge migration ability through the columnar stack. Moreover, the introduction of additional alkoxy donors in electron-rich phenanthrene attached to electron deficient cyanopyridone offers efficient D-A interaction. Consequently, the designed mesogens would show necessary optoelectronic properties for their use in optoelectronic devices.

Similarly, one more series of D-A-D' configured molecules resembling **HT₁₁₋₁₃** was designed (**HT₁₄₋₂₀**). Here, it has been aimed at incorporating various electron donors having different donating strength to cyanopyridone core in order to study their effect on mesogenic, optical, and electronic properties. In the designed molecules, 3,4,5-tridodecyloxyphenylene attached at 4th position of cyanopyridone was kept intact and varied the additional donor appended at 6th position. The diverse donors, *viz.* phenol, anisole, aniline, *N,N*-dimethylaminophenylene, thiophenyl, biphenylene, triphenylamine were conjugatively introduced to the central cyanopyridone core. It is anticipated that, due to the varied strength of D-A interaction, **HT₁₄₋₂₀** would exhibit tuneable emission.

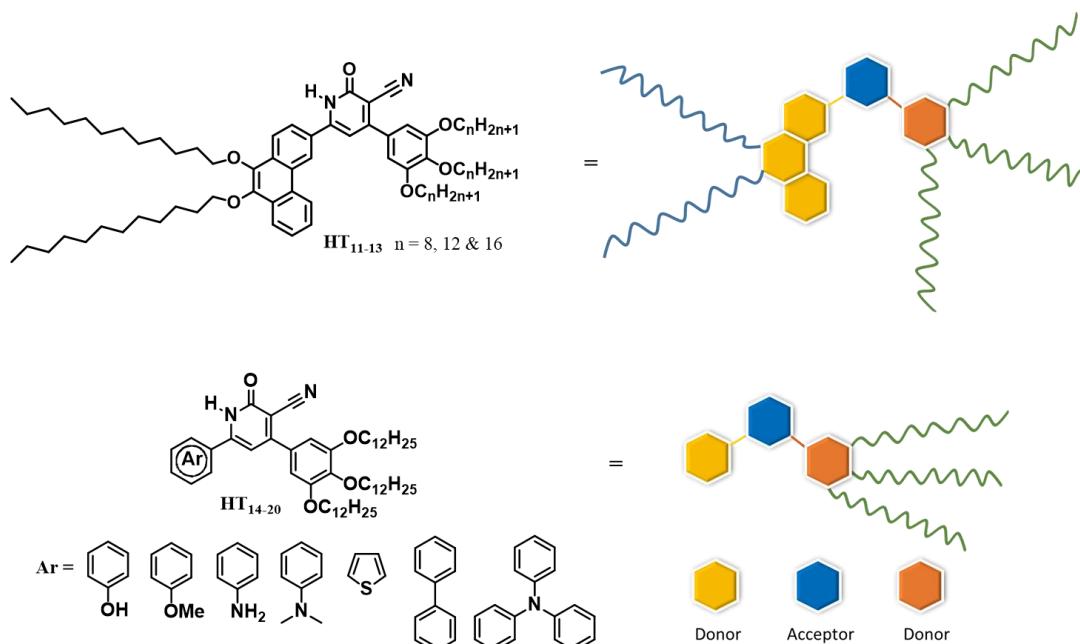
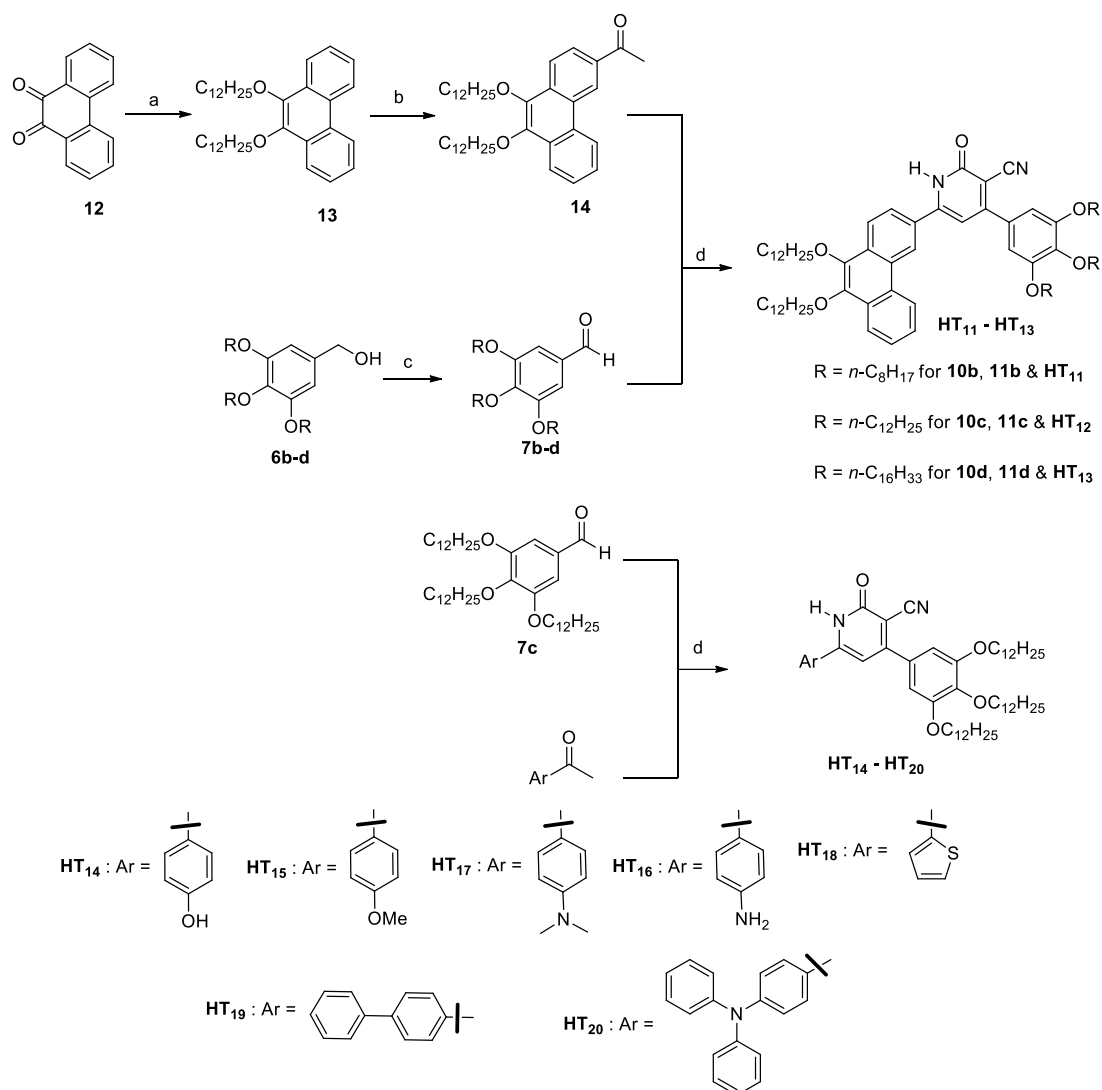


Figure 3.11 Design of D-A-D' structured molecules **HT**₁₁₋₂₀ of **Series-3**

The synthetic routes for the target compounds, **HT**₁₁₋₂₀ are depicted in **Scheme 3.3**. Firstly, 9,10-phenanthrenequinone (**12**) was reduced with $\text{Na}_2\text{S}_2\text{O}_4$ followed by alkylation using a phase transfer catalyst, Bu_4NBr in 1:1 THF and H_2O mixture to yield 9,10-didodecyloxyphenanthrene (**13**). The compound **13** was subjected to Friedel-Crafts acetylation with one equivalent of acetyl chloride under controlled conditions to give mono acetylated product **14** exclusively in good yield. All the required 3,4,5-trialkoxybenzaldehydes, **7b-d** were prepared through multi-step synthesis by adopting the reported procedures (Maruyama et al. 2010). Finally, the condensation of acetyl derivative, **14** and different aldehydes, **7b-d** with ethyl cyanoacetate yielded the target mesogenic compounds, **HT**₁₁₋₁₃. By using the same condensation protocol between 3,4,5-trialkoxybenzaldehyde (**7c**) and different aromatic ketones, the unsymmetrical dyad molecules **HT**₁₄₋₂₀ were obtained.



Scheme 3.3 Synthesis pathway for preparation of **HT₁₁₋₂₀**. Reagents and conditions: (a) $\text{Na}_2\text{S}_2\text{O}_4$, KOH, Bu_4NBr , $\text{C}_{12}\text{H}_{25}\text{Br}$, 1:1 H_2O and THF, RT, 48 hrs, 75%; (b) CH_3COCl , AlCl_3 , DCM, -5 to 25 °C, 1hr, 80 %; (c) PCC, dry DCM, 3 hrs, 80-63 %; (d) ethyl cyanoacetate, ammonium acetate, EtOH, 70 °C, 16 hrs, 25-36 %

3.2.4.1 Results and discussion

The structures of all new intermediates as well as final compounds were established by spectral tools. **Fig 3.12** displays the FTIR spectrum of representative compound **HT₁₁**, which shows bands at 2216 cm^{-1} and 1630 cm^{-1} due to stretching vibrations of cyano and carbonyl functionalities, respectively. These results indicated the formation of cyanopyridone ring. Further, its $^1\text{H-NMR}$ spectrum (**Fig 3.13**) depicts highly down fielded a broad singlet at 12.35 ppm and a unique singlet at 7.19 ppm accounting for the NH of lactam ring and its only CH proton, respectively; the

appearance of subsequent aromatic signals and up fielded signals of alkyl protons elucidate the structure. In its ^{13}C NMR, a number of distinct signals obtained in the higher frequency region are due to secondary and tertiary carbons of phenanthrene, phenyl and cyanopyridone rings. Particularly, carbonyl carbon and carbon bearing cyano group resonate at 163.65 and 161.20 ppm, respectively. In addition, the OCH_2 carbons present on two different aromatic environments resonate at 73.86 and 69.48 ppm (**Fig 3.14**). Moreover, its mass spectrum displayed the $[\text{M}+\text{H}]$ peak that is in well agreement with the theoretical mass of $\text{C}_{74}\text{H}_{112}\text{N}_2\text{O}_6$ (**Fig 3.15**). Also, its elemental analysis data match with the calculated values. The remaining members of the **Series-3** have been characterized similarly.

Some selected spectra:

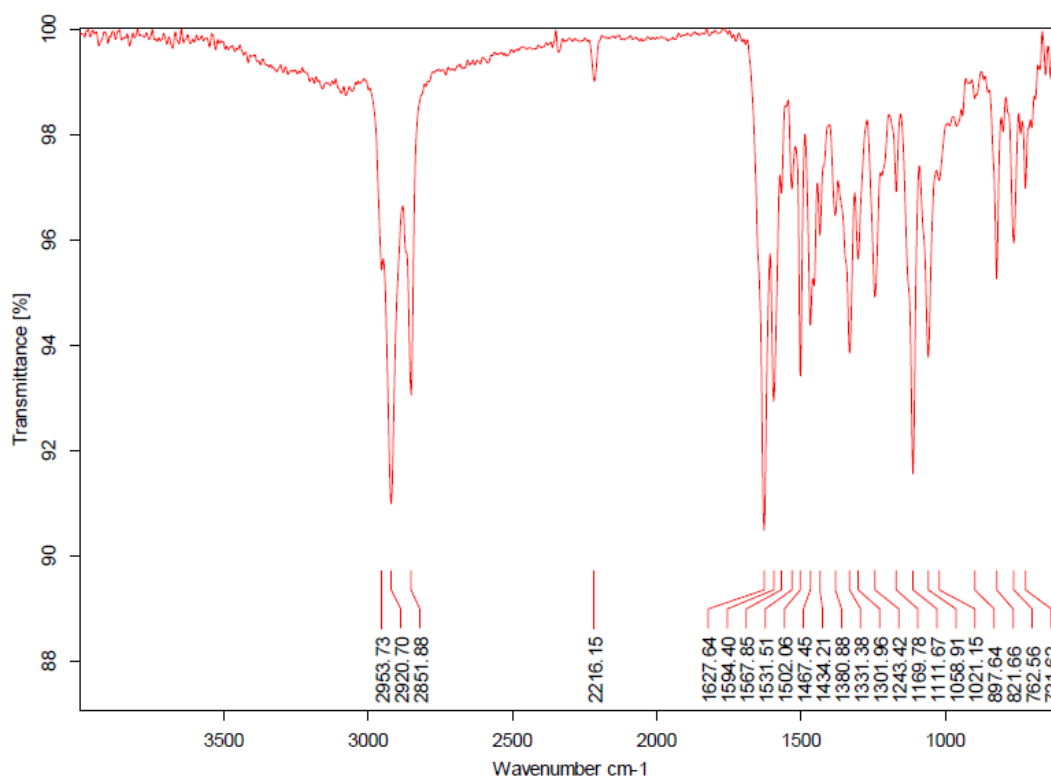


Figure 3.12 FTIR (ATR) spectrum of **HT₁₁**

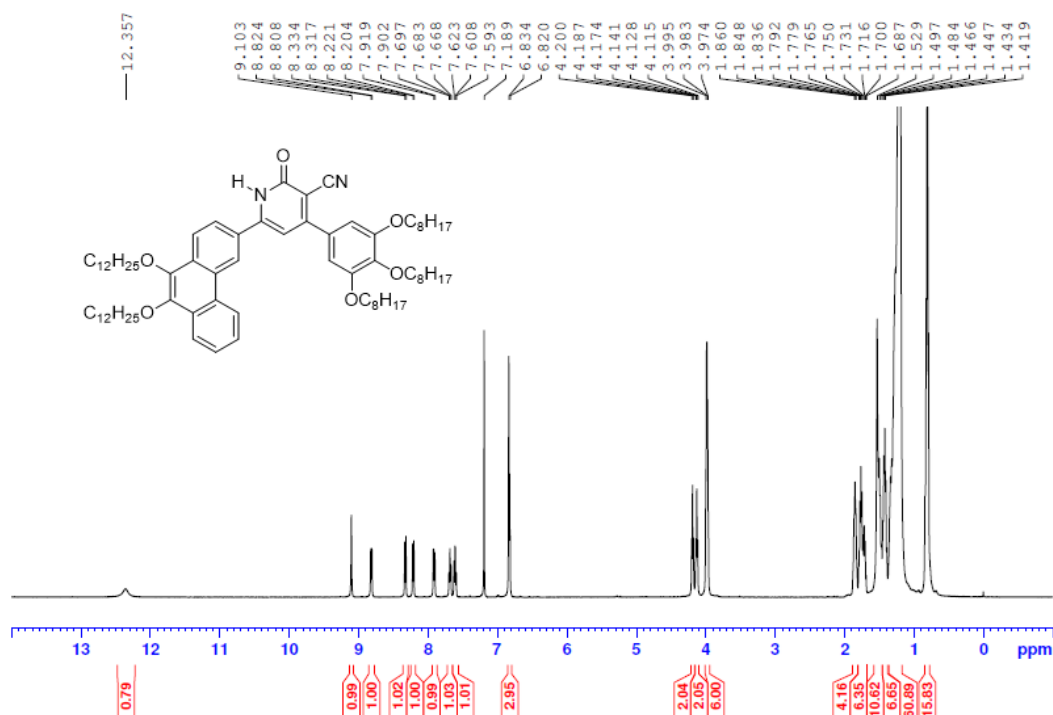


Figure 3.13 ¹H NMR (500 MHz) spectrum of HT₁₁ recorded in CDCl₃

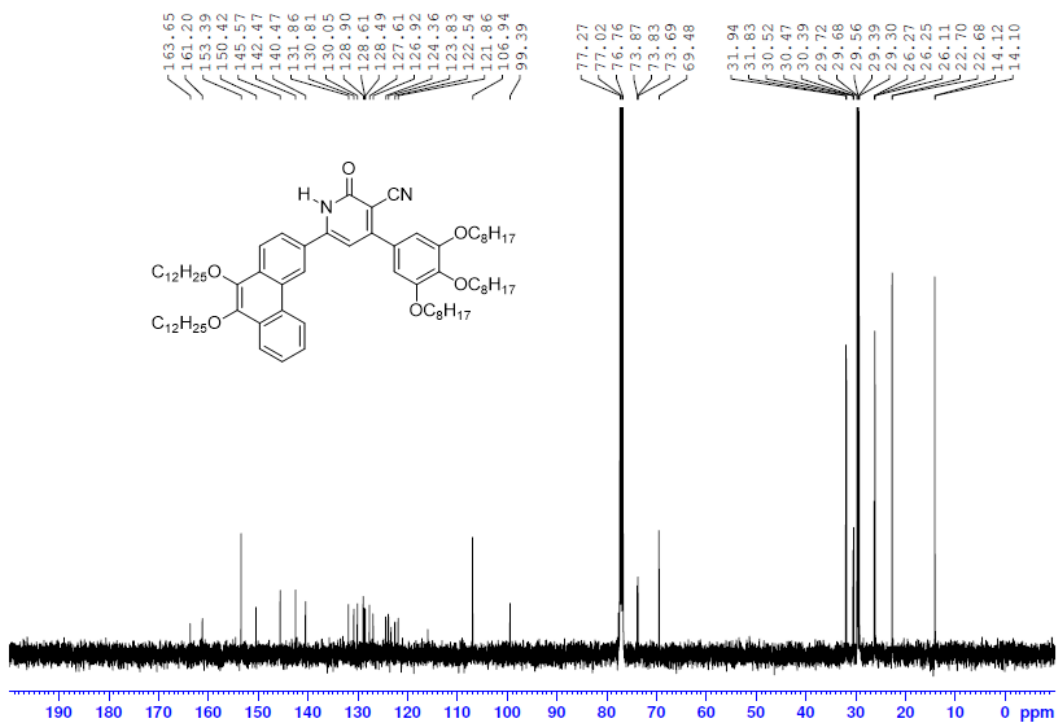


Figure 3.14 ¹³C NMR (125 MHz) spectrum of HT₁₁ recorded in CDCl₃

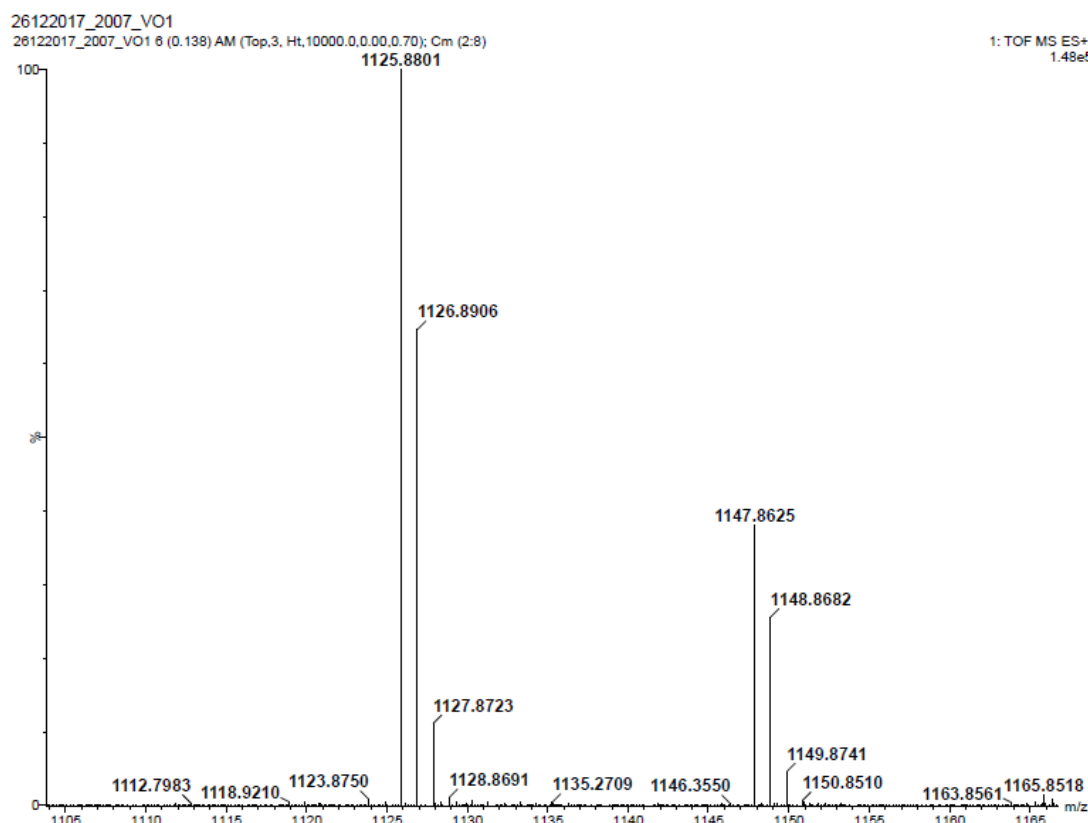


Figure 3.15 MALDI-TOF spectrum of **HT₁₁**

3.2.4.2 Experimental procedures

All the target molecules **HT₁₁₋₂₀** were synthesized by adopting simple and straightforward reactions. A detailed experimental protocols employed to prepare these compounds and their subsequent structural characterization data are deliberated as follows.

Synthesis of 9,10-bis(dodecyloxy)phenanthrene (13)

A mixture of 9,10-phenanthrenequinone (5 g, 24.0 mmol), $\text{Na}_2\text{S}_2\text{O}_4$ (22.78 g, 144 mmol) and Bu_4NBr (4.64 g, 14.4 mmol) in 200 mL THF: H_2O (1:1, v/v) was stirred for 15 mins. To this mixture, dodecyl bromide (17.95 g, 72 mmol) followed by aqueous KOH (20 g, 360 mmol, in 100 mL of H_2O) was added slowly and the stirring was continued for further 48 hrs. The reaction mixture was diluted with 150 mL of water and then extracted with ethyl acetate (200 mL \times 2). The combined organic layers was washed with water, brine, then dried over anhydrous Na_2SO_4 and evaporated the solvent to dryness. Finally recrystallized using methanol to yield product **2** as pure white solid

(Yield 75 %). FTIR (ATR): ν_{\max} in cm^{-1} 3071 (Ar C-H), 2915 (Ar C-H), 2847 (Aliph C-H), 1620 (Ar C=C); ^1H NMR (CDCl_3 , 500 MHz): δ 8.66 (m, 2H, 2 \times Ar-H), 8.26 (m, 2H, 2 \times Ar-H), 7.65 (m, 4H, 2 \times Ar-H), 4.23 (t, 4H, $J = 7$ Hz, 2 \times OCH₂), 1.94 (m, 4H, 2 \times OCH₂-CH₂), 1.59 (m, 2H, CH₂), 1.42 (m, 32H, 16 \times CH₂), 0.91 (t, $J = 7$ Hz, 6H, 2 \times CH₃); ^{13}C NMR (CDCl_3 , 125 MHz): δ 143.24, 129.64, 128.62, 126.70, 125.63, 122.58, 122.30, 73.66, 31.96, 30.56, 29.71, 29.62, 29.41, 26.31, 22.73, 14.15; Elemental Anal. Calcd (%) for $\text{C}_{38}\text{H}_{58}\text{O}_2$: C 83.46, H 10.69; Found: C 83.39, H 11.09.

Synthesis of 1-(9,10-bis(dodecyloxy)phenanthrene-3-yl)ethanone (14)

The compound **3** (5 g, 9.15 mmol) was taken in 75 mL of dry DCM, to which acetyl chloride (0.71 g, 9.15 mmol) was added and stirred at -5 °C under an argon atmosphere. At the same conditions, anhydrous AlCl_3 (1.46 g, 10.98 mmol) was then added in portion-wise. The mixture was stirred at same temperature for about 30 mins, then gradually warmed to room temperature. After confirming the completion of the reaction by TLC, the mixture was poured into ice-cooled water, extracted with DCM (50 mL \times 2) and dried over Na_2SO_4 and passed through celite. The solvent was removed under reduced pressure and crude product was purified by silica gel column chromatography (100-200 mesh size) using pet-ether and ethyl acetate (2:8) as eluents to give product **3** as pale white solid (Yield 80%). FTIR (ATR): ν_{\max} in cm^{-1} 2912 (Ar C-H), 2847 (Aliph C-H), 1666 (ketone C=O), 1612 (Ar C=C). ^1H NMR (CDCl_3 , 500 MHz): δ 9.02 (s, 1H, Ar-H), 8.66 (dd, 1H, $J = 6.0$ 3.5 Hz, Ar-H), 8.21 (dd, 1H, $J = 8.5$, 4.0 Hz, Ar-H), 8.08 (m, 2H, 2 \times Ar-H), 7.69 (m, 2H, 2 \times Ar-H), 4.18 (t, 2H, $J = 6.5$ Hz, OCH₂), 4.12 (t, 2H, $J = 6.5$ Hz, 2 \times OCH₂), 2.72 (s, 3H, COCH₃), 1.87-1.81 (m, 4H, 2 \times CH₂), 1.52-1.46 (m, 8H, 4 \times CH₂), 1.35-1.19 (m, 28H, 14 \times CH₂), 0.81 (t, $J = 6.5$ Hz, 6H, 2 \times CH₃). ^{13}C NMR (CDCl_3 , 125 MHz): δ 198.07, 145.68, 142.71, 133.93, 132.88, 129.90, 129.08, 127.95, 127.30, 126.36, 125.63, 123.76, 122.68, 122.62, 122.61, 73.77, 31.96, 30.53, 30.48, 29.60, 26.86, 26.25, 22.72, 14.14. Elemental Anal. Calcd (%) for $\text{C}_{40}\text{H}_{60}\text{O}_3$: C 81.58, H 10.27; Found: C 81.61, H 10.33.

For **7b**, FTIR (ATR): ν_{\max} in cm^{-1} 2922 (Ar C-H), 2854 (Aliph C-H), 2728 (aldehyde C-H), 1694 (aldehyde C=O), 1583 (Ar C=C). ^1H NMR (CDCl_3 , 500 MHz): δ 9.83 (s, 1H, CHO), 7.09 (s, 2H, A-H), 4.04 (m, 6H, 3 \times OCH₂), 1.85-1.72 (m, 6H, 3 \times CH₂), 1.5-1.3 (m, 30H, 15 \times CH₂), 0.9 (m, 9H, 3 \times CH₃); ^{13}C NMR (CDCl_3 , 125 MHz):

δ 191.19, 153.52, 143.88, 131.47, 107.87, 73.61, 69.23, 31.84, 30.34, 29.48, 29.30, 26.03, 22.66, 14.06. Elemental Anal. Calcd (%) $C_{31}H_{54}O_4$: C 75.87, H 11.09; Found: C 75.85, H 11.12.

For **7c**, FTIR (ATR): ν_{\max} in cm^{-1} 2915 (Ar C-H), 2847 (Aliph C-H), 2730 (aldehyde C-H), 1692 (aldehyde C=O), 1580 (Ar C=C); 1H NMR ($CDCl_3$, 500 MHz): δ 9.84 (s, 1H, \underline{CHO}), 7.10 (s, 2H, A- \underline{H}), 4.06 (m, 6H, $3 \times \underline{OCH_2}$), 1.86-1.75 (m, 6H, $3 \times \underline{CH_2}$), 1.64-1.28 (m, 54H, $17 \times \underline{CH_2}$), 0.9 (t, 9H, $J = 5.5$ Hz, $3 \times \underline{CH_3}$); ^{13}C NMR ($CDCl_3$, 125 MHz): δ 191.24, 153.53, 143.91, 131.46, 107.89, 73.63, 69.26, 31.93, 30.35, 29.58, 29.27, 26.03, 22.69, 14.09. Elemental Anal. Calcd (%) for $C_{43}H_{78}O_4$: C 78.36, H 11.93; Found: C 78.26, H 12.01.

For **7d**, FTIR (ATR): ν_{\max} in cm^{-1} 2913 (Ar C-H), 2847 (Aliph C-H), 2730 (aldehyde C-H), 1691 (aldehyde C=O), 1585 (Ar C=C); 1H NMR ($CDCl_3$, 500 MHz): δ 9.84 (s, 1H, \underline{CHO}), 7.10 (s, 2H, A- \underline{H}), 4.06 (m, 6H, $3 \times \underline{OCH_2}$), 1.86-1.75 (m, 6H, $3 \times \underline{CH_2}$), 1.64-1.28 (m, 76H, $36 \times \underline{CH_2}$), 0.9 (t, 9H, $J = 6.0$ Hz, $3 \times \underline{CH_3}$); ^{13}C NMR ($CDCl_3$, 125 MHz): δ 191.24, 153.53, 143.91, 131.46, 107.90, 73.63, 69.26, 31.93, 30.35, 29.71, 29.67, 29.63, 29.55, 29.37, 29.27, 26.03, 22.69, 14.10. Elemental Anal. Calcd (%) for $C_{55}H_{102}O_4$: C 79.80, H 12.55; Found: C 79.89, H 12.05.

General procedure for synthesis of 6-(9,10-bis(alkoxy)phenanthren-3-yl)-2-oxo-4-(3,4,5-tris(alkoxy)phenyl)-1,2-dihydropyridine-3-carbonitrile (HT₁₁₋₁₃)

A mixture of compound **3** (1 g, 1.6 mmol), **7a** (0.83 g, 1.6 mmol), ethyl cyanoacetate (0.23 g, 2.03 mmol) and ammonium acetate (1.30 g, 16.99 mmol) in 30 mL of absolute ethanol was heated to 70 °C for 16 hrs. The mixture was then allowed cool to RT, the obtained precipitate was filtered and washed with ethanol. The final compound was isolated from the mixture by columnar chromatographic method using 2 % of the ethyl acetate in the pet-ether solvent and finally recrystallized with DCM and methanol mixture to get **HT₁₁** as greenish yellow gummy solid (Yield 36%). FTIR (ATR): ν_{\max} in cm^{-1} 2920 (Ar C-H), 2851 (Aliph C-H), 2216 ($C \equiv N$), 1627 (amide C=O), 1594 (Ar C=C); 1H NMR ($CDCl_3$, 500 MHz): δ 12.35 (s, 1H, \underline{CONH}), 9.1 (s, 1H, Ar- \underline{H}), 8.81 (d, 1H, $J = 8.0$ Hz, Ar- \underline{H}), 8.32 (d, 1H, $J = 8.5$ Hz, Ar- \underline{H}), 8.21 (d, 1H, $J = 8.5$ Hz, Ar- \underline{H}), 7.91 (d, 1H, $J = 8.5$ Hz, Ar- \underline{H}), 7.68 (t, 1H, $J = 7.0$ Hz, Ar- \underline{H}) 7.60 (t, 1H, J

= 7.5 Hz, Ar-H), 6.83 (s, 2H, 2×Ar-H), 6.82 (s, 1H, pyridone-H), 4.18 (t, 2H, $J = 6.5$ Hz, OCH₂), 4.12 (t, 2H, $J = 6.5$ Hz, OCH₂), 3.98 (m, 6H, 3×OCH₂), 1.85 (m, 4H, 2×CH₂), 1.79-1.68 (m, 6H, 3×CH₂), 1.52-1.20 (m, 66H, 33×CH₂), 0.83 (m, 15H, 5×CH₃); ¹³C NMR (CDCl₃, 125 MHz): δ 163.65, 161.20, 153.39, 150.42, 145.57, 142.47, 140.47, 131.86, 130.81, 130.05, 128.90, 128.65, 128.55, 127.61, 126.92, 124.36, 123.83, 122.54, 121.86, 106.94, 99.39, 73.79, 69.48, 31.88, 30.46, 29.50, 26.21, 22.69, 14.11; Elemental Anal. Calcd (%) for C₇₄H₁₁₂N₂O₆: C 78.96, H 10.03, N 2.49. Found: C 78.76, H 10.23, N 2.42; HRMS (ESI+) exact mass calculated for C₇₄H₁₁₂N₂O₆ (M+1): 1125.8812, Found: 1125.8801.

Compounds **HT**₁₂₋₁₃ were prepared by adopting the similar procedure as described for **HT**₁₁.

For **HT**₁₂, greenish yellow (Yield 28%), FTIR (ATR): ν_{\max} in cm⁻¹ 2918 (Ar C-H), 2849 (Aliph C-H), 2218 (C≡N), 1643 (amide C=O), 1595 (Ar C=C): ¹H NMR (CDCl₃, 500 MHz): δ 12.65 (s, 1H, CONH), 9.22 (s, 1H, Ar-H), 8.93 (d, 1H, $J = 8.0$ Hz, Ar-H), 8.41 (d, 1H, $J = 8.5$ Hz, Ar-H), 8.30 (d, 1H, $J = 8.0$ Hz, Ar-H), 8.0 (d, 1H, $J = 8.5$ Hz, Ar-H), 7.78 (t, 1H, $J = 7.0$ Hz, Ar-H), 7.69 (t, 1H, $J = 7.5$ Hz, Ar-H), 6.92 (s, 3H, Ar-H, pyridone-H), 4.28 (t, 2H, $J = 6.5$ Hz, OCH₂), 4.22 (t, 2H, $J = 6.5$ Hz, OCH₂), 4.07 (m, 6H, 3×OCH₂), 1.92 (m, 4H, 2×CH₂), 1.87-1.78 (m, 6H, 3×CH₂), 1.63-1.27 (m, 90 H, 45×CH₂), 0.90 (m, 15H, 5×CH₃); ¹³C NMR (CDCl₃, 125 MHz): δ 163.82, 161.18, 153.39, 150.51, 145.57, 142.47, 140.45, 131.84, 130.82, 130.02, 128.91, 128.65, 128.47, 127.57, 126.94, 124.43, 123.36, 122.51, 121.95, 106.93, 99.32, 73.79, 69.49, 31.94, 30.50, 29.62, 26.22, 22.70, 14.12. Elemental Anal. Calcd (%) for C₈₆H₁₃₆N₂O₆: C 79.82, H 10.59, N 2.16; Found: C 80.01, H 10.60, N 2.18. HRMS (ESI+) exact mass calculated for C₈₆H₁₃₆N₂O₆ (M+1): 1294.0398, Found: 1294.2369

For **HT**₁₃, greenish yellow (Yield 25%), FTIR (ATR): ν_{\max} in cm⁻¹ 2919 (Ar C-H), 2849 (Aliph C-H), 2217 (C≡N), 1656 (amide C=O), 1630 (Ar C=C), ¹H NMR (CDCl₃, 500 MHz): δ 12.70 (s, 1H, CONH), 9.22 (s, 1H, Ar-H), 8.91 (d, 1H, $J = 8.0$ Hz, Ar-H), 8.41 (d, 1H, $J = 8.5$ Hz, Ar-H), 8.30 (d, 1H, $J = 8.0$ Hz, Ar-H), 8.0 (d, 1H, $J = 8.5$ Hz, Ar-H), 7.78 (t, 1H, $J = 7.5$ Hz, Ar-H), 7.69 (t, 1H, $J = 7.5$ Hz, Ar-H), 6.92 (s, 3H, Ar-H, pyridone-H), 4.28 (t, 2H, $J = 6.5$ Hz, OCH₂), 4.22 (t, 2H, $J = 6.5$ Hz, OCH₂), 4.07 (m, 6H, 3×OCH₂), 1.94 (m, 4H, 5×CH₂), 1.88-1.79 (m, 6H, 3×CH₂), 1.63-

1.27 (m, 114 H, 57×CH₂), 0.89 (m, 15H, 5×CH₃). ¹³C NMR (CDCl₃, 125 MHz): δ 163.82, 161.17, 153.39, 150.51, 145.57, 142.47, 140.45, 131.84, 130.82, 130.02, 128.91, 128.65, 128.46, 127.57, 126.95, 124.43, 123.78, 122.51, 121.95, 106.95, 99.32, 73.79, 69.49, 31.95, 30.49, 29.63, 26.23, 22.70, 14.12; Elemental Anal. Calcd (%) for C₉₈H₁₆₀N₂O₆: C 80.49, H 11.03, N 1.92; Found: C 80.13, H 11.59, N 1.89; HRMS (ESI+) exact mass calculated for C₉₈H₁₆₀N₂O₆ (M+1): 1462.2276, Found: 1462.1235.

General procedure for the synthesis of 6-(4-hydroxyphenyl)-2-oxo-4-(3,4,5-tris(dodecyloxy)phenyl)-1,2-dihydropyridine-3-carbonitrile (HT₁₄₋₂₀)

A mixture of aldehyde **7c** (1g, 1.51 mmol 1 equiv.), 4-hydroxy acetophenone (0.20 g 1.51 mmol 1 equiv.), ethyl cyanoacetate (0.23 g, 1.66 mmol, 1.1 equiv.) and ammonium acetate (1.40 g, 18.2 mmol, 12 equiv.) in 25 volume of absolute ethanol was refluxed for about overnight. After completion of the reaction, the mixture was evaporated to dryness under reduced pressure. Then, the mixture was poured into water and extracted twice with dichloromethane. Further, the target compound was isolated from crude by means of silica gel (100-200 mesh size) using mixture of pet-ether and ethyl acetate as eluent to get **HT₁₄** as yellow solid (Yield 41 %). FTIR (ATR): ν_{\max} in cm⁻¹ 2916 (Ar C-H), 2849 (Aliph C-H), 2218 (C≡N), 1654 (C=O), 1587 (Ar-C=C). ¹H NMR (CDCl₃, 500 MHz): δ 12.29 (s, 1H, CONH), 8.01 (d, 2H, *J* = 8.5 Hz, 2×Ar-H), 7.28 (d, 2H, *J* = 8.5 Hz, 2×Ar-H), 6.84 (s, 2H, 2×Ar-H), 6.67 (s, 1H, pyridone-H), 4.086 (t, 2H, *J* = 6.5 Hz, OCH₂), 4.022 (t, 4H, *J* = 6.5 Hz, 2×OCH₂), 1.82-0.91 (m, 60H, 30×CH₂), 0.91 (t, 9H, *J* = 6.0 Hz, 3×CH₃). ¹³C NMR (CDCl₃, 125 MHz): δ 163.97, 161.30, 160.43, 153.38, 150.88, 139.69, 131.30, 128.98, 122.78, 116.93, 106.53, 105.50, 97.68, 73.91, 69.37, 31.94, 30.32, 29.76 29.72 29.65, 26.10, 22.69 14.12. Elemental Anal. Calculated for C₅₄H₈₄N₂O₅ (%): C, 77.10; H, 10.06; N, 3.33. Found: C, 76.98; H, 10.25; N, 3.15. HRMS (ESI+) exact mass calculated for C₅₄H₈₄N₂O₅ (M+1): 841.6380, Found: 841.7825.

Compounds **HT₁₅₋₂₀** were prepared by following the similar procedure as described for **HT₁₄**.

For **HT₁₅** (Yield 44 %) FTIR (ATR): ν_{\max} in cm⁻¹ 2919 (Ar C-H), 2850 (Aliph C-H), 2217 (C≡N), 1654 (C=O), 1605 (Ar-C=C). ¹H NMR (CDCl₃, 500 MHz): δ 12.14 (s, 1H, CONH), 7.95 (d, 2H, *J* = 9.0 Hz, 2×Ar-H), 7.11 (d, 2H, *J* = 8.5 Hz, 2×Ar-H),

6.89 (s, 2H, 2×Ar-H), 6.70 (s, 1H, pyridone-H), 4.06 (m, 6H, 3×OCH₂), 3.91 (s, 3H, OCH₃), 1.88-1.77 (m, 6H, 3×CH₂), 1.54-1.38 (m, 54H, 27×CH₂), 0.91 (t, 9H, *J* = 6.0 Hz, 3×CH₃). ¹³C NMR (CDCl₃, 125 MHz): δ 162.66, 160.97, 153.38, 150.17, 140.49, 130.86, 128.90, 123.83, 116.10, 115.04, 106.94, 105.60, 98.23, 73.66, 69.49, 69.49, 55.62, 31.95, 31.93, 30.39, 29.52, 26.12, 22.10, 14.10. Elemental Anal. Calculated for C₅₅H₈₆N₂O₅ (%): C, 77.24; H, 10.14; N, 3.28. Found: C, 77.38; H, 10.07; N, 3.11. HRMS (ESI+) exact mass calculated for C₅₅H₈₆N₂O₅ (M+1): 855.6536, Found: 855.42517.

For **HT₁₆** (Yield 29 %) FTIR (ATR): ν_{\max} in cm⁻¹ 3391 3357 (Ar-NH₂), 2917 (Ar C-H), 2849 (Aliph C-H), 2219 (C≡N), 1662 (C=O), 1588 (Ar-C=C). ¹H NMR (CDCl₃, 500 MHz): δ 12.27 (s, 1H, CONH), 7.76 (d, 2H, *J* = 9.0 Hz, 2×Ar-H), 6.88 (s, 2H, 2×Ar-H), 6.83 (d, 2H, *J* = 9.0 Hz, 2×Ar-H), 6.64 (s, 1H, pyridone-H), 4.15 (s, 2H, NH₂) 4.05 (m, 6H, 3×OCH₂), 1.88-1.76 (m, 6H, 3×CH₂) 1.59-1.28 (m, 54H, 27×CH₂), 0.92 (3, 9H, 3×CH₃). ¹³C NMR (CDCl₃, 125 MHz): δ 164.03, 160.77, 153.32, 150.62, 150.16, 140.29, 131.17, 128.79, 120.75, 116.45, 115.14, 106.90, 106.90, 104.61, 97.13, 73.65, 69.47, 31.94, 30.39, 29.62, 26.13, 22.69, 14.11. Elemental Anal. Calculated for C₅₄H₈₅N₃O₄ (%): C, 77.19; H, 10.20; N, 5.00. Found: C, 77.05; H, 10.33; N, 4.60. HRMS (ESI+) exact mass calculated for C₅₄H₈₅N₃O₄ (M+1): 840.6540, Found: 840.4541.

For **HT₁₇** (Yield 33 %) FTIR (ATR): ν_{\max} in cm⁻¹ 2917 (Ar C-H), 2849 (Aliph C-H), 2211 (C≡N), 1631 (C=O), 1602 (Ar-C=C). ¹H NMR (CDCl₃, 500 MHz): δ 12.16 (s, 1H, CONH), 7.75 (d, 2H, *J* = 9.0 Hz, 2×Ar-H), 6.79 (s, 2H, 2×Ar-H), 6.74 (d, 2H, *J* = 9.0 Hz, 2×Ar-H), 6.55 (s, 1H, pyridone-H), 3.96 (m, 6H, 3×OCH₂), 3.0 (s, 6H, NCH₃), 1.78-1.67 (m, 6H, 3×CH₂) 1.42-1.40 (m, 54H, 57×CH₂), 0.81 (m, 9H, 3×CH₃). ¹³C NMR (CDCl₃, 125 MHz): δ 163.92, 160.60, 153.27, 152.61, 142.25 131.42, 128.32, 117.86, 116.52, 112.12, 106.85, 104.17, 96.37, 73.64, 69.43, 40.08, 31.95, 30.38, 29.51, 26.13, 22.70, 14.12. Elemental Anal. Calculated for C₅₆H₈₉N₃O₄ (%): C, 77.46; H, 10.33; N, 4.84. Found: C, 77.85; H, 10.12; N, 5.02. HRMS (ESI+) exact mass calculated for C₅₆H₈₉N₃O₄ (M+1): 868.6853, Found: 868.8712.

For **HT₁₈** (Yield 40 %) FTIR (ATR): ν_{\max} in cm⁻¹ 2919 (Ar C-H), 2850 (Aliph C-H), 2212 (C≡N), 1631 (C=O), 1601 (Ar-C=C). ¹H NMR (CDCl₃, 500 MHz): δ 13.26

(s, 1H, CONH), 8.32 (d, 1H, $J = 3.0$ Hz, Ar-H), 7.59 (dd, $J = 5.0$ Hz, 1H, Ar-H), 7.32 (m, 1H, Ar-H), 6.89 (m, 2H, $2 \times$ Ar-H), 6.72 (s, 1H, pyridone-H), 4.05 (m, 6H, $3 \times$ OCH₂), 1.89-1.78 (m, 6H, $3 \times$ CH₂) 1.39-1.28 (m, 54H, $27 \times$ CH₂), 0.91 (m, 9H, $3 \times$ CH₃). ¹³C NMR (CDCl₃, 125 MHz): 163.82, 161.08, 153.40, 144.09, 134.31, 130.45, 130.08, 129.73, 115.96, 106.91, 105.61, 98.62, 73.69, 69.51, 31.94, 30.39, 29.65, 26.12, 22.70, 14.12. Elemental Anal. Calculated for C₅₂H₈₂N₂O₄S (%): C, 75.13; H, 9.94; N, 3.37; S, 3.86. Found: C, 75.11; H, 10.07; N, 3.57; S, 3.42. HRMS (ESI+) exact mass calculated for C₅₆H₈₉N₃O₄ (M+1): 831.5995, Found: 831.8746.

For **HT₁₉** (Yield 49 %) FTIR (ATR): ν_{\max} in cm⁻¹ 2919 (Ar C-H), 2850 (Aliph C-H), 2212 (C≡N), 1631 (C=O), 1601 (Ar-C=C). ¹H NMR (CDCl₃, 500 MHz): δ 13.25 (s, 1H, CONH), 8.07 (d, 2H, $J = 8.5$ Hz, $2 \times$ Ar-H), 7.85 (d, 2H, $J = 8.5$ Hz, $2 \times$ Ar-H), 7.68 (t, 2H, $J = 7.0$ Hz, $2 \times$ Ar-H), 7.49 (m, 2H, $2 \times$ Ar-H), 7.42 (t, 1H, $J = 7.0$ Hz, Ar-H), 6.92 (s, 2H, $2 \times$ Ar-H), 6.83 (s, 1H, pyridone-H), 4.07 (m, 6H, $3 \times$ OCH₂), 1.89-1.78 (m, 6H, $3 \times$ CH₂) 1.64-1.28 (m, 54H, $27 \times$ CH₂), 0.91 (m, 9H, $3 \times$ CH₃). ¹³C NMR (CDCl₃, 125 MHz): 164.15, 161.00, 153.41, 150.05, 144.70, 140.52, 139.55, 130.70, 130.37, 128.99, 128.25, 128.15, 127.74, 127.28, 116.00, 106.91, 106.46, 99.30, 73.68, 69.48, 31.96, 31.94, 30.40, 29.54, 26.14, 22.71, 14.12. Elemental Anal. Calculated for C₆₀H₈₈N₂O₄ (%): C, 79.95; H, 9.84; N, 3.11. Found: C, 80.08; H, 9.74; N, 3.18. HRMS (ESI+) exact mass calculated for C₆₀H₈₈N₂O₄ (M+1): 901.6744, Found: 901.8974

For **HT₂₀** (Yield 30 %) IR (ATR): ν_{\max} in cm⁻¹ 2919 (Ar C-H), 2850 (Aliph C-H), 2218 (C≡N), 1636 (C=O), 1589 (Ar-C=C). ¹H NMR (CDCl₃, 500 MHz): δ 11.88 (s, 1H, CONH), 7.58 (d, 2H, $J = 9$ Hz, Ar-H), 7.27-7.23 (m, 4H, Ar-H), 7.10 (3, 4H, Ar-H), 7.49 (m, 2H, Ar-H), 7.03 (m, 4H, Ar-H), 6.76 (s, 2H, Ar-H), 6.53 (s, 1H, pyridone-H), 3.95 (t, 6H, $J = 6.5$ Hz, OCH₂), 1.76-1.68 (m, 6H, CH₂) 1.40 (m, 6H, CH₂), 1.22-1.18 (m, 48H, CH₂) 0.81 (m, 9H, CH₃). ¹³C NMR (CDCl₃, 125 MHz): 164.25, 160.83, 153.31, 146.35, 130.99, 129.69, 127.98, 125.86, 124.70, 123.23, 120.98, 106.83, 73.65, 69.43, 31.93, 30.38, 29.77, 29.37, 26.12, 22.70, 14.12. Elemental Anal. Calculated for C₆₆H₉₃N₃O₄ (%): C, 79.87; H, 9.45; N, 4.23. Found: C, 79.01; H, 10.0; N, 4.32. HRMS (ESI+) exact mass calculated for C₆₀H₈₈N₂O₄ (M+1): 992.7166, Found: 992.9932.

3.2.5 Design and synthesis of HT₂₁₋₂₆ (Series-4)

A series of functional rhodamine-*N*-acetic acid derivatives, **HT**₂₁₋₂₆ belonging to **Series-4** has been designed. The present design comprises a new wedge-shaped structure having a donor-acceptor configuration carrying electron rich trialkoxybenzylidene appended to electron deficient rhodamine-*N*-acetic acid (**Fig 3.16**). Further, all members of the series, **HT**₂₁₋₂₆ are discrete with respect to varying length, number or position of alkoxy chains on benzylidene ring. Here, the H-bonding ability of rhodamine-*N*-acetic acid moiety occupied at tip of wedge would stabilize the columnar liquid crystalline behaviour through specific H-bonding interactions. Moreover, because of their D-A architecture, they were expected to offer the essential optical characteristics at the self-assembled state.

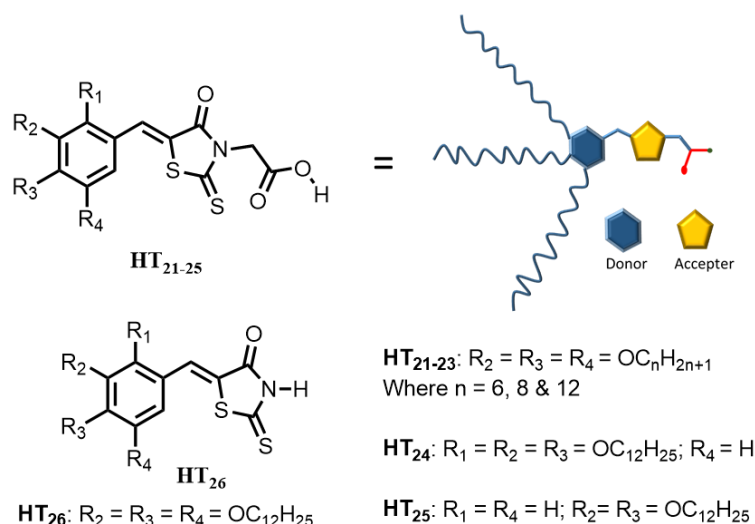
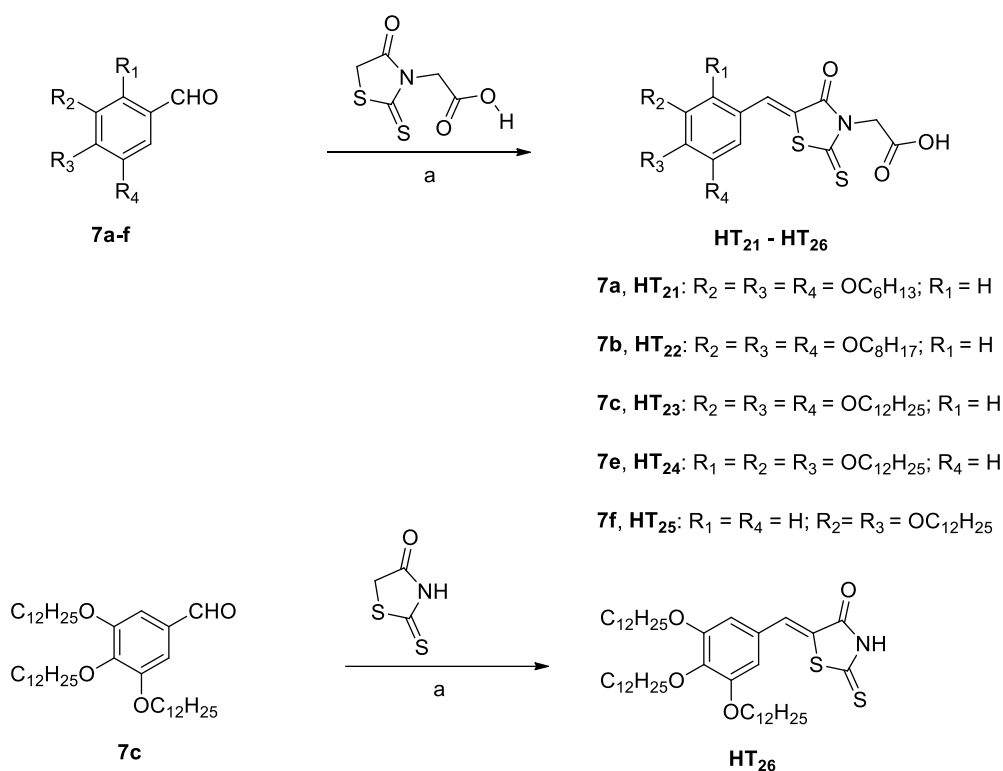


Figure 3.16 Design of wedge-shaped molecules **HT**₂₁₋₂₆ of **Series-4**

The series of alkoxybenzylidenerhodamine-*N*-acetic acid derivatives, **HT**₂₁₋₂₅ were synthesized by a straightforward ammonium acetate mediated Knoevenagel type condensation between a variety of alkoxy benzaldehydes and rhodamine-3-acetic acid. The required substituted benzaldehydes were prepared using well-documented procedures (Maruyama et al. 2010; Shanker et al. 2011). Further, a tridodecyloxybenzylidene substituted rhodamine, **HT**₂₆ was synthesized using a similar method. **Scheme 3.4** depicts the synthetic routes for the preparation of newly designed **HT**₂₁₋₂₆.

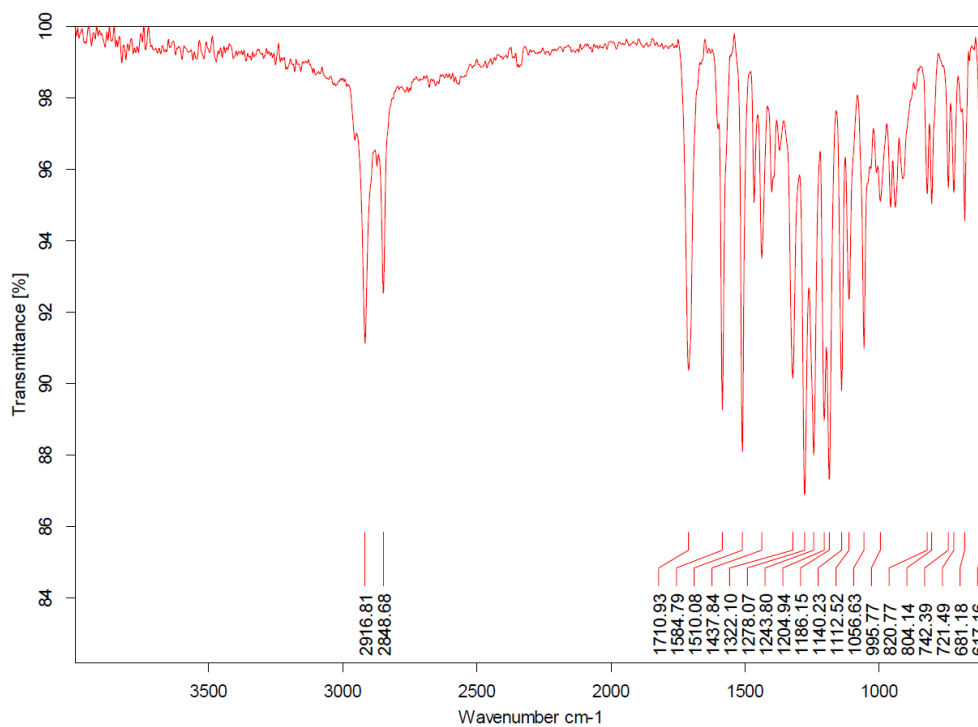
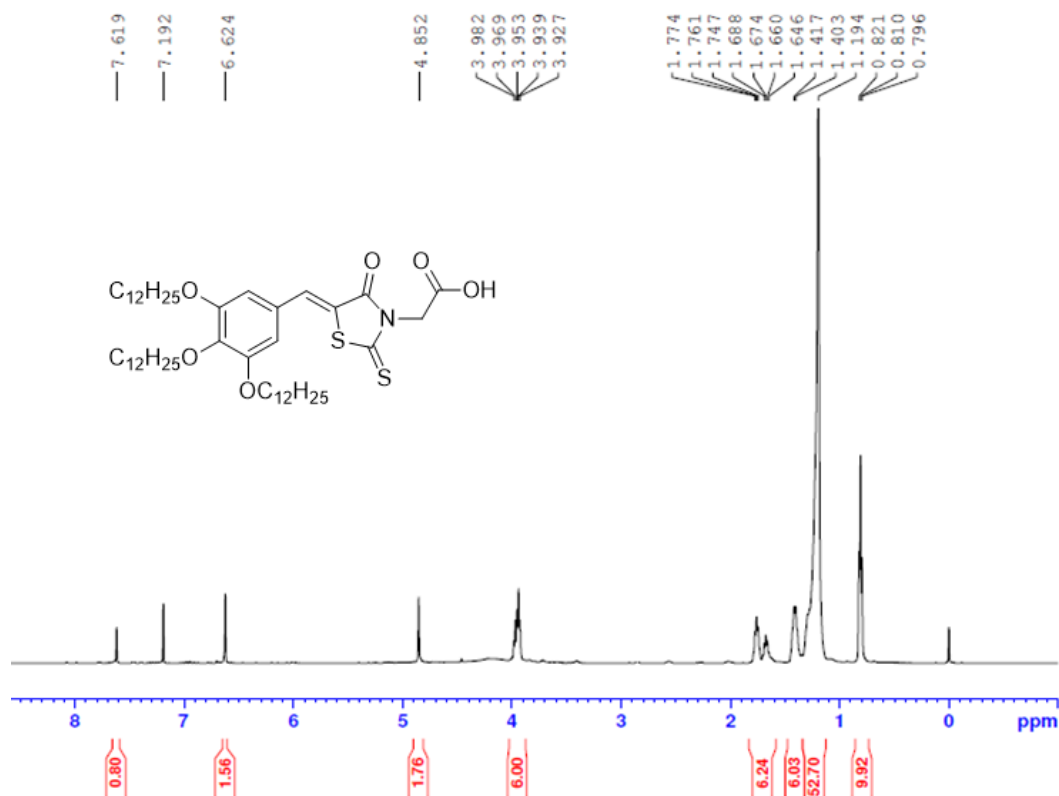


Scheme 3.4 Synthesis scheme for preparation of **HT₂₁₋₂₆**. Reagents and conditions: (a) Ammonium acetate, Acetic acid, 80 °C, 24 hrs, 40-65 %

3.2.5.1 Results and discussion

All the precursors and final compounds were characterized by means of combination of spectral techniques and elemental analysis. FTIR, ¹H-NMR and ¹³C-NMR spectra of the representative member of the series, *i.e.* **HT₂₃** are shown in **Figs 3.17, 3.18** and **3.19**, respectively. Its FTIR spectrum shows the fundamental absorption bands at 2916 (aromatic C-H_{stretch}), 2848 (aliphatic C-H_{stretch}), and 1710 cm⁻¹ (carboxylic acid C=O_{stretch}) indicating the formation of product by condensation reaction. Further, appearance of unique down fielded singlet at 7.62 ppm of olefinic proton, singlet signal at 6.62 ppm of tertiary protons of aromatic ring, sharp signal at 4.86 ppm due to CH₂ present between carboxylic acid and rhodanine ring, and rest of the characteristic lower frequency signals, in its ¹H-NMR spectrum confirmed the structure. Moreover, persisted signals at down field, *viz.* 192.85, 170.00 and 153.60 ppm in its ¹³C-NMR spectrum are attributed to highly deshielded carbons of olefinic, carboxylic acid and rhodanine ring carbonyl carbons, respectively. In addition, the elemental analysis results of the compound were in corroborated with the theoretical data. The structures of the remaining compounds of the **Series-4** were elucidated in the similar way.

Some selected spectra

Figure 3.17 FTIR (ATR) spectrum of HT₂₃Figure 3.18 ¹H-NMR (500 MHz) spectrum of HT₂₃ recorded in CDCl₃

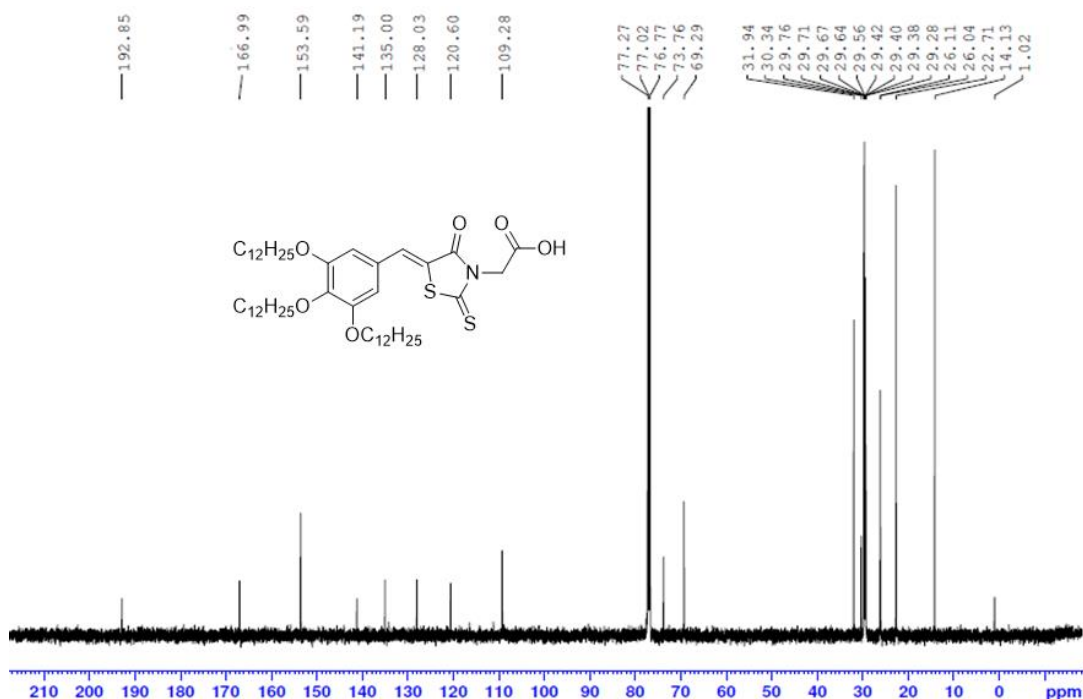


Figure 3.19 ¹³C-NMR (125 MHz) spectrum of **HT**₂₃ recorded in CDCl₃

3.2.5.2 Experimental procedures

The present section describes experimental protocols followed to synthesise the target wedge-shaped rhodanine derivatives, **HT**₂₁₋₂₆. Synthesis and characterization of key intermediates alkoxybenzaldehydes, *i.e.* **7b** and **7c** have been covered in section 3.2.4.2. The characterization data of the remaining alkyl members, *i.e.* **7a**, **7e** and **7f** are given below.

Synthesis of (Z)-2-(4-oxo-2-thioxo-5-(3,4,5-tris(hexyloxy)benzylidene)thiazolidin-3-yl)acetic acid (HT₂₁)

A mixture of alkoxybenzaldehydes (**7a**) (1g, 2.45 mmol, 1 equiv.), rhodanine-*N*-acetic acid (0.47 g, 2.45 mmol, 1 equiv.) and ammonium acetate (1.90g, 24.5 mmol, 10 equiv.) in 20 mL of glacial acetic acid was refluxed for overnight. Then, the mixture was allowed to cool at RT. The obtained yellow solid was filtered and washed with plenty of water. The crude mixture was further purified by column chromatography (100-200 mesh size) using pet-ether: ethyl acetate solvent mixture in 2:10 ratio to yield **HT**₂₁ as dark yellow solid. (Yield 59 %). FTIR (ATR) ν_{\max} in cm^{-1} 2922 (Ar C-H), 2858 (Aliph C-H), 1760 (Acid C=O), 1707 (Rhodanine, C=O), 1603 (Ar C=C). ¹H NMR

(CDCl₃, 500 MHz): δ 7.74 (s, 1H, C=CH), 6.75 (s, 2H, 2 \times Ar-H), 4.98 (s, 2H, NCH₂), 4.07 (m, 6H, 3 \times OCH₂), 1.91-1.75 (m, 6H, 3 \times CH₂), 1.55-1.31 (m, 18H, 9 \times CH₂), 0.96 (t, J = 5.0 Hz, 9H, 3 \times CH₃). ¹³C NMR (CDCl₃, 125 MHz): δ 192.82, 166.97, 153.59, 141.21, 135.03, 128.03, 120.59, 109.31, 73.76, 69.31, 31.63, 31.56, 30.27, 29.23, 25.71, 22.63, 14.04, 12. Elemental Anal. Calcd for C₃₀H₄₅NO₆S₂ (%): C, 62.14; H, 7.82; N, 2.42; S, 11.06; Found: C, 61.98; H, 7.92; N, 2.31; S, 10.99.

For **HT**₂₂, 1:9 ethyl acetate: pet-ether mobile phase (Yield 51 %). FTIR (ATR), ν_{\max} in cm⁻¹ 2919 (Ar C-H), 2850 (Aliph C-H), 1743 (Acid C=O), 1711 (Rhodanine, C=O), 1602 (Ar C=C). ¹H NMR (CDCl₃, 500 MHz): δ 7.61 (s, 1H, C=CH), 6.61 (s, 2H, 2 \times Ar-H), 4.84 (s, 2H, NCH₂), 3.95 (m, 6H, 3 \times OCH₂), 1.77-1.66 (m, 6H, 3 \times CH₂), 1.41-1.18 (m, 30H, 15 \times CH₂), 0.81 (t, J = 5.0 Hz, 9H, 3 \times CH₃). ¹³C NMR (CDCl₃, 125 MHz): δ 192.83, 166.99, 153.58, 141.21, 134.99, 128.04, 120.61, 109.33, 73.76, 69.32, 31.91, 31.82, 30.32, 29.70, 29.35, 26.12, 22.67, 14.09. Elemental Anal. Calcd for C₃₆H₅₇NO₆S₂ (%): C, 65.12; H, 8.65; N, 2.11; S, 9.66; Found: C, 65.22; H, 8.90; N, 1.99; S, 9.51.

For **HT**₂₃, 1:9 ethyl acetate: pet-ether mobile phase (Yield 45 %). FTIR (ATR) ν_{\max} in cm⁻¹ 2916 (Ar C-H), 2848 (Aliph C-H), 1710 (Rhodanine, C=O), 1584 (Ar C=C). ¹H NMR (CDCl₃, 500 MHz): δ 7.61 (s, 1H, C=CH), 6.62 (s, 2H, 2 \times Ar-H), 4.85 (s, 2H, NCH₂), 3.96 (m, 6H, 3 \times OCH₂), 1.77- 1.64 (m, 6H, 3 \times CH₂), 1.41-1.19 (m, 54H, 27 \times CH₂), 0.80 (t, J = 5.0 Hz, 9H, 3 \times CH₃). ¹³C NMR (CDCl₃, 125 MHz): δ 192.85, 166.99, 153.59, 141.19, 135.0, 128.03, 120.60, 109.28, 73.76, 69.29, 31.94, 30.32, 29.74, 29.28, 26.07, 22.71, 14.13. Elemental Anal. Calcd for C₄₈H₈₁NO₆S₂ (%): C, 69.27; H, 9.81; N, 1.68; S, 7.71; Found: C, 69.45; H, 10.13; N, 1.50; S, 7.10

For **HT**₂₄, purified by recrystallization using ethanol (Yield 61 %). FTIR (ATR) ν_{\max} in cm⁻¹ 2915 (Ar C-H), 2849 (Aliph C-H), 1704 (Rhodanine, C=O), 1576 (Ar C=C). ¹H NMR (CDCl₃, 500 MHz): δ 8.04 (s, 1H, C=CH), 7.05 (d, J = 8.5 Hz, 1H, Ar-H), 6.67 (d, J = 8.5 Hz, 1H, Ar-H), 4.84 (s, 2H, NCH₂), 4.01 (t, J = 6.5 Hz 2H, OCH₂), 3.96 (t, J = 6.0 Hz, 2H, OCH₂), 3.89 (t, J = 6.5 Hz 2H, OCH₂), 1.78- 1.67 (m, 6H, 3 \times CH₂), 1.41-1.19 (m, 54H, 27 \times CH₂), 0.81 (t, J = 5.5 Hz, 9H, 3 \times CH₃). ¹³C NMR (CDCl₃, 125 MHz): δ 192.85, 166.99, 153.59, 141.19, 135.0, 128.03, 120.60, 109.28,

73.76, 69.29, 31.94, 30.32, 29.74, 29.28, 26.07, 22.71, 14.13. Elemental Anal. Calcd for $C_{48}H_{81}NO_6S_2$ (%): C, 69.27; H, 9.81; N, 1.68; S, 7.71; Found: C, 69.55; H, 9.82; N, 1.59; S, 7.55.

For **HT₂₅**, purified by recrystallization using methanol (Yield 59 %). FTIR (ATR) ν_{\max} in cm^{-1} 2917 (Ar C-H), 2849 (Aliph C-H), 1707 (Rhodanine, C=O), 1600 (Ar C=C). 1H NMR ($CDCl_3$, 500 MHz): δ 7.65 (s, 1H, C=CH), 7.04 (d, $J = 8.5$ Hz, 1H, Ar-H), 6.90 (s, 1H, Ar-H), 6.86 (d, $J = 8.5$ Hz, 1H, Ar-H), 4.85 (s, 2H, NCH₂), 3.96 (m, 4H, 2×OCH₂), 1.77 (m, 4H, 2×OCH₂), 1.41 (m, 4H, 2×OCH₂), 1.24 (m, 4H, 2×OCH₂), 1.16 (m, 32, 16×OCH₂) 0.80 (t, $J = 5.5$ Hz, 6H, 2×CH₃). ^{13}C NMR ($CDCl_3$, 125 MHz): δ 192.85, 170.18, 167.17, 152.20, 149.48, 134.49, 125.88, 119.08, 114.84, 113.12, 69.42, 69.16, 31.92, 29.65, 29.35, 25.96, 22.68, 14.09. Elemental Anal. Calcd for $C_{36}H_{57}NO_5S_2$ (%): C, 66.73; H, 8.87; N, 2.16; S, 9.90; Found: C, 66.99; H, 8.75; N, 2.20; S, 10.12.

For **HT₂₆**, purified by recrystallization using methanol (Yield 59 %). FTIR (ATR) ν_{\max} in cm^{-1} 2917 (Ar C-H), 2849 (Aliph C-H), 1707 (Rhodanine, C=O), 1600 (Ar C=C). 1H NMR ($CDCl_3$, 500 MHz): δ 7.51 (s, 1H, C=CH), 6.59 (s, 2H, Ar-H) 3.96 (m, 6H, 3×OCH₂), 1.78-1.64 (m, 6H, 3×OCH₂), 1.41-1.19 (m, 54H, 27×CH₂), 0.81 (t, $J = 5.5$ Hz, 9H, 3×CH₃). ^{13}C NMR ($CDCl_3$, 125 MHz): δ 153.61, 141.25, 134.37, 127.81, 123.09, 73.75, 69.31, 31.93, 30.34, 29.62, 26.12, 22.70, 14.11; Elemental Anal. Calcd for $C_{46}H_{79}NO_4S_2$ (%): C, 71.36; H, 10.28; N, 1.81; O, S, 8.28; Found: C, 71.45; H, 10.02; N, 1.90; S, 8.89.

For **7a**, FTIR (ATR) ν_{\max} in cm^{-1} 2920 (Ar C-H), 2849 (Aliph C-H), 2727 (aldehyde C-H), 1695 (aldehyde C=O), 1586 (Ar C=C). 1H NMR ($CDCl_3$, 500 MHz): δ - 9.85 (s, 1H, Ar-CHO), 7.10 (s, 2H, ArH), 4.05 (m, 6H, 3×OCH₂), 1.86-1.75 (m, 6H, 3×CH₂), 1.5-1.36 (m, 18H, 9×CH₂), 0.9 (m, 9H, 3×CH₃); ^{13}C NMR ($CDCl_3$, 125 MHz): δ 191.30, 153.53, 143.89, 131.45, 107.89, 73.64, 69.26, 31.61, 30.28, 29.21, 25.69, 22.63, 14.03; Elemental Anal. Calcd for $C_{25}H_{42}O_4$ (%): C, 73.85; H, 10.41; Found: C 73.45; H, 10.11.

For **7e**, FTIR (ATR, ν_{\max} in cm^{-1}): 2916 (Ar C-H), 2849 (Aliph C-H), 2755 (aldehyde C-H), 1681 (aldehyde C=O), 1586, (Ar C=C); 1H NMR ($CDCl_3$, 500 MHz):

δ 10.27 (s, 1H, $\underline{\text{CHO}}$), 7.59 (d, $J = 9.0$ Hz, 1H, Ar- $\underline{\text{H}}$), 6.73 (d, $J = 9.0$ Hz, 1H, Ar- $\underline{\text{H}}$), 4.18 (t, 2H, $J = 6.0$ Hz, $\underline{\text{OCH}_2}$), 4.05 (t, 2H, $J = 6.0$ Hz, $\underline{\text{OCH}_2}$), 3.99 (t, 2H, $J = 6.0$ Hz, $\underline{\text{OCH}_2}$), 1.87-1.77 (m, 6H, $3 \times \underline{\text{CH}_2}$), 1.50-1.28 (m, 54H, $27 \times \underline{\text{CH}_2}$), 0.9 (t, 9H, $J = 5.5$ Hz, $3 \times \underline{\text{CH}_3}$); ^{13}C NMR (CDCl_3 , 125 MHz): δ 189.16, 159.17, 156.71, 141.06, 123.60, 108.09, 75.34, 73.77, 68.93, 31.92, 30.23, 29.65, 29.32, 26.10, 22.68, 14.09 Elemental Anal. Calcd for $\text{C}_{43}\text{H}_{78}\text{O}_4$ (%): C 78.36, H 11.93; Found: C 78.20, H 11.98.

For **7f**, FTIR (ATR) ν_{max} in cm^{-1} 2916 (Ar C-H), 2848 (Aliph C-H), 2757 (aldehyde C-H), 1684 (aldehyde C=O), 1584 (Ar C=C). ^1H NMR (CDCl_3 , 500 MHz): δ 9.85 (s, 1H, $\underline{\text{CHO}}$), 7.43 (m, 2H, $2 \times \text{Ar-}\underline{\text{H}}$), 6.97 (d, 1H, $J = 8.0$ Hz, Ar- $\underline{\text{H}}$), 4.07 (m, 4H, $2 \times \underline{\text{OCH}_2}$), 1.86 (m, 4H, $2 \times \underline{\text{CH}_2}$), 1.49-1.28 (m, 36H, $18 \times \underline{\text{CH}_2}$), 0.90 (t, 6H, $J = 6.5$ Hz, $2 \times \underline{\text{CH}_3}$). ^{13}C NMR (CDCl_3 , 125 MHz): 190.97, 154.72, 149.47, 129.90, 126.55, 111.81, 111.07, 69.15, 31.92, 29.52, 25.94, 22.68, 14.09. Elemental Anal. Calcd (%) for $\text{C}_{31}\text{H}_{54}\text{O}_3$: C, 78.43; H, 11.46; C, 78.15, H, 10.20.

3.2.6 Design and synthesis of HT₂₇₋₃₁ (Series-5)

While designing the members of **Series-5**, maleimide moiety has been introduced as a novel heterocyclic motif to achieve columnar mesomorphism. In the new design, the length of aromatic segments has been varied in order to obtain wedge-/taper-shaped mesogens and to study their structure-property relationship. **Fig 3.20** depicts newly designed maleimides. These molecules are anticipated to exhibit supramolecular LC behaviour *via* H-bonding through polar maleimide ring.

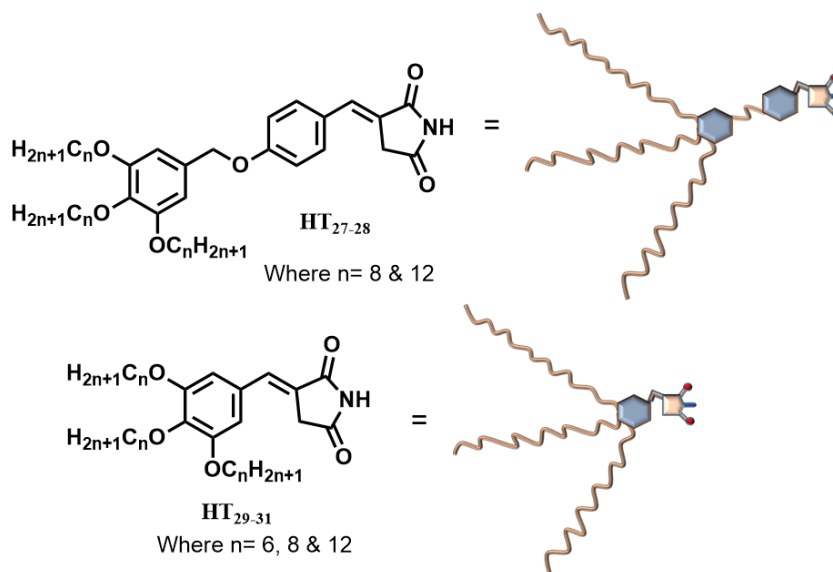
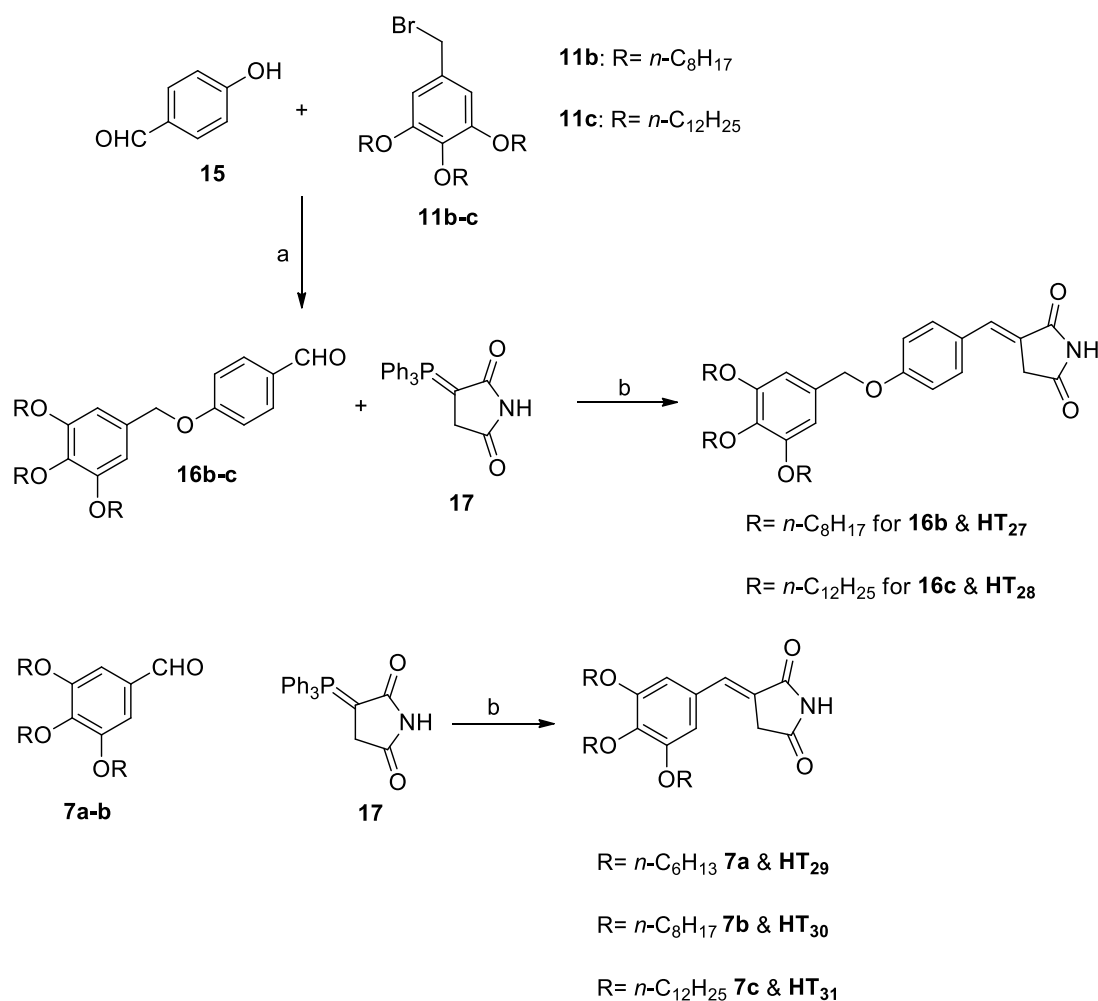


Figure 3.20 Design of new maleimides HT₂₇₋₃₁ of **Series-5**

The synthetic route for the preparation of newly designed maleimide derivatives is summarized in **Scheme 3.5**. The required key-precursors, *i.e.* trialkoxy benzyl bromides, **11b-c** and trialkoxy benzaldehydes, **7a-c** were synthesized by adopting well-documented procedures with optimized conditions. Synthesis of target compounds **HT27-28** involves a simple *O*-alkylation of 4-hydroxybenzaldehyde (**15**) with **11b-c** to get key-precursors **16b-c**, followed by the Wittig condensation of aldehydes **16b-c** with maleimide derivative **12**, which was prepared by the Michael addition reaction of triphenylphosphine to maleimide. Similarly, trialkoxybenzylidenyl maleimides, **HT27-28** were also obtained by using Wittig's protocol. The Wittig reaction, under the reflux condition in methanol, yielded the desired product with an (*E*)-configuration exclusively.



Scheme 3.5 Synthesis of maleimide derivatives. Reagents and conditions: (a) K_2CO_3 , DMF, 70°C , overnight, 78-81 %; (g) CH_3OH , reflux, 10 hrs, 45-60 %

3.2.6.1 Results and discussion

Structures of the newly synthesized compounds were determined by FTIR, ^1H -NMR, ^{13}C -NMR spectral and elemental analyses. In FTIR spectrum of **16b**, absorption band at 1688 cm^{-1} is due to stretching vibration of aldehyde carbonyl group manifesting the formation of alkylated product. The compound, in its ^1H -NMR, shows a unique singlet at 9.91 ppm due to CHO, rest of the signals attributed to the remaining protons, confirming its complete structure. The compound **HT₂₇** exhibits key IR bands at 3154 ($\text{N-H}_{\text{stretch}}$), 1768 ($\text{HNC}=\text{O}_{\text{stretch}}$) and 1705 cm^{-1} (α, β -unsaturated $\text{HNC}=\text{O}_{\text{stretch}}$) signifying the successful formation of maleimide adduct by Wittig reaction (**Fig 3.21**). In its ^1H -NMR, it displays most deshielded NH proton as singlet at 8.71 ppm, benzyloxy protons at 5.02 ppm, maleimide ring secondary protons at 3.62 ppm confirming for formation of the product. In addition, its ^{13}C -NMR spectral data have also validated the structure (**Fig 3.22**). Likewise, structures of remaining maleimide derivatives were also established. FTIR ^1H -NMR and ^{13}C -NMR spectra of one of the representative compounds, *i.e.* **HT₃₀** of the series are shown in **Figs 3.24, 3.25, and 3.26**, respectively.

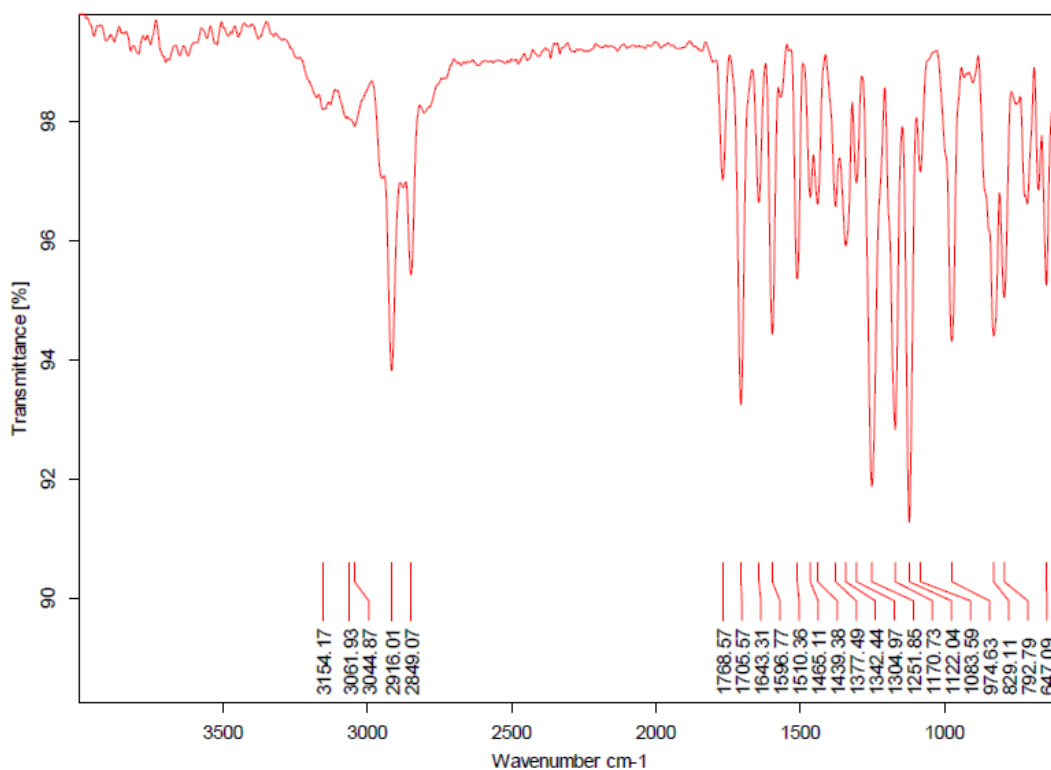


Figure 3.21 FTIR (ATR) spectrum of **HT₂₇**

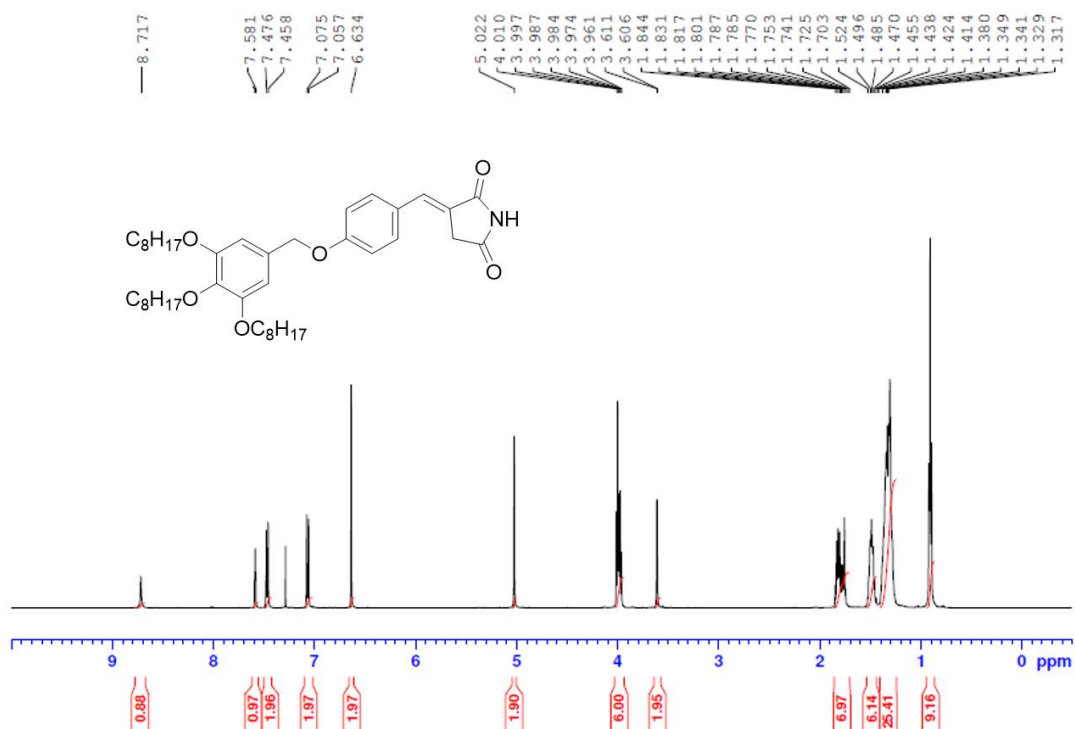


Figure 3.22 ¹H-NMR (500 MHz) spectrum of **HT**₂₇ recorded in CDCl₃

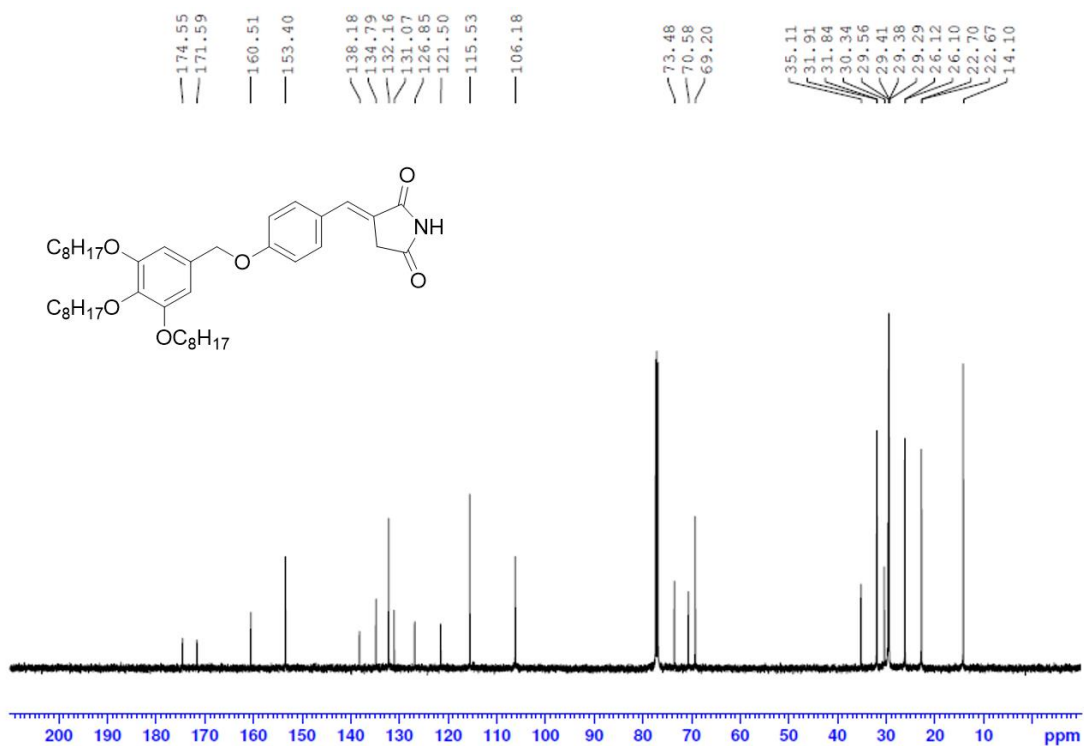
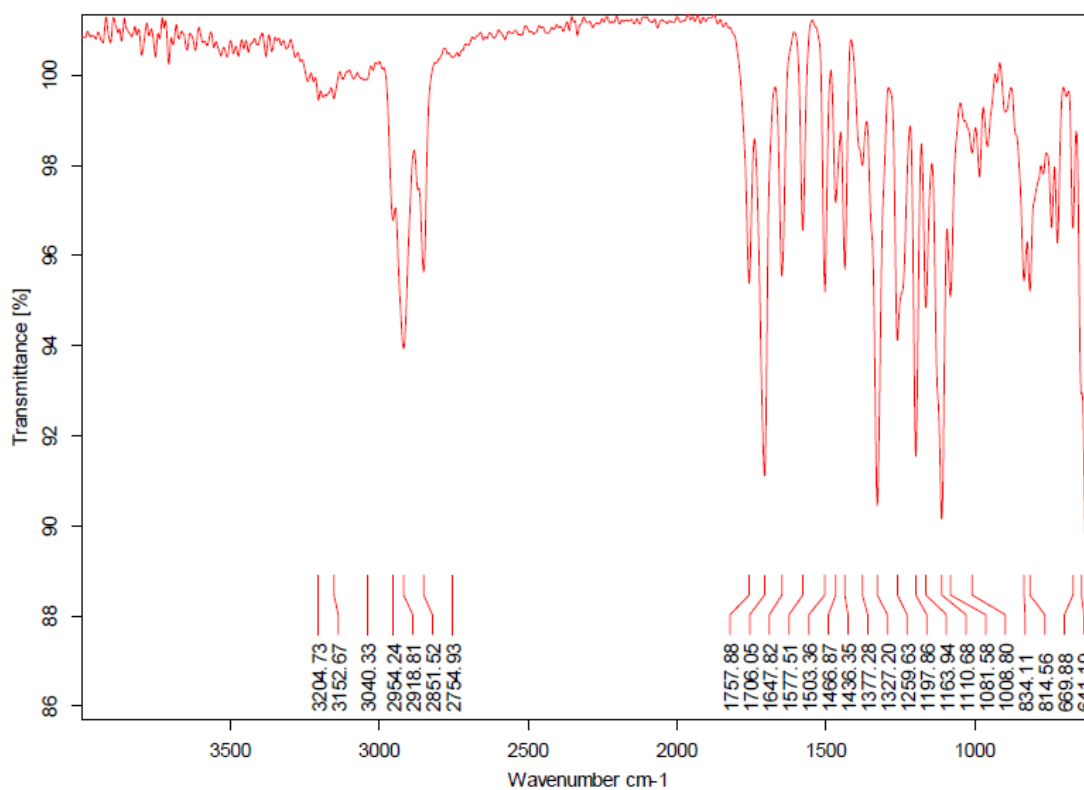
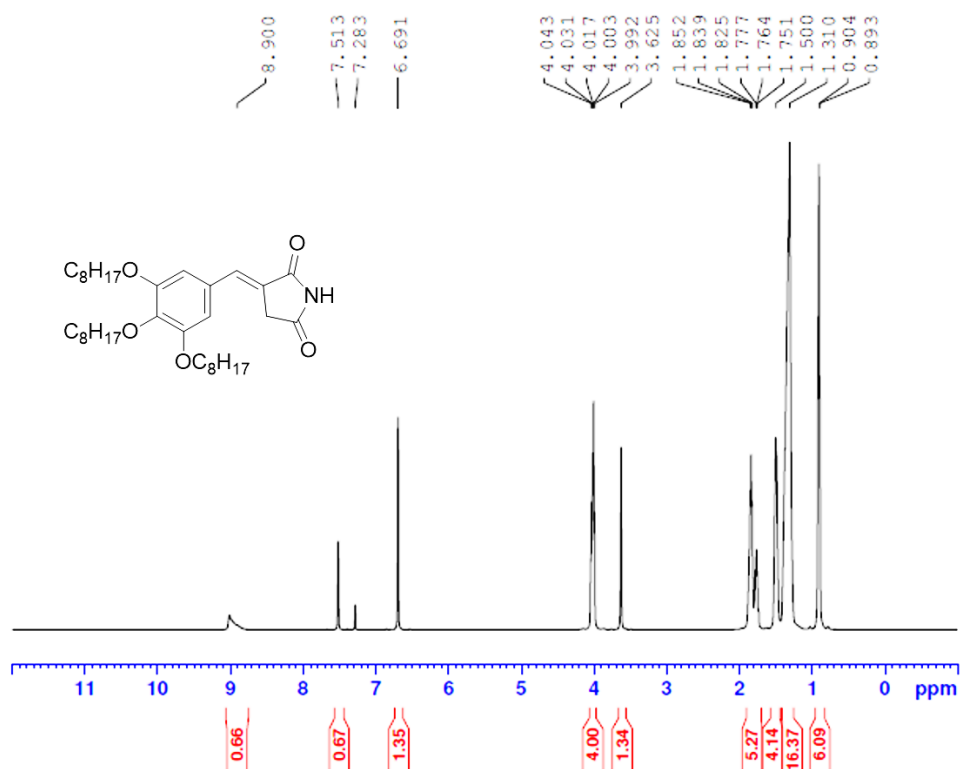


Figure 3.23 ¹³C-NMR (125 MHz) spectrum of **HT**₂₇ recorded in CDCl₃

Figure 3.24 FTIR (ATR) spectrum of HT₃₀Figure 3.25 ¹H-NMR (500 MHz) spectrum of HT₃₀ recorded in CDCl₃

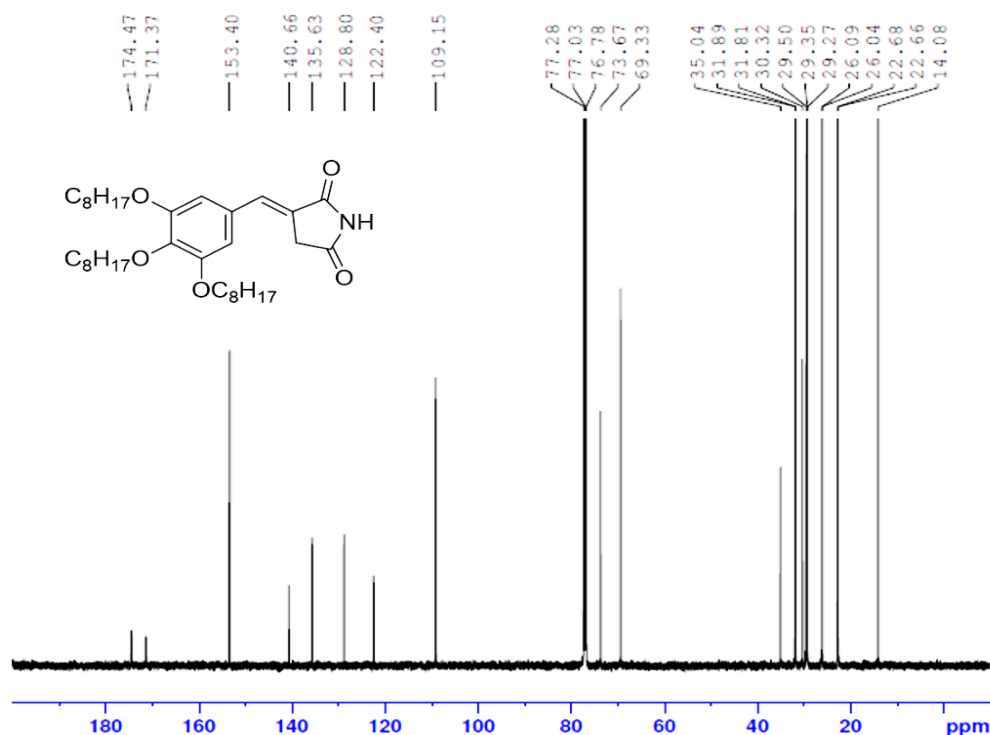


Figure 3.26 ^{13}C -NMR (125 MHz) spectrum of **HT**₃₀ recorded in CDCl_3

3.2.6.2 Experimental procedures

Experimental procedures pertaining to synthesis of the designed maleimide derivatives along with their structural characterization data are as follows.

Synthesis of 4-((3,4,5-tris(octyloxy)benzyl)oxy)benzaldehyde (16b)

A mixture of 4-hydroxybenzaldehyde (**15**) (0.2 g, 1.63 mmol), trioctyloxybenzyl bromide (**5a**) (1 g, 1.80 mmol) and anhydrous K_2CO_3 (0.45 g, 3.27 mmol) in 20 mL of dry DMF was heated to 70 °C under an argon atmosphere for overnight. Then, the mixture was poured into ice cold water and the obtained precipitate was filtered. The crude product was recrystallized from cold methanol to get the product. (Yield 81 %). FTIR (ATR): ν_{max} in cm^{-1} 2921 (Ar C-H), 2853 (Aliph C-H), 2733 (aldehyde C-H), 1688 (aldehyde C=O), 1600 (Ar C=C). ^1H NMR (CDCl_3 , 500 MHz): δ 9.91 (s, 1H, CHO), 7.86 (d, 2H, $J = 8.5$ Hz, $2 \times \text{Ar-H}$), 7.10 (d, 2H, $J = 9.0$ Hz, $2 \times \text{Ar-H}$), 6.63 (s, 1H, Ar-H), 5.05 (s, 2H, OCH_2), 3.98 (m, 6H, $3 \times \text{OCH}_2$), 1.84-1.75 (m, 6H, $3 \times \text{CH}_2$), 1.2 (m, 54H, $27 \times \text{CH}_2$), 0.96 (t, 9H, $J = 6.0$ Hz, $3 \times \text{CH}_3$). ^{13}C NMR (CDCl_3 , 125 MHz): δ 190.76, 163.78, 153.42, 153.18, 138.29, 131.98, 130.80, 130.15,

115.15, 106.22, 73.47, 70.70, 69.22, 31.91, 31.83, 30.34, 29.35, 26.10, 22.69, 14.09. Elemental Anal. Calcd for C₃₈H₆₀O₅ (%): C, 76.47; H, 10.13; Found: C, 76.32, H, 10.03.

Synthesis of 4-((3,4,5-tris(dodecyloxy)benzyl)oxy)benzaldehyde (16c)

The precursor **16c** was prepared by following the similar procedure described above (Yield 78 %). FTIR (ATR): ν_{\max} in cm⁻¹ 2918 (Ar C-H), 2850 (Aliph C-H), 2752 (aldehyde C-H), 1685 (aldehyde C=O), 1601 (Ar C=C). ¹H NMR (CDCl₃, 500 MHz): δ 9.91 (s, 1H, CHO), 7.86 (d, 2H, $J = 8.0$ Hz, 2×Ar-H), 7.10 (d, 2H, $J = 8.5$ Hz, 2×Ar-H), 6.63 (s, 1H, Ar-H), 5.05 (s, 2H, OCH₂), 3.98 (m, 6H, 3×OCH₂), 1.82-1.75 (m, 6H, 3×CH₂), 1.49-1.30 (m, 30H, 15×CH₂), 0.96 (m, 9H, 3×CH₃). ¹³C NMR (CDCl₃, 125 MHz): δ 190.76, 163.78, 153.43, 138.30, 131.98, 130.78, 130.15, 115.15, 106.23, 73.47, 70.70, 69.22, 31.95, 31.93, 30.35, 29.70, 26.14, 26.10, 22.69, 14.11. Elemental Anal. Calcd for C₅₀H₈₄O₅ (%): C, 78.48; H, 11.06; Found: C, 78.32, H, 10.99.

Synthesis of (E)-3-(4-((3,4,5-tris(octyloxy)benzyl)oxy)benzylidene)pyrrolidine-2,5-dione (HT₂₇)

An equimolar mixture of **16b** (1g, 1.6 mmol, 1 equiv.) and triphenylphosphoranylidene succinimide (**17**) (0.60 g, 1.6 mmol, 1 equiv.) in 20 mL of methanol was refluxed for 10 hrs. After completion of the reaction, the mixture was allowed to cool at room temperature. The obtained white precipitate was filtered and washed with methanol. Then, the crude product was purified by silica gel column chromatography (100-200 mesh size) eluting with 5 % ethyl acetate in pet-ether (60-70 °C) to yield final compounds, (Yield 45 %). FTIR (ATR): ν_{\max} in cm⁻¹ 3218 (amide NH), 3057 (vinyl C-H), 2922 (Ar C-H), 2852 (Aliph C-H), 1762, 1703, 1655 (amide C=O), 1598 (Ar C=C). ¹H NMR (CDCl₃, 500 MHz): δ 8.71 (s, 1H, NH), 7.58 (s, 1H, vinyl-H), 7.46 (d, 2H, $J = 9.0$ Hz, 2×Ar-H), 7.06 (d, 2H, $J = 9.0$ Hz, 2×Ar-H), 6.63 (s, 2H, 2×Ar-H), 5.05 (s, 2H, OCH₂), 3.97 (m, 6H, 3×OCH₂), 3.60 (s, 2H, CH₂), 1.84-1.70 (m, 6H, 3×CH₂), 1.52-1.31 (m, 30H, 15×CH₂), 0.91 (t, 9H, $J = 7.0$ Hz, 3×CH₃). ¹³C NMR (CDCl₃, 125 MHz): δ 174.55, 171.59, 160.51, 153.40, 138.18, 134.79, 132.16, 131.07, 126.85, 121.50, 115.53, 106.18, 73.48, 70.58, 69.20, 35.11, 31.91, 31.84, 30.34, 29.35, 26.11, 22.68, 14.10. Elemental Anal. Calcd for C₄₂H₆₃NO₆ (%): C, 74.41; H, 9.37; N, 2.07; Found: C, 74.55; H, 9.18; N, 1.99.

The remaining maleimide derivatives **HT**₂₈₋₃₁ of the series were prepared by adopting the similar procedure.

For **HT**₂₈, eluted with 5 % ethyl acetate in pet-ether, (Yield 40 %). FTIR (ATR): ν_{\max} in cm^{-1} 3218 (amide NH), 3061 (vinyl C-H), 2916 (Ar C-H), 2849 (Aliph C-H), 1768, 1705, 1643 (amide C=O), 1596 (Ar C=C). ^1H NMR (CDCl_3 , 500 MHz): δ 8.18 (s, 1H, NH), 7.58 (s, 1H, vinyl-H), 7.46 (d, 2H, $J = 8.5$ Hz, 2×Ar-H), 7.06 (d, 2H, $J = 9.0$ Hz, 2×Ar-H), 6.63 (s, 2H, 2×Ar-H), 5.02 (s, 2H, OCH₂), 3.97 (m, 6H, 3×OCH₂), 3.61 (s, 2H, CH₂), 1.84-1.73 (m, 6H, 3×CH₂), 1.50-1.28 (m, 54H, 27×CH₂), 0.90 (t, 9H, $J = 7.0$ Hz, 3×CH₃). ^{13}C NMR (CDCl_3 , 125 MHz): δ 173.89, 170.94, 160.55, 153.41, 138.23, 134.90, 132.15, 131.02, 126.81, 121.34, 115.55, 106.21, 73.47, 70.60, 69.21, 35.14, 31.95, 31.93, 30.35, 29.62, 26.12, 22.70, 14.12. Elemental Anal. Calcd for $\text{C}_{54}\text{H}_{87}\text{NO}_6$ (%): C, 76.64; H, 10.36; N, 1.66; Found: C, 76.51; H, 10.46; N, 1.71.

For **HT**₂₉, eluted with 20 % ethyl acetate in pet-ether, (Yield 55 %). FTIR (ATR): ν_{\max} in cm^{-1} 3179 (amide NH), 3074 (vinyl C-H), 2929 (Ar C-H), 2863 (Aliph C-H), 1753, 1705, 1648 (amide C=O), 1599 (Ar C=C). ^1H NMR (CDCl_3 , 500 MHz): δ 8.40 (s, 1H, NH), 7.52 (s, 1H, vinyl-H), 6.70 (s, 2H, 2×Ar-H), 4.02 (m, 6H, 3×OCH₂), 3.64 (s, 2H, CH₂), 1.85 (m, 6H, 3×CH₂), 1.51 (m, 6H, 3×CH₂), 1.37 (m, 12H, 6×CH₂), 0.94 (m, 9H, 3×CH₃). ^{13}C NMR (CDCl_3 , 125 MHz): δ 174.03, 170.92, 153.41, 140.66, 135.72, 128.78, 122.29, 109.11, 73.67, 69.32, 35.07, 31.66, 30.28, 29.31, 25.76, 25.70, 22.64, 14.04. Elemental Anal. Calcd for $\text{C}_{29}\text{H}_{45}\text{NO}_5$ (%): C, 71.42; H, 9.30; N, 2.87; Found: C, 71.55; H, 9.21; N, 2.67.

For **HT**₃₀, eluted with 10 % ethyl acetate in pet-ether, (Yield 60 %). FTIR (ATR): ν_{\max} in cm^{-1} 3204 (amide NH), 3040 (vinyl C-H), 2918 (Ar C-H), 2851 (Aliph C-H), 1757, 1706, 1647 (amide C=O), 1577 (Ar C=C). ^1H NMR (CDCl_3 , 500 MHz): δ 8.90 (s, 1H, NH), 7.51 (s, 1H, vinyl-H), 6.69 (s, 2H, 2×Ar-H), 4.01 (m, 6H, 3×OCH₂), 3.62 (s, 2H, CH₂), 1.85-1.75 (m, 6H, 3×CH₂), 1.50 (m, 6H, 3×CH₂), 1.37 (m, 24H, 12×CH₂), 0.90 (m, 9H, 3×CH₃). ^{13}C NMR (CDCl_3 , 125 MHz): δ 174.47, 171.37, 153.40, 140.66, 135.63, 128.80, 122.40, 109.15, 73.67, 69.33, 35.04, 31.89, 30.32, 29.21, 26.04, 22.67, 14.08. Elemental Anal. Calcd for $\text{C}_{35}\text{H}_{57}\text{NO}_5$ (%): C, 73.51; H, 10.05; N, 2.45; Found: C, 73.69; H, 10.00; N, 2.11.

For **HT**₃₁, eluted with 5 % ethyl acetate in pet-ether, (Yield 51 %). FTIR (ATR): ν_{max} in cm^{-1} 3204 (amide NH), 3070 (vinyl C-H), 2917 (Ar C-H), 2849 (Aliph C-H), 1756, 1714, 1647 (amide C=O), 1578 (Ar C=C). ¹H NMR (CDCl_3 , 500 MHz): δ 8.25 (s, 1H, NH), 7.52 (s, 1H, vinyl-H), 6.70 (s, 2H, 2×Ar-H), 4.03 (m, 6H, 3×OCH₂), 3.64 (s, 2H, CH₂), 1.85 (m, 6H, 3×CH₂), 1.50 (m, 6H, 3×CH₂), 1.29 (m, 48H, 24×CH₂), 0.90 (m, 9H, 3×CH₃). ¹³C NMR (CDCl_3 , 125 MHz): δ 173.93, 170.94, 153.42, 140.73, 135.70, 128.76, 122.29, 109.17, 73.67, 69.35, 35.07, 31.93, 30.34, 29.54, 26.06 22.69, 14.03. Elemental Anal. Calcd for $\text{C}_{47}\text{H}_{81}\text{NO}_5$ (%): C, 76.27; H, 11.03; N, 1.89; Found: C, 76.30; H, 11.09; N, 1.93.

3.2.7 Design and synthesis of **HT**₃₂₋₃₅ (Series-6)

In **Series-6**, a five membered organoboron complex, *i.e.* 2,2-difluoro-1,3,4,2-oxadiazaborol-3-ium-2-uide, has been introduced as novel electron deficient heterocyclic motif in the designing of D-A-D' configured hemi-disc shaped molecules. The new molecules comprise unsymmetrical conjugative attachment of two alkoxyaryl groups to BF_2 based heterocycle. The number and length of peripheral chains of one of the arms were kept intact and both the parameters were varied on the other arm to establish the structure-property relationship (**Fig 3.27**). Being D-A chromophoric molecules, they were expected to display intense fluorescence at liquid crystalline state.

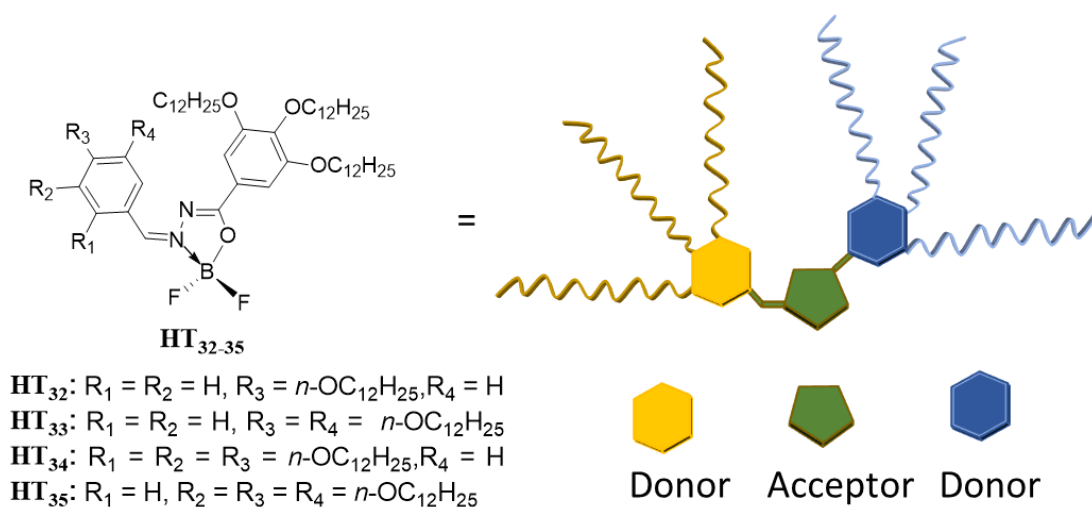
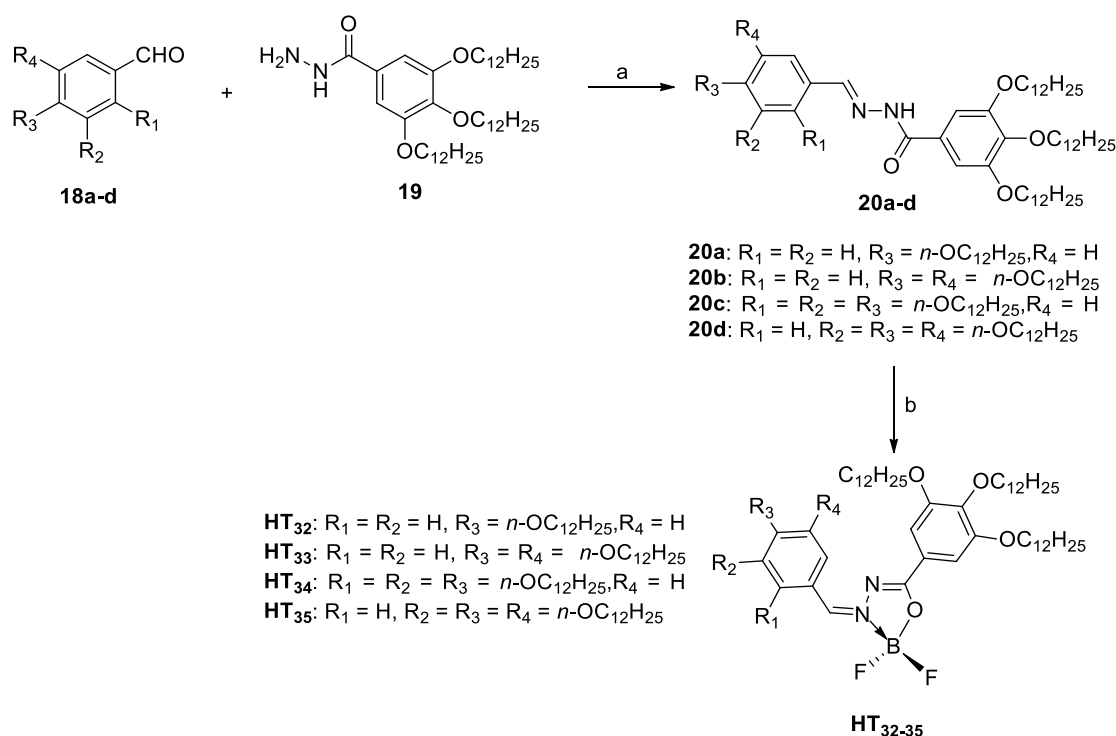


Figure 3.27 Design of D-A-D' configured new BF_2 complexes, **HT**₃₂₋₃₅ of **Series-6**

The synthetic route for the preparation of polycatenar arylhydrazones (**20a-d**) and the corresponding difluoroboron complexes (**HT₃₂₋₃₅**) is outlined in **Scheme 3.6**. The synthesis of key precursors, *i.e.* substituted arylhydrazones is often straightforward which involves simple acid catalyzed condensation of hydrazine derivative **19** with different alkoxy substituted benzaldehydes (**18a-d**) by refluxing in ethanol for two hours. The obtained Schiff bases were purified by repeated recrystallization in methanol. The required substituted aldehydes (**18a-d**) and phenylhydrazine derivative (**19**) were synthesized by adopting reported procedures with slight modifications. The obtained new hydrazone derivatives, **20a-d** exist in keto-enol forms; the coordination with the boron source prefers the enolic tautomer form. On boronation with boron trifluoride etherate in presence of *N,N*-Diisopropylethylamine, hydrazones yielded the corresponding difluoroboron complexes **HT₃₂₋₃₅** in 42-60%.



Scheme 3.6 Synthetic routes for the preparation of **HT₃₂₋₃₅**. Reagents and conditions: (a) cat. AcOH, ethanol, 70 °C, 2 hrs, 69-75 %; (b) DIPEA, BF₃OEt₂, DCE, overnight, 42-60%

3.2.7.1 Results and discussion

Structures of newly synthesized hydrazone ligands and their corresponding BF_2 complexes were confirmed by spectral and elemental analyses. The observed typical IR absorption bands at ~ 3230 and ~ 1650 cm^{-1} are owing to NH and C=O stretching vibrations, respectively in all compounds **20a-d**, suggesting the formation of benzylidenehydrazone derivatives. In their NMR spectra, the azomethine and NH protons get deshielded and appeared as unique singlets at ~ 9.47 and ~ 8.25 ppm respectively, confirming the ligand structures as shown in **Fig 3.29**. As can be seen in **Fig 3.28**, no significant shifting of IR bands was observed on complexation of hydrazones with BF_2 . However, clear changes were noticed in ^1H -NMR spectra of all complexes **HT**₃₂₋₃₅. For instance, spectrum of **HT**₃₂ shows two doublets (8.32 and 6.99 ppm) and two singlets (7.68 and 7.31 ppm) in the aromatic region, a triplet at 3.90 ppm due to OCH_2 protons, and upfield signals between 1.77 and 0.80 ppm owing to primary and secondary alkyl protons conformed the structure (**Fig 3.29**). In its ^{13}C NMR spectrum, most of the ^{13}C signals of aromatic carbons get deshielded when compared to that of its corresponding hydrazone **20a**, they occurred at 164.32, 153.10 and 149.17 ppm as shown in **Fig 3.30**, confirming the complex structure. On the similar lines, structures of remaining complexes of the series were characterized.

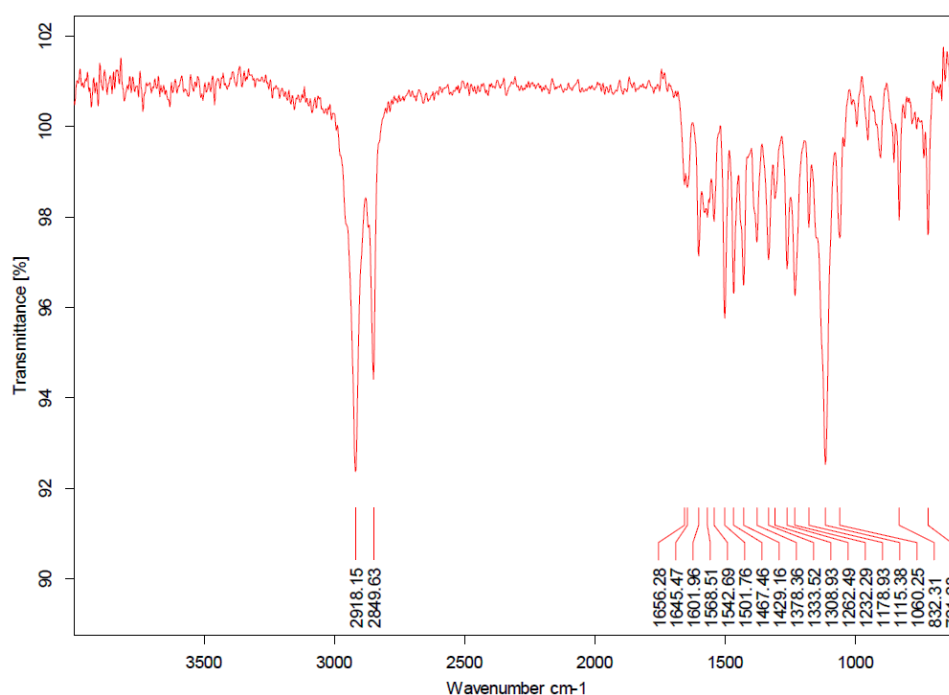


Figure 3.28 FTIR (ATR) spectrum of **HT**₃₂

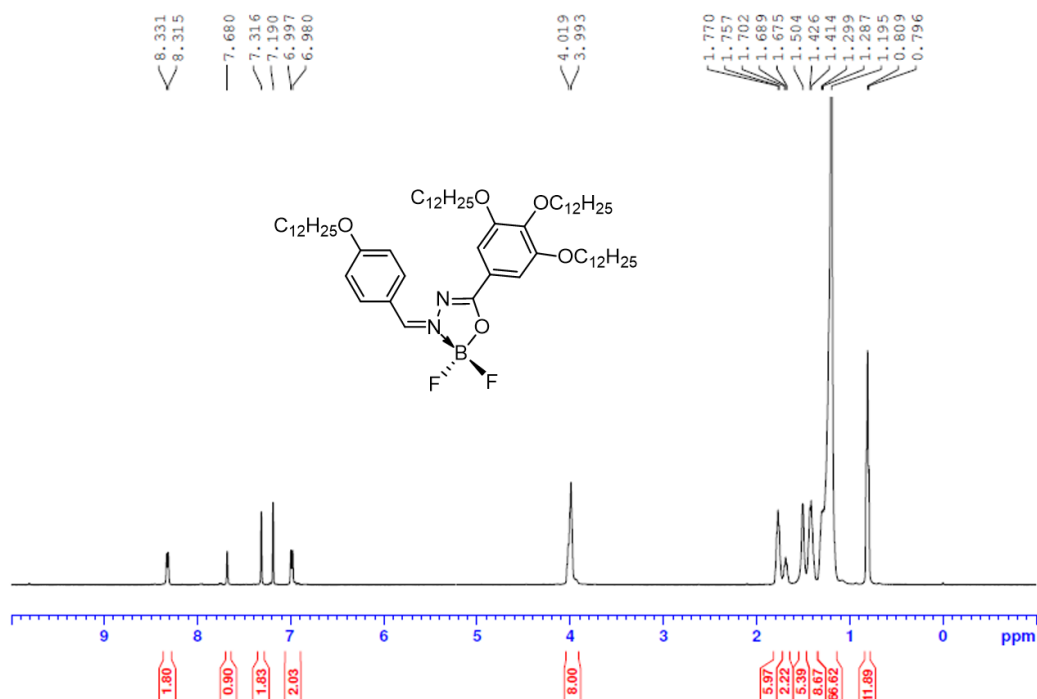


Figure 3.29 ¹H-NMR (500 MHz) spectrum of HT₃₂ recorded in CDCl₃

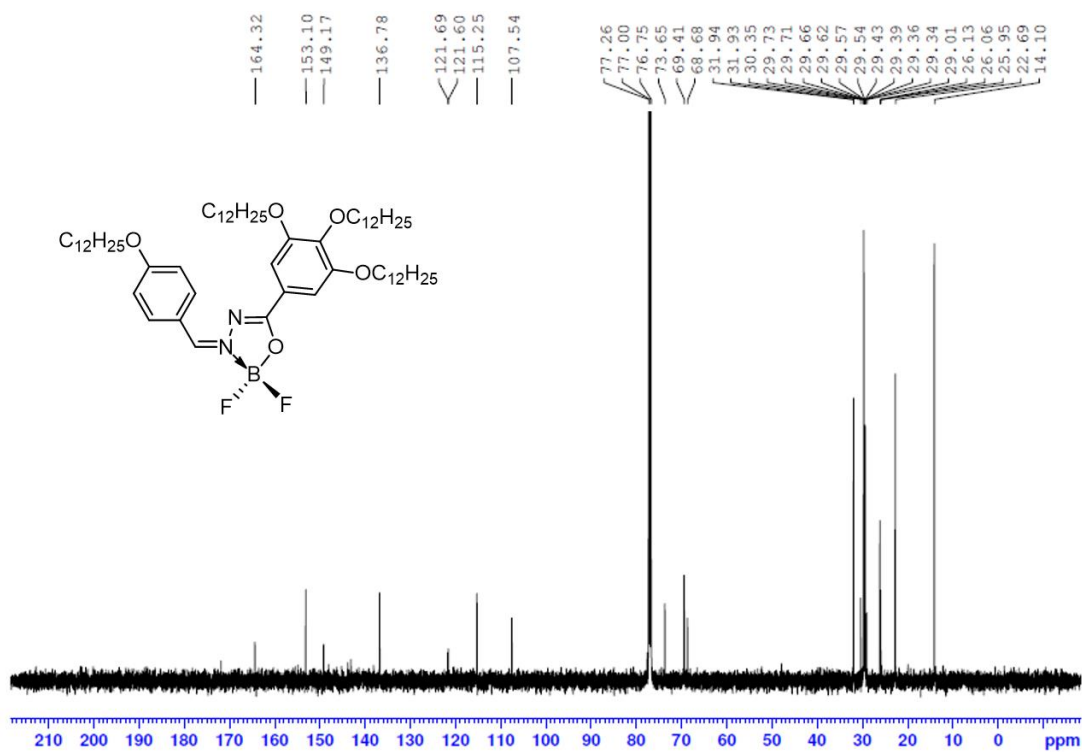


Figure 3.30 ¹³C-NMR (500 MHz) spectrum of HT₃₂ recorded in CDCl₃

3.2.7.2 Experimental procedures

The experimental procedures for the preparation of benzylidenehydrazones and their corresponding boron difluoride complexes are described below:

Synthesis of (E)-3,4,5-tris(dodecyloxy)-N'-(4-(dodecyloxy)benzylidene)benzohydrazide (20a)

An equimolar mixture of aldehyde **18a** (1 g, 3.44 mmol, 1 equiv.) and phenylhydrazide **19** (2.3 g, 3.44 mmol, 1 equiv.) was taken in 20 mL of absolute ethanol. To this mixture, catalytic amount of glacial acetic acid was added and refluxed for 2 hours. Then, the mixture was kept for cooling at ambient conditions; the obtained precipitate was filtered and washed with ethanol. The repeated recrystallization with DCM and methanol, **20a** was yielded in 75 % as white solid. FTIR (ATR) ν_{\max} in cm^{-1} 3210 (N-H), 2916 (Ar C-H), 2848 (Aliph C-H), 1646 (C=O), 1609 (Ar C=C). ^1H NMR (500 MHz, CDCl_3): δ 9.47 (s, 1H, $\text{CH}=\text{N}$), 8.25 (s, 1H, CONH), 7.66 (s, 2H, $2\times\text{Ar-H}$), 7.04 (d, 2H, $J = 8.0$ Hz, $2\times\text{Ar-H}$), 6.89 (d, 2H, $J = 8.0$ Hz, $2\times\text{Ar-H}$), 3.98 (m, 8H, $4\times\text{OCH}_2$), 1.80 (m, 8H, $4\times\text{CH}_2$), 1.46 (m, 8H, $4\times\text{CH}_2$), 1.28 (m, 64H, $32\times\text{OCH}_2$), 0.89 (t, 12H, $J = 6.5$ Hz, $4\times\text{OCH}_3$). ^{13}C NMR (125 MHz, CDCl_3): δ 161.18, 153.19, 141.47, 129.32, 126.05, 114.77, 114.68, 105.94, 73.55, 69.37, 68.16, 31.93, 30.35, 29.51, 26.08, 22.69, 14.10. Elemental Anal. Calcd (%) for $\text{C}_{62}\text{H}_{108}\text{N}_2\text{O}_5$: C, 77.45; H, 11.32; N, 2.91; Found: C, 77.94; H, 11.12; N, 2.56.

The intermediates **20b-d** were synthesized by adopting similar procedure as described for the synthesis of **20a**.

For **20b** (Yield 70 %). FTIR (ATR) ν_{\max} in cm^{-1} 3208 (N-H), 2916 (Ar C-H), 2848 (Aliph C-H), 1637 (C=O), 1578 (Ar C=C). ^1H NMR (500 MHz, CDCl_3): δ 9.19 (s, 1H, $\text{CH}=\text{N}$), 8.21 (s, 1H, CONH), 7.45 (m, 2H, $2\times\text{Ar-H}$), 7.03 (m, 3H, $3\times\text{Ar-H}$), 6.85 (d, 1H, $J = 7.5$ Hz, Ar-H), 3.98 (m, 10H, $5\times\text{OCH}_2$), 1.83-1.69 (m, 10H, $5\times\text{CH}_2$), 1.48 (m, 10H, $5\times\text{CH}_2$), 1.28 (m, 80H, $40\times\text{CH}_2$), 0.89 (t, 15H, $J = 6.5$ Hz, $5\times\text{CH}_3$). ^{13}C NMR (125 MHz, CDCl_3): δ 153.25, 151.57, 149.51, 141.58, 126.41, 122.54, 112.54, 105.89, 73.57, 69.27, 31.93, 30.34, 29.55, 26.07, 22.69, 14.10. Elemental Anal. Calcd (%) for $\text{C}_{74}\text{H}_{132}\text{N}_2\text{O}_6$: C, 77.57; H, 11.61; N, 2.44; Found: C 77.31, H 11.78, N, 2.83;

For **20c** (Yield 72 %). FTIR (ATR) ν_{\max} in cm^{-1} 3252 (N-H), 2917 (Ar C-H), 2850 (Aliph C-H), 1643 (C=O), 1576 (Ar C=C). ^1H NMR (500 MHz, CDCl_3) δ 9.16

(s, 1H, $\text{CH}=\text{N}$), 8.43 (s, 1H, CONH), 7.82 (s, 1H, $2\times\text{Ar-H}$) 6.95 (m, 2H, $2\times\text{Ar-H}$), 6.70 (s, 1H, Ar-H), 4.00 (m, 12H, $6\times\text{OCH}_2$), 1.80-1.68 (m, 12H, $6\times\text{CH}_2$), 1.48 (m, 12H, $6\times\text{CH}_2$), 1.28 (m, 96H, $48\times\text{CH}_2$), 0.90 (m, 18H, $6\times\text{CH}_3$). ^{13}C NMR (125 MHz) δ 152.75, 144.34, 141.14, 108.72, 106.17, 73.60, 68.55, 31.93, 30.30, 29.38, 26.15, 22.69, 14.09. Elemental Anal. Calcd (%) for $\text{C}_{86}\text{H}_{156}\text{N}_2\text{O}_7$: C, 77.65; H, 11.82; N, 2.11; Found: C, 80.10; H, 11.53; N, 2.25.

For **20d** (Yield 69 %). FTIR (ATR) ν_{max} in cm^{-1} 3251 (N-H), 2917 (Ar C-H), 2849 (Aliph C-H), 1641 (C=O), 1576 (Ar C=C). ^1H NMR (500 MHz, CDCl_3) δ 9.35 (s, 1H, $\text{CH}=\text{N}$), 8.22 (s, 1H, CONH), 7.28-6.94 (m, 4H, $4\times\text{Ar-H}$), 4.00 (m, 12H, $6\times\text{OCH}_2$), 1.80-1.75 (m, 12H, $6\times\text{CH}_2$), 1.47 (m, 12H, $6\times\text{CH}_2$), 1.28 (m, 96H, $48\times\text{CH}_2$), 0.91 (t, 18H, $J = 6.5$ Hz, $6\times\text{CH}_3$). ^{13}C NMR (125 MHz, CDCl_3) δ 153.31, 141.61, 140.60, 128.54, 106.18, 73.54, 69.35, 31.93, 30.36, 29.56, 26.12, 22.69, 14.19. Elemental Anal. Calcd (%) for $\text{C}_{86}\text{H}_{156}\text{N}_2\text{O}_7$: C, 77.65; H, 11.82; N, 2.11; Found: C, 77.99; H, 11.63; N, 2.49.

General procedure for the synthesis of BF_2 complexes **HT**₃₂₋₃₅

A mixture of hydrazone **20a** (0.5g, 0.52 mmol, 1 equiv.) and *N,N*-Diisopropylethylamine (0.2g, 1.56 mmol, 3 equiv.) in dichloroethane was heated to 50 °C for 15 minutes. Boron trifluoride diethyl etherate (0.11g, 0.79 mmol, 1.5 equiv.) was then added to the mixture and continued the stirring at 70 °C for overnight. After completion of the reaction, the mass was cooled and poured into ice cold water. Then, aqueous mixture was extracted twice with dichloromethane and dried the combined organic layers. Finally, the crude product was purified by silica-gel column chromatography (100-200 mesh size) using mixture of pet-ether and ethyl acetate as eluents, yielded **HT**₃₂ (Yield 42 %). FTIR (ATR) ν_{max} in cm^{-1} 2918 (Ar C-H), 2849 (Aliph C-H), 1645 (Ar C=N), 1601(Ar C=C). ^1H NMR (500 MHz, CDCl_3) δ 8.32 (d, 2H, $J = 8.0$ Hz, $2\times\text{Ar-H}$), 7.68 (s, 1H, $\text{N}=\text{CH}$), 7.31 (s, 2H, $2\times\text{Ar-H}$), 6.98 (d, 2H, $J = 8.5$ Hz, $2\times\text{Ar-H}$), 4.00 (m, 8H, $4\times\text{OCH}_2$), 1.77-1.67 (m, 8H, $4\times\text{OCH}_2$), 1.41 (m, 8H, $4\times\text{OCH}_2$), 1.19 (m, 64H, $32\times\text{OCH}_2$), 0.91 (t, 12H, $J = 6.5$ Hz, $4\times\text{OCH}_3$). ^{13}C NMR (125 MHz, CDCl_3): δ 164.32, 153.10, 149.17, 136.78, 121.69, 121.60, 115.25, 107.54, 73.65, 69.41, 68.68, 31.93, 30.35, 29.57, 26.09, 26.13, 26.06, 25.95, 22.69, 14.10.

Elemental Anal. Calcd (%) for $C_{62}H_{107}BF_2N_2O_5$; C, 73.78; H, 10.69; N, 2.78.; Found: C, 73.39; H, 10.59; N, 2.82.

The remaining members of the series, **HT**₃₃₋₃₅ were synthesized by following the similar procedure as described for the synthesis of **HT**₃₂.

For **HT**₃₃ (Yield 51 %). FTIR (ATR) ν_{\max} in cm^{-1} 2917 (Ar C-H), 2849 (Aliph C-H), 1643 (Ar C=N), 1593 (Ar C=C). 1H NMR (500 MHz, $CDCl_3$): δ 8.47 (s, 1H, N=CH), 7.74 (s, 1H, Ar-H), 7.66 (d, 1H, $J = 8.0$ Hz, Ar-H), 7.39 (s, 1H, Ar-H), 7.00 (d, 2H, $J = 8.5$ Hz, 2×Ar-H), 4.07 (m, 10H, 5×OCH₂), 1.91-1.76 (m, 10H, 5×CH₂), 1.59-1.51 (m, 10H, 5×CH₂), 1.38-1.28 (m, 80H, 40×CH₂), 0.901 (t, 15H, $J = 8.5$ Hz, 5×CH₃). ^{13}C NMR (125 MHz, $CDCl_3$): δ 153.09, 149.45, 130.71, 121.77, 112.04, 107.15, 73.66, 69.06, 31.93, 30.37, 29.43, 26.17, 25.94, 22.69, 14.10. Elemental Anal. Calcd (%) for $C_{74}H_{131}BF_2N_2O_6$: C, 74.46; H, 11.06; N, 2.35; Found: C, 74.85; H, 11.01; N, 2.23.

For **HT**₃₄ (Yield 55 %). FTIR (ATR) ν_{\max} in cm^{-1} FTIR (ATR): ν 2916 (Ar C-H), 2849 (Aliph C-H), 1638 (Ar C=N), 1587 (Ar C=C); 1H NMR (500 MHz, $CDCl_3$): δ 8.92 (d, 1H, $J = 9.0$ Hz, Ar-H), 8.27 (s, 1H, N=CH), 7.39 (s, 2H, Ar-H), 6.83 (d, 1H, $J = 9.0$ Hz, Ar-H), 4.21 (t, 2H, $J = 6.0$ Hz, OCH₂), 4.13 (t, 2H, $J = 5.5$ Hz, OCH₂), 4.07 (m, 6H, 3×OCH₂), 3.98 (t, 2H, $J = 5.5$ Hz, CH₂), 1.90-1.79 (m, 12H, 6×CH₂), 1.51 (m, 96H, 48×CH₂), 0.901 (t, 18H, $J = 6.5$ Hz, 6×CH₃). ^{13}C NMR (125 MHz, $CDCl_3$): δ 159.55, 156.45, 153.07, 145.13, 142.99, 140.95, 130.17, 121.80, 116.26, 108.21, 107.54, 75.57, 73.76, 69.29, 31.93, 30.24, 29.54, 26.13, 14.10. Elemental Anal. Calcd (%) for $C_{86}H_{155}BF_2N_2O_7$: C, 74.96; H, 11.34; N, 2.03; Found: C, 74.66; H, 11.49; N, 1.98.

For **HT**₃₅ (Yield 60 %). FTIR (ATR) ν_{\max} in cm^{-1} 2918 (Ar C-H), 2849 (Aliph C-H), 1645 (Ar C=N), 1587 (Ar C=C); 1H NMR (500 MHz, $CDCl_3$): δ 7.65 (s, 1H, Ar-H), 7.64 (s, 1H, N=CH), 7.30 (s, 2H, 2×Ar-H), 4.06 (t, 2H, $J = 6.0$ Hz, OCH₂), 4.00-3.94 (s, 10H, 5×OCH₂), 1.76-1.69 (m, 12H, 6×CH₂), 1.41 (m, 12H, 6×CH₂), 1.51 (m, 96H, 48×CH₂), 0.809 (t, 18H, $J = 6.5$ Hz, 6×CH₃). ^{13}C NMR (125 MHz, $CDCl_3$): δ 153.10, 153.02, 149.51, 144.25, 143.04, 123.49, 121.41, 112.76, 107.14, 112.76, 107.14, 73.79, 69.15, 31.93, 30.40, 29.54, 26.12, 14.10. Elemental Anal. Calcd (%) for $C_{86}H_{155}BF_2N_2O_7$: C, 74.96; H, 11.34; N, 2.03; Found: C, 74.78; H, 11.31; N, 2.12.

3.3 CONCLUSIONS

In summary, six new series (**Series-1 to 6**) comprising thirty five heterocyclic derivatives **HT₁₋₃₅** were rationally designed. The new compounds structurally consisting of different heterocyclic cores, polar groups and alkyl chains with varied numbers were successfully synthesized by following appropriate synthetic protocols as per the schemes **3.1-3.6**. The synthetic procedures for the preparation of various heterocyclic derivatives were optimized with respect to time, temperature, solvent polarity and other conditions. To purify the compounds, the standard methods like crystallization and column chromatography were established. Finally, all the newly synthesized intermediates and target compounds were characterized by means of several spectroscopic techniques including elemental analysis. The next chapter deals with the studies related to their mesomorphic, photophysical and electrochemical properties.

MESOMORPHIC, OPTOELECTRONIC AND ELECTROCHEMICAL STUDIES

Abstract

This chapter describes a detailed mesomorphic characterization of newly synthesized heterocyclic derivatives (HT₁₋₃₅). Further, their in depth photophysical characterization, i.e. absorption and emission studies, has been included. Also, it covers their electrochemical studies using experimental as well as theoretical methods. Finally, structure-property relationship of the new compounds with respect to mesogenic, optical and electrochemical behaviours has been discussed.

4.1 INTRODUCTION

In the preceding chapter, the design, synthesis and structural characterisation of six new series of heterocyclic compounds (HT₁₋₃₅) were described. The current chapter provides a detailed account on their liquid crystalline, optical and electrochemical studies. The mesomorphic study of any material would give valuable information about its self-assembling behaviour, which plays an important role in its selection for optoelectronic devices. The photophysical characterisation of the LC materials is crucial to know their optical behaviours, which are prerequisites for their utility in any optical systems. In the present study, UV-visible and photoluminescence spectroscopic methods were used to evaluate the linear optoelectronic properties as they offer the imperative key-parameters like light absorption, emission, Stokes shift, molar extinction coefficient, band gap and other related information. As electronic properties of organic compounds decide the overall character of the materials, the CV technique has been applied to obtain their electrochemical parameters. Density Functional Theory (DFT) method has been successfully used to generate the energy minimized geometries as well as to evaluate electrochemical data.

4.2 MESOMORPHIC STUDIES

The experimental methods used for LC studies followed by a detailed discussion on their results are given in the present section.

4.2.1 Experimental methods

The thermotropic phase transition sequence of all the final compounds was studied using Parkin-Elmer Pyris-1 Differential Scanning Calorimetry (DSC). For this measurement, about 3 mg of sample was hermetically sealed in aluminium pan kept under a nitrogen atmosphere. Optical textural transitions with respect to temperature of the materials were observed using Olympus BX51 Polarized Optical Microscope (POM) in conjunction with a Mettler FP82HT hot stage and FP90 central processor. A very small amount of compound was sandwiched between a glass slide and a cover slip, which was kept under cross-polarizer. The mesophase textures of the LC materials were captured on slow cooling from their respective isotropic temperatures at the rate of 2 °C/min. The type and symmetry of mesophases of LC compounds were investigated by employing variable temperature small angle powder X-ray diffraction (XRD) measurements of unoriented samples filled in a Lindemann capillary of diameter of 1 mm (Hampton Research) were carried out on DY 1042-Empyrean XRD with Pixel 3D detector at Cu-K α radiation.

4.2.2 Results and discussion

The studies on liquid crystalline phase behaviour of all the compounds of the six series are described systematically in separate subsections.

4.2.2.1 Mesomorphic behaviour of HT₁₋₇ (Series-1)

The phase transition temperatures and associated enthalpy changes of HT₁₋₇ (Series-1) are summarised in **Table 4.1**. Compound HT₁ bearing four *n*-hexyloxy peripheral tails melts at 89.48 °C ($\Delta H = 38.14 \text{ kJmol}^{-1}$) to a mesophase, which clears at 153 °C with the energy change of 22.2 kJmol⁻¹ on the heating scan. It re-enters to mesophase at 148.51 °C ($\Delta H = -15.51 \text{ kJmol}^{-1}$) on cooling, this considerable higher enthalpy change may be attributed to the significant ordered packing of molecules in the mesophase (**Fig 4.1c**). It didn't show any sign of crystallization till room temperature. Under microscopic observation, on slow cooling from its isotropic phase, small birefringent batonnets started growing in the dark homeotropic region which further resulted in a wrinkle-free mosaic pattern. The same texture persisted till room temperature and it was not shearable as depicted in **Figs 4.1a** and **4.1b**. This is one of

the characteristic optical images of the columnar phases derived from classical discotics.

Table 4.1. ^a Phase transition temperatures and corresponding enthalpies of **HT1-7**

Compd.	Phase sequence	
	Heating	Cooling
HT₁	Cr ₁ 89.48 (38.14) Col _{ob} 153.02 (22.2) I	I 148.51 (-15.51) Col _{ob} ^b
HT₂	Cr ₁ 81.34 (9.28) Cr ₂ 88.74 (42.53) Col _{ho} 135.77 (4.06) Col _{hd} 149.14 (5.84) I	I 147.40 (-6.06) Col _{hd} 134.64 (-3.67) Col _{ho} ^b
HT₃	Cr ₁ 91.10 (19.93) Cr ₂ 103.56 (74.95) Col _{ho} 120.36 (2.49) Col _{hd} 140.31 (6.31) I	I 138.96 (-6.02) Col _{hd} 122.12 (-1.86) Col _{hd} ^b
HT₄	Cr ₁ 99.94 (38.27) Cr ₂ 107.90 (65.72) Cr ₃ 115.13 (43.43)	I 112.82 (-2.27) Col _{ho} ^c 50.33 (-18.39) Cr ₄ 40.84 (-14.19) Cr ₅
HT₅	Cr 81.55 (46.04) I	I 34.22 (-27.95) Cr
HT₆	Cr 70.08 (58.16) I	I ^b
HT₇	Cr 86.62 (82.19) I	I 31.27 (-58.62) Cr

^a Peak temperatures/°C (enthalpies/ kJmol⁻¹) obtained by heating and cooling cycles at the rate of 5 °C/min; ^b Crystallization was not observed till room temperature; ^c The mesophase observed was monotropic; Cr₁, Cr₂, Cr₃, Cr₄ and Cr₅ are different crystalline solid phases; Col_{ho} = ordered columnar hexagonal phase; Col_{hd} = disordered columnar hexagonal phase and I = isotropic liquid phase

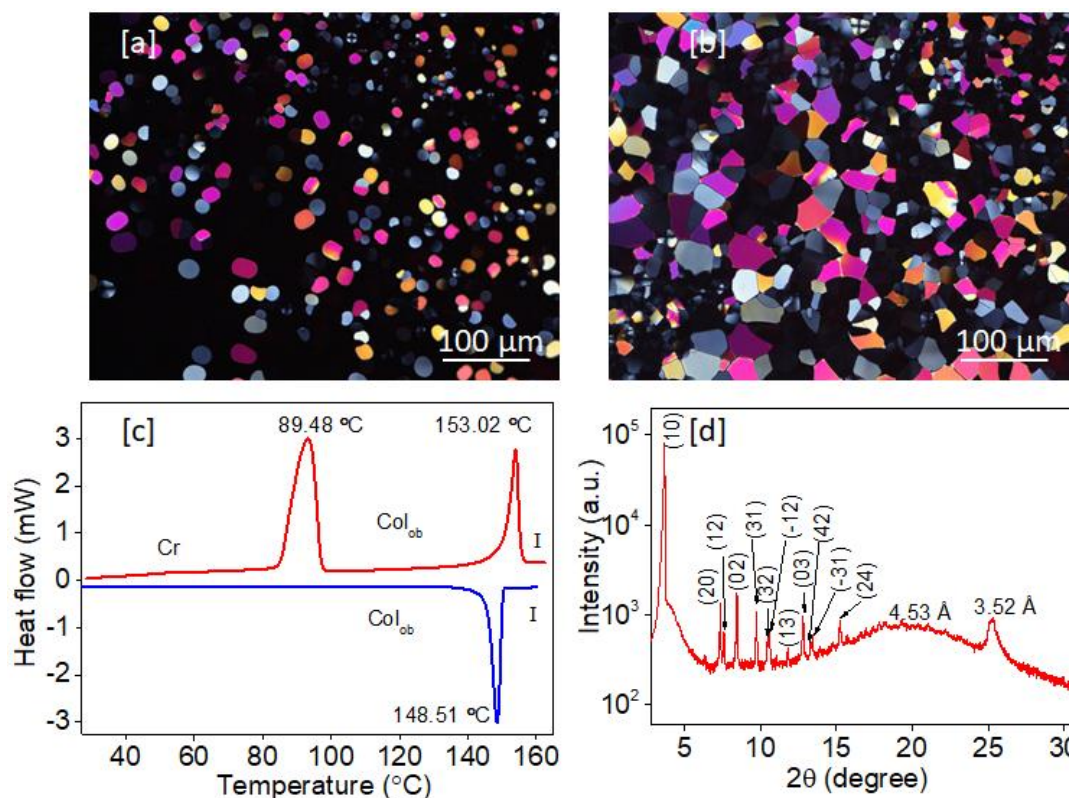


Figure 4.1 POM images of **HT**₁: (a) at 150 °C and (b) 30 °C on cooling from the isotropic phase; (c) DSC thermogram of **HT**₁ (red trace is heating cycle and blue trace is cooling cycle obtained at the rate of 5 °C/min under nitrogen atmosphere); (d) XRD profile obtained for Col_{ob} phase for the compound **HT**₁ at 144 °C

The XRD patterns obtained for **HT**₁ throughout the mesophase range were almost similar. For instance, the spectrum obtained at 144 °C is shown in **Fig 4.1d**. The spacings and the Miller indices of the peaks in this pattern are summarized in **Table 4.2**. In addition to the twelve sharp reflections over the low to middle angle region, a broad halo at 4.53 Å and a relatively sharp peak at 3.52 Å were seen in the wide angle region, the latter two being due to the fluidic nature of alkyl chains and aromatic core-core interactions, respectively. The indexing of the data in accordance with **Eq. 4.1** to an oblique lattice provided the least differences between the experimental and calculated values, whereas attempts to fit a rectangular lattice resulted in substantial deviations.

$$\frac{1}{d^2} = \frac{\left(\frac{h^2}{a^2} + \frac{k^2}{b^2} - \frac{2hk\cos\gamma}{ab}\right)}{\sin^2\gamma} \quad (4.1)$$

The obtained columnar phase with an oblique lattice has the lattice parameters, $a = 26.85 \text{ \AA}$ and $b = 23.34 \text{ \AA}$ with the angle of 64.10° . Further, the number of molecules per columnar slice (Z) was calculated using **Eq. 4.2** (Wang et al. 2014). For **HT₁**, the value of Z was estimated to be 1.81, indicating that a pair of molecules constitutes a hexagonal lattice site. The lattice area $S = a \times b \times \sin\gamma$ and molecular volume $V = h_c \times S$ were calculated to be 563.7 \AA^2 and 1984.2 \AA^3 , respectively.

$$Z = \frac{\sqrt{3} a^2 h_c \rho N_A}{2 M_w} \quad (4.2)$$

Table 4.2 XRD characterization data of **HT₁** at 144 °C

Compd.	Phase ($T/^\circ\text{C}$)	d_{obs} (\AA)	d_{cal} (\AA)	Miller Indices (hk)	Lattice parameters a (\AA), b (\AA), Lattice area S (\AA^2), Molecular volume V (\AA^3)
HT₁	Col _{ob} (144)	24.15	24.15	(1 0)	$a = 26.85$
		12.04	12.08	(2 0)	$b = 23.34$
		11.66	11.67	(1 2)	$\gamma = 64.10$
		10.49	10.50	(0 2)	$S = 563.7$
		9.09	8.94	(3 1)	$V = 1984.2$
		8.46	8.40	(3 2)	$Z = 1.81$
		8.36	8.38	(-1 2)	
		7.50	7.68	(1 3)	
		6.92	7.00	(0 3)	
		6.66	6.63	(4 2)	
		6.59	6.61	(-3 1)	
		5.81	5.83	(2 4)	
		4.53(h_a)			
		3.52(h_c)			

d_{obs} , Experimental lattice spacing; d_{cal} , calculated from the lattice parameters; a and b , lattice parameters deduced for Col_{ob} with columnar tilt angle γ ; h_a , alkyl chains correlation peak value; h_c , core-core spacing; Z , number of molecules per columnar slice; S , lattice area; V , molecular volume

The second member of the series, **HT₂** showed two distinct crystalline transitions at $81.34 \text{ }^\circ\text{C}$ and $88.74 \text{ }^\circ\text{C}$. A weak transition peak centred at $136 \text{ }^\circ\text{C}$ ($\Delta H = 4.06 \text{ kJmol}^{-1}$) cleared at $149.14 \text{ }^\circ\text{C}$ ($\Delta H = 5.84 \text{ kJmol}^{-1}$) to an isotropic liquid phase. In

cooling cycle, the two exothermic transitions at 147.4 °C ($\Delta H = -6.06 \text{ kJmol}^{-1}$) and 134.64 °C ($\Delta H = -3.67 \text{ kJmol}^{-1}$) were observed without any crystallization peak. This perceived the existence of two different mesophases as a function of temperature (**Fig 4.2a**). On slow cooling from isotropic phase, it developed the birefringent mosaic type of texture at 141 °C. Further cooling at 120 °C, some of the birefringent texture became completely dark and these observations were consistent with DSC results (**Figs 4.2b** and **4.2c**). The observed textural changes suggest that there may be deviations in the packing order of the molecules in mesophase (Cho and Kim 2014).

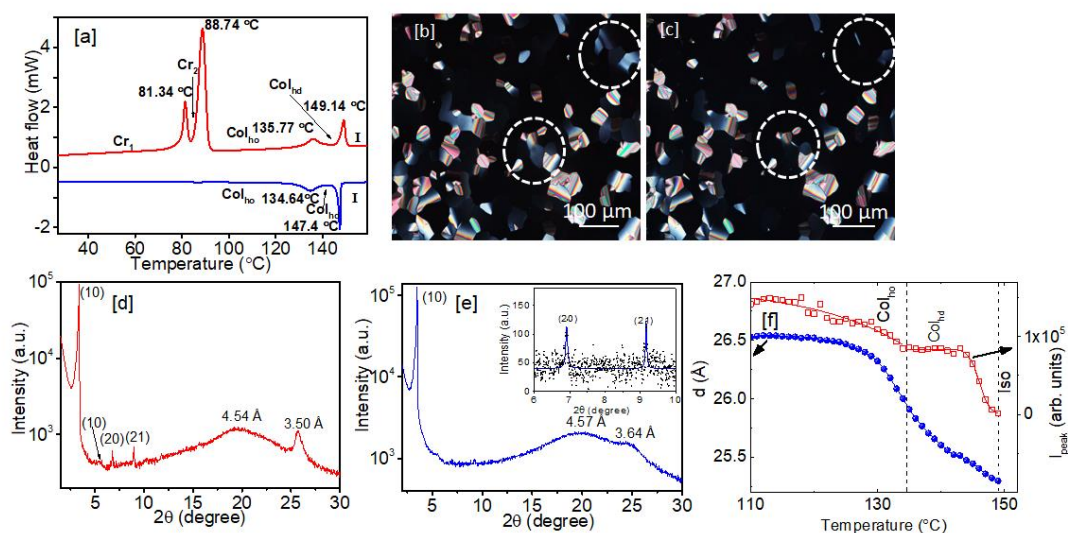


Figure 4.2 (a) DSC thermogram of **HT₂** (red trace represents cycle and blue trace represents cooling cycle obtained at 5 °C/min under nitrogen atmosphere); POM images of **HT₂** at (b) 141 °C and (c) 120 °C captured on cooling from the I phase (circular region indicates the change of texture); XRD profiles obtained for **HT₂** at (d) 120 °C and (e) 142 °C; (f) plot of temperature *v/s* layer spacing and the peak intensity of (10) peak

The XRD patterns obtained for both the LC phases of **HT₂** were similar, but for the reflection due to core-core ordering. The diffraction pattern at 120 °C showed the lower angle reflection peaks corresponding to Bragg's spacing of 26.08 Å, 15.62 Å, 13.08 Å, and 9.83 Å in the ratio of 1:1/ $\sqrt{3}$:1/ $\sqrt{2}$:1/ $\sqrt{7}$ and they can be indexed to (10), (11), (20) and (21) planes of hexagonal lattice according to **Eq. 4.3**. Whereas in the wide angle region, the presence of a broad halo at 4.54 Å corresponds to the packing of flexible alkyl chains and the relatively sharp peak appeared at 3.50 Å is due to aromatic core-core interactions (**Fig 4.2d**).

$$a = d_{100} \frac{2}{\sqrt{3}} \quad (4.3)$$

The observed moderately smaller intracolumnar distance suggests that the LC phase is an ordered columnar hexagonal (Col_{ho}). While reflection peaks (at 142 °C) obtained in the higher temperature mesophase range could be indexed to same planes as assigned to the pattern obtained at 120 °C (**Fig 4.2d**) for Col_{hd}. However, the core-core correlation peak is very weak and it occurs at a higher spacing value of 3.64 Å. Therefore, this LC phase was assigned as disordered columnar hexagonal, Col_{hd} (**Fig 4.2e**). The hexagonal cell parameter a was found to be 30.11 Å and 29.20 Å for Col_{ho} and Col_{hd}, respectively. On the basis of the XRD data obtained at 120 °C assigned to Col_{ho}, the columnar cross-section area ($S = 2/\sqrt{3}d_{10}^2$), and molecular volume ($V = S \times h_c$), were found to be 7854 Å² and 2670.3 Å³, respectively. The value of Z for these two columnar hexagonal phases was calculated by means of **Eq. 4.4** and that was found to be 2.0. The detailed XRD characterization data are given in **Table 4.3**. The calculated d values were estimated using the following **Eq. 4.4**.

$$Z = \frac{\sqrt{3}}{2} \left(\frac{a^2 h N_A \rho}{M_w} \right) \quad (4.4)$$

$$\frac{1}{d_{cal}} = \frac{4}{3} \left(\frac{h^2 + hk + k^2}{a^2} \right) \quad (4.5)$$

The wide-angle XRD patterns of **HT₂** were acquired at different temperatures on heating as well as on cooling process. As temperature elevates, the aromatic stacking reflection becomes gradually weaker, an abrupt broadening at 140 °C (endset of transition peak for Col_{ho} and Col_{hd}) takes place and it continues till the isotropic phase, which indicates the intracolumnar transition from ordered to the disordered packing of the discs. Further, temperature dependent layer spacing against the intensity of the (10) peak was plotted (**Fig 4.2f**). From the graph, it is evident that both parameters exhibit clear changes at the transition between the two columnar phases. The dashed lines indicate the transition temperature as obtained from DSC scans. The layer thickness calculated from the (10) peak shows a significant increase right from the isotropic phase, presents an ‘inflection point’ variation in the vicinity of this intracolumnar transition, and at much lower temperatures has a limiting behaviour. Interestingly, the

peak intensity of the (10) reflection also exhibits clear changes marking the Col_{ho}-Col_{hd} transition.

The compound **HT**₃ bearing fourfold dodecyl chains, melts completely at 103.56 °C ($\Delta H = 74.95 \text{ kJmol}^{-1}$) followed by the weak endothermic transition at 120.36 °C ($\Delta H = 2.49 \text{ kJmol}^{-1}$) and then clears at 140.31 °C ($\Delta H = 6.31 \text{ kJmol}^{-1}$). It was not crystallized on cooling until room temperature (**Fig 4.3a**). The textural observations on slow cooling indicated the existence of columnar mesomorphism (**Figs 4.3b-c**). The XRD patterns obtained at different temperatures over the entire mesophase range confirmed that, the weak transition within the mesophase range is an intracolumnar transition of a columnar hexagonal mesophase.

The XRD trace of **HT**₃ at 110 °C is depicted in **Fig 4.3d** and the observed small angle reflection peaks are assigned to the columnar hexagonal lattice. Whereas, a broad diffused maxima at a spacing of 4.53 Å is attributed to conformational disorder of the peripheral chains and a moderately sharp peak at 3.45 Å is due to the ordered stacking of aromatic segments. At 130 °C, **HT**₃ showed similar reflection pattern except for peak due to intracolumnar spacings, which was observed at 3.52 Å (**Fig 4.3e**). Therefore, the higher temperature mesophase can be assigned to Col_{hd} and the lower temperature mesophase to the Col_{ho}. Further, the wide-angle XRD spectra recorded at different temperatures in Col_{ho} and Col_{hd} mesophase ranges. Evidently, the core-core peak intensity and its position throughout the two thermal mesophase ranges, as well as their changes at the transition temperatures, further confirm the intracolumnar transitions. The conformational motions of mesogenic units within the columnar axis can be further confirmed by examining the FWHM of peak signifies the intracolumnar distance. The plot of full width at half maxima (FWHM) of the core-core peak as a function of temperature for one of the compounds, **HT**₃ is shown in **Fig 4.3f**. In the Col_{ho} phase range, the FWHM show negligible changes, whereas the abrupt increase at 125 °C and continuation of the same trend at higher temperature confirm intercolumnar changes. The results are fairly consistent with the DSC transitions. The compound **HT**₄ carrying longer *n*-hexadecyloxy substitutions characterized to shown a monotropic hexagonal columnar mesophase behaviour.

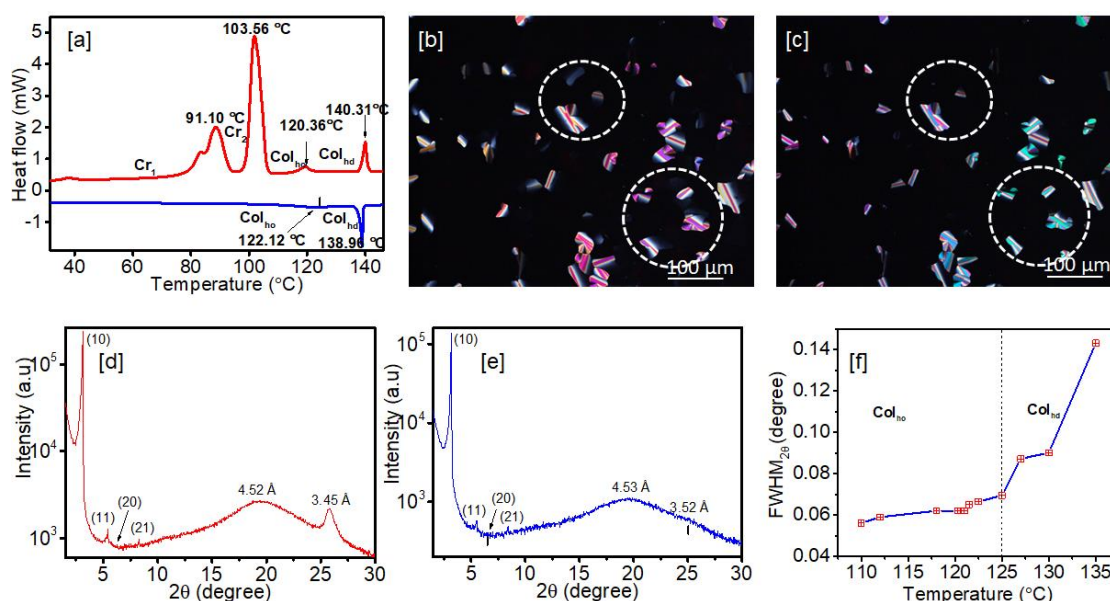


Figure 4.3 (a) DSC thermogram of **HT₃**; POM images of **HT₃** captured on slow cooling from I state at (b) 135 °C and (b) 100 °C; XRD profiles obtained for the compound **HT₃** at (d) 110 °C and (e) 130 °C; (f) variation of FWHM of the aromatic stacking peak as a function of temperature

The thermotropic phase behaviour of **HT₁₋₄** reveals that, increase in peripheral chain lengths has caused destabilization of their mesomorphic nature. Interestingly, **HT₁** with four hexyloxy chains displayed a columnar oblique exclusively. Whereas in **HT₂**, increasing the chain length by two methylene groups, it demonstrated two distinct columnar hexagonal mesophases, which may be probably due to increase in diameter size of the overall disc. Depending on the molecular order along the columnar axis, **HT₂** and **HT₃** exhibited an intracolumnar transition from Col_{ho} to Col_{hd} phases. Thus, the chain length plays a key role in deciding the symmetry of Col phases observed in this type of mesomolecules. The enthalpy changes observed for an order to disordered columnar transitions of **HT₂** and **HT₃** were noted to be 4.06 kJmol⁻¹ and 2.49 kJmol⁻¹, respectively. The observed high enthalpy values for the weaker columnar transitions are attributed to strong intermolecular H-bonding as well as dipolar interactions owned by the mesogens in Col_{ho} phase. Then, it requires a substantial energy to disturb the molecular ordering. Hence, such intracolumnar changes can be assigned to be first order transitions (Cho and Kim 2014), but similar changes were also reported to be second order transitions (Park and Cho 2015). Besides, the data indicate the system's tendency to have a Col_{ho} phase, as the chain length is increased. This could be owing to the well

established between the strongly correlated H-bonded core region and the floppy hydrocarbon regions.

Table 4.3. XRD characterization data of **HT₂₋₄** at different temperatures

Compounds	Phase ($T/^\circ\text{C}$)	d_{obs} (Å)	d_{cal} (Å)	Miller Indices (hk)	Lattice parameter a (Å), Lattice area S (Å ²), Molecular volume V (Å ³)
HT₂	Col _{ho} (120)	26.08	26.08	(10)	$a = 30.11$
		15.62	15.05	(11)	$S = 785.4$
		13.08	13.03	(20)	$V = 2670.3$
		9.83	9.85	(21)	$Z = 2.0$
		4.54 (h_a)			
		3.50 (h_c)			
	Col _{hd} (142)	25.29	25.29	(10)	$a = 29.20$
		12.61	12.64	(20)	$S = 738.5$
		9.55	9.55	(21)	$V = 2658.7$
		4.57 (h_a)			$Z = 2.0$
3.64 (h_c)					
HT₃	Col _{ho} (110)	28.25	28.25	(10)	$a = 32.62$
		16.30	16.05	(11)	$S = 921.5$
		14.07	13.76	(20)	$V = 3179.2$
		10.67	10.47	(21)	$Z = 1.9$
		4.52 (h_a)			
		3.45 (h_c)			
	Col _{hd} (130)	27.84	27.84	(10)	$a = 32.14$
		16.05	16.07	(11)	$S = 894.9$
		13.76	13.91	(20)	$V = 3150.3$
		10.47	10.52	(21)	$Z = 1.9$
4.53 (h_a)					
	3.52 (h_c)				
HT₄	Col _h (108)	33.34	33.34	(10)	$a = 38.49$
		19.12	19.24	(11)	$S = 1283.5$
		16.57	16.66	(20)	$V = 4453.8$
		12.68	12.60	(21)	$Z = 2.1$
		4.52 (h_a)			
		3.47 (h_c)			

d_{obs} , experimental lattice spacing; d_{cal} , calculated from the lattice parameter, a for the hexagonal lattice; h_a , alkyl chains correlation peak value; h_c , core-core spacing; Z , number of molecules per columnar slice; S , lattice area; V , molecular volume

According to the XRD results, columnar mesophases generated by **HT**₁₋₄ consist of two molecules per slice of column ($Z = 2$). So, it has been assumed that the central cyanopyridone ring might have involved in the formation of dimer through intermolecular H-bonding to yield disc-shaped structures. In order to validate this assumption, one more series of molecules was synthesized, **HT**₅₋₇, by replacing the central cyanopyridone unit with 2-methoxy-3-cyanopyridine, which are devoid of H-bonding sites. However, they do not display any mesomorphism, as confirmed by DSC traces clearly indicating the role of the central core in dimer formation. Conclusively, the H-bonding interaction is a deciding factor for the formation of mesophase in the bird-shaped cyanopyridones.

Molecular models have been proposed for the columnar mesophases of new cyanopyridones using XRD data and Density Functional Theory (DFT) calculations. The DFT calculations were performed at B3LYP/6-31G* level of theory using the Spartan 10 software in vacuum. According to theoretical simulations of **HT**₂ molecule, the conjugatively connected two dialkoxyphenyl rings are not co-planar with the central cyanopyridone ring, wherein lactam and dialkoxyphenyl rings are at the top and lower sides, respectively with the dihedral angle of 159°. The observed average end to end diagonal distance were found to be 31.50 Å. An overall geometry seems to be flying bird shape.

As discussed in the preceding section, H-bonding plays a key role among the non-covalent interactions in the molecular self-assembly of these cyanopyridone molecules. Such an important interaction can be theoretically studied by chemical functional description method (CFD), thereby it is possible to observe potential electron acceptor/donor, proton donor/acceptor sites in the molecules. **Fig 4.4a** depicts the DFT based energy-minimized structure of **HT**₂ molecule and **Fig 4.4b** portrays chemical functional descriptors (CFDs), wherein the various blue regions represent the proton donor sites that include the NH group of lactam ring and alkyl carbon atoms, while the green regions signify the proton acceptor sites located on carbonyl oxygen, CN and ether linkages. Therefore, this efficient proton donor and acceptor nature facilitate the formation of a strong H-bonding to form a cyclic structure between two cyanopyridone rings. To understand the structural conformations of cyanopyridone based dimeric segments in the columnar mesophase, an energy-minimized structure of an H-bonded

dimeric unit for **HT**₂ has been obtained. As visualized in **Fig 4.4c**, one of dioctyloxyphenyl rings from each of the **HT**₂ units rotate with respect to cyanopyridone ring at $\sim 90^\circ$ when compared to its monomeric counterpart for stabilizing the dimeric structure. According to simulations, the obtained intermolecular hydrogen bonding between the oxygen atom of the C=O group and amidic proton CO-NH of adjacent lactam ring (labelled a and b in green colour) are 2.14 Å and 1.921 Å, respectively. The maximum end to end diagonal distance was found to be 36.234 Å.

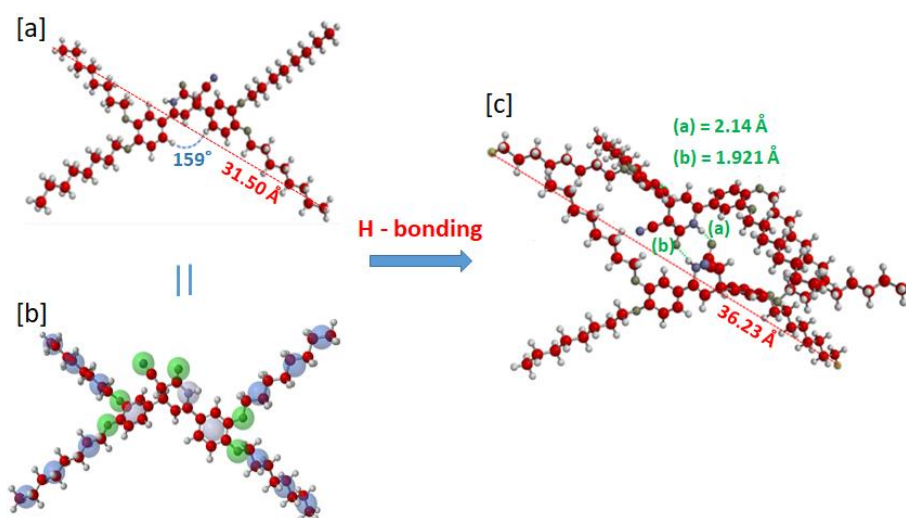


Figure 4.4 (a) DFT based energy-minimized structure of **HT**₂; (b) energy-minimized structure of **HT**₂ showing chemical functional descriptors (CFDs); (c) energy-minimized structure of H-bonded dimer for **HT**₂

As XRD results and theoretical simulations of **HT**₁ reveal that, the two molecules undergo space filling dimerization which further stack into columns with the intermolecular spacing of 3.52 Å. The resulting columns arranged in an oblique lattice. Since the angle of lattice sides is $64.11^\circ \neq 90^\circ$, the shape of the lattice would be parallelogram. As mentioned in the previous section, the mesogens **HT**₂ and **HT**₃ display two distinct columnar hexagonal mesophases as a function of temperature. The hexagonal cell parameter ‘a’ for Col_{ho} and Col_{hd} phases of **HT**₂ were found to be 30.11 Å and 29.20 Å, respectively and these values are 17% and 20% smaller than the average diameter of the H-bonded dimeric unit. This may be due to intercalation and/or folding of alkyl chains. Moreover, these observations are mainly owing to changes in their intracolumnar spacings. Such transitions in these propeller-like mesogens are known

to be ascribed to conformational motions, which increase the mesogenic fluctuations along the columnar axis, resulting in the changes in intercolumnar ordering. Keeping these things in view, it can be considered that, in the Col_{hd} phase the discs within a column whose positions are truly liquid-like, but gain significant correlation in the Col_{ho} phase. The liquid-like correlations in the former appear to permit tilting of the discs within the column, a feature that could also be responsible for the much lower intercolumnar distance, when compared to the model-determined length of the dimer. Understandably, the ordering of the discs in the Col_{ho} phase reduces this degree of freedom causing the spacing to increase by ~ 1.0 Å. **Fig 4.5** schematically illustrates the self-assembly of **HT**₂ molecules in ordered and disordered columnar hexagonal mesophase.

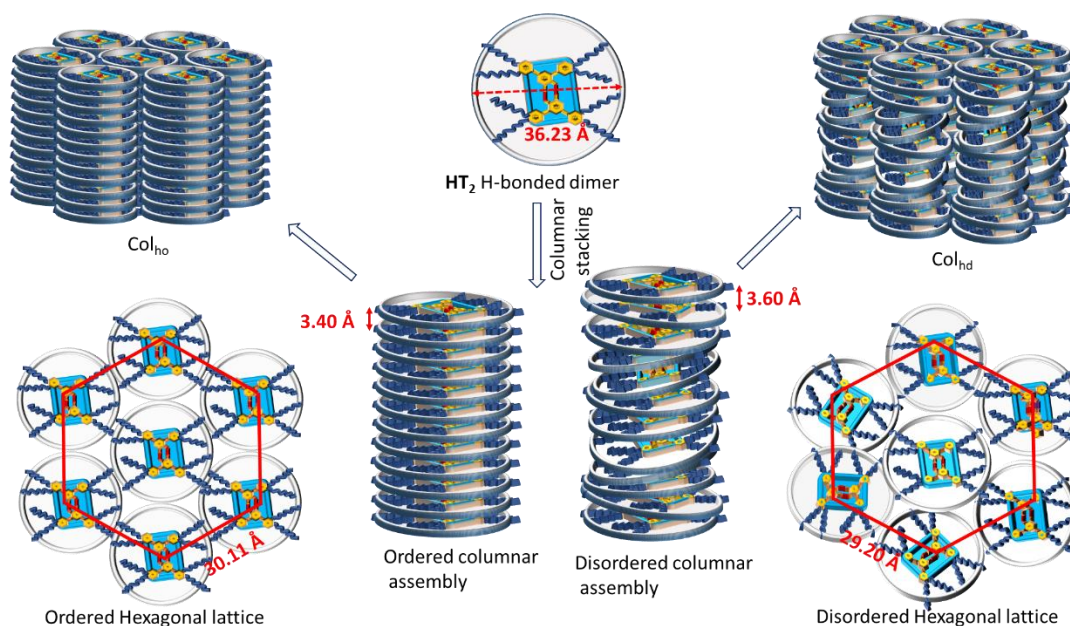


Figure 4.5 Schematic demonstration of the self-assembly of **HT**₂ in ordered and disordered columnar hexagonal mesophase (for the XRD patterns obtained at 120 °C and 142 °C)

To summarize, all the cyanopyridones displayed thermotropic mesophase behaviour by means of self-assembly of more or less disc-shaped H-bonded dimers. Furthermore, the role of H-bonding interactions in the stabilization of mesophases was determined by the support of one more similar series of molecules. The investigated cyanopyridones adopted various columnar mesophases, *viz* Col_{ob}, Col_{ho} or Col_{hd}

depending on the dynamics of the H-bonded dimeric entities in the columnar stack as well as the length of the terminal alkyl chains.

4.2.2.2 Mesomorphic behaviour of HT₈₋₁₀ (Series-2)

The thermal properties of three newly synthesized compounds were investigated by the combination of POM and DSC techniques. All members of the series, **HT₈₋₁₀** showed stable thermotropic LC behaviour at room temperature with very low isotropic points. Their phase transition peak temperatures and associated enthalpy changes are presented in **Table 4.4**.

The DSC traces of all the compounds are displayed in **Fig 4.6**. In the DSC trace of **HT₈** bearing symmetrical terminal alkoxy chains, a broad endothermic transition peak at 54.16 °C (onset at 45 °C) with the enthalpy of 4.03 kJmol⁻¹ corresponding to clearing of mesophase to isotropic liquid phase and a relatively sharp exothermic transition peak at 48.20 °C ($\Delta H = -2.82$ kJmol⁻¹) was observed (**Fig 4.6a**). Whereas, **HT₉** with unsymmetrical alkoxy substitutions showed a reduced thermal mesophase range when compared to **HT₈**. On heating, the LC phase was stable till 42 °C (**Fig 4.6b**). The higher chain analogue compound **HT₁₀** displayed reversible transition at very low temperature with reasonably trivial energy change, which was assigned to glass transition. In addition, an endothermic LC clearing point was observed at 29.48 °C with even more reduced mesophase range as depicted in **Fig 4.6c**. The thermotropic mesophase behaviour was further confirmed by microscopic observations using cross-POM. They showed highly bright and fluidic birefringent textures and the observed textural transitions were quite consistent with DSC results. On slow cooling from their respective I phase, all the compounds showed a typical mosaic pattern which was stable even at much lower temperature as displayed in **Fig 4.7a-f**. These results are characteristic indication of existence of columnar mesomorphism in these materials (Gupta et al. 2018; Kumar 2016; Kumar and Gupta 2011).

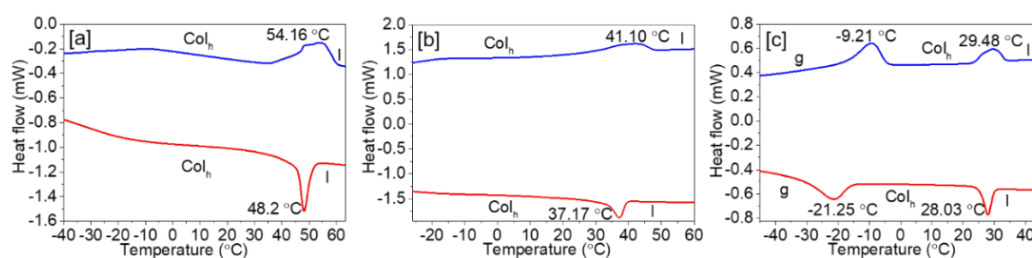
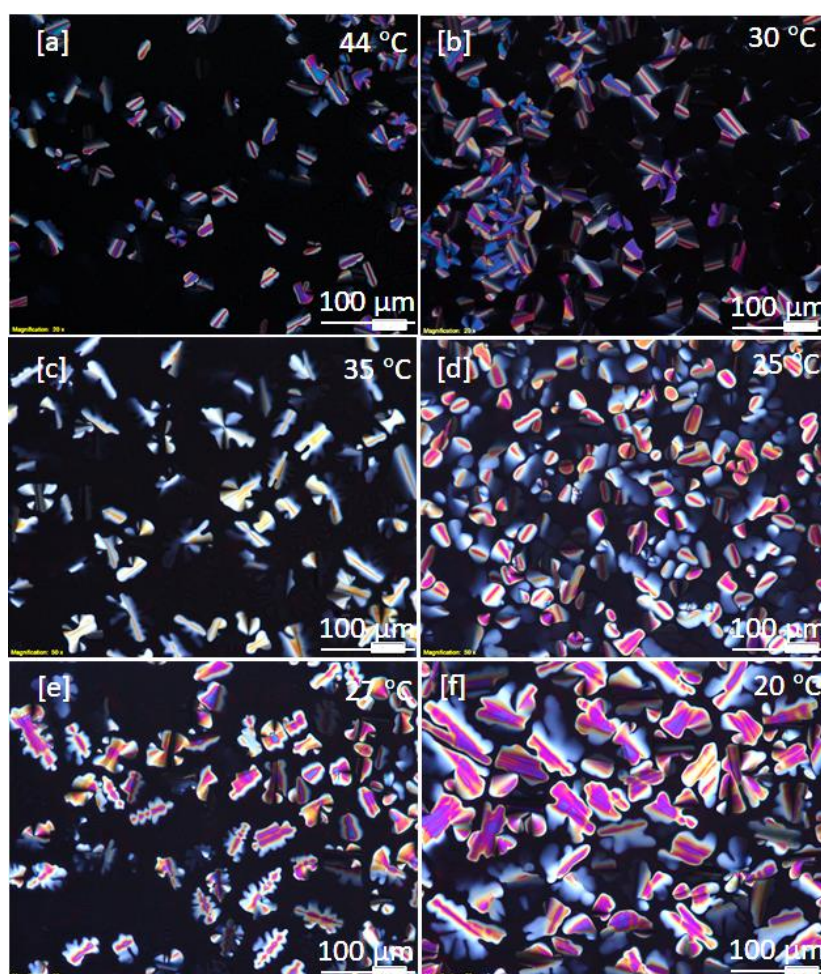


Figure 4.6 DSC thermograms of compounds: (a) **HT₈**; (b) **HT₉**; (c) **HT₁₀**

Table 4.4 ^a Phase transition temperatures and corresponding enthalpies of **HT**₈₋₁₀

Compd.	Phase sequence	
	Heating	Cooling
HT ₈	Col _h 54.16 (4.03) I	I 48.20 (-2.82) Col _h
HT ₉	Col _h 41.10 (2.13) I	I 37.17 (-1.87) Col _h
HT ₁₀	g -9.21 (7.71) Col _h 28.66 (3.13) I	I 28.03 (-2.85) Col _h -21.25 (-6.14) g

^a Peak temperatures/°C (enthalpies/kJmol⁻¹) obtained by second heating and cooling at rate of 5 °C/min; g = Glassy phase; Col_h = Columnar hexagonal phase; I = Isotropic liquid phase.

**Figure 4.7** Polarized optical micrographs of the compounds: **HT**₈ at (a) 44 °C and (b) 30 °C; **HT**₉ at (c) 35 °C and (d) 25 °C; **HT**₁₀ at (e) 27 °C and (f) 20 °C

To get further insight into the nano-segregation of star-shaped molecules in the mesophase, temperature-dependent X-ray diffraction experiments were carried out. The XRD spectra for **HT**₈ were acquired at different temperatures in the entire mesophase range and they were found to be quite similar. The spectra obtained at 35 °C and 24 °C are depicted in **Fig 4.8a** and **Fig 4.8b**, respectively. At 35 °C and 24 °C, the four lower angle reflections were observed in a relative ratio of $1:1/\sqrt{3}:1/2:1/\sqrt{7}$, respectively. This set of signals can be assigned to (10), (11), (20) and (21) planes of hexagonal lattice geometry according to **Eq. 4.3**. In addition, a diffused peak at 4.31 Å corresponding to packing of liquid-like alkyl chains and a weak broad peak centred at 3.50 Å due to periodic stacking of aromatic cores within the columns were seen at both the temperature points (**Fig 4.8a-b**).

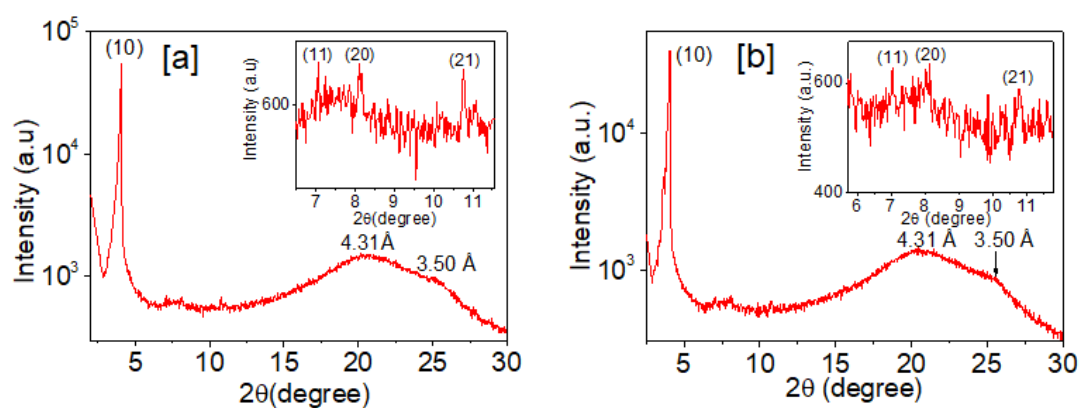


Figure 4.8 XRD spectra obtained for **HT**₈: (a) at 35 °C and (b) at 24 °C (insets show the focused area of lower angle region)

At 35 °C, the lattice constant, lattice area, and the molecular volume were determined to be 25.05 Å, 543.2 Å² and 1919 Å³, respectively. The number of molecules per slice of hexagonal lattice was calculated by using **Eq. 4.4** assuming the density “ ρ ” of the molecules as 1 g/cm. Accordingly, Z was found to be 1.08 for Col_h phase of **HT**₈ at this temperature. The results clearly suggested that, each stratum of the columns has been occupied by single non-symmetrical star-shaped molecule. There were no considerable deviations in lattice parameters observed at different temperatures within the mesophase range as indicated in **Table 4.5**. Similarly, **HT**₉ and **HT**₁₀ were also indexed to columnar hexagonal mesophase and the associated data are tabulated in **Table 4.5**.

Table 4.5 XRD characterization data of new mesogens **HT**₈₋₁₀ at different temperatures

Compd.	Phase (<i>T</i> /°C)	<i>d</i> _{obs} [Å]	<i>d</i> _{cal} [Å]	Miller Indices (<i>hk</i>)	Lattice parameter <i>a</i> [Å], Lattice area <i>S</i> [Å ²], Molecular volume <i>V</i> [Å ³], Number of molecules per lattice site <i>Z</i>
HT ₈	Col _h (35)	21.69	21.69	(10)	<i>a</i> = 25.05
		12.54	12.52	(11)	<i>S</i> = 543.2
		10.85	10.84	(20)	<i>V</i> = 1918.8
		8.17	8.19	(21)	<i>Z</i> = 1.08
		4.31 (<i>h</i> _a) 3.50 (<i>h</i> _c)			
	Col _h (24)	21.79	21.79	(10)	<i>a</i> = 25.16
		12.57	12.58	(11)	<i>S</i> = 548.3
		10.83	10.89	(20)	<i>V</i> = 1919
		8.20	8.23	(21)	<i>Z</i> = 1.09
		4.31 (<i>h</i> _a) 3.50 (<i>h</i> _c)			
HT ₉	Col _h (36)	22.70	22.70	(10)	<i>a</i> = 26.21
		11.36	11.34	(11)	<i>S</i> = 595.0
		4.30 (<i>h</i> _a)			<i>V</i> = 2088.5
		3.51 (<i>h</i> _c)			<i>Z</i> = 1.09
	Col _h (30)	22.74	22.74	(10)	<i>a</i> = 26.25
		11.36	11.36	(11)	<i>S</i> = 597.1
		4.34 (<i>h</i> _a)			<i>V</i> = 2066
		3.46 (<i>h</i> _c)			<i>Z</i> = 1.08
HT ₁₀	Col _h (23)	24.37	24.37	(10)	<i>a</i> = 28.14
		4.33 (<i>h</i> _a)			<i>S</i> = 685.8
		3.54 (<i>h</i> _c)			<i>V</i> = 2427.6 <i>Z</i> = 1.1

*d*_{obs}, observed spacings; *d*_{cal}, calculated spacings from the lattice parameter *a* for the hexagonal lattice; *h*_a, alkyl chains correlation peak value; *h*_c, core-core spacing; *Z*, number of molecules per columnar slice; *S*, lattice area; *V*, molecular volume

To get fully optimized structure of these star-shaped molecular discs, density functional theory (DFT) calculations were performed for one of the isolated molecules *i.e.* **HT**₉ in vacuum at the B3LYP/6-31G* level of theory using the Spartan 10 software. (Pandith et al. 2017) According to the quantum chemical calculations, the

energy minimized structure of **HT₉** was found to be planar and possess almost disc-like structure with the average diameter of 28.5 Å (**Fig 4.9a**). Apparently, the trialkoxybenzene ring is coplanar with central cyanopyridine ring although it is connected through flexible benzyloxy group. As described in the previous section, the number of molecules per slice of column (*Z*) was found to be approximately one and the molecules possess considerable order within the one-dimensional columnar stack as recognized by core-core reflections (3.46-3.51 Å) in its XRD spectra (**Fig 4.9c**). For **HT₉**, the average hexagonal cell parameter '*a*' throughout the mesophase range (26.23 Å) was found to be smaller than its molecular diameter (28.5 Å), which may be attributed to intercalation of peripheral alkyl substituents. Thus, based on the XRD results and theoretical simulations, a molecular model was proposed for the Col_h self-assembly of **HT₉**, as shown in **Fig 4.9**.

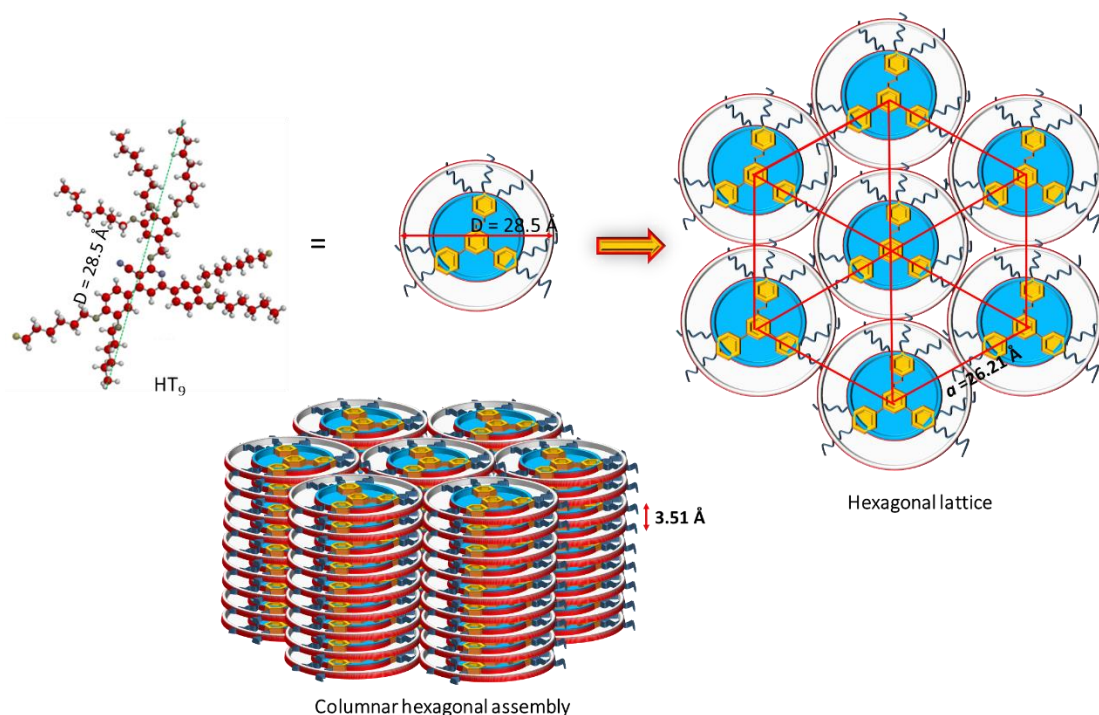


Figure 4.9 Schematic model for hexagonal columnar self-assembly of **HT₉**

In summary, three new cyanopyridine based unsymmetrical star-shaped molecules were investigated to be self-organized into an imperative columnar mesophase stabilized at ambient conditions. It is evident that, in these unsymmetrical star-shaped mesogens, increase in the length of alkyl chains at the benzylic arm brings about decrease in thermal stability of the mesophase. Moreover, they showed stable

columnar phase at room temperature with the low clearing points, which is one of the important favourable key factors for device fabrication.

4.2.2.3 Mesomorphic behaviour of HT₁₁₋₂₀ (Series-3)

Thermotropic phase behavior of all the new cyanopyridone derivatives, **HT**₁₁₋₂₀ was studied by DSC and POM techniques. Further, the molecular self-assembly in the different mesophase structures was deliberated by XRD experiments. The resulted phase transition temperatures and the associated energy changes are summarized in **Table 4.6**. Evidently, the compounds, **HT**₁₁₋₁₃ were found to exhibit enantiotropic mesophase behaviour at room temperature and stabilized over wide temperature range with relatively lower isotropization points (**Fig 4.10a-c**). Whereas the compounds **HT**₁₄₋₂₀ did not showed any LC phase transitions, instead they showed polymorphism (**Fig 4.10d-j**). The lack mesomorphism in these derivatives may be due to the insufficient number of alkyl chains to cover the space around the central core

Apparently, the DSC trace of compound **HT**₁₁ did not show any sign of melting on the heating scan, instead, it displayed two distinct transitions at 89.48 °C and 104.30 °C with smaller enthalpy changes of 1.09 kJmol⁻¹ and 0.20 kJmol⁻¹ due to LC-LC and LC-I transitions, respectively (**Fig 4.10a**). On cooling cycle, both the transition peaks reoccurred at 96.10 °C and 75.52 °C without any crystallization transition till room temperature. The perceived very low enthalpy changes may be attributed to high fluidic nature of the mesophases. The compound, **HT**₁₂ carrying longer alkyl chains also showed two separate mesophases at a relatively higher temperature having clearing point at 132.95 °C than that of **HT**₁₁. On cooling, both the LC phases reappeared and did not exhibit any signal for crystallization as depicted in **Fig 4.10b**. Also, the analogue compound **HT**₁₃ bearing much longer terminals (hexadecyloxy) displayed two mesomorphic states which clear at 121.19 °C (**Fig 4.10c**). It was observed that, this set of compounds has not shown any regular trend in their mesophase thermal stability, despite there exists a linear increase in the alkyl chain length at phenyl arm.

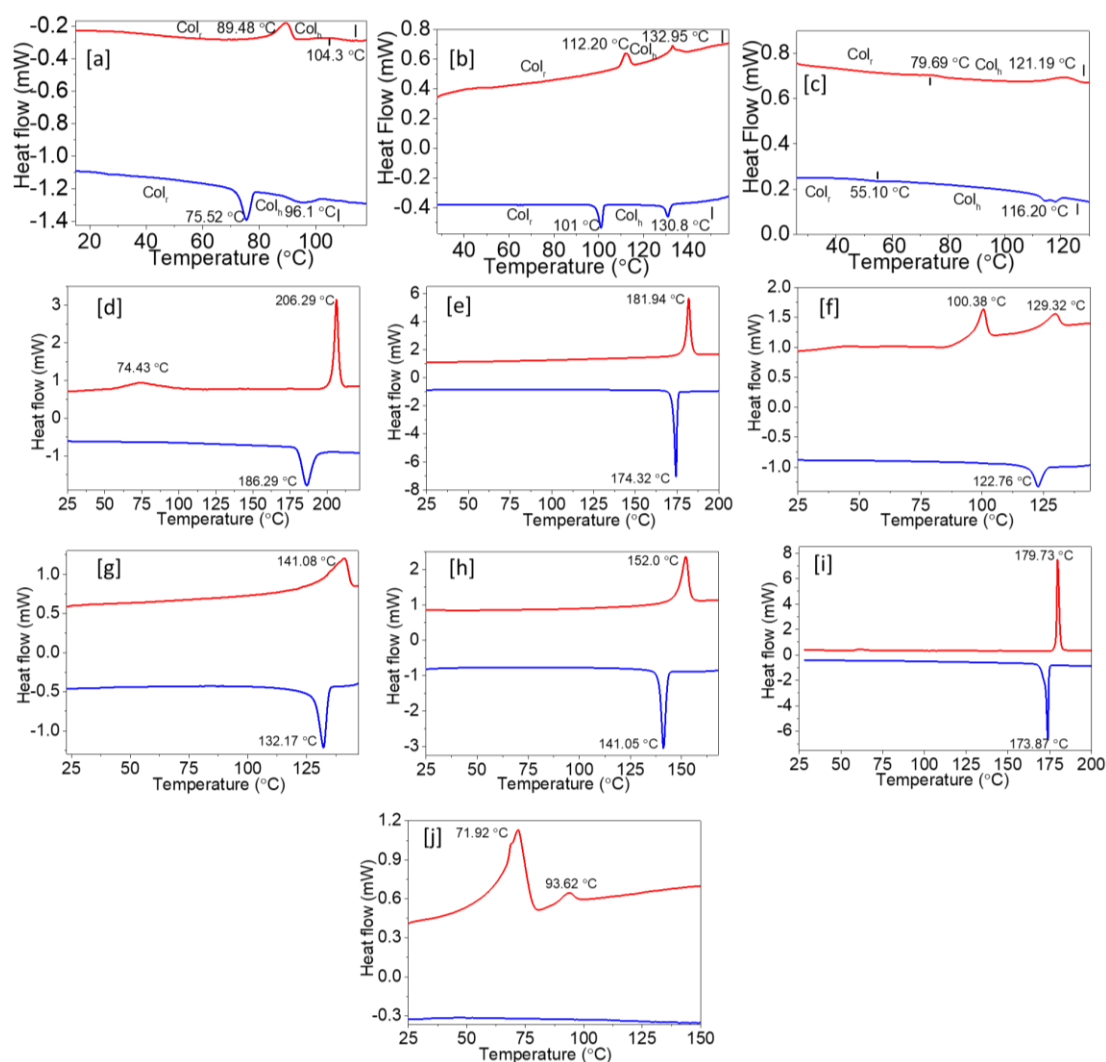


Figure 4.10 DSC thermograms: (a) **HT**₁₁; (b) **HT**₁₂; (c) **HT**₁₃ (d) **HT**₁₄; (e) **HT**₁₅; (f) **HT**₁₆; (g) **HT**₁₇; (h) **HT**₁₈; (i) **HT**₁₉; (j) **HT**₂₀ (red and blue traces represent second heating and first cooling cycles, respectively)

Under POM, highly birefringent mosaic type of pattern was observed on slow cooling of compound **HT**₁₁ from its isotropic state, which was high fluidic and shearable even at room temperature (**Fig 4.11a-b**). This is a typical indication of the existence of columnar mesomorphism (Kumar 2011). Seemingly, on cooling down from the higher temperature mesophase to its lower one, a remarkable decline of optical birefringence was noticed in some of the bright areas as shown in **Fig 4.11a-b**, which may be due to inter and/or intracolumnar transitions. The observed optical textural changes were fairly consistent with the DSC transitions. Whereas in the case of **HT**₁₂, dendritic growth appeared initially which in turn formed a typical mosaic pattern at lower temperature LC phase and it remained unchanged until further much lower

temperatures (**Fig 4.11c-d**). As seen in **Fig 4.11d-e**, the compound **HT₁₃** displayed similar characteristic optical textures for columnar phases featuring a combination of mosaics with linear and fan-shaped birefringent defects as well as homeotropic regions. The POM images of **HT₁₁₋₁₃**, captured in both the mesophase ranges are shown in **Fig 4.11a-f**.

Table 4.6. ^a Phase transition temperatures and corresponding enthalpies of **HT₁₁₋₂₀**

Com pd.	Phase sequence	
	Heating	Cooling
HT₁₁	Col _r 89.48 (1.09) Col _h 104.30 (0.20) I	I 96.1 (-0.50) Col _h 75.52 (-1.12) Col _r
HT₁₂	Col _r 112.20 (2.36) Col _h 132.95 (2.04) I	I 130.80 (-1.21) Col _h 101.0 (-2.37) Col _r
HT₁₃	Col _r 73.69 (0.24) Col _h 121.19 (1.41) I	I 116.20 (-1.08) Col _h 55.10 (-0.19) Col _r
HT₁₄	Cr ₁ 74.43 (8.46) Cr ₂ 206.29 (22.22) I	I 186.29 (-19.81) Cr ₂
HT₁₅	Cr 181.94 (22.86) I	I 174.32 (-22.57) Cr
HT₁₆	Cr ₁ 100.38 (5.86) Cr ₂ 129.72 (3.73) I	I 122.76 (-3.57) Cr ₂
HT₁₇	Cr 141.08 (12.46) I	I 132.17 (-12.62) Cr
HT₁₈	Cr 152.0 (14.64) I	I 141.05 (-14.92) Cr
HT₁₉	Cr 179.75 (28.58) I	I 173.87 (-26.23) Cr
HT₂₀	Cr ₁ 71.92 (-28.95) Cr ₂ 93.62 (2.36)	^b I

^a Peak temperatures/°C (enthalpy/kJmol⁻¹) obtained by second heating and first cooling at the rate of 5 °C/min; Cr₁ and Cr₂ = Different crystalline states, Col_r = Columnar rectangular phase; Col_h = Columnar hexagonal phase; I = Isotropic liquid phase; ^bCrystallization was not observed till room temperature

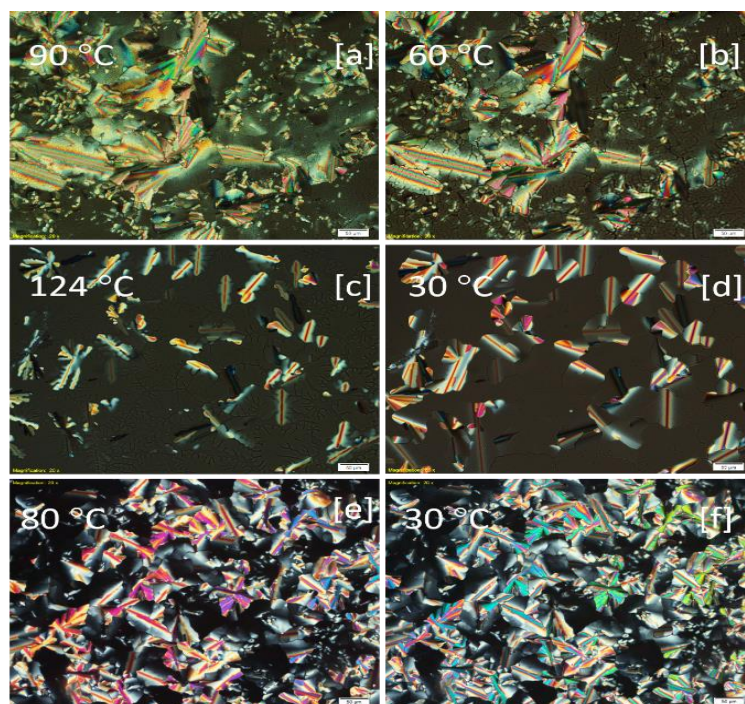


Figure 4.11 Optical images captured for **HT**₁₁₋₁₃ under cross-POM on slow cooling from their respective isotropic phase: (a) at 90 °C and (b) at 60 °C for **HT**₁₁; (c) at 124 °C and (d) at 30 °C for **HT**₁₂; (e) at 80 °C and (f) at 30 °C for **HT**₁₃

In order to get further insight into self-organization of the molecules in the different mesophase structures, powder X-ray diffraction studies were carried out for non-aligned samples of all the new mesogens. As indicated by the DSC traces, they were found to be bi-mesomorphic in nature. Definitely, the XRD patterns gained for **HT**₁₁ in both the LC phase ranges were quite different, indeed they are almost similar within their respective mesophase range at different temperature points (**Figs 4.12a-b**). For instance, the XRD trace at 90 °C (within the higher temperature mesophase range) showed two sharp reflections in the lower angle region in the reciprocal ratio of $1:\sqrt{3}$. Whereas in the wide angle region, a rather diffused halo was observed at 4.39 \AA reminiscent of the liquid-like aliphatic chains (**Fig 4.12a**). The observed two lower angle signals can be assigned to (10) and (11) planes of hexagonal symmetry with a parameter $a = 30.41 \text{ \AA}$. In fact, only these reflections do not unambiguously elucidate the hexagonal lattice. Nevertheless, such observations are frequent in hexagonal mesophases bred by diverse mesogenic structures (Alvarez et al. 2006; Barberá et al. 2000; Beltrán et al. 2012; Cavero et al. 2007; Hayer et al. 2006; Kumar and Gupta 2011; Yelamaggad et al. 2007; Zheng et al. 1996). This may be due to a minimum in the form

factor, which prevents the appearance of peaks in the lower angle region. Moreover, the appearance of typical optical textures strappingly indicating the columnar hexagonal phase. The lattice area S and molecular volume V were estimated to be 801 \AA^2 and 3517 \AA^3 , respectively.

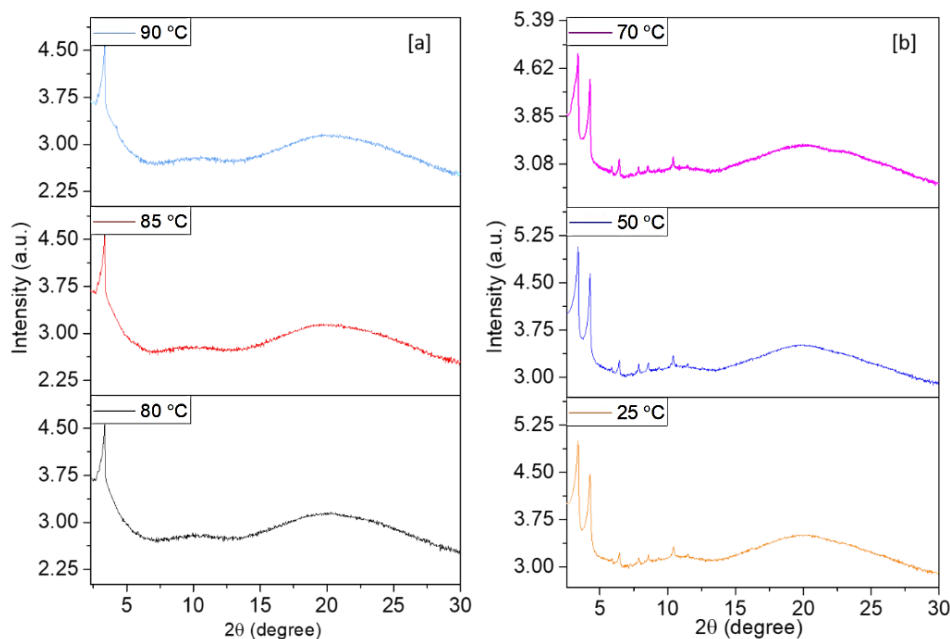


Figure 4.12 XRD patterns obtained for **HT₁₁** at various temperatures (a) in the higher temperature mesophase and (b) the lower temperature mesophase ranges

The XRD pattern of lower temperature mesophase range (obtained at room temperature) showed a number of reflections in the lower angle region (**Fig 4.12b**). In addition, a broad halo has centred at 4.43 \AA due to alkyl chain correlations. The set of signals are assigned to (01), (11), (21), (30), (31) and (32) diffractions of the rectangular lattice with the unit cell parameters $a = 33.86 \text{ \AA}$ and $b = 26.01 \text{ \AA}$ according to **Eq 4.6**.

$$\frac{1}{d_{cal}^2} = \frac{h^2}{a^2} + \frac{k^2}{b^2} \quad (4.6)$$

Similarly, the XRD patterns of **HT₁₂** were obtained at discrete temperatures in both the mesophase ranges. The lower angle reflections are in the ratio of $1:\sqrt{3}$ and they can be entrusted to (10) and (11) planes of the hexagonal lattice. Their lattice parameters were calculated to be 32.34 and 32.36 \AA , respectively. Whereas the XRD pattern at lower temperature mesophase of **HT₁₂** (obtained at $25 \text{ }^\circ\text{C}$) showed a set of reflections which are certainly assigned to a columnar rectangular phase owing to the lattice

parameters $a = 33.79 \text{ \AA}$ and $b = 27.72 \text{ \AA}$. Similarly, mesogen **HT**₁₃ adopted Col_r and Col_h phases at lower and higher temperatures, respectively. A detailed XRD indexing is summarized in **Table 4.7**.

Table 4.7. XRD characterization data of **HT**₁₁₋₁₃ at different temperatures

Compd.	Phase ($T/^\circ\text{C}$)	d_{obs} [\AA]	d_{cal} [\AA]	Miller Indices (hk)	Lattice parameter a [\AA], Lattice area S [\AA^2], Cell volume V [\AA^3]	
HT ₁₁	Col _h (90)	26.34	26.03	(10)	$a = 30.41$	
		15.15	15.20	(11)	$S = 801.1$	
		4.39 (h_a)			$V = 3516.9$	
					$Z = 1.88$	
		Col _r (25)	26.01	26.01	(10)	$a = 33.86$
			20.60	20.59	(11)	$b = 26.01$
	13.80		14.18	(21)	$S = 880.7$	
	11.13		11.28	(30)	$V = 3901$	
	10.22		10.35	(31)	$Z = 2.08$	
	8.45		8.50	(32)		
	HT ₁₂	Col _h (115)	28.03	28.03	(10)	$a = 32.36$
			16.13	16.18	(11)	$S = 907.2$
4.48 (h_a)					$V = 4064$	
Col _r (25)					$Z = 1.89$	
		27.72	27.72	(01)	$a = 33.79$	
		21.43	21.43	(11)	$b = 27.72$	
		15.99	16.89	(20)	$S = 936$	
		14.51	14.43	(21)	$V = 3587$	
		12.79	12.82	(12)	$Z = 1.66$	
		8.88	8.91	(13)		
		3.83 (h_c)				
		4.40 (h_a)				
HT ₁₃	Col _h (80)	30.05	30.05	(10)	$a = 34.69$	
		17.29	17.34	(11)	$S = 1042$	
		4.45 (h_a)			$V = 4645.5$	
	Col _r (25)				$Z = 1.91$	
		29.66	29.66	(01)	$a = 34.06$	
		22.37	22.36	(11)	$b = 29.66$	
		17.13	17.03	(20)	$S = 1010$	
		15.25	14.83	(02)	$V = 4424$	
		13.58	13.59	(12)	$Z = 1.82$	
4.43 (h_a)						

d_{obs} , observed spacings; d_{cal} , calculated spacings h_a , alkyl chains correlation peak value; h_c , π - π spacing; Z , number of molecules per each columnar slice. Alkyl halo was considered for the calculations, when the core-core peak is absent

The obtained results indicated that, all members of the series displayed two distinct columnar mesophases as a function temperature. The compound **HT**₁₂ having critical chain length among the series was chosen as a representative example to understand the molecular assembly in their mesomorphic states. Initially, the number of molecules occupied in each columnar stratum (Z) of Col_h (Eq. 4.4) and Col_r (Eq. 4.7) were estimated by assuming the density equal to 1 g cm⁻³ (Tang et al. 2012). Accordingly, nearly two molecules are involved in each columnar slice of both the mesophases to ensure the space filling disc-like structure. It should be noted that, the central cyanopyridone core, capable of forming closed-type hydrogen bonding may stabilize the dimeric unit through a strong intermolecular H-bonding.

$$Z = \frac{abc \times \rho N_A}{M_W} \quad (4.7)$$

As seen in many classical and unconventional discotics, all the compounds showed a thermodynamical intercolumnar transition from rectangular to hexagonal columnar assembly, which was evidenced by the observed small enthalpy changes, optical variations and differences in XRD patterns (Wöhrle et al. 2015). Further, the dimeric structures form a columnar array with rectangular and hexagonal symmetry wherein the position of molecules is not fixed, rather it is truly liquid-like. This may be attributed to its propeller-like structures whose conformational motions would increase the mesogenic fluctuations and intracolumnar tilting, which could be responsible for the disappearance of the core-core peak in the XRD pattern for Col_h. This type of mesophase is sometimes termed as ‘disordered columnar mesophases’ in order to distinguish from the ordered assemblies (Park and Cho 2015). However, these molecules may possess some degree of order due to intermolecular hydrogen-bonding along the columnar axis through the central ring. Additionally, its D-A-D core-structure would also stabilize the mesophase by strong intracolumnar donor-accepter interactions. Keeping all these facts in view, a schematic model is proposed for the molecular self-assembly of **HT**₁₂ in Col_r as well as Col_h with plausible H-bonding interactions, as shown in Fig 4.13.

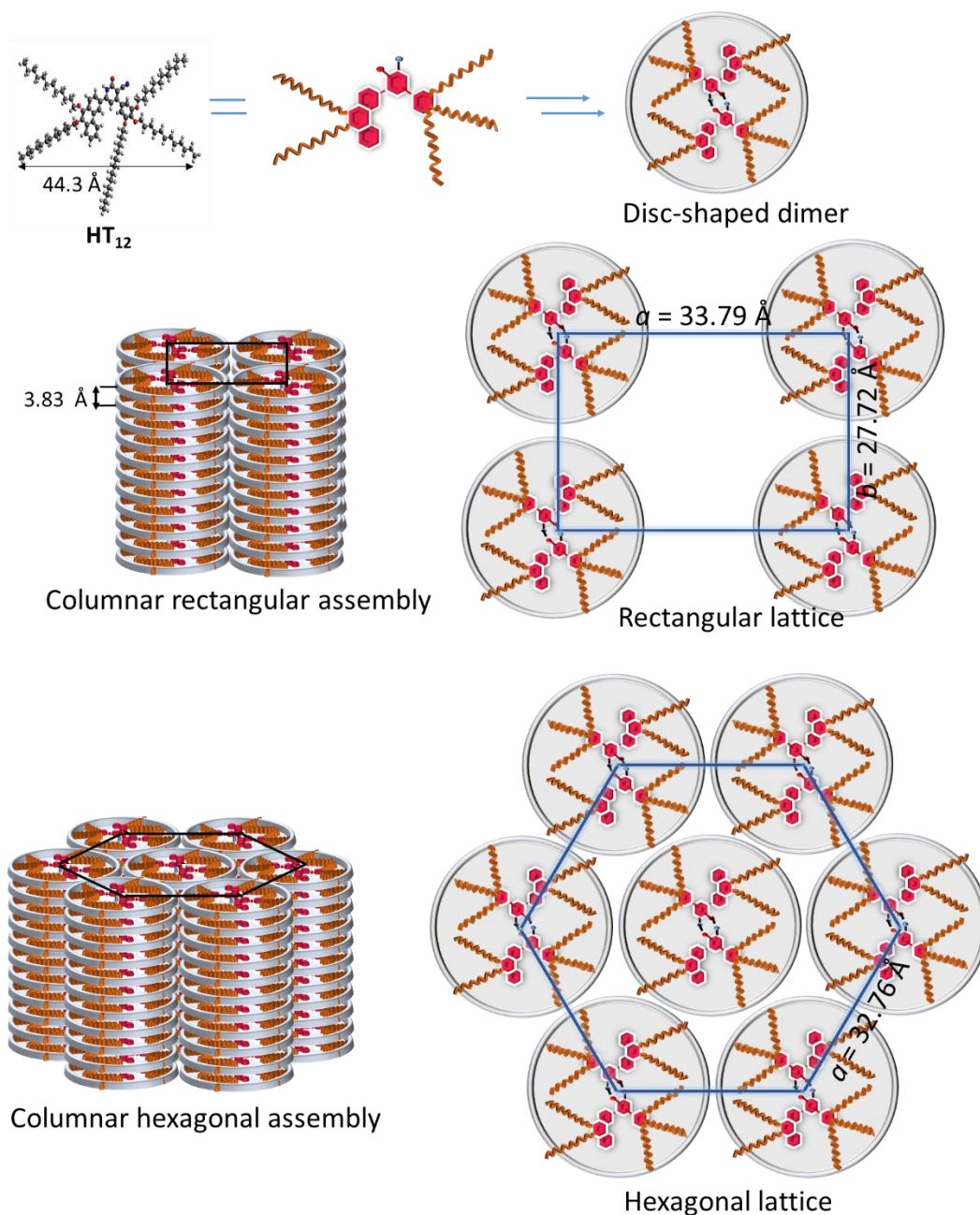


Figure 4.13 Schematic model showing the energy-minimized structure of **HT₁₂** (obtained by MM2 method) and its self-assembly in Col_h and Col_r phases with plausible H-bonding (XRD data at 115 °C and 25 °C were used for the illustration)

In total, only three members containing phenanthrene ring in their basic structure was found to exhibit LC phase. From the results it is evident that, no general trend was noticed in thermal stability of mesophases in spite of systematic sequential variation in length of peripheral chains on phenanthrene-cyanopyridone hybrid core

structure. Thus, mesophase type and ranges are independent of terminal chain lengths in these molecules. This may be due to numerous structural conformations of two arms with lengthy flexible chains of the central cyanopyridone core. However, all the compounds have organized into similar mesophase with two different lattice structures. They showed supramolecular bi-columnar mesomorphism, which is stable even under ambient conditions. The XRD results revealed that, these half-disc shaped molecules self-assembled into disc-like dimeric structures that further organized into Col_h and Col_r as a function of temperature.

4.2.2.4 Mesomorphic behaviour of HT₂₁₋₂₆ (Series-4)

The thermotropic self-assembling properties of alkoxyoxybenzylidene based compounds **HT**₂₁₋₂₆ were studied by set of techniques. The relevant phase transition sequence with their respective enthalpy changes (ΔH) are compiled in **Table 4.8**.

The DSC results of 3,4,5-trihexyloxybenzylidene derivative **HT**₂₁ and its trioctyloxy counterpart, **HT**₂₂ showed a direct melting from a crystalline state to an isotropic liquid phase at 90.35 and 88.98 °C on heating scan, respectively. The similar observations were noticed under POM also, wherein no birefringence was identified. However, in the higher alkoxy analogue, **HT**₂₃ bearing dodecyloxy terminals exhibits a trivial transition centred at 74.10 °C with an enthalpy change of 1.26 kJmol⁻¹ on heating which is assigned to transition from mesophase to an isotropic phase. On cooling trace, the LC phase has reappeared at 69.50 °C (-1.28 kJmol⁻¹) and it was crystallized at -9.84 °C (-9.84 kJ mol⁻¹) as shown in **Fig 4.14a**. On slow cooling from the liquid phase of **HT**₂₃, a dendritic growth appeared initially in the dark homeotropic region which in turn resulted in a typical mosaic pattern, as shown in (**Fig 4.14b-c**). The optical transitions were well consistent with the DSC results. The phase was shearable and highly fluidic in nature which witnessed very low clearing enthalpy. Here, the observed intense birefringent mosaic textures are the typical indication of columnar mesomorphism (Kumar 2011).

Table 4.8. ^a Phase temperatures (°C) and enthalpy changes (kJmol⁻¹) of HT₂₁₋₂₆

Compd.	Phase sequence	
	Heating	Cooling
HT ₂₁	Cr 90.35 (37.39) I	I ^b
HT ₂₂	Cr ₁ 62.92 (20.26) Cr ₂ 88.98 (14.44) I	I 11.78 (-10.2) Cr
HT ₂₃	Col _h 74.10 (1.26) I	I 69.50 (-1.28) Col _h -9.84 (-9.33) Cr
HT ₂₄	Cr ₁ 72.90 (5.95) Cr ₂ 100.50 (47.43) I	I 64.73 (-47.62) Cr
HT ₂₅	Cr 151.72 (79.23) I	I 132.59 (-71.35) Cr
HT ₂₆	Cr 108.07 (40.86) I	I 102.36 (-37.95)

^a Peak temperatures/°C (enthalpy/kJmol⁻¹) obtained by second heating and first cooling at the rate of 5 °C/min; ^b Crystallization was not observed; Cr, Cr₁ and Cr₂ = different crystalline phases; Col_h = Columnar hexagonal mesophase; I = liquid phase

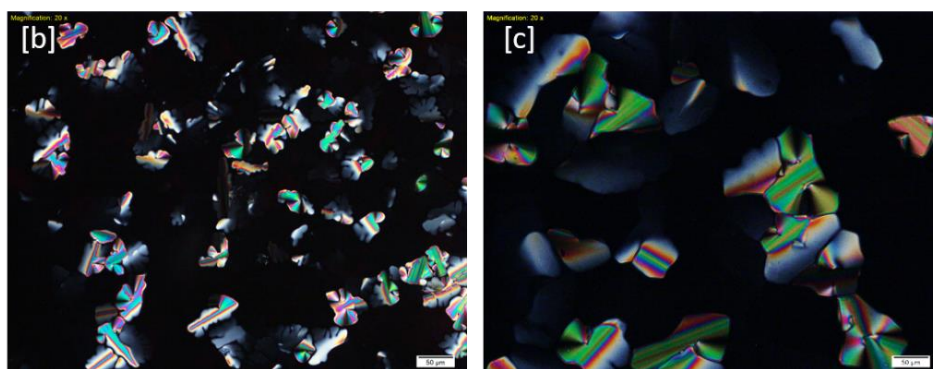
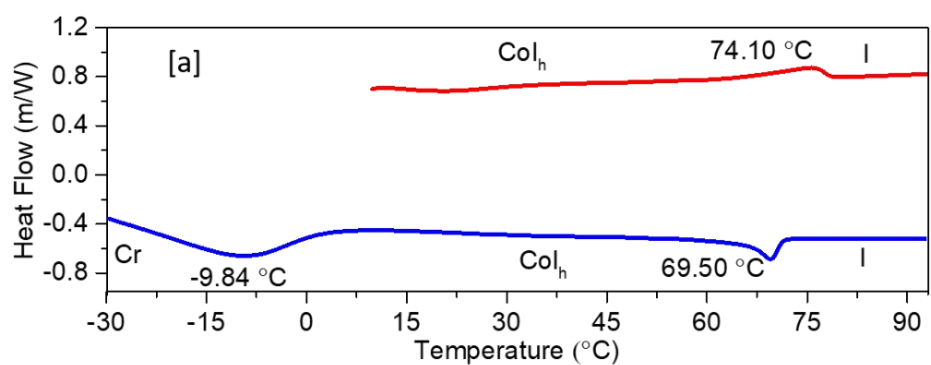


Figure 4.14 (a) DSC trace obtained for HT₂₃ at a rate of 5 °C/min (red and blue traces represent second heating and first cooling traces, respectively); POM textures observed on slow cooling from its I phase at a rate of 5 °C/min: (b) at 65 °C and (c) at 25 °C

In order to get further insight into the molecular self-assembly of **HT₂₃**, variable temperature X-ray diffraction experiments were carried out for its non-aligned sample. The XRD patterns gained all over the mesophase range at different temperature points were found to be almost similar. For instance, the XRD spectra acquired at 55 °C and room temperature are depicted in **Figs 4.15a-b**. As can be seen in the pattern obtained at 55 °C, two lower angle reflection peaks were observed at the Bragg's d -spacings of 35.15 and 17.57 Å. While appearance of a broad halo at 4.31 Å due to the liquid-like motion of peripheral chains (**Fig 4.15a**). The resulted two diffractions were assigned to (10) and (20) lattice planes for a hexagonal geometry with a lattice parameter $a = 40.89$ Å. Though it is not explicit to assign the Col_h phase from the observation of two reflections peak at the lower angle. It is quite common in both conventional and non-conventional discotics (Beltrán et al. 2012; Westphal et al. 2010; Yoon et al. 2012). The absence of other peaks have been attributed to a minimum in the form factor. The hexagonal lattice area, S and volume, V were found to be 1426 Å² and 6148 Å³, respectively. The lower temperature (at 25 °C) XRD pattern was almost similar to high-temperature diffractions, obviously with some variations in spacing values (**Fig 4.15b**). The two similar diffractions were indexed to Col_h with the intercolumnar distance of 40.58 Å. A detailed XRD characterization data is summarised in **Table 4.9**.

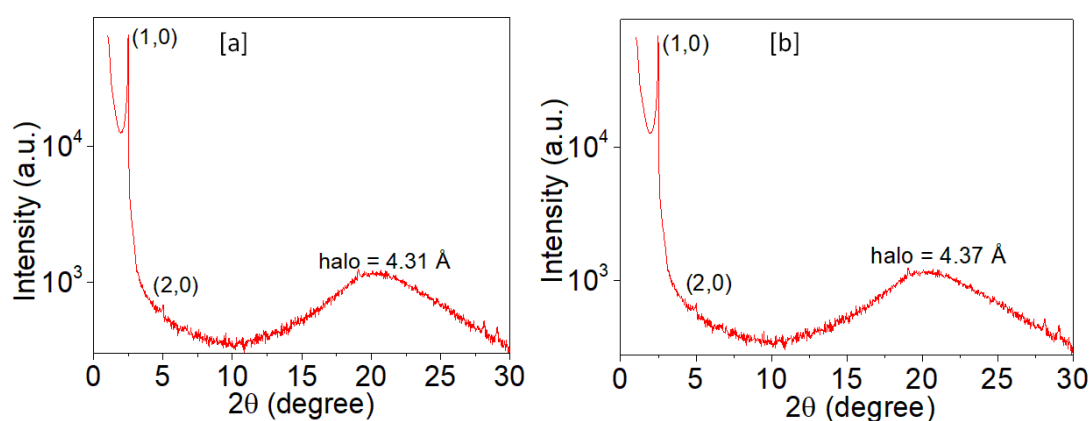


Figure 4.15 XRD pattern for Col_h phase of **HT₂₃**: (a) at 55 °C and (b) at 25 °C (the spectra obtained on slow cooling for its isotropic liquid state)

It has been observed that, the experimentally obtained hexagonal cell parameter (40.89 Å at 55 °C) for **HT₂₃** is much larger than its calculated molecular length at the fully optimized structural conformation (28.05 Å). Also, the nondiscoid molecular geometry has caused the columnar liquid crystalline behavior in it. These two facts

reveal that, each columnar stratum constituting more than one molecule. Therefore, number of molecules per columnar slice (Z) was calculated by assuming the density equal to 1.0 gcm^{-3} . Since, the Col_h structure of **HT**₂₃ did not show any intracolumnar stacking peak (c), alkyl halo center (h_a) was used in the afore mentioned calculations (Moyano et al. 2013). The values of Z were found to be 3.3 and 3.4 at $55 \text{ }^\circ\text{C}$ and $25 \text{ }^\circ\text{C}$, respectively for Col_h structure, which confirms that, more than three molecules occupied in each columnar unit. It is well-known that, hydrogen bonding interactions stabilize the columnar mesophases induced by supramolecular aggregates of non-discoid molecules. As wedge-shaped **HT**₂₃ possesses renowned hydrogen bonding group, *i.e.* carboxylic acid at its tip, which can induce strong polar H-bonding network and facilitate the space filling by the aliphatic chains. The plausible disc-shaped H-bonding superstructure of **HT**₂₃ as evidenced by XRD data is depicted in **Fig 4.16**.

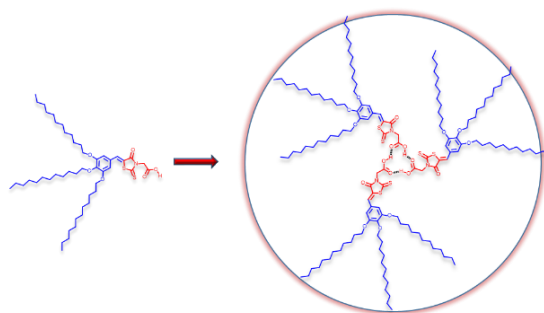


Figure 4.16 Supramolecular disc of **HT**₂₃

Table 4.9 XRD characterization data of **HT**₂₃ at different temperatures

Compd.	Phase ($T/^\circ\text{C}$)	d_{obs} [\AA]	d_{cal} [\AA]	Miller Indices (hk)	Lattice parameter a [\AA], Lattice area S [\AA^2], Molecular volume V [\AA^3], Number of molecules per columnar slice Z
HT ₂₃	Col_h (55)	35.15	35.15	(10)	$a = 40.89$
		17.51	17.57	(20)	$S = 1426.6$
		4.31 (h_a)			$V = 6148.8$ $Z = 3.3$
	Col_h (25)	35.42	35.42	(10)	$a = 40.58$
		17.65	17.70	(20)	$S = 1448.6$
		4.37 (h_a)			$V = 6330.6$ $Z = 3.4$

d_{obs} , observed spacings; d_{cal} , estimated spacings from the lattice parameter a for the Col_h lattice; h_a , peak centre of alkyl halo; V , molecular volume; S , lattice area; Z , number of molecules per unit lattice

A schematic models have been proposed for the supramolecular self-assembly of **HT**₂₃ in the columnar mesophases based on XRD data and quantum chemical simulations (DFT). The DFT calculations were performed using GAUSSIAN-09 program at the DFT-B3LYP correlation. Geometry optimized structure of **HT**₂₃ was obtained by using the basic set 6-311G (d,p). The simulated structure seems to be clear wedge-shaped, as shown in **Fig 4.17**. Evidently, three molecules associate in a single frame which leads to the formation of discs with a total of nine alkoxy chains. Here, the polar units form the columnar centers bounded by the rigid benzylidene aromatic segments with the lipophilic continuum, which further self-stack to attain hexagonal lattice symmetry, as schematically pictured in **Fig 4.17**.

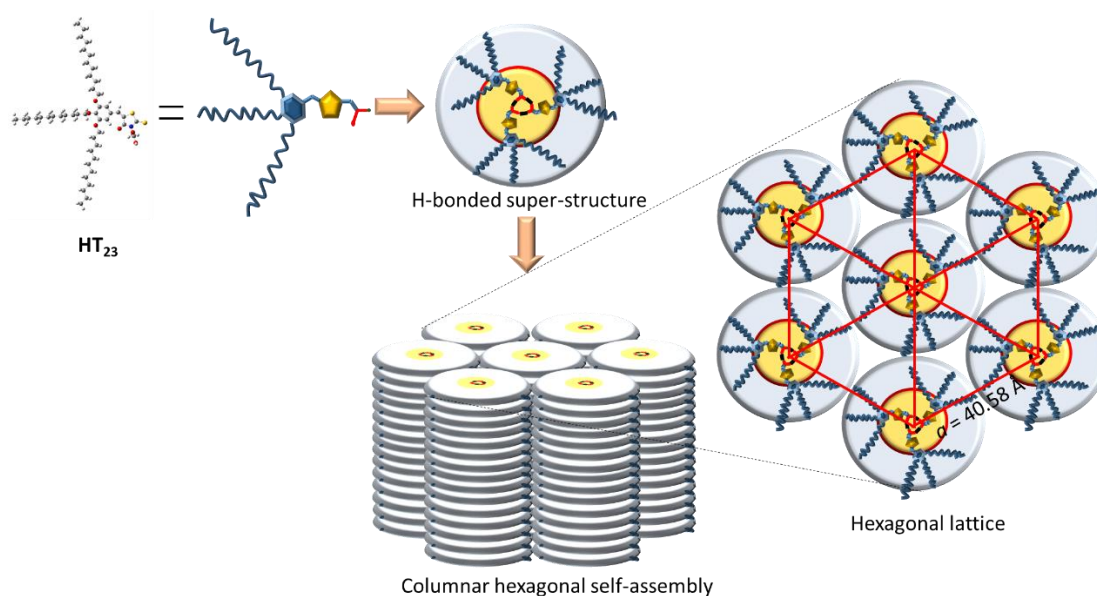


Figure 4.17. A schematic model for the Col_h self-assembly of **HT**₂₃

A regioisomer of **HT**₂₃ having alkoxy chains at 2nd, 3rd and 4th positions, *i.e.* **HT**₂₄ turned out to be crystalline in nature. It showed two distinct crystalline states and cleared directly to isotropic liquid as evidenced by thermal and optical observations. The non-mesogenicity of **HT**₂₄ may be due to the presence of longer terminals at the immediate positions of the H-bonding polar group, thereby causing steric hindrance, which would restrict the formation of H-bonded discotic super-structure. Also, a dialkoxy substituted rhodanine derivative, **HT**₂₅ did not show any mesogenic property because of its inability of space filling around the polar core. Further, an analogous compound with a free rhodanine group bearing suitable alkyl density, *i.e.* **HT**₂₆ failed

to show any mesomorphic behavior. The observed results validate the proposed hypothesis for **HT**₂₃ wherein the presence of rhodanine-*N*-acetic acid unit has a key role in the formation of mesophase through the H-bonding network, while only rhodanine with wedge-shaped benzylidene does not induce the mesomorphism.

Conclusively, only **HT**₂₃ with a critical hydrophobic chain length exhibits columnar mesomorphism by supramolecular self-assembly through H-bonded interactions. Its XRD results expose that, trimerization of the molecules leading to a disc-like super-structure which displays a columnar hexagonal mesomorphism over a wide range of temperature including room temperature.

4.2.2.5 Mesomorphic behaviour of **HT**₂₇₋₃₁ (Series-5)

The self-assembling behaviour of tapered-shaped, **HT**₂₇₋₂₈ and wedge-shaped, **HT**₂₉₋₃₁ was systematically studied by using DSC, POM and XRD analytical techniques. The compound, **HT**₂₇ bearing triple octyloxy chains showed two distinct crystalline states, which clear at 100.21 °C on heating. In cooling scan, a trivial transition peak was observed at 89.69 °C with an enthalpy of -2.0 kJmol⁻¹ which could be assigned to an I-LC transition and on further cooling, the compound has crystallized. In the DSC scan of longer chain analogue, *i.e.* **HT**₂₈, two endothermic peaks corresponding to Cr-Cr transition and a small LC-I transition (100.34 °C) were observed. The mesophase was reappeared at 99.14 °C (-1.39 kJmol⁻¹) on cooling cycle and no sign of crystallization was noticed till room temperature (**Fig 4.18**).

The observed thermotropic transitions were further confirmed by polarized optical microscope and they were identified to be quite consistent with DSC results. As shown in **Fig 4.18**, both the compounds displayed birefringent pseudo focal-conic texture on slow cooling from their respective isotropic phase, which are commonly encountered textures for smectic A phases of calamitic and bent-core LC systems (Achalkumar et al. 2014; Dobbs et al. 2009; Ren et al. 2017).

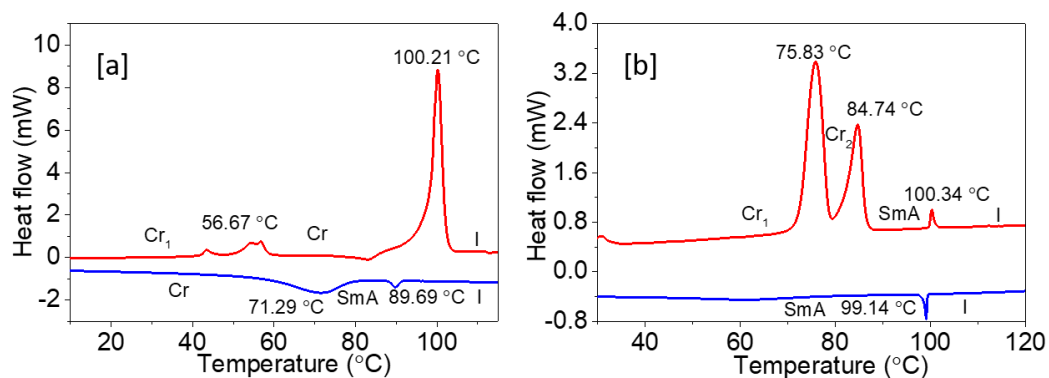


Figure 4.18 DSC thermograms of (a) **HT₂₇** and (b) **HT₂₈** recorded at a rate of 5 °C/min under a nitrogen atmosphere (red and blue traces represent heating and cooling scans, respectively)

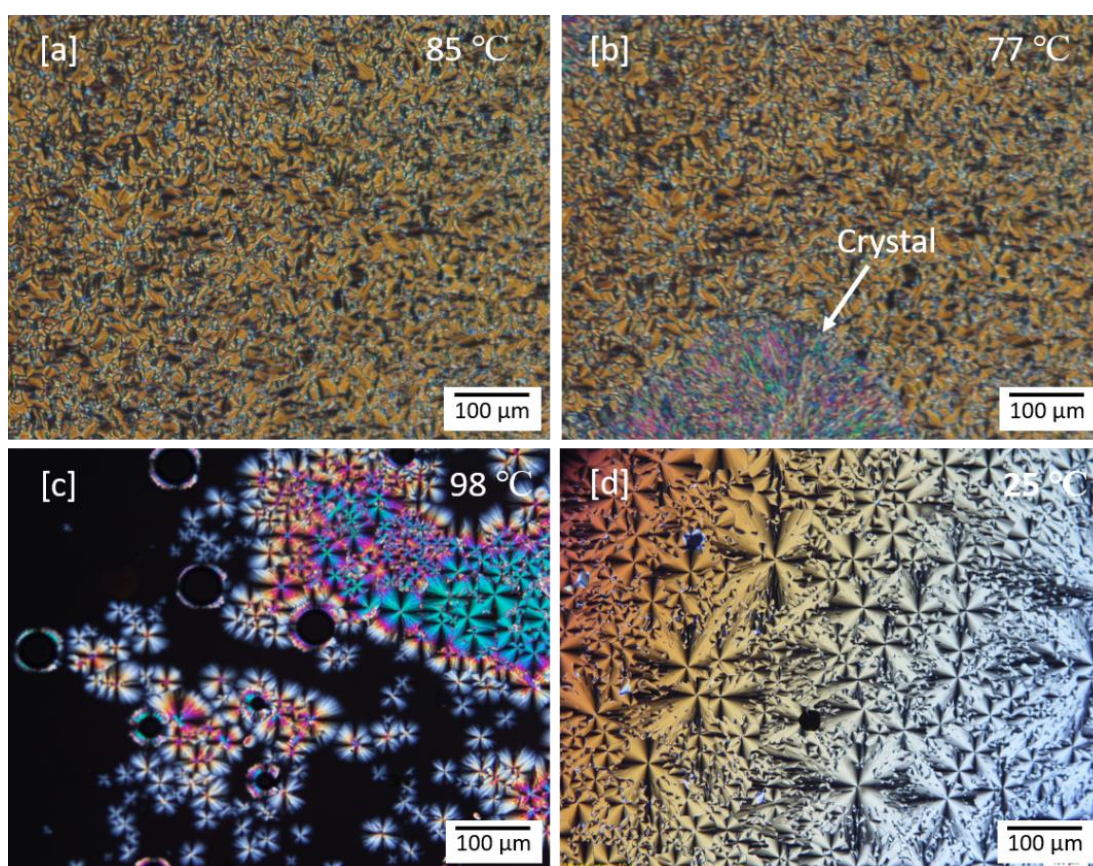


Figure 4.19 Microphotographs of **HT₂₇** captured on slow cooling at (a) 85 °C and (b) 77 °C; textures of **1 HT₂₈** obtained at (c) 98 °C and (d) 25 °C

Table 4.10. ^a Phase transitions and corresponding enthalpy changes of **HT**₂₇₋₃₁

Compd.	Phase sequence	
	Heating	Cooling
HT ₂₇	Cr ₁ 56.67 (4.97) Cr ₂ 100.21 (45.24) I	89.69 (-1.20) Sm A ^b 71.29 (-16.60) Cr
HT ₂₈	Cr ₁ 75.83 (53.90) Cr ₂ 84.74 (27.03) Sm A 100.34 (1.44) I	99.14 (-1.39) Sm A ^c
HT ₂₉	Cr ₁ 57.37 (22.78) Cr ₂ 124.25 (29.89) I	115.39 (-29.42) Cr ₂
HT ₃₀	Cr ₁ 63.22 (5.62) Cr ₂ 124.16 (32.71) I	122.75 (-3.65) Col _h ^b 112.76 (-28.28) Cr ₂
HT ₃₁	Cr ₁ 33.38 (14.84) Cr ₂ 118.42 (23.52) I	113.27 (-23.33) Cr ₂ 30.60 (-16.67) Cr ₁

^a Peak temperatures/°C (enthalpies/kJmol⁻¹) obtained by endothermic and exothermic cycles at the rate of 5 °C/min; ^b monotropic mesophase; ^c Crystallization transition was not noticed till RT; Cr, Cr₁ and Cr₂, are different crystalline states; SmA = Smectic A mesophase; Col_h = columnar hexagonal mesophase; I = isotropic liquid state

In order to get further insight into the molecular self-assembling in the smectic phase of taper-shaped amphiphilic systems, we recorded XRD spectra of **HT**₂₈ at different temperatures throughout its LC phase range. The obtained spectra are depicted in **Fig 4.20** and the relevant data are summarized in **Table 4.11**. At all the four temperatures, the XRD profile has evidently two common features: a sharp and intense peak at low angles and a diffuse broad one at wider angles. These features are typical of a layered smectic phase, a fact corroborated by POM textures. For further description, a profile at the lowest temperature, *i.e.* at T = 55 °C has been considered, shown in **Fig 4.20**, as the additional features become more clear at this temperature. Three more peaks, one at low angles, sharp albeit very weak, a diffuse one at low angles and another diffuse peak at large angles, again weak. The identification of second reflection in the lower angle is easy since its spacing is exactly half of that of the fundamental (first reflection). Thus, it is the second harmonic, which is barely seen at T = 95 °C, but picks up intensity as the temperature is lowered. The presence of another diffuse peak at the spacing ~16.5 Å is somewhat intriguing. In the light of the fact that, this value matches the longitudinal dimension of the core portion of the molecules, we

propose that, the core regions of the neighbouring molecules completely overlap and the phasmidic chains stick out as the two termini of this dimer pair (**Fig 4.21**). Thus, the thickness of this partially interdigitated layer would be the dimension of the core plus the twice the length of terminal chain. With the length of 12-carbons being ~ 14 Å, the determined dimer length of 45 Å matches with the experimentally obtained layer thickness.

Since the bifurcation between the core and the hydrocarbon chain is better defined in the phasmidic arrangement, the overlapped core region can be considered to be a sub-layer, giving rise to its own X-ray diffraction. This results in the peak at ~ 16.5 Å, which is the dimension of the core. However, unlike the layer interfaces determined by the extreme ends of the dimer, there is enough libration possible for the overlapped region of the core resulting in a spread of the diffraction pattern. The diffuse peak in higher angle region corresponding to ~ 3.42 Å, is commonly seen in columnar phases of discotic molecules. Except in systems wherein the terminal chains have different character, such as hydrocarbon/fluorocarbon or hydrocarbon/cholesteryl (Kumar et al. 2017; Mandal et al. 2014), it is not seen in smectic phases. Extending the argument made for the case of discotic systems, we propose that, peak spacing 3.42 Å arises due to the correlation between the core-parts of the neighbouring molecules. As expected, this correlation improves on lowering the temperature, and from the peak width, it is seen that, about 6 molecules are correlated. As observed commonly, increasing the layer spacing on lowering the temperature is owing to stretching of the chains (moving towards all-trans). However, the consequent negative thermal expansion (d/dT) layer spacing of ~ 0.09 Å/°C is quite large than usual smectics (Lobo et al. 2004).

Table 4.11. XRD characterization data of **HT₂₈** at different temperatures

Compound	d_{obs} [Å] at 25 °C	d_{obs} [Å] at 55 °C	d_{obs} [Å] at 75 °C	d_{obs} [Å] at 95 °C
	45.48	43.32	40.66	39.11
	24.81	21.59	20.32	19.64
HT₂₈	16.51	16.37	16.08	16.03
	4.35	4.41	4.43	4.46
	3.38	3.42		

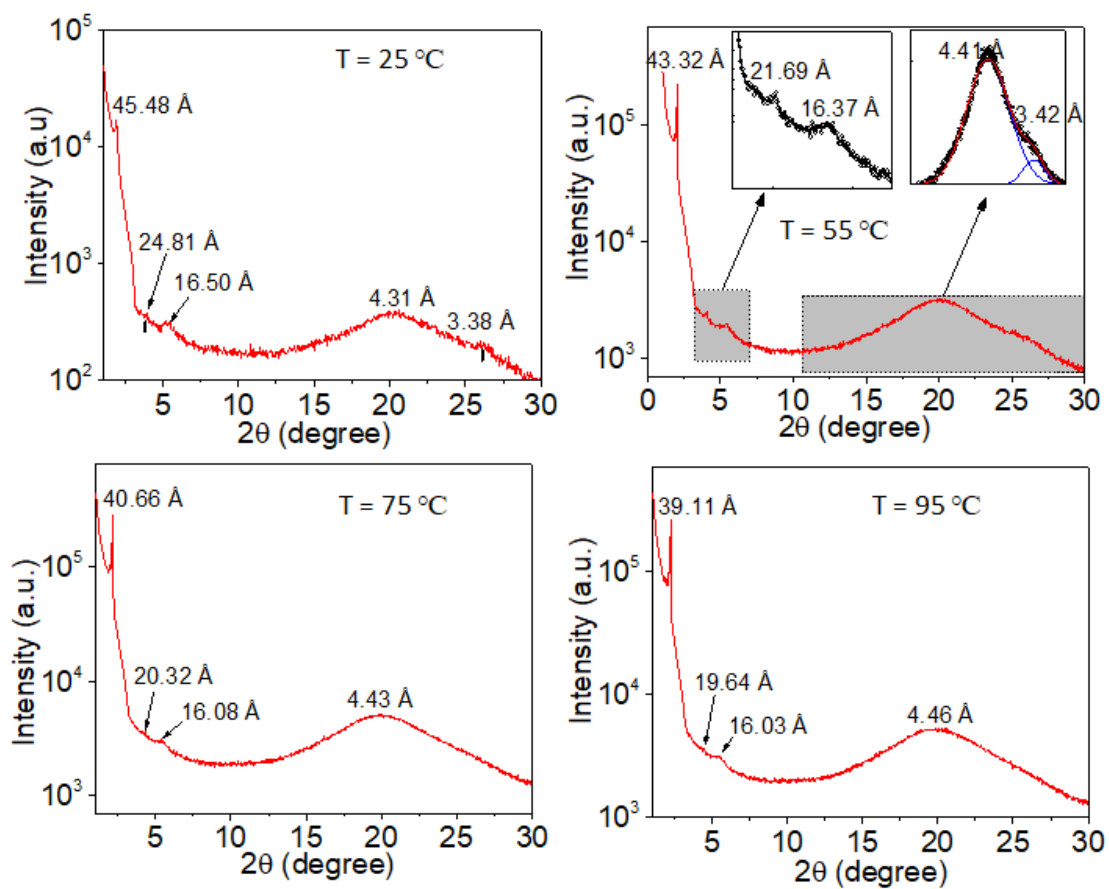


Figure 4.20 XRD patterns obtained for **HT₂₈** at various temperatures

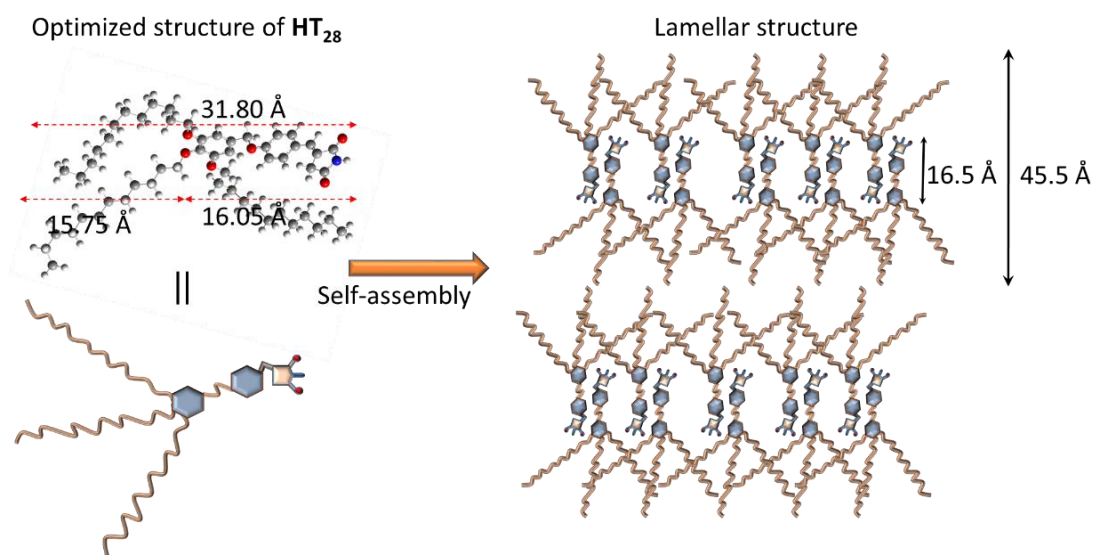


Figure 4.21 Schematic illustration of SmA mesophase structure of **HT₂₈**

On reducing the hydrophobic part in the design, wedge configured molecules were obtained (**HT**₂₉₋₃₁), wherein three alkoxy groups are attached to phenyl ring connected with polar maleimide ring. DSC traces of all the three compounds with varied aliphatic chain lengths reveal that, they exhibit polymorphic nature as a function of temperature. Among them, the midst member, *i.e.* **HT**₃₀ has shown a monotropic mesophase behaviour as apparent in its first cooling cycle of DSC scan, which was further confirmed by immediate reheating and cooling scans as shown in **Fig 4.22b**. Under POM, slow cooling from its I phase brings about a bright mosaic pattern which is a typical indication of presence of columnar organization (**Fig 4.22c-d**) (Kumar 2011).

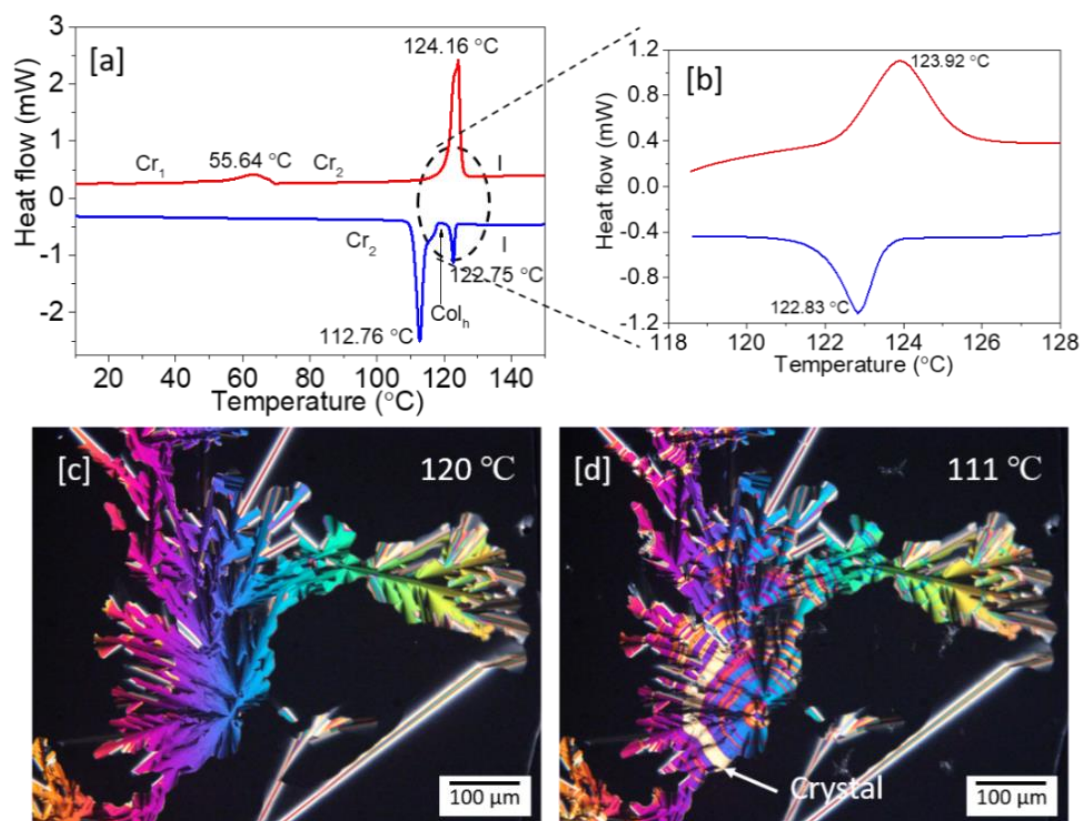


Figure 4.22 DSC traces of **HT**₃₀: (a) first heating and cooling scan and (b) second cycle; POM textures of **HT**₃₀ captured at (c) at 120 °C and (d) 111 °C

To understand the structure of columnar mesophase of **HT**₃₀, the XRD spectra within its short thermal range were carefully recorded on slow cooling from I phase as depicted in **Fig 4.23**. For instance, the spectrum obtained at 125 °C displayed three reflections at the Bragg's d-spacings 27.57, 16.01 and 13.44 Å with the reciprocal ratio

of 1: $\sqrt{3}$: 2 in the lower angle region. In addition, a broad halo appears at wide angle region ascribed to liquid-like motion of the alkyl chains. The lower angle reflection could be indexed to (10), (11), (20) planes of two-dimensional hexagonal geometry with the lattice parameter $a = 31.83 \text{ \AA}$. Further, the number of molecules (Z) occupied in each hexagonal unit cell was estimated using the XRD results, assuming the density value for these molecules is 1 g cm^{-3} (Cheng et al. 2018) (**Table 4.12**). For this calculation, a much needed parameter, *i.e.* the height or thickness of the columnar stratum is unknown. This is because of the absence of a wide angle reflection responsible for intracolumnar spacing as a consequence of the lack of long-range periodicity along the columnar axis. Nevertheless, we deduced the value of Z by using the alkyl halo (h_a), and it was found to be three. The results indicated that, each slice of the columns has composed of three molecules and this value is consistent with the calculated large lattice area, $S = 877.69 \text{ \AA}^2$ and volume, $V = 3923.29 \text{ \AA}^3$.

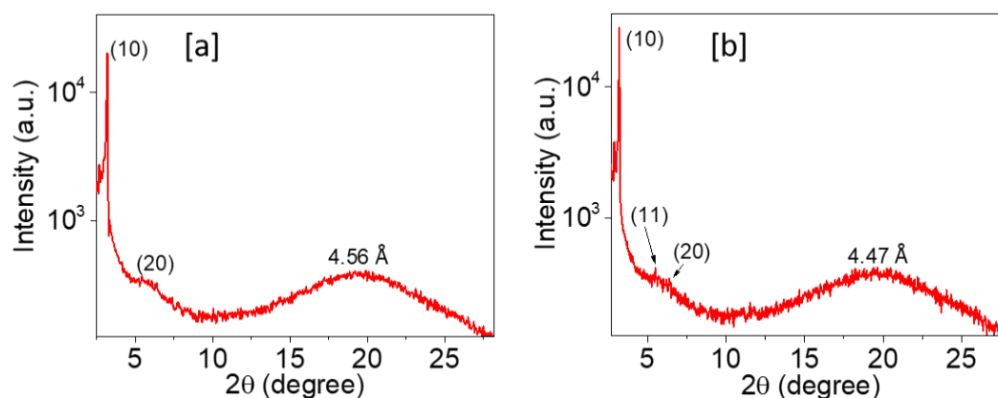


Figure 4.23 XRD patterns of **HT₃₀** at (a) 123 °C and (b) 125 °C

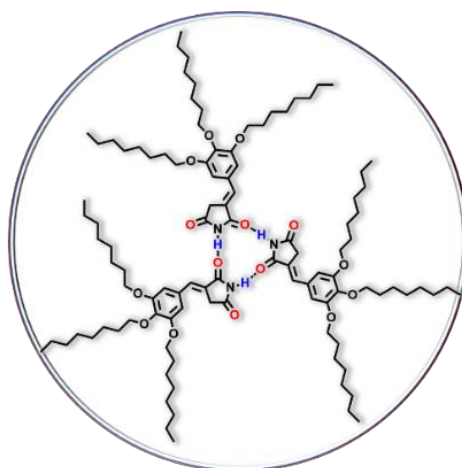


Figure 4.24 H-bond driven supramolecular disc of **HT₃₀**

As mentioned earlier, it is clear that, each columnar stratum of Col_h phase of **HT**₃₀, comprises three wedge-shaped molecules. Since tip of these molecules is bearing a polar maleimide group, capable of forming H-bonding, they can assemble comfortably to form a supramolecular disk by means of H-bonded interaction. The resulting H-bond driven macrocyclic structure is depicted in **Fig 4.24**. These superstructures form a long-range columnar assemblies in the hexagonal fashion. On the basis of XRD results, we proposed a schematic model for the self-assembly of wedge-shaped maleimide **HT**₃₀, as illustrated in **Fig 4.25**.

Table 4.12. XRD characterization data of **HT**₃₀ at different temperatures

Compd.	Phase (<i>T</i> /°C)	<i>d</i> _{obs} [Å]	<i>d</i> _{cal} [Å]	Miller Indices (<i>hk</i>)	Lattice parameter <i>a</i> [Å], Lattice area <i>S</i> [Å ²], Molecular volume <i>V</i> [Å ³]
HT ₃₀	Col _h (123)	27.61	27.61	(10)	<i>a</i> = 31.88
		13.83	15.76	(20)	<i>S</i> = 880.24
		4.56 (<i>h</i> _a)			<i>V</i> = 4013.9
					<i>Z</i> = 3.2
	Col _h (125)	27.57	26.034	(10)	<i>a</i> = 31.83
		16.01	15.91	(11)	<i>S</i> = 877.69
13.44		13.78	(20)	<i>V</i> = 3923.29	
4.47 (<i>h</i> _a)				<i>Z</i> = 3.1	

*d*_{obs}, observed spacings; *d*_{cal}, calculated spacings from the lattice parameter *a* for the hexagonal lattice; *h*_a, alkyl chains correlation peak value; *Z*, number of molecules per columnar unit

In conclusion, it was observed that, the length of hydrophobic segment has significant influence on their LC behaviour. Further, two molecules with tapered-shape have been shown to exhibit a room temperature mesophase with a notable smectic order, irrespective of length of alkyl chains. While, the only midst alkyl member of wedge-shaped derivatives demonstrated an imperative supramolecular columnar phase with hexagonal lattice geometry. From the XRD analysis, it can be clinched that totally three wedge-shaped molecules occupied in each slice of Col_h of **HT**₃₀, which may be attributed to the possible close-type intermolecular H-bonding through polar maleimide functionality.

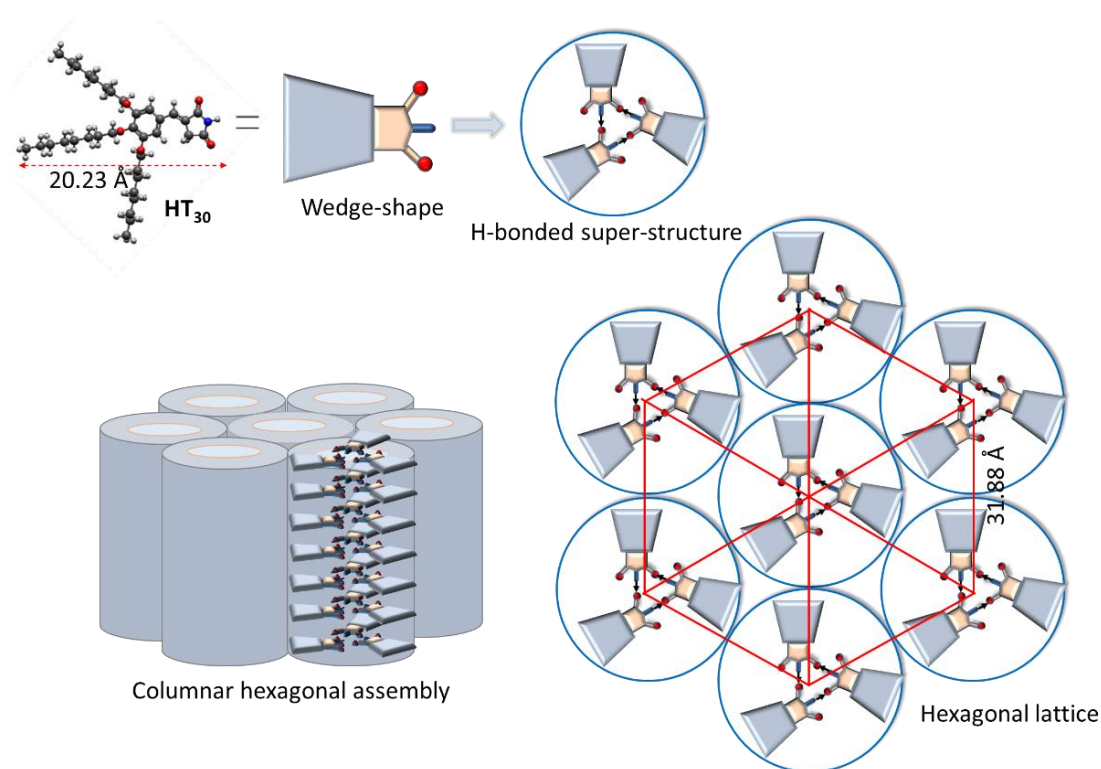


Figure 4.25. Schematic illustration of columnar hexagonal self-assembly of **HT₃₀**

4.2.2.6 Mesomorphic behaviour of HT₃₂₋₃₅ (Series-6)

The thermotropic phase behaviour and the thermodynamic features of boron complexes (**HT₃₂₋₃₅**) were studied by using POM, DSC and XRD techniques. Their preliminary studies revealed that, both hydrazones and their boron complexes displayed thermotropic mesomorphism. Their LC characterization has been described separately under two subsections.

Mesomorphism of benzylidenehydrazones (20a-d):

The DSC thermogram of first member of the series **20a** bearing four dodecyloxy peripheral chains displayed single reversible transition owing to crystal to isotropic transition without any mesomorphic behaviour. In contrast, hydrazone **20b** with an increased number of alkyl chains exhibited an enantiotropic mesophase transition as evidenced by its DSC scan (**Fig 4.26**). On heating cycle, it showed two distinct crystalline morphology and transformed into a mesophase (104.39 °C) which clears at 145.5 °C with the energy change of 1.46 kJmol⁻¹. The observed phases were certainly reappeared in the cooling scan as well. These thermotropic transitions were further

confirmed by POM; under cross polarizers, **20b** displayed a pseudo-focal conic fan-shaped texture with dark homeotropic regions and it crystallized below 92 °C as visualized in **Figs 4.26a-b** indicating the existence of optically uniaxial columnar phase (Shanker et al. 2011). The thermodynamic data are tabulated **Table 4.13**.

Table 4.13. ^a Phase temperatures (°C) and corresponding enthalpy changes (kJmol⁻¹)

Compd.	Phase sequence	
	Heating	Cooling
20a	Cr 71.03 (82.076) I	I -14.39 (-6.14) Cr
20b	Cr ₁ 94.24 (54.50) Cr ₂ 104.39 (24.55) Col _h 145.50 (1.46) I	I 141.45 (-1.29) Col _h 92.01 (-24.79) Cr ₂ 82.29 (-59.91) Cr ₁
20c	Cr 8.47 (23.67) Col _h 154.70 (2.74) I	150.44 (-2.94) Col _h 0.0 (-27.79) Cr
20d	Col _{h1} 93.59 (3.12) Col _{h2} 174.23 (13.79) I	I 171.70 (-12.26) Col _{h2} 92.25 (-2.66) Col _{h1} 0.13 (-37.40) Cr

^a Peak temperatures/°C (enthalpy/kJmol⁻¹) obtained by second heating and first cooling at the rate of 5 °C/min; Col_h = Columnar hexagonal phase; I = Isotropic liquid phase

To get further insight into the nature of columnar assembly of **20b**, its X-ray diffraction patterns were obtained at various temperatures within the mesophase thermal region and they were found to be similar as shown in **Fig 4.26d**. For instance, a pattern gained at 135 °C showed a single reflection in its lower-angle region at the *d*-spacing of 23.0 Å, which could be indexed to (10) plane of hexagonal symmetry with lattice parameter *a* = 26.55 Å. Additionally, a noticed diffused halo in the wide-angle region at the maxima of 4.55 Å and the absence of core-core reflection manifested the fluidic property of the mesophase. In fact, the occurrence of single lower angle reflection can't elucidate the hexagonal lattice unambiguously. Nevertheless, this kind of patterns are commonly observed in various discotics. Indeed, the typical birefringent textural features strappingly confirm the Col_h mesophase. Further, the hexagonal lattice area, *S* and its volume, *V* were estimated to be 611 Å² and 2779 Å³, respectively.

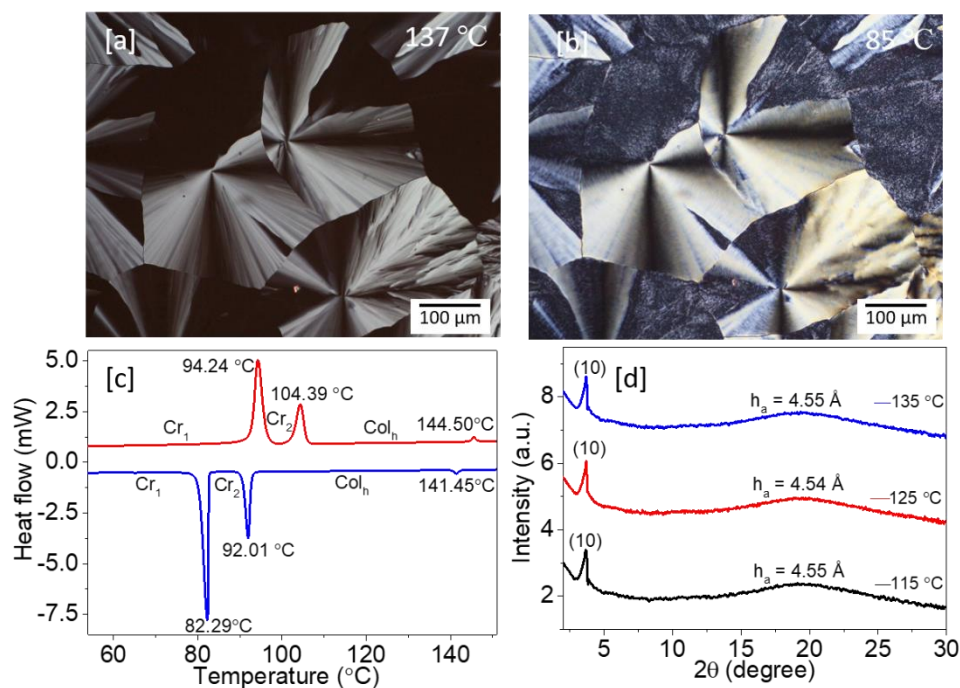


Figure 4.26. POM texture of **20b** at (a) 137 °C and (b) 85 °C; (c) DSC thermogram of **20b** (red and blue traces represent heating and cooling scan, respectively); (d) XRD pattern of **20b** at various temperature points

The hexacatenar hydrazone, **20c** was easily be sheared between the two glass slides and it looked birefringent under POM indicating that, the compound is already in LC state at RT. Seemingly, the optical transitions were well consistent with its DSC results and it also exhibits the pseudo-focal conic texture on slow cooling below its isotropic temperature 150.44 °C, confirming the columnar hexagonal mesophase (**Fig 4.27**). As noticed in case of **20b**, the XRD patterns of **20c** also showed a single reflection at lower-angle region (23.90 Å at 55 °C) with a wide-angle broad hump at 4.55 Å which is attributed to the fluidic assembly of alkyl chains as depicted in **Fig 4.28a**. The first intense peak can be indexed into a hexagonal lattice with $a = 27.59$ Å and the calculated mesophase parameters are summarized in **Table 4.14**. The compound **20d** behaves thermotropically different from **20c**, although they are regioisomeric derivatives. **20d** has two distinct mesophases with the isotropic transition at 174.23 °C, which is the highest clearing temperature among the four investigated hydrazones and it shows crystallization at 0.13 °C on cooling below lower temperature phase (**Figure 4.28b**). As can be seen in **Figs 4.27e-f**, the material displayed fan type of texture below I phase, which on further cooling slight increase in brightness of the

birefringent domains was realized. To identify the symmetry of the columnar phase, XRD data were collected at the different temperatures in both higher and lower temperature mesophase ranges on cooling from its liquid phase. The patterns obtained in both the mesophase regions were apparently similar and their lower angle reflections were indexed to (10) plane of the hexagonal lattice (**Fig 4.28b**). To differentiate between these two mesophases, lower temperature mesophase has been named as Col_{h1} and higher temperature mesophase has been termed as Col_{h2} , since there is a clear thermodynamic transition with considerable enthalpy change (3.12 kJmol^{-1}) associated with it. This kind of transition was frequently observed in compounds with non-discoidal molecular geometry.

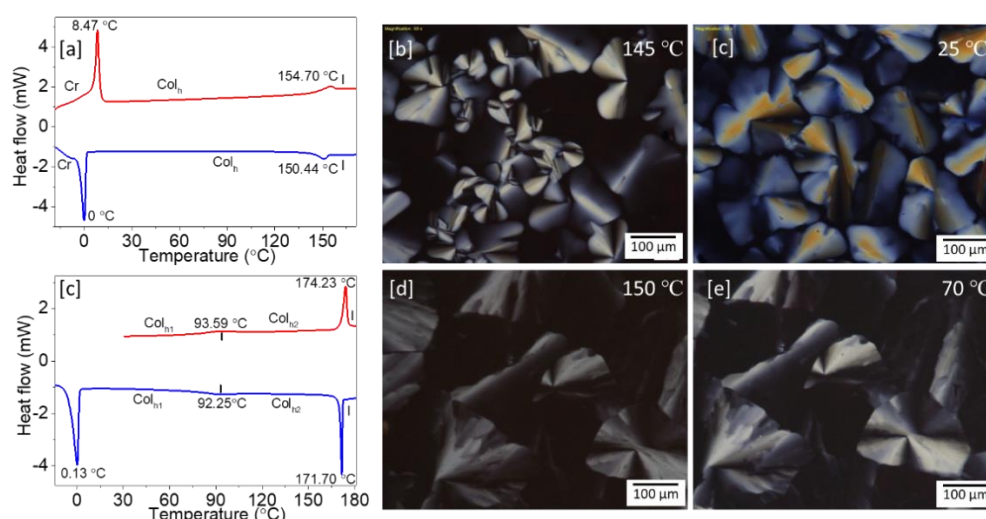


Figure 4.27 (a) DSC thermogram of **20c** (red and blue traces represent heating and cooling scan, respectively); POM texture of **20c** captured at (b) 145 °C and (c) 25 °C; (d) DSC thermogram of **20d** (red and blue traces represent heating and cooling scan, respectively); POM texture of **20d** at (e) 150 °C and (f) 70 °C

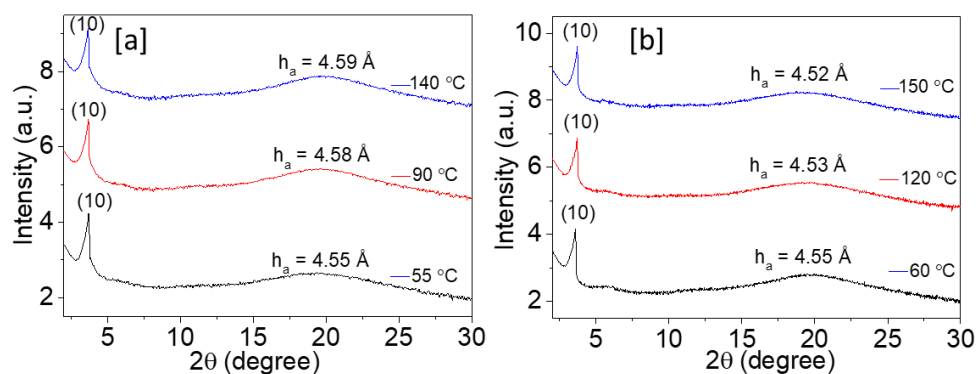


Figure 4.28 (a) XRD pattern obtained for Col_h phase of **20c** and (b) Col_{h1} and Col_{h2} phases of **20d** at various temperatures

To understand the possible molecular packing in these hydrazone derivatives, the number of molecules accompanied per each columnar stratum Z was calculated, assuming the density $\rho = 1 \text{ g cm}^{-3}$. Subsequently, the Z was found to be 1.5, 1.35 and 1.4 for **20b**, **20c** and **20d**, respectively. The observed non-integral values suggest that, there may be folding and/or intercalation of peripheral tails in the columnar cross-section. It is reported that, this kind of benzylidenehydrazones stabilize the columnar phase by the formation of helical superstructures wherein the H-bonded chain of $\text{N-H}\cdots\text{O}=\text{C}$ adopts a helical conformation. Because of this reason, they embrace more than one molecules per columnar unit in order to maintain the average circular cross-section for organizing in a hexagonal lattice (Shanker et al. 2011).

Table 4.14. XRD characterization data of **20b-d**

Compd.	Phase ($T/^\circ\text{C}$)	d_{obs} (\AA)	d_{cal} (\AA)	Miller Indices (hk)	Lattice parameter a (\AA), Lattice area S (\AA^2), Molecular volume V (\AA^3)
20b	$\text{Col}_h(135)$	23.0 4.55 (h_a)	23.0	(10)	$a = 26.55$ $S = 610.83$ $V = 2779.3$ $Z = 1.46$
20c	$\text{Col}_h(55)$	23.90 4.55 (h_a)	23.90	(10)	$a = 27.59$ $S = 659.6$ $V = 3001.1$ $Z = 1.35$
20d	$\text{Col}_{h1}(60)$	24.67 4.43(h_a)	24.67	(10)	$a = 28.48$ $S = 702.76$ $V = 3113.23$ $Z = 1.40$
20d	$\text{Col}_{h2}(150)$	23.82 4.56(h_a)	23.82	(10)	$a = 27.50$ $S = 655.16$ $V = 2992.0$ $Z = 1.35$

d_{obs} , experimental lattice spacing; d_{cal} , calculated from the lattice parameter, a for the hexagonal lattice; h_a , alkyl chains correlation peak value; h_c , core-core spacing; Z , number of molecules per columnar slice; S , lattice area; V , molecular volume

Mesomorphism of boron difluoride complexes (HT₃₂₋₃₅):

The thermotropic phase behaviour of all the boron difluoride complexes was also investigated systematically. Evidently, upon coordination with BF₂ the mesomorphism of hydrazones **20a-d** was completely altered. The thermal phase sequence and corresponding thermodynamic parameters of **HT₃₂₋₃₅** are tabulated in **Table 4.15**. The first member of the series bearing four alkyl tails was crystalline in nature, it melted at the same temperature (~71.0 °C) as its ligand **20a**. However, the enthalpy change for the melting transition of **HT₃₂** was found to be much higher than **20a** indicating the greater thermal stability of **HT₃₂** complex in the solid state. Unlike **20b**, its boron complex **HT₃₃** was characterized to be non-mesogenic, instead it showed three distinct crystalline morphology as evidenced by its DSC thermogram. The non-mesomorphism of **HT₃₃** may be due to the lack of space occupation by only five alkyl chains around the central aromatic segment. While its ligand molecules (**20b**) segregated into columnar phase because of co-operative intermolecular hydrogen bonding as discussed earlier.

Table 4.15. ^aPhase temperatures (°C) and the corresponding energy changes (kJmol⁻¹)

Compd.	Phase sequence	
	Heating	Cooling
HT₃₂	Cr 71.25 (71.91) I	I -14.39 (-54.36) Cr
HT₃₃	Cr ₁ 44.19 (14.31) Cr ₂ 66.83 (10.57) Cr ₃ 96.98 (50.45) I	I 86.50 (-52.19) Cr ₃ 61.99 (-9.14) Cr ₂ 41.48 (-12.44) Cr ₁
HT₃₄	Cr ₁ 10.48 (7.39) Cr ₂ 31.03 (23.92) Col _h 35.01 (0.62) I	I 32.08 (-1.09) Col _h 2.20 (-22.10) Cr
HT₃₅	Col _h 66.19 (23.83) Col _r 96.65 (15.82) I	I 87.78 (-15.97) Col _r 61.11 (-23.61) Col _h

^a Peak temperatures/°C (enthalpy/kJmol⁻¹) obtained by second heating and first cooling at the rate of 5 °C/min; Col_r = Columnar rectangular phase; Col_h = Columnar hexagonal phase; I = Isotropic liquid phase

The two regioisomers, **HT**₃₄ and **HT**₃₅ bearing six peripheral chains exhibit entirely different thermotropic phase transitions from each other. The isomer **HT**₃₄ having dodecyloxy chains at 2nd, 3rd and 4th positions showed a trivial endothermic transition at 35.01 °C ($\Delta H = 0.62 \text{ kJmol}^{-1}$) which could be assigned to an LC to I transformation. On cooling scan, the transition occurred at 32.08 °C ($\Delta H = -1.09 \text{ kJmol}^{-1}$) and the phase gets crystallized at 2.20 °C as shown in **Fig 4.29a**. The perceived mosaic pattern was the typical indication of presence of columnar mesomorphism (**Figs 4.29b-c**).

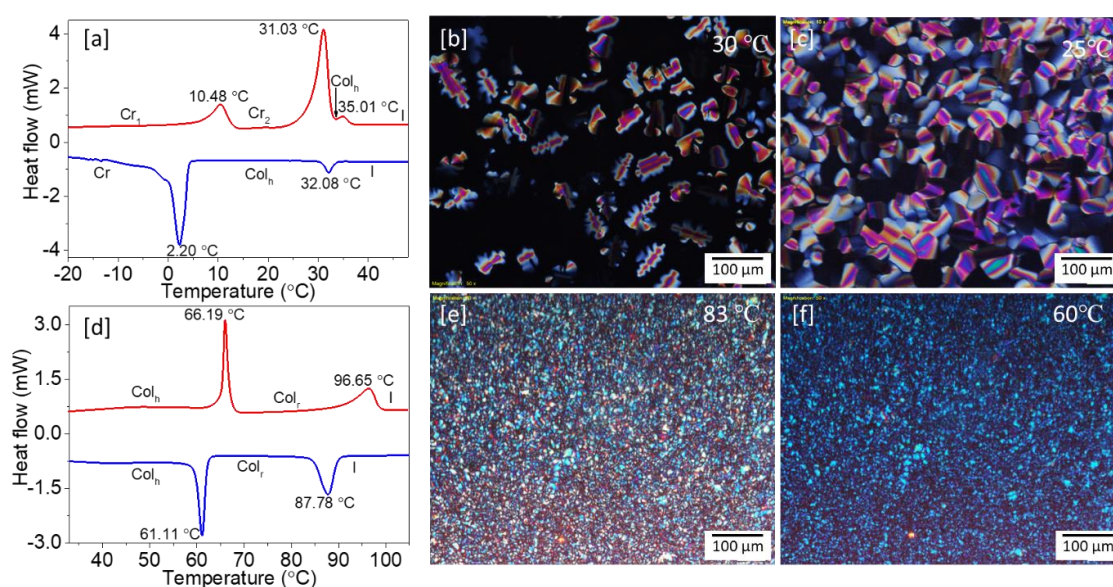


Figure 4.29 (a) DSC thermogram of **HT**₃₄ (red and blue traces represent heating and cooling scan, respectively); POM texture of **HT**₃₄ captured at (b) 30 °C and (c) 25 °C; (d) DSC thermogram of **HT**₃₅ (red and blue traces represent heating and cooling scan, respectively); POM texture of **HT**₃₅ at (e) 83 °C and (f) 60 °C

Further, XRD pattern of **HT**₃₄ confirms the hexagonal lattice structure with the lattice parameter $a = 28.39 \text{ \AA}$ (**Fig 4.30a**). Whereas, its isomeric derivative **HT**₃₅ having dodecyloxy chains at 3rd, 4th and 5th positions exhibited two distinct enantiotropic mesophases as demonstrated in DSC trace (**Fig 4.29d**). It displayed two reversible transitions with slightly larger enthalpy values ($\Delta H = 24 \text{ kJmol}^{-1}$ for LC-LC and $\Delta H = 16 \text{ kJmol}^{-1}$ for LC-I). The observed ΔH is much higher than that of its isomer **HT**₃₄, this could be due to the compact arrangement of **HT**₃₅ in the mesophase. These results reveal that, changing the position of the peripheral chains in the non-discoidal molecules significantly stabilizes the mesophase. The lower temperature phase of **HT**₃₅

was assigned to Col_h mesophase (**Fig 4.30b**). A number of XRD reflections in the lower-angle region at higher temperature mesophase have been indexed to a centre rectangular columnar geometry with space group symmetry of $C2mm$ as the peak indexation follows the extinction rule $h+k = \text{even number}$ (**Fig 4.30c**). The unit cell parameters calculated from the diffraction pattern are $a = 30.34 \text{ \AA}$ and $b = 62.38 \text{ \AA}$. This unusual transition from hexagonal to rectangular columnar results in doubling of the lattice volume and hence the number of constituent molecules also doubles in each unit cell (**Table 4.16**). This kind of hexagonal to rectangular phase transition was previously observed in case of triphenylene derivatives (Levelut 1983). Based on the XRD results, a molecular model was proposed to demonstrate the self-assembly of **HT35** molecules as illustrated in **Fig 3.31**.

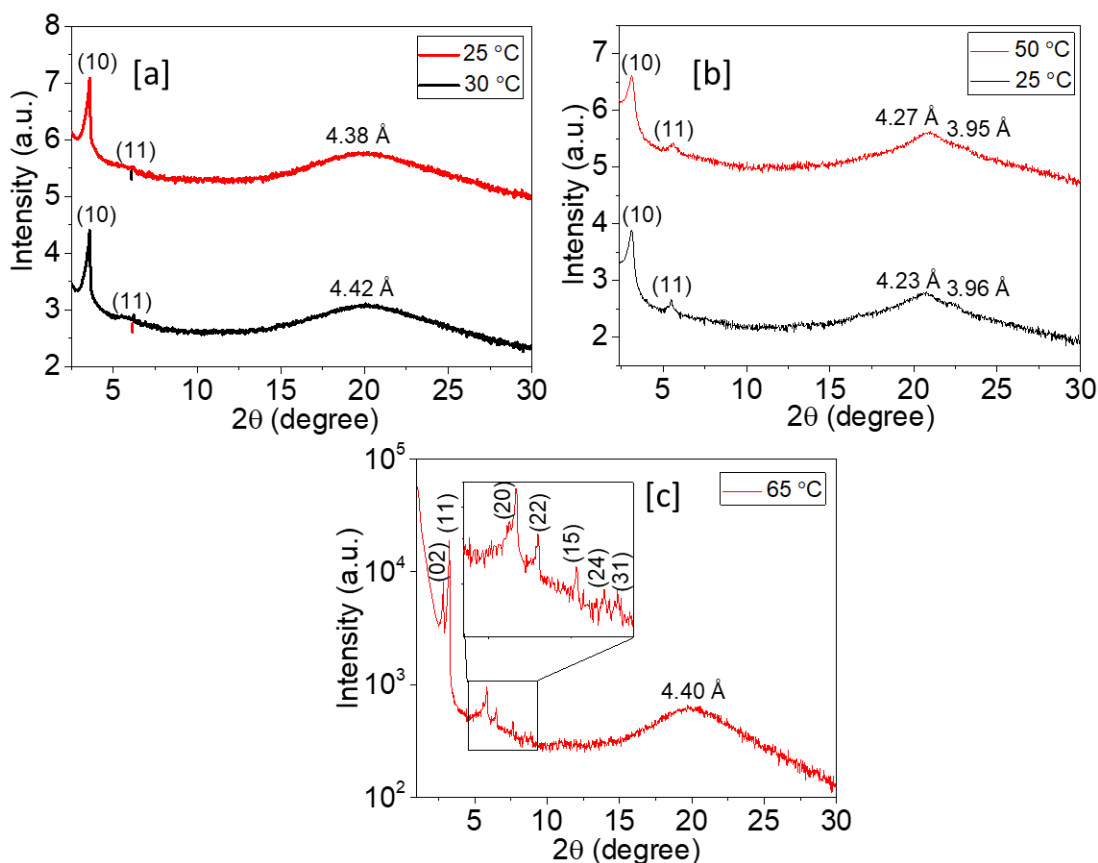


Figure 4.30 XRD pattern obtained for (a) Col_h phase of **HT34**; XRD traces recorded within (b) lower and (c) high-temperature mesophase ranges of **HT35**

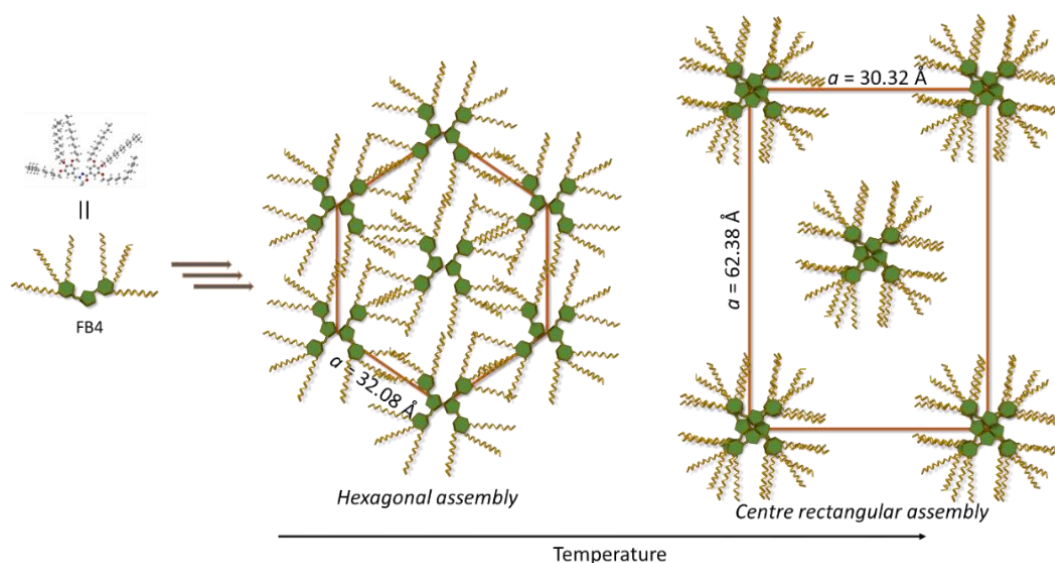


Figure 4.31 Schematic illustration of phase transition of **HT₃₅**

Table 4.16 XRD characterization data of **HT₃₂₋₃₅** at different temperatures

Compounds	Phase ($T/^\circ\text{C}$)	d_{obs} (\AA)	d_{cal} (\AA)	Miller Indices (hk)	Lattice parameter a (\AA), Lattice area S (\AA^2), Molecular volume V (\AA^3)
HT₃₄	Col _h (27)	24.59	24.59	(10)	$a = 28.39$
		14.26	14.19	(11)	$S = 698.2$
		4.42 (h_a)			$V = 3086.1$
					$Z = 1.34$
HT₃₅	Col _h (25)	28.24	28.24	(10)	$a = 32.08$
		16.04	16.30	(11)	$S = 920.0$
		4.23 (h_a)			$V = 3646.7$
		3.96 (h_c)			$Z = 1.73$
	Col _r (65)	31.19	31.19	(02)	$a = 30.32$
		27.27	27.27	(11)	$b = 62.38$
		15.15	15.16	(20)	$S = 1891.7$
		13.61	13.63	(22)	$V = 8322.0$
					$Z = 3.60$
		11.56	11.53	(15)	
		10.42	10.87	(24)	
		9.95	9.97	(31)	
		4.40 (h_a)			

d_{obs} , d_{cal} , are observed and calculated values of d spacings. Lattice parameter, a for the hexagonal lattice; h_a , alkyl chains correlation peak value; h_c , core-core spacing; Z , number of molecules per unit cell; S , lattice area; V , molecular volume

To summarize, a novel series of organoboron complexes (**HT**₃₂₋₃₅) featuring dyad structural motif with a critical chain length was subjected to in-depth liquid crystalline studies. Interestingly, the key-precursors benzylidenehydrazones (**20a-d**) exhibited columnar mesophase with the hexagonal structure mainly by means of cooperative intermolecular hydrogen bonding, at ambient conditions. Contrary, their corresponding BF₂ complexes showed different thermotropic phase behaviour. The mesomorphic properties of these hemi-discoidal boron complexes are greatly dependent on number and position of fluidic chains around the aromatic-core. Consequently, the isomeric complexes **HT**₃₄ and **HT**₃₅ displayed dissimilar thermotropic phase behaviour and showed distinct columnar mesophase at different temperature ranges.

4.3 PHOTOPHYSICAL STUDIES

Optical properties of new **HT**₁₋₃₅ possessing donor-accepter configuration in their structural backbone were studied by examining their light absorption and emission ability in solution as well as solid states. Also, some selected LC materials have been subjected to solvatochromic studies.

4.3.1 Experimental methods

The UV-visible absorption spectra of liquid crystalline materials were recorded at room temperature using SPECORD S 600 spectrophotometer and their fluorescence spectra were acquired on a Perkin Elmer LS55 Fluorescence spectrophotometer. Further, fluorescence quantum yields were determined by relative method using quinine sulphate monohydrate as a reference ($\Phi_F = 0.54$ in 0.1 M H₂SO₄) and in some cases PL quantum efficiency were estimated using an integrated sphere set-up EDINBURGH (UK) and FLS 980 TCSPC instrument. Furthermore, fluorescence life time was estimated by employing the Time Correlated Single Photon Counting (TCSPC) technique using a nano-LED with a spectral width of 1.2 nm as an excitation source and their decay profiles were best fitted using DAS6 software.

All the solvents used for the optical characterisations were of AR grade and they were used after drying by standard methods. The aggregated state optical behaviour was accomplished by recording absorption and emission spectra for spin coated thin films on sigma make quartz plates.

4.3.2 Results and discussion

In this section, a detailed discussion on photophysical data of **HT**₁₋₃₅ has been given series-wise.

4.3.2.1 Optical properties of **HT**₁₋₄ (Series-1)

Both UV-visible absorption and emission spectra were recorded for **HT**₁₋₄ solutions in DCM ($c = 2 \times 10^{-5}$ M) and the results are summarised in **Table 4.17**. Structurally, all the mesogenic materials differ only in the length of the alkyl chains, which has minimum effect on their energy of absorption and emission. Consequently, all these D-A-D type materials exhibit analogous absorption and emission bands. They display one absorption maximum (λ_{abs}) in the range of 381-383 nm, attributed to $n-\pi^*$ transition and the two shoulder bands (231-236 and 267-267 nm) due to $\pi-\pi^*$ transition (**Fig 4.32a**). Their emission spectra were recorded by exciting at their respective absorption maxima (λ_{abs}).

All members of the series displayed emission maximum (λ_{em}) at around 454 nm as shown in **Fig 4.32b**, with the Stoke shift of about 71 nm. The optical band gaps ($E_{\text{g,op}}$) were calculated by using the equation, $E_{\text{g,op}} = 1242/\lambda_{\text{onset,abs}}$ eV, where $\lambda_{\text{onset,abs}}$ are onset wavelength of their respective absorption spectrum and found to be in the range of 2.82-2.87 eV. The same solution samples in the quartz containers were kept under the illumination of 365 nm light in a UV chamber and the emission was photographed. A deep bluish green emission was observed and their corresponding photos are shown in **Fig 4.32d**. The fluorescence lifetimes of **HT**₁₋₄ at 2×10^{-5} M concentration in DCM were measured using time-correlated single photon counting technique and the observed decay profiles are shown in **Fig 4.32c**. Fluorescence lifetimes (τ) of the excited species formed were measured by monitoring at their emission maxima. The decays fitted tri-exponentially with three excited species for all the solution samples in the range of 0.1-0.13, 0.85-0.92 and 2.56-3.12 ns, respectively. The fluorescence quantum efficiency values of these materials were estimated by the relative method. Their quantum yields were calculated with respect to quinine sulfate solution (0.1 M H₂SO₄) (Brouwer 2011; Crosby and Demas 1971; Pal et al. 2017; Yvon 2012). The quantum efficiency of the compounds was found to be in the range of 0.19-0.22.

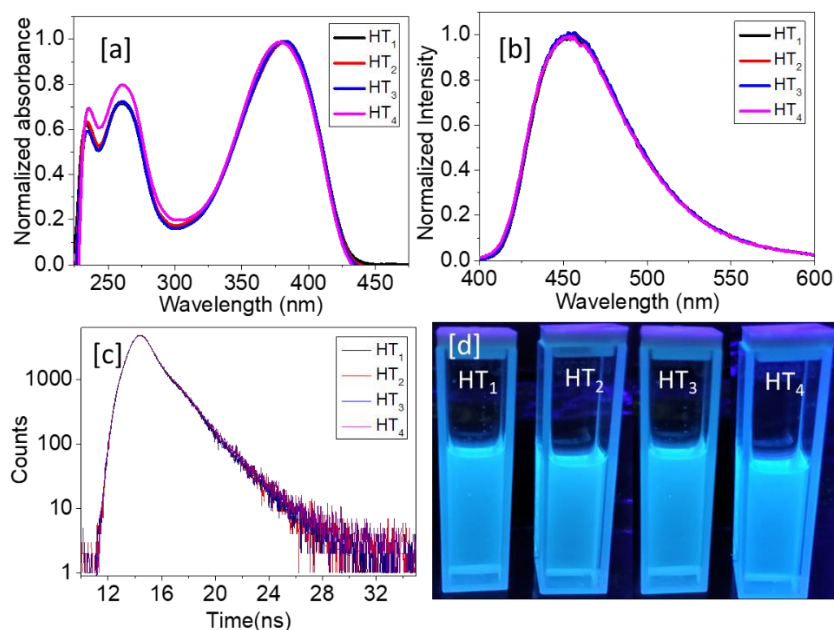


Figure 4.32 (a) UV-visible absorption spectra of **HT**₁₋₄; (b) Fluorescence spectra (excited at their respective λ_{abs}); (c) Time-resolved fluorescence decay profile and (d) the emission hue for sample solutions under 365 nm irradiation.

In order to examine the photophysical properties of the new LC materials in solvents with different polarity, absorption and emission behaviour for a representative compound, **HT**₁ in various solvents with different polarity were examined. The resulted spectra are depicted in **Fig 4.33** and their corresponding data are collected in **Table 4.18**. The dilute solutions of **HT**₁ have not shown any significant changes with respect to solvent polarity in their absorption as well as emission behaviours. The results showcase that, both ground and excited states of it are nearly non-polar in nature.

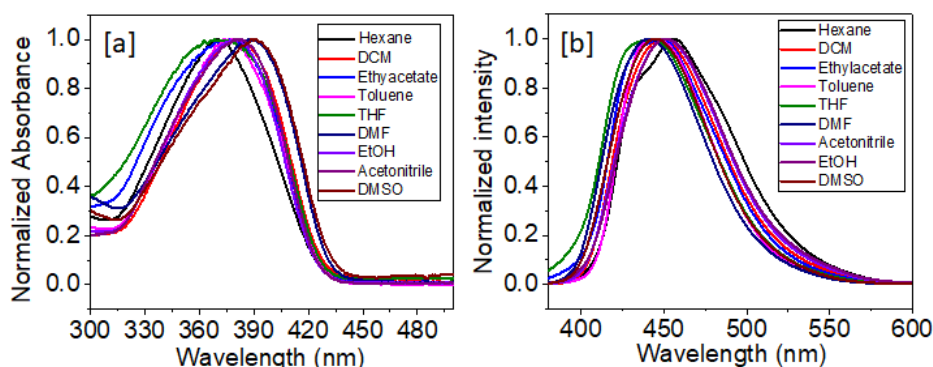


Figure 4.33 (a) Absorbance and (b) emission spectra of **HT**₁ in various solvents

Further, in order to study photophysical properties of new LC materials in the solid state, good quality thin films of the samples were obtained on quartz plates from

their DCM solutions, following spin coating technique. Their emission spectra were obtained by exciting at their λ_{abs} , obtained from their corresponding solution states (**Fig 4.34a**). The samples displayed the emission band maxima in the range of 478-486 nm, with the bathochromic shift of ~ 25 nm when compared to their respective maxima in solution state. This is attributed to their molecular aggregations in the film state. On irradiation with 365 nm UV light, these LC materials in bulk, as well as thin films, emit visually perceivable bright bluish green colour, as seen in **Fig 4.34b-c**.

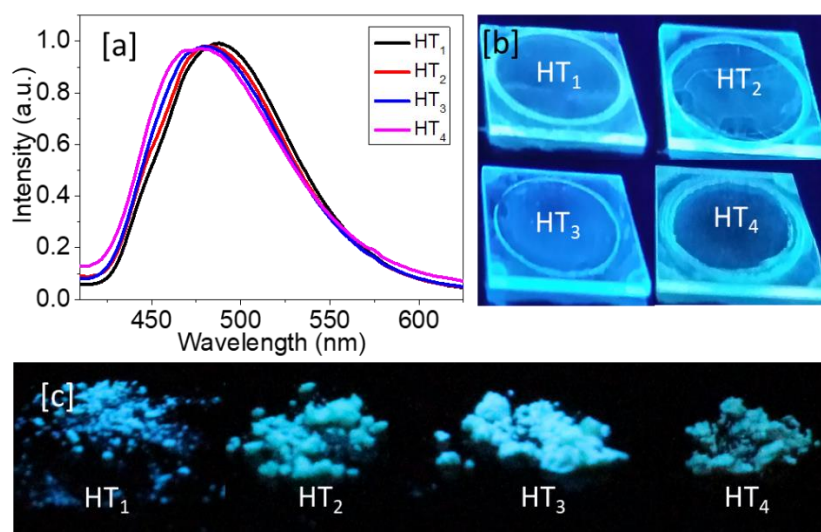


Figure 4.34 (a) Fluorescence spectra of spin-coated thin films of samples; (b) the emission hue of same thin films under 365 nm UV irradiation and (c) powder samples

4.3.2.2 Optical properties of HT₈₋₁₀ (Series-2)

The photophysical properties of new DLCs, **HT₈₋₁₀** were studied by recording their UV-visible absorption and photoluminescence spectra in solution as well as in their LC states. The spectra were acquired in their DCM solution at the concentration of $2 \times 10^{-5} \text{ molL}^{-1}$ and the obtained spectra are depicted in **Fig 4.35**. Since all the members of the series are structurally discrete with regard to length of the alkyl substitutions only, there exists minimum effect on their energy of absorption and emission. Thus, all compounds showed a major peak and a shoulder band having absorbance in the region ~ 352 nm and ~ 261 nm, respectively (**Fig 4.35a**) and they exhibit emission in the pure blue region ~ 425 nm with the similar Stokes shift values (**Fig 4.35b**). The optical band gaps were calculated using absorption onset and found to be ~ 3.0 eV. The fluorescence quantum yield (Φ_{F}) was estimated by relative method using quinine sulphate standard ($\Phi_{\text{F}} = 0.54$) (Diaz et al. 2017). These LC materials

showed relatively good quantum efficiency in the range of 0.52-0.56. The fluorescence life times of solution samples at $c = 2 \times 10^{-5} \text{ molL}^{-1}$ for all the compounds were determined using single photon counting technique by exciting them using a 350 nm pulsed NanoLED as source of excitation and probe to 425 nm (**Fig 4.35c**). The resulted fluorescence kinetic traces were fitted to bi-exponential decay values and they were found to be in the range of 1.30-1.40 ns and 2.17-2.38 ns. **Fig 4.35d** shows deep blue emission hue of the solutions, when illuminated under the light of 365 nm.

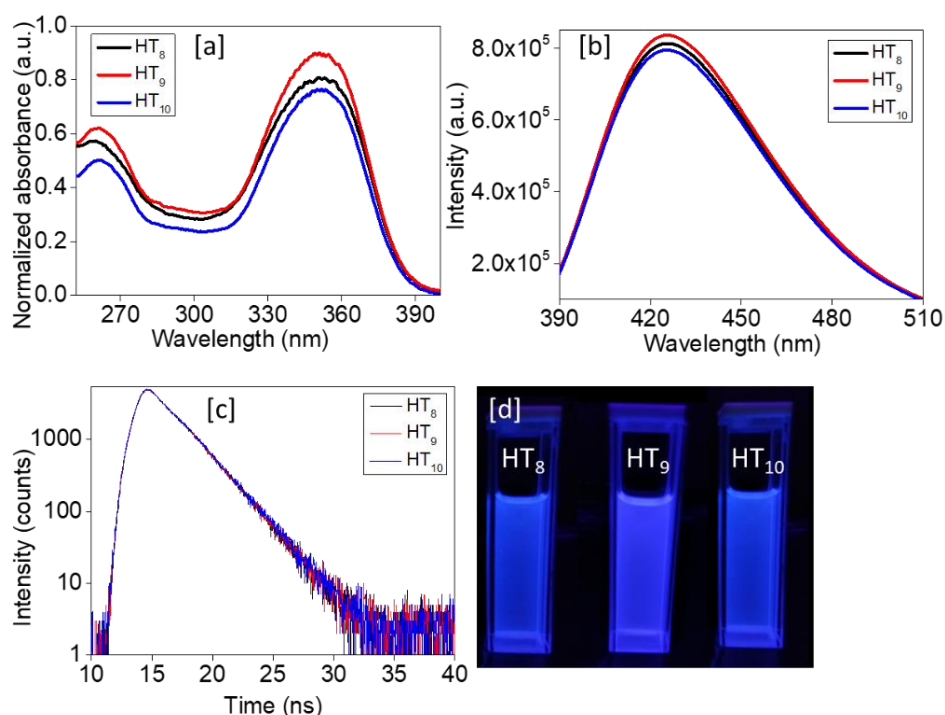


Figure 4.35 (a) Absorption spectra in DCM solution of concentration molL^{-1} (b) Emission spectra of same solution excited at their respective λ_{abs} (c) Logarithmic time-resolved fluorescence decay profiles of **HT₈₋₁₀** mesogens (d) Emission hue of solutions under 365 nm

To understand the nature of excited state of these DLCs, the photophysical behaviour of a representative compound, *i.e.* **HT₈** was investigated in various solvents having different Reichardt polarity indices ($E_{\text{T}}(30)$) (Reichardt 1994). The resulted spectra are shown in **Fig 4.36a-b** and the relevant data are summarized in **Table 4.18**. The lack of solvent dependent absorption property of this material clearly indicated its non-polar ground state. This result signifies the smaller ground state dipole moment, suggesting a strong ICT transition. In contrast, a remarkable solvatochromic fluorescence was noticed on varying the solvent polarity. It showed red-shift of

emission maxima with broadening of emission band upon increasing the solvent polarity from non-polar hexane to highly polar DMSO (386 nm in hexane, 454 nm in DMSO). The fluorescence shift towards longer wavelength in polar solvents is attributed to the emission from solvent relaxed excited state. This feature may be due to the photo induced ICT from trialkoxyphenylene donor to cyanopyridine acceptor in the excited state. Obviously, the observed ICT dominated optoelectronic results are in well corroborated with quantum chemical simulation, as it demonstrates the clear distribution of HOMO and LUMO in the star-shaped electronic structure. Also, this has been confirmed by smaller ground state dipole moment (2.28 D).

Solvatochromism of excited state was further examined by using Lippert-Mataga and Stokes shift *verses* Reichardt-Dimorth's $E_T(30)$ correlations (**Fig 4.36c-d**). In both cases, these LC material reveals the progressive linear relationship with marginal variation in stokes shift, which implies presence of single excited state. The resulted positive slope of plots and larger excited state dipole moment when compared to ground state also confirmed the more pronounced ICT for these DLCs in the excited state.

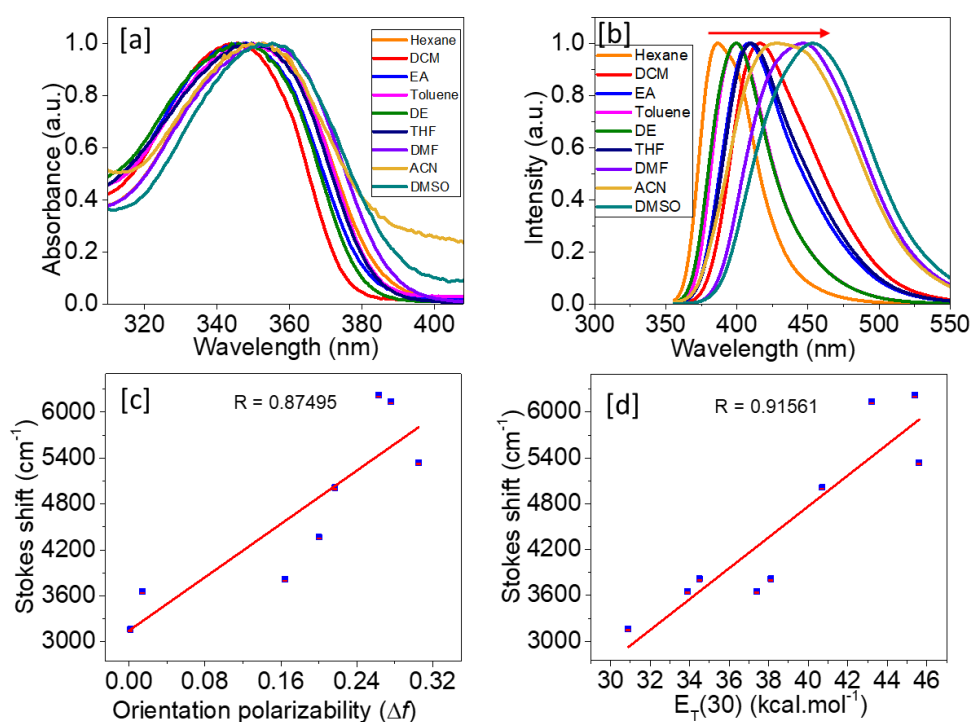


Figure 4.36 (a) Absorption and (b) Emission spectra of **HT8** ($c = 2 \times 10^{-5} \text{ molL}^{-1}$) in different solvents; (c) Lippert-Mataga plot and (d) Stokes shift *vs* $E_T(30)$ of **HT8** (EA = Ethyl acetate, DE = Diethyl ether)

In order to study optophysical characteristics of new materials in LC state, their thin films of good quality were prepared using spin coating technique and their emission spectra were recorded. **Fig 4.37a** depicts the emission spectra of spin coated thin films of **HT₈₋₁₀**; the compounds displayed emission maxima of 448, 441 and 440 nm, respectively with the bathochromic shift of 15-20 nm, when compared to their emission maxima obtained in solution state. Surprisingly, fluorescence intensity of thin films were found to be 30 % higher than that of solutions. This may be generally due to aggregation of the molecules in the slipped-stack form called ‘J-type aggregation’ or molecular interactions in the solid state which induces the emission enhancement with the bathochromic shift (Würthner et al. 2011). Since all the compounds are proved to exhibit columnar hexagonal mesomorphism at ambient conditions, the possibility of J-type aggregation is unlikely. Therefore, the observed red-shift with increased fluorescence intensity may be attributed to the interactions of in-plane dipoles, which orient the transition dipole moments of stacking molecules so as to maintain them not being parallel (H-type aggregation) (Achalkumar et al. 2012; Setia and Pal 2016). Consequently, these new discotics are fugitive from notorious aggregation caused quenching (ACQ), which is detrimental for the fabrication OLEDs (Yuan et al. 2013; Zhao 2016).

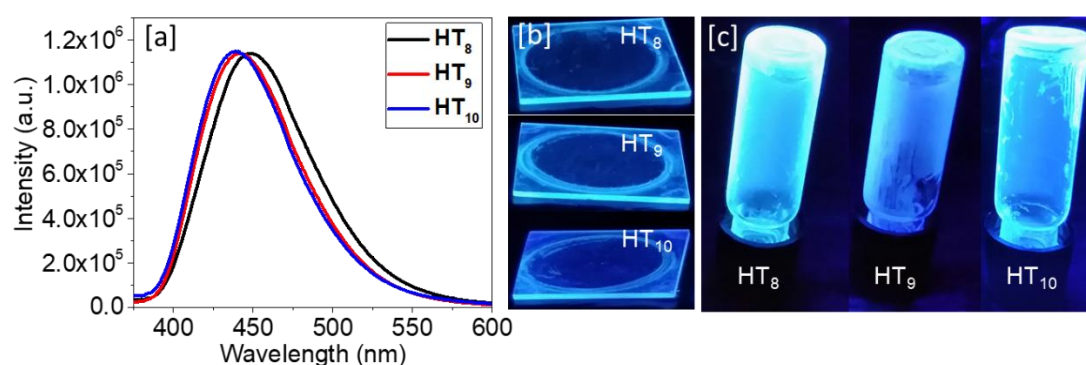


Figure 4.37 (a) Emission spectra of spin-coated thin films (excited at their solution λ_{abs}); (b) emission hue of the same thin films and (c) LCs in bulk under 365 nm

4.3.2.3 Optical properties of **HT₁₁₋₂₀** (Series-3)

Phenanthrene-cyanopyridone hybrid molecules (HT₁₁₋₁₃):

The optical behaviour of **HT₁₁₋₁₃** was examined by recording their electronic absorption and emission spectra. The spectra were run in dichloromethane at $c = 2 \times 10^{-5}$ M. structurally, all members of the series differ only in the length of saturated alkyl

chains which usually causes a negligible effect on their optoelectronic properties. Consequently, all the compounds displayed similar characteristic absorption and emission spectra. They showed three distinct absorption maxima, *viz.* a strong band at ~258 nm, a weak peak at ~300 nm and a prominent maxima centred at ~395 nm as shown in **Fig 4.38**. The first two bands arise due to $\pi-\pi^*$ transitions and the longer wavelength absorption band ascribes to intramolecular charge transport from dialkoxyphenylene and trialkoxybenzene donors to cyanopyridone acceptor. On exciting at their respective longest absorption wavelengths, they displayed a single emission band at ~502 nm with relatively higher Stokes shift values in the range of 5396-5420 cm^{-1} . The observed large Stokes shift signifies the effective ICT property in these π -conjugated structures and it is a most advantageous feature for a desired emitter in the fabrication of OLEDs. The optical band gaps were found to be in the range of 2.72-2.75 eV. For an ideal fluorophore, fluorescence quantum yield (Φ_F) is one of the deciding factors. In view of this, their absolute solution PL quantum yields were estimated and they were found to be noticeably high in the range of 0.48-0.52. A detailed optical data of **HT₁₁₋₁₃** are summarized in **Table 4.17**.

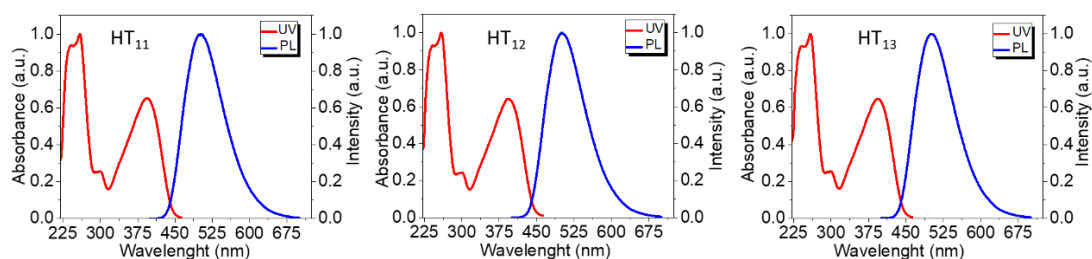


Figure 4.38 Absorption and emission spectra of **HT₁₁₋₁₃** in DCM at $c = 2 \times 10^{-5}$ M

The fluorescence life-time of new mesogenic materials was estimated for the samples in DCM ($c = 2 \times 10^{-5}$ M) using TCSPC technique by probing at their respective emission maxima. The resulted fluorescence kinetic decay profiles are depicted in **Fig 4.39a**. The traces fitted with biexponential decay showed average lifetime values of 2.54 ($\chi^2 = 1.0$), 2.51 ($\chi^2 = 0.99$) and 2.51 ($\chi^2 = 1.01$) for **HT₁₁**, **HT₁₂** and **HT₁₃**, respectively (**Table 4.17**). The same samples were illuminated under a longer wavelength radiations and their photographs are depicted in **Fig 4.39b**. To study the photoluminescence behaviour of these materials at liquid crystalline state, their neat thin films were prepared by spin coating technique and the fluorescence spectra were

obtained by exciting them at their respective solution absorption maxima (**Fig 4.39c**). Interestingly, no much shift in emission wavelength (504-508 nm) was noticed when compared to solution emission maxima (501-502 nm). A visually perceivable emission was observed when they were illuminated under the light of 365 nm as shown in **Fig 4.39d**.

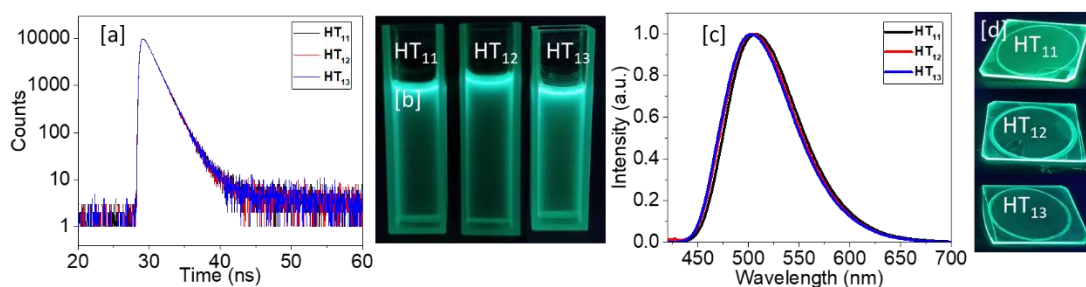


Figure 4.39 (a) Fluorescence decay profiles obtained for DCM solution and (b) their emission hue; (c) fluorescence spectra obtained for thin films and (d) their emission hue

Further, the effect of solvent polarity on optophysical properties of these emitting LC materials was examined by studying the absorption and emission characteristics of a representative compound, **HT₁₁**. Its UV-visible and fluorescence spectra are depicted in **Fig 4.40** and the relevant data are compiled in **Table 4.18**. Evidently, it showed a lack of solvent dependence absorption profile, indicating a non-polar ground state. Whereas a slight red-shift of emission bands on increasing solvent polarity demonstrated the trivial positive fluorescence solvatochromism. Notably, the unusual bathochromic shift perceived in DCM arises due to effective solvation in the solvent induced by an instant stabilization of polarizable electrons during the electronic excitation (Konidena et al. 2016).

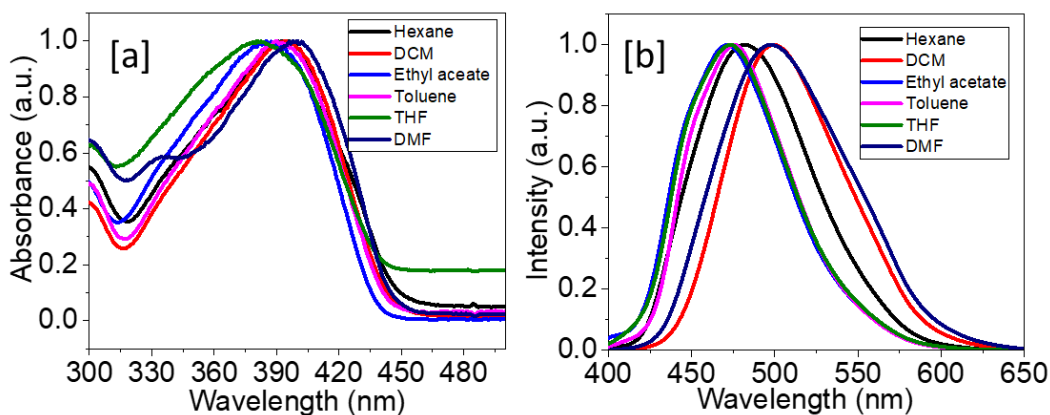


Figure 4.40 (a) Absorption and (b) emission spectra of **HT₁₁** recorded in solvents of varied polarity

Thus, the observed larger Stokes shift, biexponential PL decay, and the nonlinear solvatochromic shift indicated the existence of locally excited (LE), as well as charge transfer (CT) states in these D-A-D luminogens. In addition, DFT calculations interpret a slight twist of donor moieties with respect to the central acceptor core suggesting that, the second exciton species might have arise due to twisted intramolecular charge transfer (TICT) (Sasaki et al. 2016). This sort of coexistence of LE and CT character is generally called ‘hybridized local and charge transfer’ (HLCT) state, which is known to contribute for enhancement of fluorescence radiative decay; this improves the electroluminescence efficiency of OLEDs (Li et al. 2012; Zhang et al. 2013, 2015).

Trialkoxyphenyl cyanopyridone derivatives (HT₁₄₋₂₀):

The linear optical properties of new dyad materials, **HT₁₄₋₂₀** were evaluated by recording their steady-state UV-Visible absorption and emission spectra at the concentration of 10^{-5} M in DCM. The subsequent spectra are shown in **Fig 4.41** and the key parameters are summarized in **Table 4.17**. Typically, all the compounds displayed three well distinguishable absorption bands. A higher energy band observed at ~231 nm is due to localized π - π^* electronic transition of trialkoxyphenyl ring; the band appeared at 265-296 nm stems from localized π - π^* electronic transition of auxiliary chromophore units, indicating the extent of electron density of the donor groups; perceived predominant longer wavelength band is assigned to delocalized intramolecular charge transfer (ICT) transitions from π (D) to π^* (A) of the molecule. It is observed that, the compounds **HT₁₄**, **HT₁₅**, **HT₁₈** and **HT₁₉** exhibit similar ICT bands due to more or less same donor strength of their respective secondary donors, whereas **HT₁₆**, **HT₁₇** and **HT₂₀** display red-shifted ICT bands, which are attributed to relatively higher donor strength of amino chromophores of these dyads. Particularly, both **HT₁₇** and **HT₂₀** showed absorption bands at 429 nm, even though the former dyad has a stronger triphenylamine secondary donor than *N,N*-dimethylamino phenyl ring of the latter. This is because of the fact that, the nitrogen lone pair of triphenylamine group is in conjugation with the π -electrons of phenyl rings causing the reduced donor strength, which results in absence of expected red shift. Further, optical band gap of all the dyads

were estimated by means of the onset wavelength of the absorption spectra and it was in the range of 2.48-2.92 eV.

The emission spectra of all the dyad compounds **HT**₁₄₋₂₀ were recorded at the same concentration in DCM and they are depicted in **Fig 4.41b**. When they were excited at their respective longer λ_{abs} , they demonstrated emission profile bearing single maxima without any vibronic fine structure suggesting the floppy nature of the excited state (Konidena et al. 2016). On varying the auxiliary donor in these D-A-D' systems, emission colour from blue to orange was achieved with large Stokes shift. As can be seen in the **Figs 4.41b-c**, the perceived PL intensity is in the order of **HT**₁₈ < **HT**₁₉ < **HT**₁₄ < **HT**₁₅ < **HT**₂₀ < **HT**₁₆ < **HT**₁₇. Among them, the cyanopyridone appended with amino donors exhibited high fluorescence in DCM solution due to strong ICT transition from donor to acceptor. Interestingly, the compound **HT**₁₇ results 2.3 times higher fluorescence intensity than the **HT**₂₀, although the secondary donor of **HT**₁₇ is weaker than that of **HT**₂₀. This may be ascribed to greater structural reorganization of **HT**₁₇ having smaller *N,N*-dimethylamino phenyl donor than that of **HT**₂₀ bearing larger triphenylamine donor in the excited state. Evidently, the larger Stokes shift is one of the advantageous key factors for their application in OLEDs. Further, the absolute solution quantum efficiency was evaluated to be high in dyads bearing amino chromophores while the rest of them showed low quantum yield.

In addition, steady-state time-dependent fluorescence decay profiles for these high emissive materials, *viz.* **HT**₁₆, **HT**₁₇ and **HT**₂₀ were obtained in DCM solution. These results provide a clear evidence on the excited state of fluorophores. The data accomplished by means of time-correlated single photon counting (TCSPC) method and the fitted data are summarized in **Table 4.17**. The fluorescence kinetic profile of **HT**₁₆ dyad was fitted to mono exponential decay with life-time of 1.90 ns, indicating the relatively faster radiative decay. Whereas fluorophores **HT**₁₇ and **HT**₂₀ exhibited three excited species; in case of **HT**₁₇ one has ultrafast decay < 1 ns and the other two show relaxed emissive decay, while **HT**₂₀ displays two faster non-radiative decays and the third implies for the intense emission.

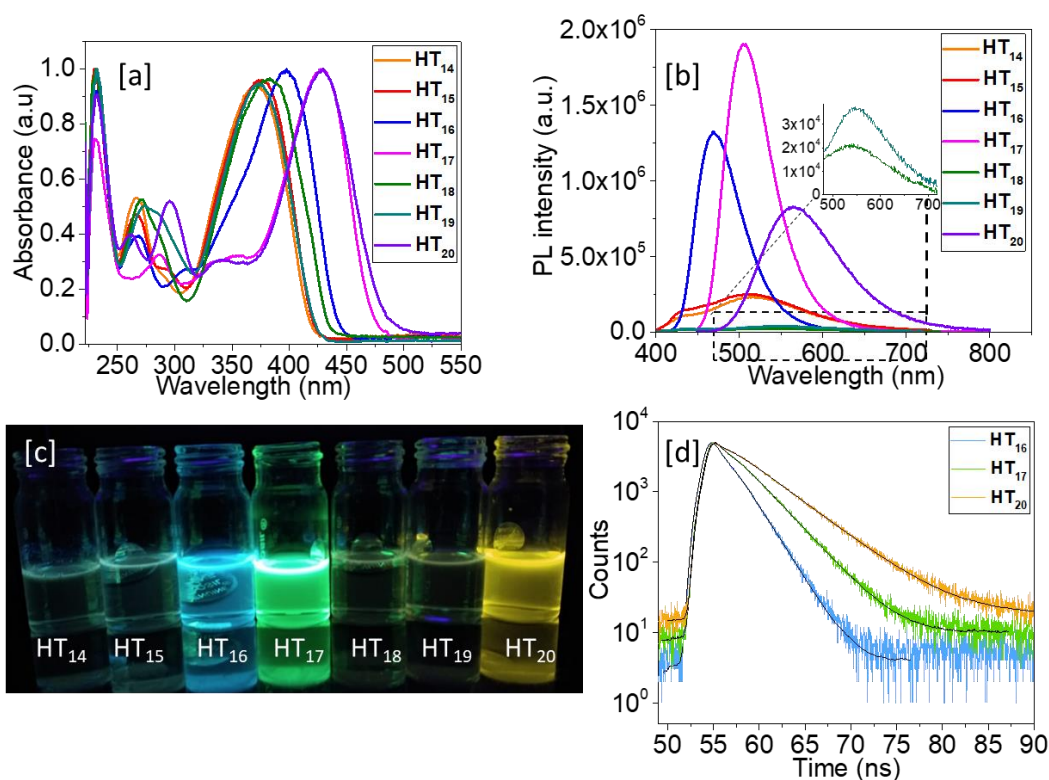


Figure 4.41 (a) UV-Visible absorption spectra, (b) emission spectra and (c) emission hue under 360 nm of **HT**₁₄₋₂₀; (d) fluorescence life-time traces of selected lumenogens

To understand their emission behaviour in thin film state, emission spectra were recorded for solution drop-casted films. On excitation at their respective solution λ_{abs} , all the lumenogens elicited featureless broad emission profile ranging from 500 to 552 nm. Except **HT**₁₆ and **HT**₁₇, all of them showed blue-shifted emission maxima when compared to that in DCM solution state. This may be due to the H-type aggregation of the dye molecules in the solid state. Excitingly, the sequence of PL intensity of thin films was found to be entirely different from that of solution state. From the results it is clear that, their intensity is in the order of **HT**₁₄ < **HT**₁₆ < **HT**₁₇ < **HT**₁₈ < **HT**₁₉ < **HT**₁₅ < **HT**₂₀. It is interesting to compare emission behaviour of **HT**₁₇ and **HT**₂₀ in solution and that in aggregated state. The **HT**₁₇ showed the highest PL intensity among all fluorophores, whereas **HT**₂₀ was found to be the third intense emitter with longest wavelength of 564 nm in solution state. Contrary, thin film of **HT**₁₇ displayed relatively lower emission intensity than the highest intense **HT**₂₀. In addition, former one demonstrated the bathochromic shift, while the latter revealed hypsochromic shifted solid state emission. The observed emission features may be ascribed to intermolecular

interaction in the aggregated state as well as molecular orientation in the excited state of the thin film. Eventually, the relative blue-shifted solid state emission of **HT**₂₀ is due to restriction of aggregations realized for the non-planar trigonal geometry of triarylamine chromophore and larger dihedral angle between central cyanopyridone nucleus and triarylamine unit (Konidena and Thomas 2017).

All the investigated cyanopyridone dyads showed visually perceivable emission in their solution as well as thin film states when illuminated under a UV light of 365 nm as pictured in **Figs 4.41c** and **4.42b**, respectively.

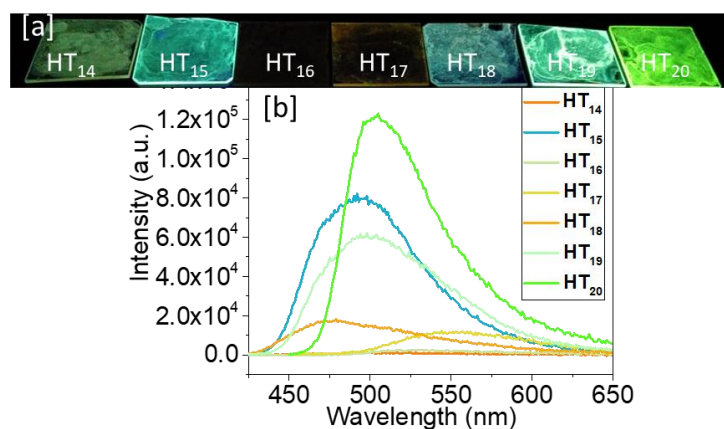


Figure 4.42 (a) Emission hue of drop-casted thin films under the light of 365 nm and (b) Emission profile (excited at their solution λ_{abs}) of **HT**₁₄₋₂₀

Systematic solvatochromic studies were conducted for the selected luminescent materials, *viz.* **HT**₁₄, **HT**₁₆, **HT**₁₇ and **HT**₂₀ to get further insight into the nature of excited state of these fluorophores. Their absorption and emission spectra were recorded for the dyads in five solvents owing different polarity parameters starting from non-polar toluene to highly polar ethanol at the micro-molar concentrations (Reichardt 1994). The solvatochromic absorption spectra of all the four compounds are displayed in **Fig 4.43**. Apparently, these dyes have been shown to exhibit lack of solvent dependent absorption, indicating the non-polar ground state and smaller dipole moment associated with it. Contrarily, **HT**₁₆, **HT**₁₇ and **HT**₂₀ exhibit pronounced positive solvatochromic emission; however **HT**₁₄ has deviated from the solvent dependent emission. The progressive red-shift of emission maxima on sequential increase of solvent polarity was noticed in the above mentioned set of three dyads. At the same

time, a manifesting decrease in fluorescence intensity was observed. This significance can be pragmatic through the naked eyes; changing from blue to green in **HT**₁₆, and bluish green to orange in both **HT**₁₇ and **HT**₂₀ (**Fig 4.44**). This can be ascribed to the significant intramolecular charge transport (ICT) from the donor to acceptor unit in the excited state. Thus, the dyads demonstrate the polar excited state with larger associated dipole moment.

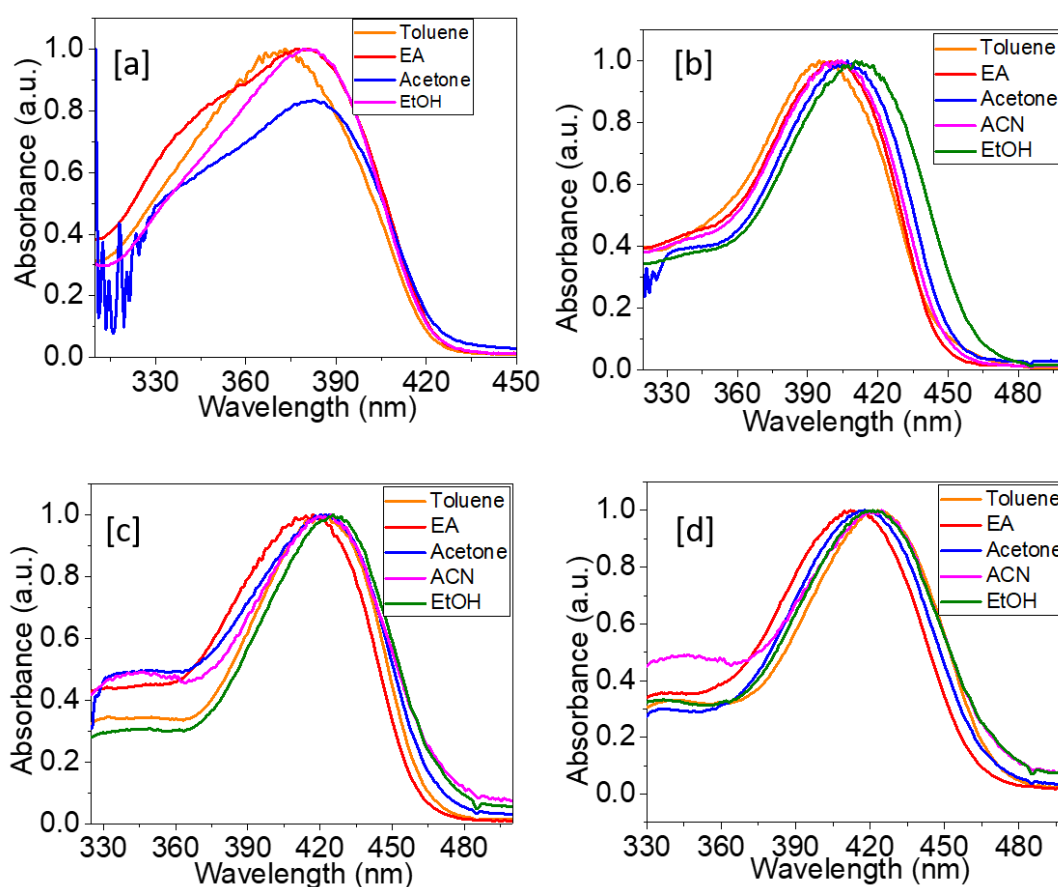


Figure 4.43 Normalized electronic absorption spectra for (a) **HT**₁₄ (b) **HT**₁₆ (c) **HT**₁₇ and (d) **HT**₂₀ in solvents of different polarity index

In order to establish the relation between the emission feature of dyads **HT**₁₆, **HT**₁₇ and **HT**₂₀ with solvent parameters, Lippert-Mataga plot and $E_T(30)$ index of solvent *versus* Stokes shift were used (**Figs 4.44e-f**). Seemingly, both the correlation plots demonstrated progressive linear relationship which suggests the presence of single excited state with slight deviations in Stokes shift of these fluorophores. Moreover, considerably large Stokes shift and large positive slope of linear relation are indication of reasonable higher dipole moment of excited state than that of the ground state. Thus,

the observed positive difference in the dipole moment impels the domination of ICT character in these fluorescent materials (Wu et al. 2015). The obtained solvatochromic data are summarized in **Table 4.18**.

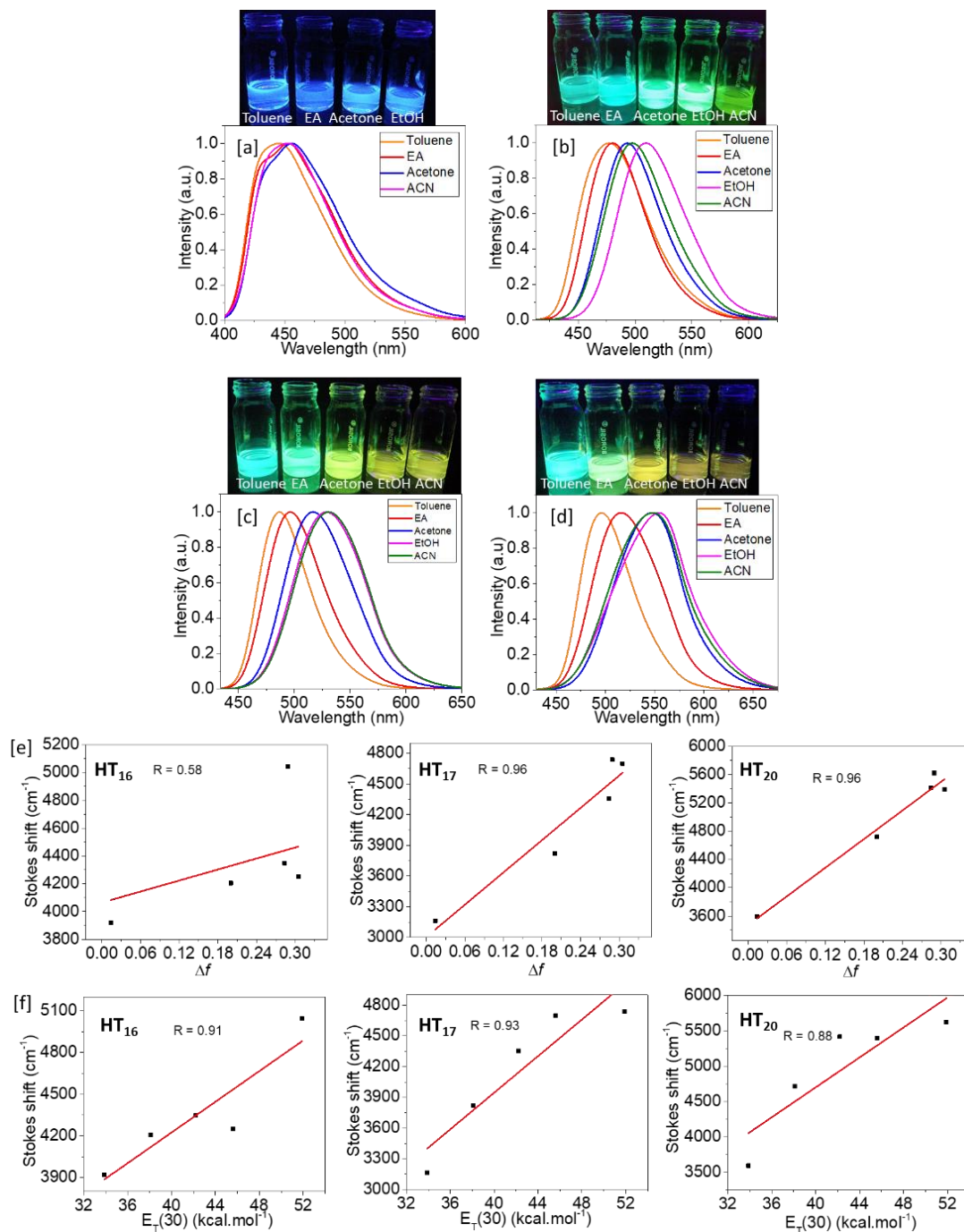


Figure 4.44 Normalized emission spectra for (a) HT₁₄ (b) HT₁₆ (c) HT₁₇ and (d) HT₂₀; (e) solvents of different polarity index Lippert-Mataga and (f) Stokes shift vs $E_T(30)$ correlation plots for selected dyads

4.3.2.4 Optical properties of HT₂₁₋₂₆ (Series-4)

The opto-physical properties of D-A configured HT₂₁₋₂₆ were studied by using their steady-state UV-visible absorption and photoluminescence data. Both the spectra were recorded for all the samples with a concentration of 2×10^{-5} M in dry dichloromethane at room temperature. The characteristic UV-visible (**Fig 4.45a**) and photoluminescence spectra (**Fig 4.45b**) demonstrated multiple absorption bands for all the compounds and the peaks are well-distinguishable. Since HT₂₁₋₂₃ are discrete only in terms of alkoxy chain lengths, they showed similar absorption and emission spectral properties. They displayed three absorption bands in the range of 233-235, 289-290 and 409-411 nm; three emission maxima at 437, 465-498 and 494-498 nm with a considerable Stokes shift in the range of 15-83 nm. The optical band gap of HT₂₁₋₂₃ was calculated using the onset of the absorption curve, to be ~ 2.57 eV. In case of HT₂₄ no significant changes have been noticed. Surprisingly, HT₂₅ with only two alkoxy donors exhibited a slight red-shifted absorption and blue shifted PL bands when compared to its analogue bearing three alkoxy donors (HT₂₁₋₂₃). However, HT₂₆ carrying no carboxylic group showed a small redshift absorption and a blue-shifted emission when compared to its rhodanine acetic acid counterpart. These results showcased the good light absorbing ability of all the compounds, consequently they can be potentially used in light harvesting devices like solar cells. A detailed optical characterization data is tabulated in **Table 4.17**.

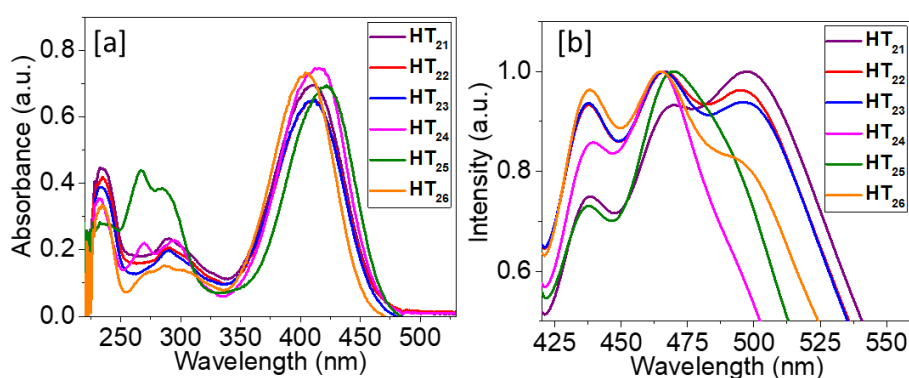


Figure 4.45 (a) UV-Visible absorption and (b) photoluminescence spectra of HT₂₁₋₂₆

The effect of solvent polarity on the optical properties of liquid crystalline dye, *i.e.* HT₂₃ was investigated by recording its absorption and emission spectra in six solvents showing different Reichardt polarity indices ($E_T(30)$) (Reichardt 1994). Its

spectra in various solvents are depicted in **Figs 4.46a-b** and the relevant data are summarized in **Table 4.18**. Obviously, the observed solvent independent absorption indicated a non-polar ground state of the molecule. However, a slight solvatochromic emission shift has been observed which signifies the greater polar excited state than the ground state. Further, an unusual red-shift was noticed in case of hexane which may be attributed to effective solvation of the dye molecules in the solvent-induced polarizable electrons during the electronic excitation process (Konidena et al. 2016). Furthermore, Lippert-Mataga correlation plot showing a positive slope demonstrated a general trend in the solvatochromism on increasing solvent polarity, as shown in **Fig 4.46c**.

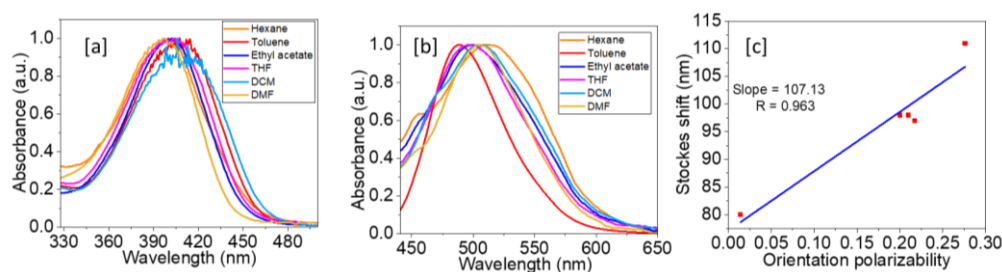


Figure 4.46 (a) UV-Visible absorption; (b) photoluminescence spectra in different solvents and (c) corresponding Lippert-Mataga plot of **HT₂₃**

4.3.2.5 Optical properties of **HT₃₂₋₃₅** (Series-6)

The optical properties of newly synthesized D-A-D' configured boron difluoride complexes **HT₃₂₋₃₅** were studied by recording their steady-state absorption and emission spectra in DCM solution ($c = 2 \times 10^{-5}$ M) at room temperature. The obtained spectra are depicted in **Fig 4.47a-b**, and the subsequent key parameters are summarized in **Table 4.17**. Seemingly, a variation in number of alkoxy chains has least influence on their absorption property; whereas they exert a slight impact on their emission behaviour. In their absorption spectra, the observed higher energy bands at ~ 230 nm are due to localized π - π^* electronic transition of alkoxyphenyl rings and the intense longer wavelength bands (377-385 nm) are assigned to delocalized ICT transitions from π (D) to π^* (A) of the molecules. On exciting at their absorption maxima, they showed single featureless broad emission bands indicating the floppy nature of the excited state (Konidena et al. 2016). Their emission maxima were noticed in the range of 492-524 nm; interestingly, **HT₃₂** bearing four alkoxy donors displayed red-shifted emission compared to **HT₃₃** and **HT₃₄** having five and six alkoxy substitutions, respectively. This may be related to the structural reorganization of the

molecules in the excited state. Certainly, they exhibited larger Stokes shift in the range of $5514 - 7331 \text{ cm}^{-1}$ confirming the pronounced ICT behaviour of these unsymmetrical dyad systems and the property is one of the key factors in the fabrication of OLED devices. Further, to understand the emission behaviour of the complexes in the solid state, the PL spectra were recorded for their drop-casted thin films and the resulting spectra are shown in **Fig 4.47c**. Evidently, they showed blue-shifted emission maxima when compared to their respective peaks in solution. The fact may be due to the H-type aggregation of the molecules in the solid state. Furthermore, the optical band gap values of these materials were estimated by considering red-edge of their respective absorption spectrum and they were found to be in the range of 2.81-2.90 eV.

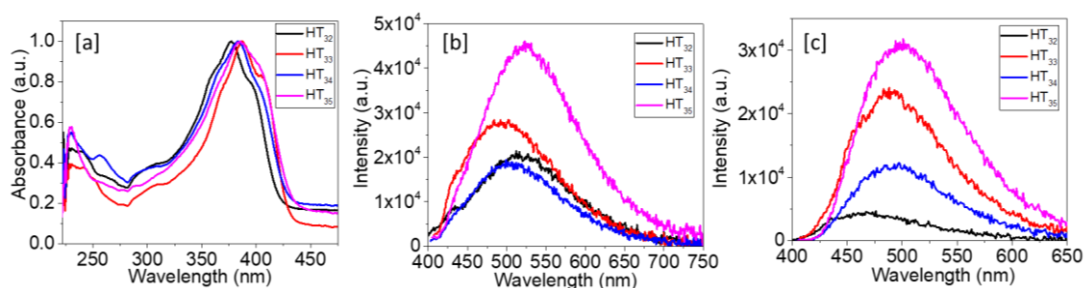


Figure 4.47 (a) UV-Visible absorption and (b) photoluminescence spectra of **HT₃₂₋₃₅** at $c = 2 \times 10^{-5} \text{ M}$ DCM solution; (c) drop-casted thin film photoluminescence spectra of **HT₃₂₋₃₅**

Conclusively, photophysical behaviours of all five series except **Series-5** as the members of it show no colour, were examined. The in depth studies revealed that, all the compounds of the **Series-1** to **Series-3** were found to be intense emitters with considerable quantum efficiency due to presence of effective donor-accepter interactions, which led to a delocalized intramolecular charge transfer (ICT) transitions from π (D) to π^* (A) of the molecules. Interestingly, they exhibit high luminescence both in solution and solid states. While compounds of **Series-4** and **Series-6** bearing rhodanine and BF_2 complex as accepters, respectively showed good absorption behaviour, but not the emission. This may be due to insufficient electronic communication within the structure at ground as well as excited states.

Since the members of **Series-1** to **Series-3** possess imperative columnar phase at room temperature with preserved intense emission, they can be employed as emissive layer in simple and multilayer OLEDs.

Table 4.17 Optical characterization data of new heterocyclic derivatives

Series	Comp.	^a λ _{abs} (nm)	^a λ _{em} (nm)	^a Stokes shift (cm ⁻¹)	^b E _{g opt} (eV)	^{a, c} Φ _F	^d λ _{em} (nm)	^e τ (ns) τ ₁ / τ ₂ / τ ₃
1	HT₁	234, 261, 383	454	4083	2.82	0.21	486	0.11/0.85/2.5
	HT₂	234, 261, 383	454	4083	2.83	0.22	482	0.11/0.88/2.8
	HT₃	233, 261, 382	453	4103	2.85	0.21	480	0.12/0.89/2.9
	HT₄	235, 260, 381	453	4171	2.87	0.19	478	0.13/0.92/3.1
2	HT₈	261, 351	426	5015	3.00	0.56	448	1.3/2.17
	HT₉	259, 352	425	4880	3.03	0.52	441	1.52/2.38
	HT₁₀	262, 352	425	4880	3.06	0.55	440	1.40/2.30
3	HT₁₁	259, 302, 394	501	5420	2.72	504	0.52	2.39/4.31
	HT₁₂	258, 300, 395	502	5396	2.73	506	0.49	2.41/4.61
	HT₁₃	258, 300, 395	502	5396	2.75	508	0.48	2.28/3.71
	HT₁₄	231, 266, 371	518	7619	2.92	510	0.05	
	HT₁₅	231, 265, 375	512	7135	2.91	494	0.08	
	HT₁₆	233, 268, 397	469	3866	2.77	527	0.31	1.90
	HT₁₇	231, 284, 429	506	3547	2.58	552	0.63	0.04/3.31/3.2
	HT₁₈	231, 270, 382	538	7590	2.84	478	0.02	
	HT₁₉	231, 276, 372	548	8633	2.90	500	0.09	
	HT₂₀	233, 296, 429	564	5579	2.48	504	0.55	0.85/0.19/4.4
4	HT₂₁	234, 290, 409	498	3082	2.57			
	HT₂₂	235, 290, 411	494	2826	2.57			
	HT₂₃	233, 289, 409	495	2944	2.56			
	HT₂₄	232, 294, 417	465	2475	2.58			
	HT₂₅	234, 267, 286	467	2283	2.56			
	HT₂₆	235, 285, 404	495	3247	2.60			
6	HT₃₂	228, 377	521	7331	2.90	468		
	HT₃₃	228, 387	492	5514	2.85	488		
	HT₃₄	230, 384	508	6357	2.84	494		
	HT₃₅	230, 385	524	6890	2.81	501		

^a Determined for solution in dichloromethane (2×10⁻⁵ M); ^b Optical band gap estimated by red edge of absorption band in UV-visible spectrum; ^c Quantum yield; ^d Emission maxima for spin-coated thin film; ^e Fluorescence life-time

Table 4.18 Solvatochromic data of selected new heterocyclic derivatives

Series	Solvent	^a λ_{abs} (nm)	^b λ_{em} (nm)	^a Stokes shift (cm ⁻¹)	
1	HT₁	Hexane	368	456	5244
		Toluene	378	444	3932
		EA	375	449	4394
		THF	371	443	4380
		DCM	383	454	4083
		EtOH	381	452	4122
		DMSO	390	455	3663
		DMF	388	440	3045
		ACN	379	451	4212
2	HT₈	Hexane	344	386	3163
		Toluene	349	400	3653
		DE	347	400	3818
		EA	347	400	3818
		THF	349	410	3653
		DCM	351	426	5015
		DMSO	354	454	6222
		DMF	352	449	6137
		ACN	351	432	5341
3	HT₁₁	Hexane	394	481	4591
		Toluene	391	475	4522
		EA	385	472	4788
		THF	382	473	5037
		DCM	394	501	5420
		DMF	398	499	5085
	HT₁₄	Toluene	374	445	4266
		EA	381	453	4172
		Acetone	383	455	4131
		EtOH	382	452	4054
	HT₁₆	Toluene	398	478	4205
		EA	404	480	3919
		Acetone	406	493	4347
		EtOH	405	509	5044
		ACN	411	498	4250
	HT₁₇	Toluene	422	487	3163
		EA	417	496	3820
		Acetone	422	517	4354
		EtOH	423	529	4737
		ACN	425	531	4697
	HT₂₀	Toluene	421	496	3592
EA		415	516	4716	
Acetone		422	547	5415	
EtOH		423	555	5622	
ACN		423	548	5392	
4	HT₂₃	Hexane	400	514	5545
		Toluene	409	489	4000
		EA	400	498	4920
		THF	402	500	4876
		DCM	409	506	4687
		DMF	395	506	5554
^a Micromolar solutions in different solvents; ^b Excited at their respective absorption maxima					

4.4 ELECTROCHEMICAL STUDIES

The electrochemical studies of any organic materials provide exact information with regard to their oxidation and reduction behaviours, by which it is possible to estimate the important energies of HOMO and LUMO as well as energy band gap. Hence, the semiconductivity of the material can be assessed conveniently. In the present work, electronic properties of some selected LC materials were studied by means of CV. This section deals with a detailed electrochemical studies of some new LC compounds including experimental data discussion.

4.4.1 Experimental methods

Electrochemical properties of LC materials were studied by recording cyclic voltammograms using CH-instrument connected to CHI660E software. The CV experiments were carried out by employing Ag/AgCl as reference electrode which was calibrated with ferrocene/ferrocenium (Fc/Fc⁺) redox couple having absolute energy of 4.8 eV to vacuum, glassy carbon as working electrode, platinum wire as counter electrode and Tetrabutyl ammonium perchlorate (0.1 M) as supporting electrolyte in dry dichloromethane solvent. The CV measurements were carried out by using 1mM solution of LC materials. The voltammograms were obtained at the scan rate of 100 mVs⁻¹.

4.4.2 Results and discussion

The electrochemical parameters of selected new columnar liquid crystalline materials have been discussed in the following sections.

4.4.2.1 Electrochemical properties of HT₁₋₄ (Series-1)

The obtained electrochemical data of HT₁₋₄ from their CV analysis are tabulated in **Table 4.19**. Evidently, all the compounds of the series displayed irreversible oxidation and reduction curves, as shown in **Fig 4.48**. The energies of HOMO, LUMO and their gaps were calculated using the **Eqs. 4.8-4.10**, respectively.

$$E_{HOMO} = - [4.8 - E_{1/2, Fc/Fc^+} + E_{1oxd}] \text{ eV} \quad (4.8)$$

$$E_{LUMO} = - [4.8 - E_{1/2, Fc/Fc^+} + E_{1red}] \text{ eV} \quad (4.9)$$

$$E_g = [E_{LUMO} - E_{HOMO}] \text{ eV} \quad (4.10)$$

The energies of HOMO and LUMO levels of the materials were estimated to be in the range of -5.59 to -5.63 and -3.62 to -3.66 eV, respectively with the band gap ranging from 1.95 to 2.00 eV. From the data, it is clear that, the calculated electrochemical band gap values were found to be smaller than that of optical band gaps of all the materials.

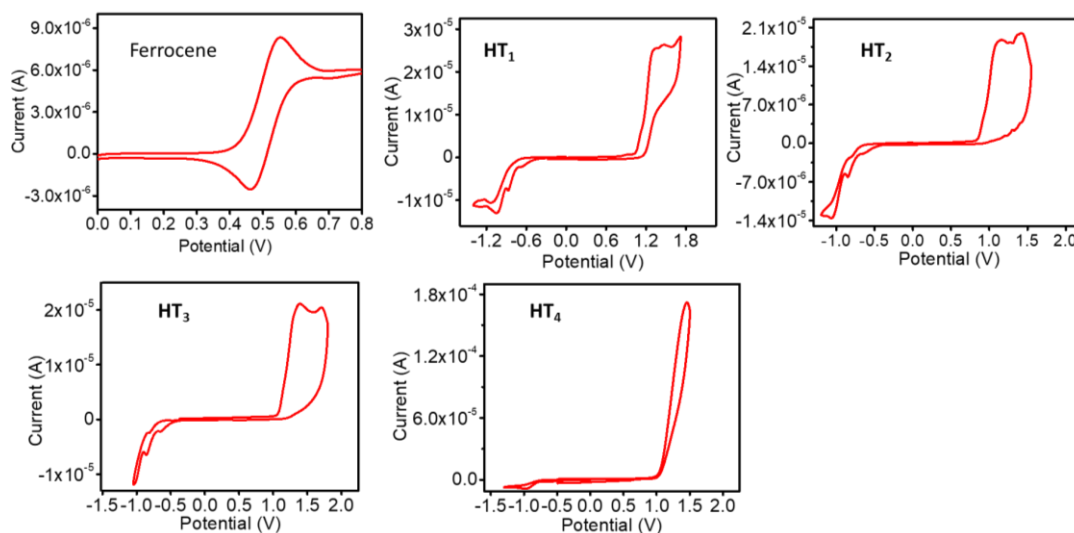


Figure 4.48 Cyclic voltammograms of LCs HT₁₋₄

4.4.2.2 Electrochemical properties of HT₈₋₁₀ (Series-2)

The CV curves of all the compounds of the **Series-2** are displayed in **Fig. 4.49** and their relevant data are tabulated in **Table 4.19**. As can be seen in their CV traces, they showed irreversible oxidation and reduction onsets at the potential around 1.2 and -0.8 V, respectively. They exhibited HOMO and LUMO energy levels in the range of -5.45 to -5.44 eV and -3.51 to -3.54 eV, respectively with the corresponding energy gaps of around 2 eV, according to **Eqs. 4.8-1.10**. The obtained electrochemical band gaps were found to be more narrow than the corresponding optical band gaps as estimated by the UV-visible spectra (~3.0 eV) (Bala et al. 2017; Gupta et al. 2015). Indeed, the observed optical band gaps are well matching with the theoretical (DFT) band gaps (~3.0 eV).

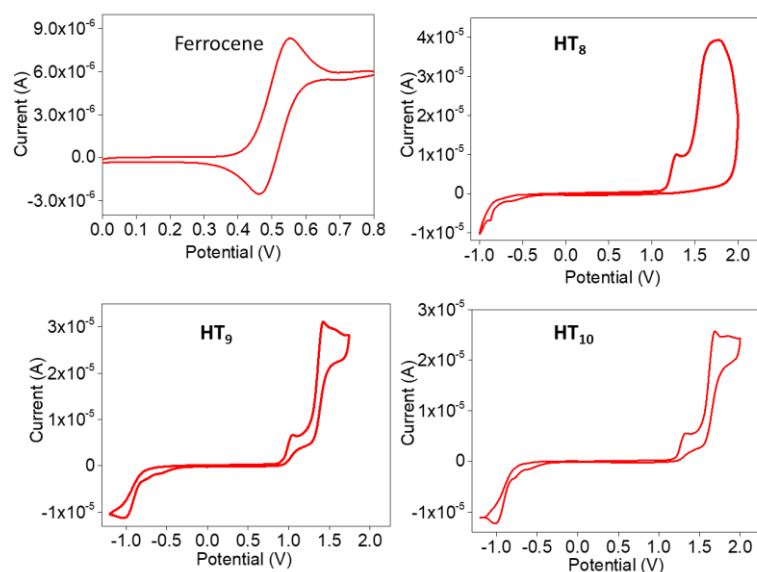


Figure 4.49. Cyclic voltammograms of HT₈₋₁₀

4.4.2.3 Electrochemical properties of HT₁₁₋₁₃ (Series-3)

The CV results of HT₁₁₋₁₃ (Series-3) are showcased in **Fig. 4.50** and the subsequent redox data are tabulated in **Table 4.19**. Evidently, all the three compounds showed irreversible oxidation and reduction waves at the onset in the range of 1.41 to 1.45 V and -0.83- to -0.87 V, respectively. Accordingly, the energies of HOMO and LUMO levels and band gaps were estimated using **Eqs. 4.8-4.10**. The obtained electrochemical HOMO-LUMO energy band gaps (2.28-2.32 eV) are in good agreement with the optical band gaps (2.72- 2.75 eV).

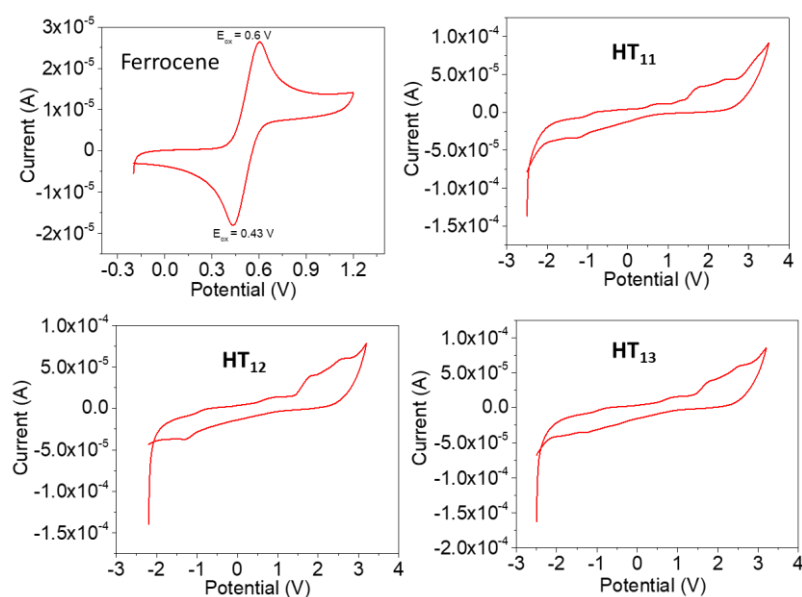


Figure 4.50. Cyclic voltammograms of HT₁₁₋₁₃

4.4.2.4 Electrochemical properties of HT₂₃ (Series-4)

Fig. 4.51 shows the recorded voltammogram of the only liquid crystalline compound **HT₂₃** of the **Series-4** and the corresponding data are given in **Table 4.19**. It showed irreversible oxidation and reduction onsets at the potential (first signals) of 1.48 and -0.68 V, respectively. The pertinent HOMO has an energy of -5.37 eV and LUMO has -3.62 eV with a band gap of 2.08 eV, as estimated from **Eqs. 4.8-4.10**.

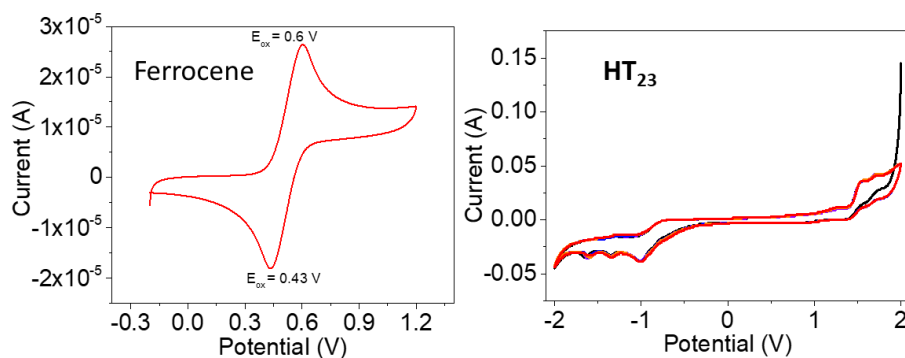


Figure 4.51. Cyclic voltammograms of **HT₂₃**

Table 4.19 Electrochemical data new LC materials

Series	Compd.	$E_{1\text{red}}^b$ (V)	$E_{1\text{oxd}}^c$ (V)	E_{LUMO}^d (eV)	E_{HOMO}^e (eV)	$E_{\text{g CV}}^f$ (eV)
1	HT ₁	-0.68	1.32	-3.62	-5.62	2.00
	HT ₂	-0.66	1.29	-3.64	-5.59	1.95
	HT ₃	-0.64	1.31	-3.66	-5.61	1.95
	HT ₄	-0.65	1.33	-3.65	-5.63	1.98
2	HT ₈	-0.782	1.15	-3.51	-5.45	2.00
	HT ₉	-0.755	1.14	-3.54	-5.44	1.90
	HT ₁₀	-0.767	1.15	-3.53	-5.45	1.91
3	HT ₁₁	-0.83	1.45	-3.46	-5.74	2.28
	HT ₁₂	-0.87	1.44	-3.41	-5.73	2.32
	HT ₁₃	-0.86	1.41	-3.43	-5.70	2.27
4	HT ₂₃	-0.68	1.40	-3.62	-5.70	2.08

^a Recorded in 1×10^{-3} M DCM solution; ^b Onset potential of reduction; ^c Onset potential of oxidation; ^d Estimated by using the formula $E_{\text{LUMO}} = -[4.8 - E_{1/2, \text{Fc}/\text{Fc}^+} + E_{1\text{red}}]$ eV; ^e Estimated by using the formula $E_{\text{HOMO}} = -[4.8 - E_{1/2, \text{Fc}/\text{Fc}^+} + E_{1\text{oxd}}]$ eV; where, $E_{1/2, \text{Fc}/\text{Fc}^+}$ was found to be 0.50 V; ^f Calculated from the formula $E_{\text{g CV}} = E_{\text{LUMO}} - E_{\text{HOMO}}$

To summarize, the investigated LC compounds were shown to be good redox active materials. The electrochemical data as estimated from their respective FMO levels evidenced for the low lying LUMO levels and hence the narrow energy band gap. Consequently, these materials owing preferable HOMO and LUMO levels with good semiconducting behaviour would be the potential candidates for optoelectronic devices like OLEDs, OPV and OTFT.

4.5 THEORETICAL INVESTIGATION

At present, in the field of organic electronics, computational studies play a key role, which helps to realize the relationship between molecular electronic structure and the optoelectronic device performance. It is even possible to generate the electronic spectra of the unknown compounds computationally, which gives the clear idea about the electronic nature of the material before its synthesis. In relevance to present study, the theoretical calculation would provide the useful information regarding ground state optimized structure of the molecules that helps for the exact identification of mesophase and conceive the type of molecular self-assembly in a particular mesomorphism. Also, it aids to realize the frontier molecular orbital (FMO) distributions and their energies in the newly designed molecules.

4.5.1. Simulations

In the current work, Density Function Theory (DFT) simulations were used to accomplish the electronic nature of the LC molecule. The calculations were performed for the isolated molecules in vacuum. The quantum chemical simulations were executed using the SPARTAN 10 program or Gaussian 09 program depending on the requirements. Geometry optimizations were performed using the Becke three-parameter exchange functional and the Lee-Yang-Parr B3LYP exchange correlation functionals with the 6-31+G* or 6-31G(d,p) basis set for C, H, N, S, B and O. Calculations were performed under vacuum.

4.5.2. Results and discussion

The simulation results, *i.e.* optimized geometries, HOMO, LUMO and band gap energies of representative structures have been discussed in the following sections.

4.5.2.1 Molecular modelling of HT₁₋₄ (Series-1)

The representative structure of **Series-1**, *i.e.* **HT₂** was chosen for theoretical simulation to realize the frontier molecular orbital (FMO) distributions and its theoretical energy. **Fig 4.52** displays the simulated HOMO, LUMO band gap energies and MEP charge distributions of **HT₂**. Seemingly, the full geometry optimized structure of **HT₂** is similar to flying bird kind of shape (**Fig 4.4b**). According to simulations, the HOMO orbitals localized throughout the aromatic domain, whereas LUMO orbitals distributed on cyanopyridone ring only (**Fig 4.52a**). This significant intramolecular charge transfer (ICT) has led to efficient light emission. The calculated band gap energies were corroborated with electronic transitions observed in UV-Visible spectra. However, HOMO and LUMO electronic oxidation and reduction potentials showed variations (~ 1.5 eV) with retaining general tendency in it. That could be due to the solvent as well as counter ion effect in electroanalytical technique. Because of the technical limitations, DFT based energy minimized structure calculations were not successful in the solvent model. Such deviations could be attributed to the solvents, pH, temperature, ionic strength as well as the solid surface of electrodes during electron transfer process. The obtained HOMO, LUMO distributions and molecular electrostatic potential map (MEP) have validated the clear electronic distributions with relatively high ground state dipole moment (5.53 D) oriented, towards electron deficient cyanopyridone unit (**Fig 4.52b**).

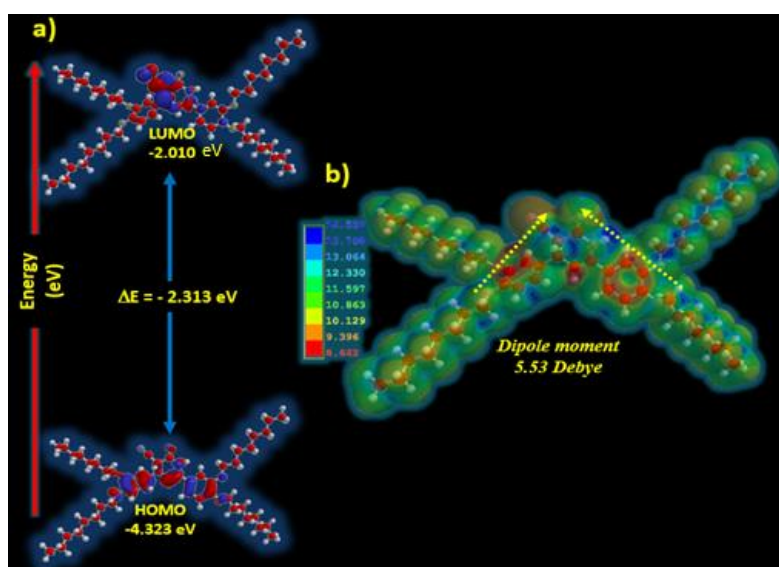


Figure 4.52 (a) HOMO, LUMO and band gap energies; (b) MEPs showing the ground state dipole moments and charge distributions of **HT₂**

4.5.2.2 Molecular modelling of HT₈₋₁₀ (Series-2)

The geometrical optimized structure for a representative molecule **HT₈** of the **Series-2** was obtained as shown in **Fig 4.9**. The HOMO orbitals have localized on trialkoxybenzyl ring, whereas the LUMO orbitals have located over the central cyanopyridine core and conjugatively attached two dialkoxyphenyl rings with the energy of -4.70 and -1.65 eV, respectively (**Fig 4.53**). Here, the clear distribution of FMOs confirmed that, these discotic molecules possess substantial intramolecular charge transfer ability, which was further evidenced by the electrostatic potential map with the dipole moment of 2.28 *D*.

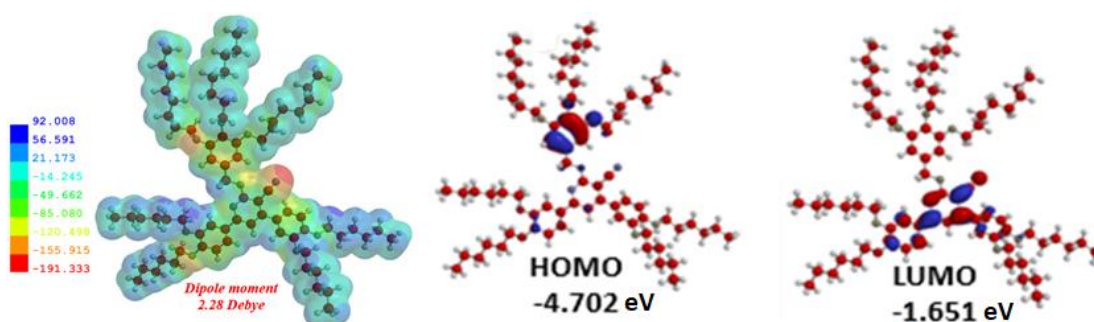


Figure 4.53 DFT based electrostatic potential map and FMOs of **HT₈**, as calculated using 6-31G* basis set

4.5.2.3 Molecular modelling of HT₁₁₋₂₀ (Series-3)

Phenanthrene-cyanopyridone hybrid molecules:

The simulated energy minimized geometry and HOMO-LUMOs of a model structure (**4.54a**) are depicted in **Fig 4.54**. In order to reduce the computational time and cost, a model molecular structure **4.54a** has been considered representing phenanthrene based molecules. Here, the longer alkoxy chains were replaced by simple methoxy groups. It has been presumed that, reducing the length of the alkyl chains would not affect the required energy parameters. Apparently, both dialkoxyphenanthrene and trialkoxyphenyl rings are not coplanar with the central cyanopyridone core, which resulted in a bowl-shaped structure. As shown in **Fig 4.54**, the HOMOs have concentrated over dialkoxyphenanthrene and cyanopyridone rings while LUMOs have delocalized throughout the molecule. These results confirm the

presence of a moderate intramolecular charge transfer behaviour, which validates the experimental electro-optical studies.

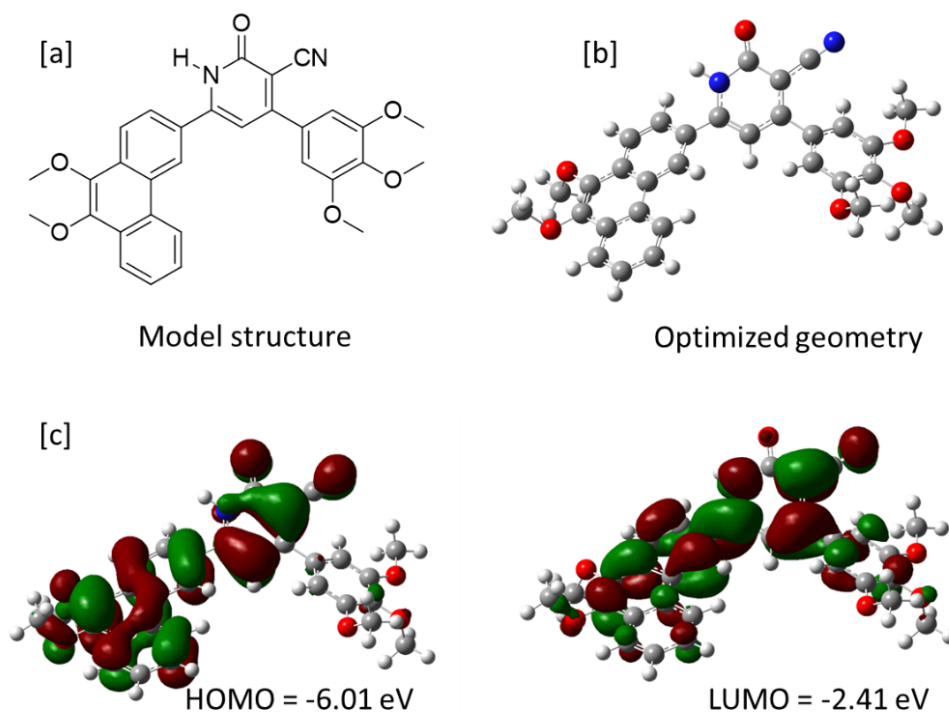


Figure 4.54 (a) Model structure; (b) simulated optimized geometry; (c) HOMOs and LUMOs of the model structure

Trialkoxyphenyl cyanopyridone derivatives:

In simulations of **HT**₁₄₋₂₀, the longer alkyl chains were simplified to save the computational time and cost. The computed energy optimized molecular geometries of seven structures and their frontier molecular orbital (FMO) distribution plots are shown in **Fig 4.55**. As visualised in the plots, HOMO orbitals have localized on donor segments; in contrast, LUMOs have concentrated on central cyanopyridone moiety with minor contribution of trialkoxybenzene ring. The non-overlapping HOMO and LUMO indicates that, the observed emission is originated mainly by ICT transition in these luminophores. Obviously, this has been experimentally proved by existence of excellent positive solvatochromism. The simulated energy gap between HOMO and LUMO levels is quite higher than their respective optical band gap. However, the trend of $E_{g\text{ DFT}}$ is exactly matching with experimental band gap, $E_{g\text{ Opt}}$.

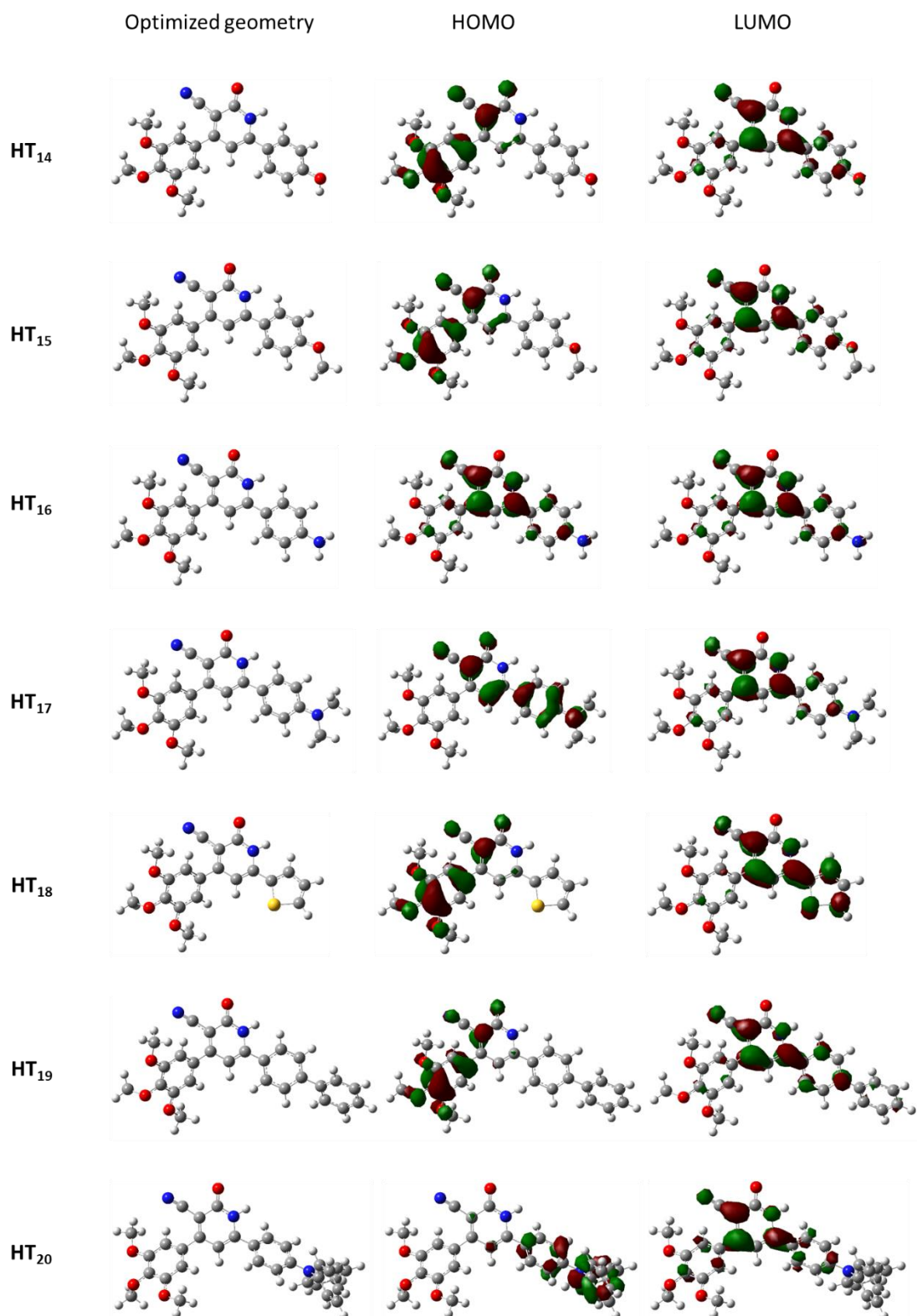


Figure 4.55 Energy minimized structures of new dyads and electron density distributions of their HOMO and LUMO orbitals

4.5.2.4 Molecular modelling of HT₁₁₋₂₀ (Series-4)

The simulated optimized geometry and HOMO-LUMO plots of illustrative molecule, *i.e.* HT₂₃ of Series-4 are shown in Fig 4.56. Apparently, both HOMO and LUMO energy orbitals have delocalized throughout the aromatic part of the wedge-shaped molecule. These orbitals have energy of -5.867 and -2.720 eV, respectively with the band gap of 3.147 eV. The observed difference in the optical, electrochemical and theoretical energy-band gaps may be ascribed to ionic strength, pH, solvents, temperature, in addition to the nature of the solid surface of electrodes during electron transfer.

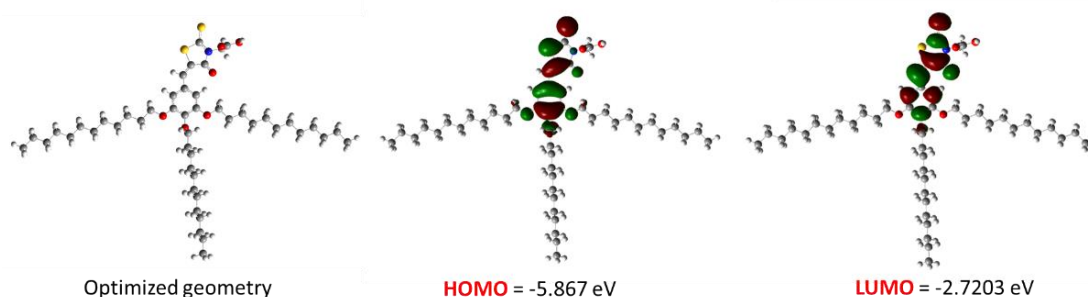


Figure 4.56 Electron density distributions in HOMO and LUMO orbitals

4.5.2.5 Molecular modelling of HT₃₂₋₃₅ (Series-6)

Fig 4.57a-b and Fig 4.58 showcase the optimized geometries and HOMO/LUMO plots of compounds HT₃₂₋₃₅ (Series-6), respectively. As visualized in Fig 4.57b, central core-system comprising three rings adopts entirely planar geometry which fundamentally helps for the stabilization of columnar arrangement. Further, the alkyl chains surrounded by this planar core moiety facilitate to acquire more or less disc-shaped molecules. The HOMOs have localized over the two alkoxyphenyl rings with a slight contribution from the boron-containing central core (Fig 4.58). Contrary, LUMOs have concentrated on the central ring and the alkoxyphenyl ring attached through imine linkage. The results clearly indicate the electronic migration from the donor to acceptor units, which manifests the ICT behaviour of the complexes. The observed fact has reflected in experimental absorption spectral measurements. The simulated HOMO and LUMO energy levels were found to be in the range of -5.56 to 5.69 and -2.02 to -2.21 eV, respectively. The calculated energy band gap (E_g) was

noticed to be slightly higher than that of the optical band gap. However, the trend of E_g is in good agreement with the experimental values.

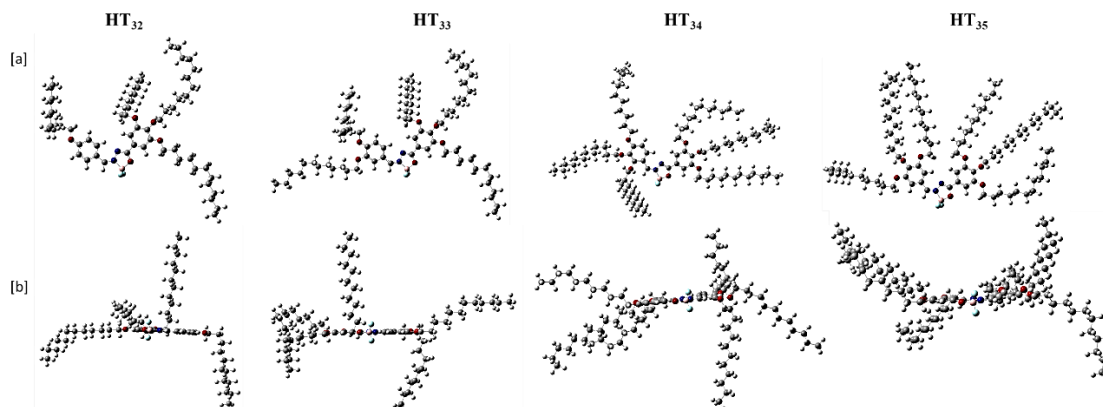


Figure 4.57 (a) Energy minimized structures of new BF_2 complexes and (b) their side view

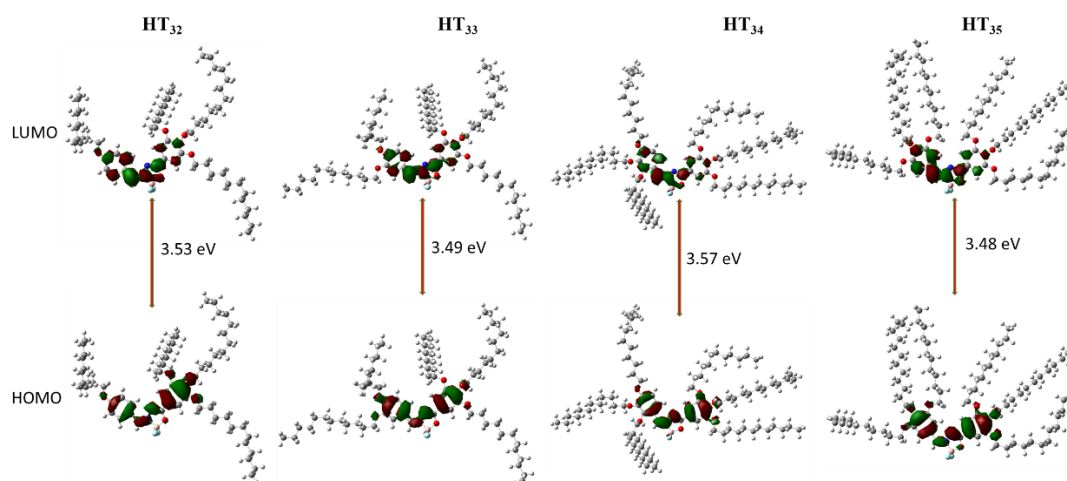


Figure 4.58 Electronic distributions in the FMOs of new BF_2 complexes

In conclusion, the DFT studies explored that, most of the newly synthesized molecules possess intense intramolecular transport ability due to the presence of conjugative electron rich alkoxyphenyl rings and electron deficient heterocyclic systems in their structural backbone.

4.6 CONCLUSIONS

In summary, all the newly synthesized six series of molecules, **HT**₁₋₃₅ were subjected to the detailed mesomorphic, photophysical and electrochemical characterizations. Most of the investigated compounds exhibited stable thermotropic liquid crystalline property in wide range of temperatures. Despite of the diverse shapes,

they have self-assembled into columnar structures of different geometries. Depending on the dynamics of the molecules within the columnar stacks and the structural aspects of the constituent mesogens, the obtained columnar structures have organized into either hexagonal, rectangular or oblique lattices. The results of photophysical studies revealed that, most of them are eminent light absorbers and intense emitters in the wide spectral range. Depending on the extent of D-A interactions, the investigated heterocyclic derivatives displayed tuneable emission with reasonable quantum efficiencies both in solution and solid states. The effect of solvent polarity on the optical properties has been studied by examining absorption and emission in various solvents of different polarities and the results indicated that, the investigated materials possess polar ground state and nonpolar excited state. Further, the electrochemical studies explored their redox behaviour and semiconducting nature. Finally, the experimental results were corroborated with quantum chemical simulation (DFT) data. Based on the favourable properties like conductive columnar mesomorphism, intense fluorescence, appropriate HOMO-LUMO energy levels *etc.* shown by the members of the **Series-1** and **-3**, a few representative compounds were selected for OLED device fabrication studies, which have been dealt in the next chapter.

OLED DEVICE FABRICATION STUDIES

Abstract

*This chapter deals with host-guest OLED device fabrication by employing selected new columnar LC materials, **HT**₂ and **HT**₁₂ as components of emissive layer. Also, it deliberates a detailed account on structure-device performance study.*

5.1. INTRODUCTION

An OLED (organic light-emitting diode) is a light-emitting diode in which the emissive electroluminescent layer is a film of organic compound that emits light in response to an electric current. At present, the OLEDs are being widely used to create digital displays in devices such as television screens, computer monitors, portable systems *etc.* Nevertheless, the current challenges of this area are the development of ideal light emitting device materials, engineering of the device structures and their optimization to get more efficient and long-life devices (Jou et al. 2015).

Certainly, the emissive layer is a vital component which determines the overall efficiency of the device. Till today a large variety of luminescent materials has been developed, so as to improve the device performance (Chen 2004; Chen et al. 2014; Godumala et al. 2016; Kamtekar et al. 2010; Kido and Okamoto 2002; Li et al. 2013; Segura 1998; Yang et al. 2015; Zhu and Yang 2013). Presently, one of the major challenges is the development of efficient fluorophores with high charge transport property as well as the preserved solid-state emission for high-performance non-doped OLEDs. In this context, columnar liquid crystals (CLCs) were shown to be better alternatives to the insulating amorphous solids as well as expensive single crystalline fluorophores due to their effective combination of π - π self-stacking with long-range order, self-healing, easily processability, good luminescence ability and intrinsic charge carrier property in the soft condensed state (Bushby and Kawata 2011; Chen et al. 2018; Kaafarani 2010; Kumar 2016; Laschat et al. 2007; O'Neill and Kelly 2011; Sergeev et al. 2007).

In the present work, two columnar liquid crystalline luminescent materials, *i.e.* **HT**₂ and **HT**₁₂ showing greenish blue and pure greenish yellow emission respectively, were employed separately as emissive components in the fabrication of OLEDs. A

detailed experimental methods used for the device fabrication and their device performance study are described in this chapter.

5.2. MATERIALS AND METHODS

The patterned indium tin oxide (ITO, Kintec, Hong Kong) coated glass substrates with a sheet resistance of $15 \Omega/\text{square}$ and ITO thickness of 120 nm were used as transparent anodes. All the organic and cathode materials were used as received without further purification. A 50 nm thick poly(3,4-ethylenedioxythiophene)/poly(styrene-sulfonate) (PEDOT: PSS, Sigma Aldrich) film was used as hole injection material. The poly(9-vinylcarbazole) was employed as host as well as a hole transport material. Bathocuproine (BCP, Sigma Aldrich) was selected as a hole blocking material and tris-(8-hydroxyquinoline) aluminium (Alq_3 , Sigma Aldrich) was used as an electron transport material. The lithium fluoride (LiF, Sigma Aldrich) and aluminium (Al, Alfa Aesar) layers were used as cathode materials.

The light-emitting area was 1.6 mm^2 as defined by the overlap of the cathode and anode. Electroluminescence spectra were acquired using a Horiba Jobin Yvon iHR320 spectrophotometer with an attached charge-coupled device (CCD) camera. Opto-electrical characteristics were recorded in a customized setup using a computer-controlled programmable Keithley 2400 SMU for recording the current-voltage characteristics, while the luminance was measured by a Keithley 6485 picoammeter using a calibrated Si photodiode (SM1PD2A). CIE coordinates were calculated from the EL spectra. All the devices were driven under DC conditions.

5.3. EXPERIMENTAL

Prior to the deposition of organic materials, the ITO substrates were treated by the UV-Ozone after a careful chemical cleaning process (Ulla et al. 2017). The PEDOT: PSS composite was then spin-coated on the ITO substrates from aqueous dispersion and baked at $120 \text{ }^\circ\text{C}$ for 30 min. Subsequently, luminescent LC or a mixture of LC (HT_2 or HT_{12}): PVK was spin-coated onto the PEDOT: PSS layer, the thickness of which was controlled as 80 nm by adjusting the solution concentration and the spin rate. The substrates after coating the emission layer was annealed at $140 \text{ }^\circ\text{C}$ for 2 hrs and slowly cooled at a rate of $1 \text{ }^\circ\text{C}/\text{min}$. The substrates were then transferred into a deposition chamber to deposit the remaining layers with a base pressure of 10^{-5} torr. On

the substrate, the hole blocking material (BCP) and the electron transport material (Alq₃) were deposited in sequences and thicknesses appropriate for the intended device structure by thermal evaporation method. Finally, to improve electron injection, a bilayer cathode consisting of lithium fluoride LiF and Al layers were sequentially deposited on the electron transporting material as the cathode. All the measurements were carried out at room temperature under dark and ambient conditions without any encapsulation.

5.4. RESULTS AND DISCUSSION

The results of electroluminescence studies of **HT₂** and **HT₁₂** in fabricated OLED devices **A-G** have been discussed in the following section.

5.4.1 OLED device performance of **HT₂** (Series-1)

The electroluminescence performance of a selected LC material, *i.e.* **HT₂** with highest quantum efficiency among the members of the **Series-1** was evaluated in fabricated OLED devices. In the present study, four different device architectures were designed as follows.

Devices A: ITO/ PEDOT: PSS/ **HT₂**/ LiF/ Al

Devices B: ITO/ PEDOT: PSS/ PVK: **HT₂**/ LiF /Al

Devices C: ITO/ PEDOT: PSS/ PVK: **HT₂**/ BCP/ Alq₃/ LiF /Al

Devices D: ITO/ PEDOT: PSS/ PVK/ PVK: **HT₂**/ BCP/ Alq₃/ LiF /Al

In the case of **device A**, **HT₂** acted as a sole emitter; whereas for **devices B, C, and D**, 10 wt% of **HT₂** was doped in host PVK (Poly(9-vinylcarbazole)). Here, PVK was used because of its good miscibility with numerous emitting materials and excellent film-forming capability (Yadav et al. 2017). The energy level diagram of the OLEDs and the different device configurations used in this study are shown in **Fig 5.1**. In the devices, patterned indium tin oxide (ITO) coated glass substrate acts as a transparent anode. Poly(3,4-ethylenedioxy-thiophene)/poly(styrene-sulfonate) (PEDOT: PSS) was used as a hole injection material. It has the ability to smoothen the ITO surface which in turn decreases the turn-on voltage and reduces the probability of electrical shorts and hence extends the life-time of the device. The performance data of new OLEDs are tabulated in **Table 5.1**. The current density-voltage-luminance (J-V-L) characteristics are shown in **Fig 5.2a**.

The **Device A** composing of **HT₂** as an emitter showed very weak emission. However, **Device B** composed of **HT₂** (10 wt.%) as dopant in PVK host as an emitting material shows high drive voltage (V_{onset} , corresponding to 1 cdm^{-2}) of 7.12 V, low luminance (L_{max}) of 261 cdm^{-2} , current efficiency (η_c) of 0.33 cdA^{-1} , power efficiency (η_p) of 0.09 lmW^{-1} and external quantum efficiency (η_{EQE}) of 0.14 % at 100 cd m^{-2} . Here, high drive voltage indicates the presence of high charge injection barriers in the device. On the other hand, a significant improvement in the device performance (L_{max} of 673 cdm^{-2} , η_c of 0.86 cdA^{-1} , η_p of 0.26 lmW^{-1} and η_{EQE} of 0.14 %) was noticed with PVK: **HT₂** (10 wt.%) as an emitting material (**Device C**) together with bathocuproine (BCP) and tris-(8-hydroxyquinoline)aluminum (Alq₃) as hole blocking material and electron transport material, respectively. In addition, the device exhibited a relatively low V_{onset} of 6.41 V. The improvement in the performance of the **Device C** can be ascribed to efficient transfer of exciton energy to emissive dopant from the host material and/or a balanced injection of charge carriers (hole/electron) into the emitter layer (Ulla et al. 2014, 2017). Here BCP confines the reductant holes in the emitting layer that didn't recombine with the electrons in the emitting zone (Chidirala et al. 2016). Further improvement in the performance of the device was noticed for **Device D** with PVK as a hole transport material which showed better efficiencies of η_c : 1.06 cdA^{-1} , η_p : 0.35 lmW^{-1} , η_{EQE} : 0.69 % and L_{max} of 1055 cdm^{-2} than that of **Device C**. Here, V_{onset} was further reduced to 5.69 V. All the OLEDs under investigation emitted in the yellowish green region when ITO was positively biased. The steady-state electroluminescence (EL) spectra (**Fig 5.2b**) of the OLEDs operating at the 20 V showed emission peaks at $\sim 560 \text{ nm}$ with a full-width half maxima of $\sim 89 \text{ nm}$. It can be noted that, the EL spectrum and thin film fluorescence spectrum of **HT₂** (**Fig 5.2b**) are almost same indicating that, both are originating from the same excited state. **Fig 5.2c** shows that, there is no change in the shape and peak of the EL spectra demonstrating that, the devices possess excellent spectral stability. The CIE chromaticity coordinates (0.425, 0.553) corresponding to bright green emission were determined using the EL spectra of the OLEDs at 15 V. **Fig.5.2d** depicts the chromaticity diagram of the OLEDs. It is worth mentioning that, the investigated OLEDs are unoptimized. The device performance can be improved by further optimizations. These observations offer the potential use of **HT₂**

in OLED applications with an additional scope to improve, by slight modifications in the molecular design and device architecture.

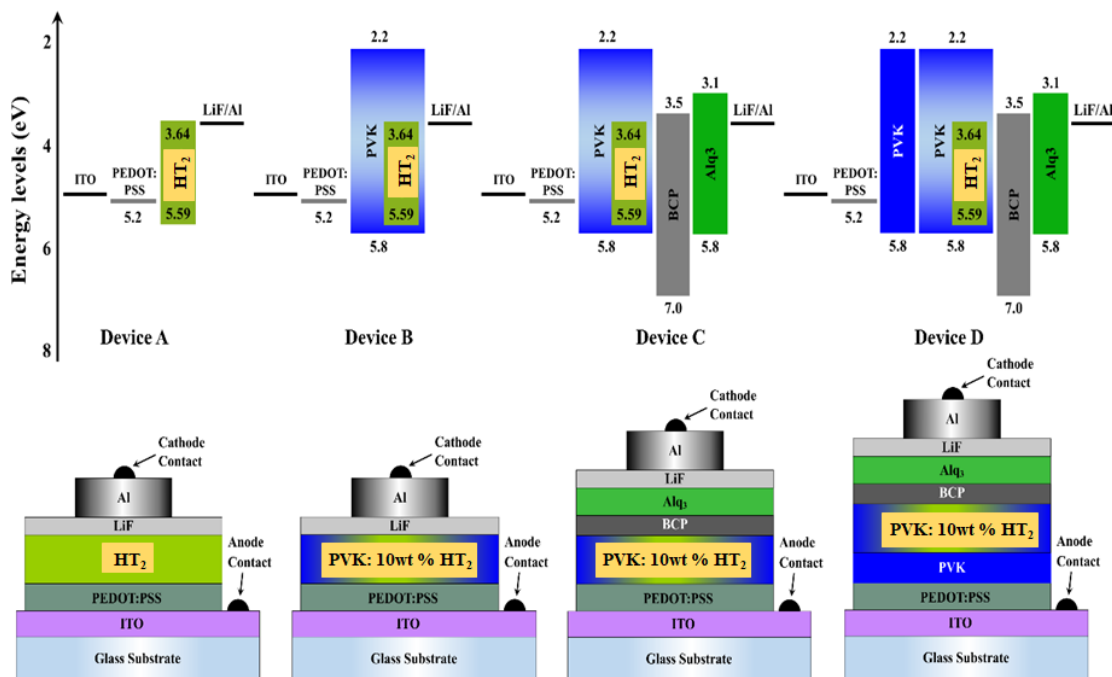


Figure 5.1 Energy-level diagram of the materials used and schematic of the different OLED architectures

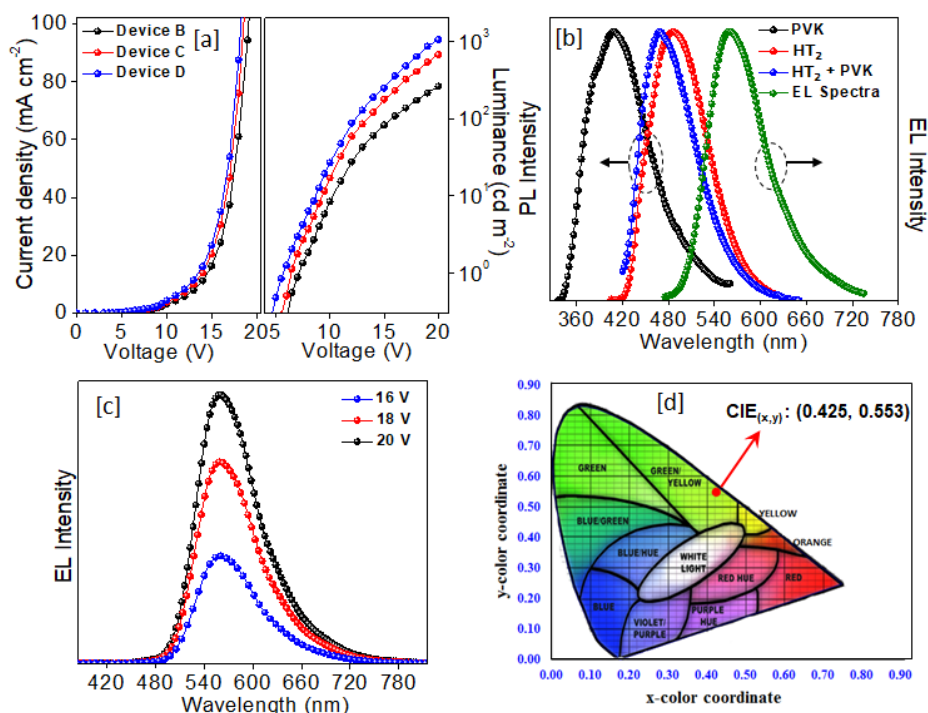


Figure 5.2 (a) J-V-L characteristics; (b) PL spectra of PVK, HT₂, PVK:10 wt% HT₂ thin films and EL spectra of **Device D**; (c) EL spectra of **Device D** at different bias voltages and (d) Chromaticity diagram of the OLEDs

5.4.2 OLED device performance of HT₁₂ (Series-3)

Among the alkyl members of **Series-3**, **HT₁₂** was used as a representative electroluminescent material for the OLED fabrication. In the device study, it was employed as a sole emissive material as well as an emissive dopant material with three different device architectures. The schematic illustration of the different device structures and the energy level diagram of the materials used in the device are depicted in **Figs 5.3a-b**. The new device structures are as follows:

Device E: ITO/ PEDOT: PSS/ **HT₁₂**/ LiF/ Al

Device F: ITO/ PEDOT: PSS/ PVK: **HT₁₂**/ LiF /Al

Device G: ITO/ PEDOT: PSS/ PVK: **HT₁₂**/ BCP/ Alq₃/ LiF /Al

In case of device **E**, **HT₁₂** acted as a sole emissive material; whereas in devices **F** and **G**, 10 wt% of **HT₁₂**, doped in the host poly(9-vinylcarbazole) (PVK) served as the emissive material with appropriate device structures. **Table 5.1** summarizes the key performance data of the newly fabricated LC based OLEDs.

Fig 5.3c displays the (J-V-L) features of the fabricated OLEDs. The **Device E** composing of only **HT₁₂** as an emissive material showed low L_{\max} of 258 cdm^{-2} with η_c of 0.44 cdA^{-1} , η_p of 0.12 lmW^{-1} , and η_{EQE} of 0.29 % at 100 cd m^{-2} . Also, the high drive voltage (V_{onset} , corresponding to 1 cdm^{-2}) of the device was found to be as high as 7.07 V. However, a drastic enhancement in the device performance was observed with PVK: **HT₁₂** (10 wt.%) emitting composite (**Device F**). The increase in the performance of device **F** can be ascribed to the fact that, there is an effective transfer of exciton energy from PVK (host material) to **HT₁₂** (emissive dopant) (Gupta et al. 2018; Yadav et al. 2017). Although the **Device F** showed superior performance compared to the **Device E**, it still had high drive voltage (V_{onset} : 5.79 V) indicating the presence of high charge injection barriers in the device. A balanced flow of charge carriers (electron and hole) is important to obtain maximum recombination, which eventually will result in the high performance of the devices as imbalanced charge transport in emissive layer hampers the performance of the device. Hence, to further improve the device performance and reduce the drive voltage, BCP and Alq₃ were hired as hole blocking material and electron transporting material respectively which is designated as **Device G**. Consequently, the device **G** showed improvement in the device performance (L_{\max} of 1898 cdm^{-2} , η_c of 1.65 cdA^{-1} , η_p of 0.66 lmW^{-1} and η_{EQE} of 0.98 %) with a significant

reduction in the drive voltage (V_{onset} : 4.23 V) compared to **Device E**. The improved device performance can be attributed to the effective transfer of exciton energy from PVK (host) material to **HT**₁₂ (dopant) and due to balanced charge transport in the emissive layer. Also, use of BCP as HBM assisted in confining the reductant holes in the emitting layer which didn't recombine with the electrons in the emitting zone (Chidirala et al. 2016; Tagare et al. 2017, 2018).

All the fabricated OLEDs emitted green light when ITO was positively biased. **Fig. 5.3d** demonstrates EL spectra of the devices at 20 V with peak at ~531 nm and FWHM of ~72 nm. From the **Fig. 5.3d** (inset), it is evident that, the thin film PL spectra of PVK and PVK: 10 wt. % **HT**₁₂ exactly overlap each other revealing that, both are originating from the same excited state. In addition, the shapes of the EL spectra of the devices were similar to the thin film PL spectra of PVK: **HT**₁₂ (**Fig 5.3d**) which is also due to same excited state origin. The devices demonstrated excellent spectral stability as the EL spectra over a wide range of operating voltages did not show any change in shape and peak. This also indicated that, during device operation, **HT**₁₂ exhibits excellent thermal stability. The CIE chromaticity coordinates determined using the EL spectra of the OLEDs at 20 V are (0.312, 0.606) corresponding to green emission. It is to note that, the investigated OLEDs are unoptimized. Further optimizations can improve the device performance. The results revealed that, these phenanthrene-cyanopyridone based emissive LC materials have considerable potentiality in OLED applications with further scope to molecular design and device architecture.

Table 5.1 Electroluminescent performance data of newly fabricated OLEDs

	Device	^a V_{onset} (V)	^b L_{max} (cd m ⁻²)	^c η_{c} (cd A ⁻¹)	^d η_{p} (lm W ⁻¹)	^e η_{EQE} (%) ^f
Series-1	A ^f	11.0	-	-	-	-
	B	7.12	261	0.33	0.09	0.14
	C	6.41	673	0.86	0.26	0.51
	D	5.69	1055	1.06	0.35	0.69
Series-3	E	7.07	258	0.44	0.12	0.29
	F	5.79	1463	1.33	0.38	0.73
	G	4.23	1898	1.65	0.66	0.98

^a V_{onset} , turn-on voltage at luminance of 1 cd m^{-2} ; ^b Luminance at 20 V, ^c current efficiency, ^d power efficiency and ^e external quantum efficiency at 100 cd m^{-2} , ^f Very weak emission was observed

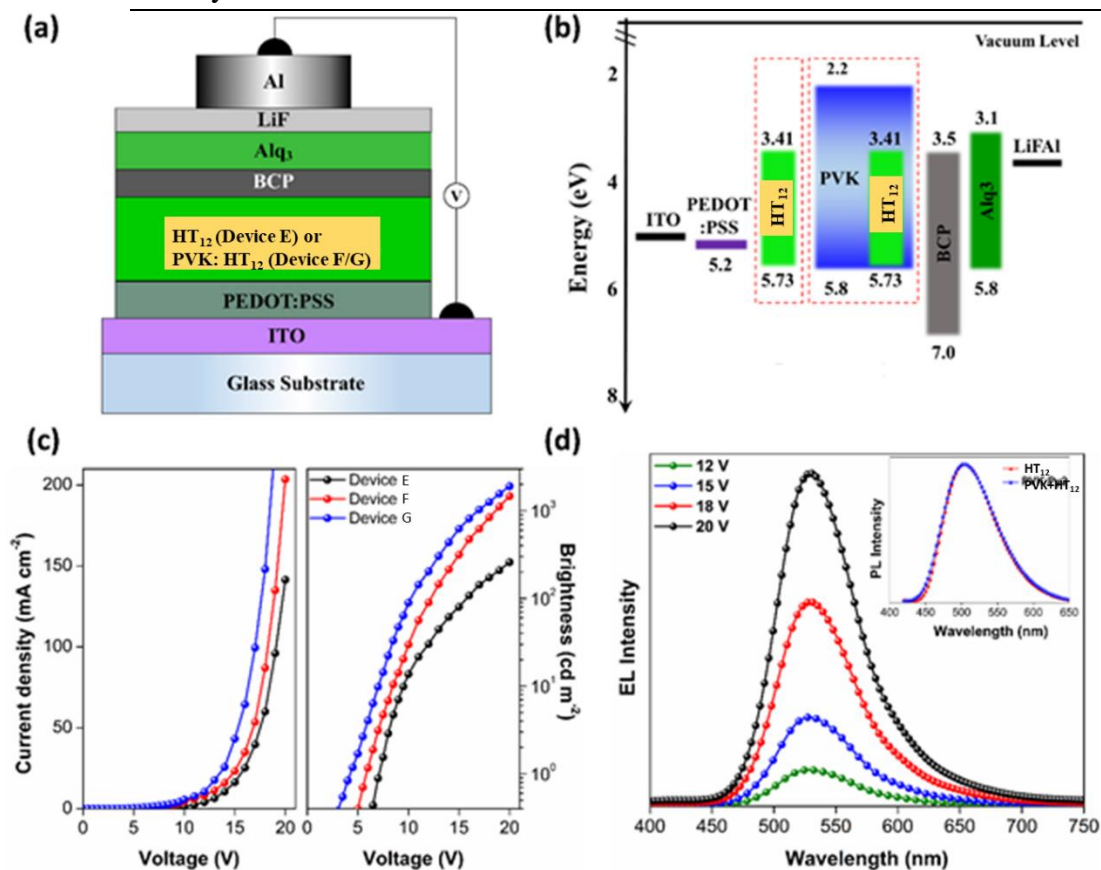


Figure 5.3 (a) Schematic diagram of OLEDs (b) energy-level diagram of the different OLED architectures; (c) J-V-L characteristics; (d) EL spectra of **Device G** at different bias voltages (the inset shows the PL spectra of **HT₁₂** and **PVK: HT₁₂** thin films)

5.5 CONCLUSION

The electroluminescence performance of **HT₂** and **HT₁₂** in the doped and non-doped OLED devices (**Devices-A to G**) displayed encouraging results. Among them, a doped device composed of **HT₁₂** as an emissive layer marks the highest deep-green electroluminescence with a brightness of 1898 cd m^{-2} at 4.23V having CIE coordinates (0.312, 0.606). Evidently, the observed results suggested that, new design strategies for emitters offer efficient materials for OLEDs with improved efficiency. Thus, by proper tailoring of donors attached to heterocyclic core, it would be possible to improve the quantum yield of the materials and hence further enhancement in device efficiency.

SUMMARY AND CONCLUSIONS

Abstract

This chapter contains the summary and significant conclusions drawn from the present research study. It also includes a brief account on scope of the future work.

6.1 SUMMARY

Organic π -conjugated molecules are gaining substantial attention because of their promising candidature in low-cost, eco-friendly, flexible and large-area electronics. Amongst them, the nano segregation of disc-like molecules into one-dimensional columnar (Col) stacking through the non-covalent interactions mainly by co-facial π - π stacking along the longer axis are noteworthy. Moreover, discotics offer advantageous features of highly anisotropic ordered self-assembly, self-healing and great sensitivity towards external stimuli without losing ordered structures. These features render them efficient platform materials in the fabrication of various optical and electronic devices. Till today, a wide range of DLCs were designed and developed to realize the successful employment in various optoelectronic devices.

In this context, the present research work mainly focused on the molecular design and synthesis of unconventional structural molecules based on various heterocyclic cores, which favour the formation of thermodynamically stable mesophases with exciting optical and electronic properties. Also, it has been aimed to develop the optoelectronic device by employing the new mesogenic materials.

Based on the thorough literature survey, six new series (**Series 1-6**) of heterocyclic structures (**HT₁₋₃₅**) were designed by using donor-accepter strategy. In the designed molecules, various heterocycles such as cyanopyridone (**Series-1** and **3**), cyanopyridine (**Series-2**), rhodanine (**Series-4**), maleimide (**Series-5**), boron difluoride complex (**Series-6**) were integrated as core moieties along with variety of alkoxy aryl motifs. The designed molecules were successfully synthesised by adopting numerous straightforward and multistep synthesis protocols. Their structures were confirmed by set of spectral techniques and elemental analysis. Further, all the compounds were subjected to detailed mesomorphic studies with the help of combination of three methods. Furthermore, photophysical and electrochemical properties were studied by

experimental methods and theoretical simulations to examine their potentiality in the optoelectronic devices. Based on the material properties, two compounds **HT₂** and **HT₁₂** were used as active emissive component to fabricate the multi-layer OLED devices and their performances in the devices were studied in detail.

6.2 CONCLUSIONS

On basis of results of the present research work, the following significant conclusions were drawn.

- 1 Based on the literature survey, six new series of (35) molecules carrying cyanopyridone, cyanopyridine, rhodanine and maleimide and BF₂ complex heterocyclic cores appended to different aromatic moieties with variable peripheral alkoxy tails were successfully designed and synthesized through multi-step synthetic routes. The reaction conditions were rationally optimized with respect to many parameters to get compounds with maximum yield. Further, purification methods were developed.
- 2 The chemical structures of all the newly synthesized intermediates as well as target compounds were established by various spectral techniques.
- 3 The mesomorphic investigations of the final compounds explored that, stable columnar morphology is dominating in almost all the series of compounds, although they are structurally dissimilar.
- 4 The flying bird shaped cyanopyridone derivatives (**HT₁₋₄**) of **Series-1** were shown to exhibit H-bonded assisted Col_{ob}, Col_{ho}, Col_{hd} mesophases; the unsymmetrical star-shaped cyanopyridine structures (**HT₈₋₁₀**) of **Series-2** exclusively displayed room temperature Col_h mesomorphism; the geometrically pseudodiscoidal cyanopyridone-phenanthrene hybrids (**HT₁₁₋₁₃**) of **Series-3** exhibited mesomorphic transition from Col_r to Col_h as a function of temperature; among the alkyl members of **Series-4**, the wedge-shaped derivative with longer alkoxy chains at appropriate position (**HT₂₃**) was found to be self-assembled into supramolecular Col_h by the formation of disc-like H-bonded trimer; the maleimide derivatives with varied aromatic core segments

resulting tapered configuration (**HT**₂₈₋₂₉) of **Series-5** and wedge (**HT**₃₀) structures of **Series-5** displayed SmA and Col_h mesophases, respectively; BF₂ heterocyclic complexes (**HT**₃₂₋₃₅) of **Series-6** were found to organize into Col_h and Col_r morphologies.

- 5 The photophysical studies revealed that, except compounds of **Series-5**, all the new materials were good dyes and they emit light in wide spectral regions including pure blue (~350 nm), greenish blue (~380 nm) and greenish yellow (~ 510 nm). In addition, they possess non-polar ground state and slightly polar excited states as evidenced by solvatochromic studies.
- 6 The experimental and theoretical studies on electrochemical behaviour of LC materials exposed their considerable redox property and low lying LUMO levels with narrow energy band gap (1.95-2.32 eV), as well as semiconducting nature.
- 7 The two high luminescence columnar LC materials derived from cyanopyridone core (**HT**₂ and **HT**₁₂) were employed as emissive layer in the fabrication of multi-layer OLED devices with different configuration. Among the device structures of **HT**₂, the host-guest configured device fabricated with hole blocking material and electron transport material showed highest efficiencies with high luminance (L_{\max}) of 1055 cdm^{-2} , current efficiency (η_c) of 1.06 cdA^{-1} , power efficiency (η_p) of 0.35 lmW^{-1} , external quantum efficiency (η_{EQE}) of 0.69 % and low driving voltage (V_{onset} , corresponding to 1 cdm^{-2}) of 5.69 V. Whereas, host-guest OLED device composed of **HT**₁₂ emissive component witnessed superior performance ($L_{\max} = 1898 \text{ cdm}^{-2}$, $\eta_c =$ of 1.65 cdA^{-1} , $\eta_p =$ of 0.66 lmW^{-1} , $\eta_{\text{EQE}} = 0.98 \%$ and $V_{\text{onset}} 4.23 \text{ V}$) over **HT**₂ based devices, which may be due to the presence of π -rich phenanthrene core and mesomorphism at room temperature at ambient conditions with higher PL quantum yield of **HT**₁₂.

6.3 SCOPE FOR FUTURE WORK

The present work provided a novel guideline and versatile approach to the design and development of new unconventional molecules to achieve imperative columnar mesomorphism in virtue of their application in the fabrication of efficient OLEDs. For the first time, OLEDs were fabricated by using emissive H-bond-assisted columnar liquid crystals. Therefore, adequate tailoring of donors and accepters, it would be possible to improve the quantum yield of the materials and hence further enhancement in device efficiency. These CLC-based OLEDs can be used as a potential backlight for liquid crystal displays (LCDs) by replacing the expensive backlight and absorbing colour filters, which correspondingly reduces the overall cost of the device and significantly enhances the emission efficiency.

It is anticipated that these materials, exhibiting dye property at the highly ordered columnar LC state with the 1-D semiconducting behaviour are promising candidates for their application in other optoelectronic devices like OPV and OTFT.

REFERENCES

- Achalkumar, A. S., Hiremath, U. S., Rao, D. S., Prasad, S. K., and Yelamaggad, C. V. (2012). "Self-assembly of hekates-tris (N-salicylideneaniline)s into columnar structures: synthesis and characterization." *J. Org. Chem.*, 78(2), 527–544.
- Achalkumar, A. S., Rao, D. S. S., and Yelamaggad, C. V. (2014). "Non-symmetric dimers comprising chalcone and cholesterol entities: an investigation on structure–property correlations." *New J. Chem.*, 38(9), 4235–4248.
- Alvarez, L., Barberá, J., Puig, L., Romero, P., Serrano, J. L., and Sierra, T. (2006). "Supramolecular chirality of columnar mesophases consisting of H-bonded complexes of melamine and polycatenar benzoic acids." *J. Mater. Chem.*, 16(38), 3768–3773.
- Attias, A.-J., Cavalli, C., Donnio, B., Guillon, D., Hapiot, P., and Malthête, J. (2002a). "Columnar mesophase from a new disclike mesogen based on a 3, 5-dicyano-2, 4, 6-tristyrylpyridine core." *Chem. Mater.*, 14(1), 375–384.
- Bala, I., Singh, H., Battula, V. R., Gupta, S. P., De, J., Kumar, S., Kailasam, K., and Pal, S. K. (2017). "Heptazine: an Electron-Deficient Fluorescent Core for Discotic Liquid Crystals." *Chem.- Eur. J.*, 23(59), 14718–14722.
- Barberá, J., Giménez, R., and Serrano, J. L. (2000). "Mesogenic pyrazaboles: synthesis, properties, and structural characterization." *Chem. Mater.*, 12(2), 481–489.
- Beltrán, E., Cavero, E., Barberá, J., Serrano, J. L., Elduque, A., and Giménez, R. (2009). "Self-Assembly in Helical Columnar Mesophases and Luminescence of Chiral 1H-Pyrazoles." *Chem.- Eur. J.*, 15(36), 9017–9023.
- Beltrán, E., Serrano, J. L., Sierra, T., and Giménez, R. (2010). "Tris (triazolyl) triazine via click-chemistry: AC 3 electron-deficient core with liquid crystalline and luminescent properties." *Org. Lett.*, 12(7), 1404–1407.
- Beltrán, E., Serrano, J. L., Sierra, T., and Giménez, R. (2012). "Functional star-shaped tris (triazolyl) triazines: columnar liquid crystal, fluorescent, solvatofluorochromic and electrochemical properties." *J. Mater. Chem.*, 22(16), 7797–7805.

Blanco, H., Iguarbe, V., Barberá, J., Serrano, J. L., Elduque, A., and Giménez, R. (2016a). "Supramolecular Columnar Liquid Crystals with Tapered-Shape Simple Pyrazoles Obtained by Efficient Henry/Michael Reactions." *Chem.- Eur. J.*, 22(14), 4924–4930.

Blanco, H., Iguarbe, V., Barberá, J., Serrano, J. L., Elduque, A., and Giménez, R. (2016b). "Supramolecular Columnar Liquid Crystals with Tapered-Shape Simple Pyrazoles Obtained by Efficient Henry/Michael Reactions." *Chem. Eur. J.*, 22(14), 4924–4930.

Brouwer, A. M. (2011). "Standards for photoluminescence quantum yield measurements in solution (IUPAC Technical Report)." *Pure Appl. Chem.*, 83(12), 2213–2228.

Brütting, W., Frischeisen, J., Schmidt, T. D., Scholz, B. J., and Mayr, C. (2013). "Device efficiency of organic light-emitting diodes: Progress by improved light outcoupling." *Phys. Status Solidi A*, 210(1), 44–65.

Buckley, A. (2013). "*Organic light-emitting diodes (OLEDs): Materials, devices and applications.*" Elsevier.

Bushby, R. J., and Kawata, K. (2011). "Liquid crystals that affected the world: discotic liquid crystals." *Liq. Cryst.*, 38(11–12), 1415–1426.

Camerel, F., Donnio, B., and Ziessel, R. (2011). "Liquid-crystalline functional carbazole and naphthalene platforms." *Soft Matter*, 7(2), 412–428.

Cavero, E., Uriel, S., Romero, P., Serrano, J. L., and Giménez, R. (2007). "Tetrahedral zinc complexes with liquid crystalline and luminescent properties: interplay between nonconventional molecular shapes and supramolecular mesomorphic order." *J. Am. Chem. Soc.*, 129(37), 11608–11618.

Chandrasekhar, S., Sadashiva, B. K., and Suresh, K. A. (1977). "Liquid crystals of disc-like molecules." *pramana*, 9(5), 471–480.

- Chen, C.-T. (2004). "Evolution of red organic light-emitting diodes: materials and devices." *Chem. Mater.*, 16(23), 4389–4400.
- Chen, D., Su, S.-J., and Cao, Y. (2014a). "Nitrogen heterocycle-containing materials for highly efficient phosphorescent OLEDs with low operating voltage." *J. Mater. Chem. C*, 2(45), 9565–9578.
- Chen, H.-W., Lee, J.-H., Lin, B.-Y., Chen, S., and Wu, S.-T. (2018). "Liquid crystal display and organic light-emitting diode display: present status and future perspectives." *Light Sci. Appl.*, 7(3), 17168.
- Cheng, H., Gao, H., Wang, T., Xia, M., and Cheng, X. (2018). "Polycatenar bent-shaped liquid crystals with columnar and cubic phases: Synthesis multi-responsive organogels and chemosensors." *J. Mol. Liq.*, 249, 723–731.
- Cheng, X.-H., and Gao, H.-F. (2015). "Hydrogen Bonding for Supramolecular Liquid Crystals." *Hydrog. Bond. Supramol. Mater.*, Springer, 133–183.
- Chidirala, S., Ulla, H., Valaboju, A., Kiran, M. R., Mohanty, M. E., Satyanarayan, M. N., Umesh, G., Bhanuprakash, K., and Rao, V. J. (2016). "Pyrene–Oxadiazoles for Organic Light-Emitting Diodes: Triplet to Singlet Energy Transfer and Role of Hole-Injection/Hole-Blocking Materials." *J. Org. Chem.*, 81(2), 603–614.
- Cho, B.-K., and Kim, S.-H. (2014). "Supramolecular transformation from ordered columnar to disordered columnar to tetragonal micellar structures in clicked dodeca-alkylated discotic triphenylene liquid crystals." *Soft Matter*, 10(4), 553–559.
- Crosby, G. A., and Demas, J. N. (1971). "Measurement of photoluminescence quantum yields. Review." *J. Phys. Chem.*, 75(8), 991–1024.
- Dai, H., Yang, X., Tan, X., Su, F., Cheng, X., Liu, F., and Tschierske, C. (2013). "Liquid crystalline 2-thienyl-4, 6-diamino-1, 3, 5-triazines exhibiting Im 3 [combining macron] m and Pm 3 [combining macron] n micellar cubic phases in an inverted sequence." *Chem. Commun.*, 49(90), 10617–10619.

Detert, H., Lehmann, M., and Meier, H. (2010). "Star-shaped conjugated systems." *Materials*, 3(5), 3218–3330.

Diaz, E., Elgueta, E., Sanchez, S. A., Barberá, J., Vergara, J., Parra, M., and Dahrouch, M. (2017). "Hybrid photoluminescent materials containing a benzobisthiazole core for liquid crystal and gel applications." *Soft Matter*, 13(9), 1804–1815.

Feringán, B., Romero, P., Serrano, J. L., Folcia, C. L., Etxebarria, J., Ortega, J., Termine, R., Golemme, A., Giménez, R., and Sierra, T. (2016). "H-Bonded Donor–Acceptor Units Segregated in Coaxial Columnar Assemblies: Toward High Mobility Ambipolar Organic Semiconductors." *J. Am. Chem. Soc.*, 138(38), 12511–12518.

Fuchs, P., Tschierske, C., Raith, K., Das, K., and Diele, S. (2002). "A thermotropic mesophase comprised of closed micellar aggregates of the normal type." *Angew. Chem.*, 114(4), 650–653.

Gallardo, H., Ferreira, M., Vieira, A. A., Westphal, E., Molin, F., Eccher, J., and Bechtold, I. H. (2011). "Columnar mesomorphism of bent-rod mesogens containing 1, 2, 4-oxadiazole rings." *Tetrahedron*, 67(49), 9491–9499.

Gaspar, D. J., and Polikarpov, E. (2015). "*OLED fundamentals: materials, devices, and processing of organic light-emitting diodes.*" CRC Press.

Godumala, M., Choi, S., Cho, M. J., and Choi, D. H. (2016). "Thermally activated delayed fluorescence blue dopants and hosts: from the design strategy to organic light-emitting diode applications." *J. Mater. Chem. C*, 4(48), 11355–11381.

Goodby, J. W., Collings, P. J., Kato, T., Tschierske, C., Gleeson, H. F., and Raynes, P. (2014). "Handbook of liquid crystals." Wiley-VCH

Gorp, J. J. van, Vekemans, J. A., and Meijer, E. W. (2002). "C₃-symmetrical supramolecular architectures: Fibers and organic gels from discotic trisamides and trisureas." *J. Am. Chem. Soc.*, 124(49), 14759–14769.

Gupta, R. K., Pathak, S. K., De, J., Pal, S. K., and Achalkumar, A. S. (2018). "Room temperature columnar liquid crystalline self-assembly of acidochromic, luminescent,

star-shaped molecules with cyanovinylene chromophores.” *J. Mater. Chem. C*, 6(7), 1844–1852.

Gupta, R. K., Pathak, S. K., Pradhan, B., Rao, D. S., Prasad, S. K., and Achalkumar, A. S. (2015). “Self-assembly of luminescent N-annulated perylene tetraesters into fluid columnar phases.” *Soft Matter*, 11(18), 3629–3636.

Gupta, R. K., Ulla, H., Satyanarayan, M. N., and Sudhakar, A. A. (2018). “A Perylene-Triazine-Based Star-Shaped Green Light Emitter for Organic Light Emitting Diodes.” *Eur. J. Org. Chem.*, 2018(13), 1608–1613.

Hayer, A., De Halleux, V., Köhler, A., El-Garouhy, A., Meijer, E. W., Barberá, J., Tant, J., Levin, J., Lehmann, M., and Gierschner, J. (2006). “Highly fluorescent crystalline and liquid crystalline columnar phases of pyrene-based structures.” *J. Phys. Chem. B*, 110(15), 7653–7659.

Hirschberg, J. K., Brunsveld, L., Ramzi, A., Vekemans, J. A., Sijbesma, R. P., and Meijer, E. W. (2000). “Helical self-assembled polymers from cooperative stacking of hydrogen-bonded pairs.” *Nature*, 407(6801), 167.

Huck, D. M., Nguyen, H. L., Donnio, B., and Bruce, D. W. (2004). “Polycatenar, bent-core pyridines and their discotic complexes with silver (I).” *Liq. Cryst.*, 31(4), 503–507.

Jiao, S., Men, J., Ao, C., Huo, J., Ma, X., and Gao, G. (2015). “Synthesis and mesophases of C_{3h}-symmetric 2, 4, 6-tris (2-hydroxyphenyl)-1, 3, 5-triazine derivatives with intramolecular hydrogen bonding networks.” *Tetrahedron Lett.*, 56(37), 5185–5189.

Jou, J.-H., Kumar, S., Agrawal, A., Li, T.-H., and Sahoo, S. (2015). “Approaches for fabricating high efficiency organic light emitting diodes.” *J. Mater. Chem. C*, 3(13), 2974–3002.

Kaafarani, B. R. (2010). “Discotic liquid crystals for opto-electronic applications.” *Chem. Mater.*, 23(3), 378–396.

- Kalyani, N. T., and Dhoble, S. J. (2012). "Organic light emitting diodes: Energy saving lighting technology—A review." *Renew. Sustain. Energy Rev.*, 16(5), 2696–2723.
- Kamtekar, K. T., Monkman, A. P., and Bryce, M. R. (2010). "Recent advances in white organic light-emitting materials and devices (WOLEDs)." *Adv. Mater.*, 22(5), 572–582.
- Kido, J., and Okamoto, Y. (2002). "Organo lanthanide metal complexes for electroluminescent materials." *Chem. Rev.*, 102(6), 2357–2368.
- Kleppinger, R., Lillya, C. P., and Yang, C. (1995a). "Self-Assembling Discotic Mesogens." *Angew. Chem. Int. Ed.*, 34(15), 1637–1638.
- Konidena, R. K., and Thomas, K. J. (2017). "Star-Shaped Asymmetrically Substituted Blue Emitting Carbazoles: Synthesis, Photophysical, Electrochemical and Theoretical Investigations." *ChemistrySelect*, 2(25), 7514–7524.
- Konidena, R. K., Thomas, K. J., Singh, M., and Jou, J.-H. (2016). "Thienylphenothiazine integrated pyrenes: an account on the influence of substitution patterns on their optical and electroluminescence properties." *J. Mater. Chem. C*, 4(19), 4246–4258.
- Kozhevnikov, V. N., Donnio, B., and Bruce, D. W. (2008). "Phosphorescent, terdentate, liquid-crystalline complexes of platinum (II): stimulus-dependent emission." *Angew. Chem.*, 120(33), 6382–6385.
- Kumar, M., Gowda, A., and Kumar, S. (2017). "Discotic Liquid Crystals with Graphene: Supramolecular Self-assembly to Applications." *Part. Part. Syst. Charact.*, 34(9), 1700003.
- Kumar, P., Shankar Rao, D. S., Krishna Prasad, S., and Jayaraman, N. (2017). "Connector type-controlled mesophase structures in poly(propyl ether imine) dendritic liquid crystals of identical dendrimer generations." *J. Polym. Sci. Part Polym. Chem.*, 55(22), 3665–3678.
- Kumar, S. (2011). *Chemistry of discotic liquid crystals: from monomers to polymers*. Boca Raton (FL): Taylor and Francis, CRC Press.

- Kumar, S., and Gupta, S. K. (2011). "Novel triphenylenoimidazole discotic liquid crystals." *Tetrahedron Lett.*, 52(41), 5363–5367.
- Laschat, S., Baro, A., Steinke, N., Giesselmann, F., Haegele, C., Scalia, G., Judele, R., Kapatsina, E., Sauer, S., and Schreivogel, A. (2007). "Discotic liquid crystals: from tailor-made synthesis to plastic electronics." *Angew. Chem. Int. Ed.*, 46(26), 4832–4887.
- Lee, C.-H., and Yamamoto, T. (2002). "Synthesis of liquid-crystalline, highly luminescent π -conjugated 1, 3, 5-triazine derivatives by palladium-catalyzed cross-coupling reaction." *Mol. Cryst. Liq. Cryst.*, 378(1), 13–21.
- Lee, H.-K., Lee, H., Ko, Y. H., Chang, Y. J., Oh, N.-K., Zin, W.-C., and Kim, K. (2001). "Synthesis of a nanoporous polymer with hexagonal channels from supramolecular discotic liquid crystals." *Angew. Chem.*, 113(14), 2741–2743.
- Lehmann, M. (2009). "Star Mesogens (Hekates)—Tailor-Made Molecules for Programming Supramolecular Functionality." *Chem.-Eur. J.*, 15(15), 3638–3651.
- Lehmann, O. (1889). "Über fließende krystalle." *Z. Für Phys. Chem.*, 4(1), 462–472.
- Levelut, A. M. (1983). "Structures des phases mésomorphes formées de molécules discoïdes." *J. Chim. Phys.*, 80, 149–161.
- Li, D., Zhang, H., and Wang, Y. (2013). "Four-coordinate organoboron compounds for organic light-emitting diodes (OLEDs)." *Chem. Soc. Rev.*, 42(21), 8416–8433.
- Li, W., Liu, D., Shen, F., Ma, D., Wang, Z., Feng, T., Xu, Y., Yang, B., and Ma, Y. (2012). "A Twisting Donor-Acceptor Molecule with an Intercrossed Excited State for Highly Efficient, Deep-Blue Electroluminescence." *Adv. Funct. Mater.*, 22(13), 2797–2803.
- Lobo, C. V., Prasad, S. K., and Rao, D. S. (2004). "X-ray and dielectric measurements of the smectic-A–hexatic-B transition in bulk and confined geometries." *Phys. Rev. E*, 69(5), 051706.

- Maly, K. E., Dauphin, C., and Wuest, J. D. (2006). "Self-assembly of columnar mesophases from diaminotriazines." *J. Mater. Chem.*, 16(48), 4695–4700.
- Mandal, J., Krishna Prasad, S., Rao, D. S., and Ramakrishnan, S. (2014). "Periodically clickable polyesters: study of intrachain self-segregation induced folding, crystallization, and mesophase formation." *J. Am. Chem. Soc.*, 136(6), 2538–2545.
- Maruyama, S., Sato, K., and Iwahashi, H. (2010). "Room temperature liquid porphyrins." *Chem. Lett.*, 39(7), 714–716.
- Meier, G., Sackmann, E., and Grabmaier, J. G. (2012). *Applications of liquid crystals*. Springer Science & Business Media.
- Moyano, S., Barberá, J., Diosdado, B. E., Serrano, J. L., Elduque, A., and Giménez, R. (2013). "Self-assembly of 4-aryl-1 H-pyrazoles as a novel platform for luminescent supramolecular columnar liquid crystals." *J. Mater. Chem. C*, 1(18), 3119–3128.
- Nguyen, M. L., Shin, T. J., Kim, H.-J., and Cho, B.-K. (2017). "Oriented columnar films of a polar 1, 2, 3-triazole-based liquid crystal prepared by applying an electric field." *J. Mater. Chem. C*, 5(32), 8256–8265.
- O'Neill, M., and Kelly, S. M. (2011). "Ordered materials for organic electronics and photonics." *Adv. Mater.*, 23(5), 566–584.
- Pal, S. K., Bala, I., Gupta, S. P., and De, J. (2017). "Room temperature columnar nematic and soft crystalline columnar assemblies of a new series of perylene-centered disc tetramers." *Chem.-Eur. J.*, 23(52), 12767-12778
- Pandith, A., Uddin, N., Choi, C. H., and Kim, H.-S. (2017). "Highly selective imidazole-appended 9, 10-N, N'-diaminomethylantracene fluorescent probe for switch-on Zn²⁺ detection and switch-off H₂PO₄⁻ and CN⁻ detection in 80 % aqueous DMSO, and applications to sequential logic gate operations." *Sens. Actuators B Chem.*, 247, 840–849.

- Park, S., and Cho, B.-K. (2015). "Sequential phase transformation of propeller-like C 3-symmetric liquid crystals from a helical to ordered to disordered hexagonal columnar structure." *Soft Matter*, 11(1), 94–101.
- Pieterse, K., Hal, P. A. van, Kleppinger, R., Vekemans, J. A., Janssen, R. A., and Meijer, E. W. (2001). "An electron-deficient discotic liquid-crystalline material." *Chem. Mater.*, 13(8), 2675–2679.
- Pieterse, K., Lauritsen, A., Schenning, A. P., Vekemans, J. A., and Meijer, E. W. (2003). "Symmetrical Electron-Deficient Materials Incorporating Azaheterocycles." *Chem. Eur. J.*, 9(22), 5597–5604.
- Pradhan, B., Gupta, M., Pal, S. K., and Achalkumar, A. S. (2016). "Multifunctional hexacatenar mesogen exhibiting supergelation, AIEE and its ability as a potential volatile acid sensor." *J. Mater. Chem. C*, 4(41), 9669–9673.
- Reichardt, C. (1994). "Solvatochromic dyes as solvent polarity indicators." *Chem. Rev.*, 94(8), 2319–2358.
- Reinitzer, F. (1888). "Beiträge zur kenntniss des cholesterins." *Monatshefte Für ChemieChemical Mon.*, 9(1), 421–441.
- Reinitzer, F. (1989). "Contributions to the knowledge of cholesterol." *Liq. Cryst.*, 5(1), 7–18.
- Ren, Y., Zhang, R., Yan, C., Wang, T., Cheng, H., and Cheng, X. (2017). "Self-assembly, AIEE and mechanochromic properties of amphiphilic α -cyanostilbene derivatives." *Tetrahedron*, 73(35), 5253–5259.
- Roy, B., De, N., and Majumdar, K. C. (2012). "Advances in Metal-Free Heterocycle-Based Columnar Liquid Crystals." *Chem.- Eur. J.*, 18(46), 14560–14588.
- Sasaki, S., Drummen, G. P., and Konishi, G. (2016). "Recent advances in twisted intramolecular charge transfer (TICT) fluorescence and related phenomena in materials chemistry." *J. Mater. Chem. C*, 4(14), 2731–2743.

- Segura, J. L. (1998). "The chemistry of electroluminescent organic materials." *Acta Polym.*, 49(7), 319–344.
- Sergeyev, S., Pisula, W., and Geerts, Y. H. (2007). "Discotic liquid crystals: a new generation of organic semiconductors." *Chem. Soc. Rev.*, 36(12), 1902–1929.
- Setia, S., and Pal, S. K. (2016). "Unsymmetrically substituted room temperature discotic liquid crystals based on hexa-peri-hexabenzocoronene core." *ChemistrySelect*, 1(5), 880–885.
- Shanker, G., Prehm, M., Yelamaggad, C. V., and Tschierske, C. (2011). "Benzylidenehydrazine based room temperature columnar liquid crystals." *J. Mater. Chem.*, 21(14), 5307–5311.
- Sivadas, A. P., Kumar, N. S., Prabhu, D. D., Varghese, S., Prasad, S. K., Rao, D. S., and Das, S. (2014). "Supergelation via purely aromatic π - π driven self-assembly of pseudodiscotic oxadiazole mesogens." *J. Am. Chem. Soc.*, 136(14), 5416–5423.
- Suarez, M., Lehn, J.-M., Zimmerman, S. C., Skoulios, A., and Heinrich, B. (1998). "Supramolecular liquid crystals. Self-assembly of a trimeric supramolecular disk and its self-organization into a columnar discotic mesophase." *J. Am. Chem. Soc.*, 120(37), 9526–9532.
- Tagare, J., Ulla, H., Kajjam, A. B., Satyanarayan, M. N., and Vaidyanathan, S. (2017). "Star-Shaped Phenanthroimidazole-Triphenylamine-Based Yellow Organic Emitter for Organic Light Emitting Diodes." *ChemistrySelect*, 2(8), 2611–2620.
- Tagare, J., Ulla, H., Satyanarayan, M. N., and Vaidyanathan, S. (2018). "Synthesis, photophysical and electroluminescence studies of new triphenylamine-phenanthroimidazole based materials for organic light emitting diodes." *J. Lumin.*, 194, 600–609.
- Tagare, J., Ulla, H., Satyanarayan, M. N., and Vaidyanathan, S. (2018). "Efficient non-doped bluish-green organic light emitting devices based on N1 functionalized star-shaped phenanthroimidazole fluorophores." *J. Photochem. Photobiol. Chem.*, 353, 53–64.

- Tanabe, K., Yasuda, T., Yoshio, M., and Kato, T. (2007). "Viologen-based redox-active ionic liquid crystals forming columnar phases." *Org. Lett.*, 9(21), 4271–4274.
- Tang, C. W., and VanSlyke, S. A. (1987). "Organic electroluminescent diodes." *Appl. Phys. Lett.*, 51(12), 913–915.
- Tang, J., Huang, R., Gao, H., Cheng, X., Prehm, M., and Tschierske, C. (2012). "Columnar mesophases of luminescent polycatenar liquid crystals incorporating a 1, 3-substituted benzene ring interconnecting two 1, 3, 4-oxadiazoles." *Rsc Adv.*, 2(7), 2842–2847.
- Tschierske, C. (2013). "Development of Structural Complexity by Liquid-Crystal Self-assembly." *Angew. Chem. Int. Ed.*, 52(34), 8828–8878.
- Tsujimura, T. (2017). *OLED display fundamentals and applications*. John Wiley & Sons.
- Ulla, H., Kiran, M. R., Garudachari, B., Ahipa, T. N., Tarafder, K., Adhikari, A. V., Umesh, G., and Satyanarayan, M. N. (2017). "Blue emitting 1, 8-naphthalimides with electron transport properties for organic light emitting diode applications." *J. Mol. Struct.*, 1143, 344–354.
- Ulla, H., Raveendra Kiran, M., Garudachari, B., Satyanarayan, M. N., Umesh, G., and Isloor, A. M. (2014). "Blue emitting halogen–phenoxy substituted 1,8-naphthalimides for potential organic light emitting diode applications." *Opt. Mater.*, 37(Supplement C), 311–321.
- Varghese, S., Kumar, N. S. S., Krishna, A., Rao, D. S. S., Prasad, S. K., and Das, S. (2009). "Formation of Highly Luminescent Supramolecular Architectures Possessing Columnar Order from Octupolar Oxadiazole Derivatives: Hierarchical Self-Assembly from Nanospheres to Fibrous Gels." *Adv. Funct. Mater.*, 19(13), 2064–2073.
- Wang, L. (2016). "Self-activating liquid crystal devices for smart laser protection." *Liq. Cryst.*, 43(13–15), 2062–2078.

Wang, L., Huang, D., Lam, L., and Cheng, Z. (2017). “Bowlics: history, advances and applications.” *Liq. Cryst. Today*, 26(4), 85–111.

Wang, L., and Li, Q. (2016). “Stimuli-Directing Self-Organized 3D Liquid-Crystalline Nanostructures: From Materials Design to Photonic Applications.” *Adv. Funct. Mater.*, 26(1), 10–28.

Wang, L., and Li, Q. (2018). “Photochromism into nanosystems: towards lighting up the future nanoworld.” *Chem. Soc. Rev.*, 47(3), 1044–1097.

Wang, Z., Lan, Y., Zhong, K., Liang, Y., Chen, T., and Jin, L. Y. (2014). “Liquid Crystalline Assembly of Coil-Rod-Coil Molecules with Lateral Methyl Groups into 3-D Hexagonal and Tetragonal Assemblies.” *Int. J. Mol. Sci.*, 15(4), 5634–5648.

Westphal, E., Bechtold, I. H., and Gallardo, H. (2010). “Synthesis and optical/thermal behavior of new azo photoisomerizable discotic liquid crystals.” *Macromolecules*, 43(3), 1319–1328.

Westphal, E., Prehm, M., Bechtold, I. H., Tschierske, C., and Gallardo, H. (2013). “Room temperature columnar liquid crystalline phases of luminescent non-symmetric star-shaped molecules containing two 1, 3, 4-oxadiazole units.” *J. Mater. Chem. C*, 1(48), 8011–8022.

Wöhrle, T., Wurzbach, I., Kirres, J., Kostidou, A., Kapernaum, N., Litterscheidt, J., Haenle, J. C., Staffeld, P., Baro, A., and Giesselmann, F. (2015). “Discotic liquid crystals.” *Chem. Rev.*, 116(3), 1139–1241.

Wu, Y., Lu, H., Wang, S., Li, Z., and Shen, Z. (2015). “Asymmetric boron-complexes containing keto-isoindoliny and pyridyl groups: solvatochromic fluorescence, efficient solid-state emission and DFT calculations.” *J. Mater. Chem. C*, 3(47), 12281–12289.

Würthner, F., Kaiser, T. E., and Saha-Möller, C. R. (2011). “J-Aggregates: From Serendipitous Discovery to Supramolecular Engineering of Functional Dye Materials.” *Angew. Chem. Int. Ed.*, 50(15), 3376–3410.

- Xu, R.-P., Li, Y.-Q., and Tang, J.-X. (2016). “Recent advances in flexible organic light-emitting diodes.” *J. Mater. Chem. C*, 4(39), 9116–9142.
- Yadav, A. K., Pradhan, B., Ulla, H., Nath, S., De, J., Pal, S. K., Satyanarayan, M. N., and Achalkumar, A. S. (2017). “Tuning the self-assembly and photophysical properties of bi-1, 3, 4-thiadiazole derivatives through electron donor-acceptor interactions and their application in OLEDs.” *J. Mater. Chem. C*, 5(36), 9345–9358.
- Yagai, S., Goto, Y., Karatsu, T., Kitamura, A., and Kikkawa, Y. (2011). “Catenation of Self-Assembled Nanorings.” *Chem.-Eur. J.*, 17(49), 13657–13660.
- Yagai, S., Goto, Y., Lin, X., Karatsu, T., Kitamura, A., Kuzuhara, D., Yamada, H., Kikkawa, Y., Saeki, A., and Seki, S. (2012). “Self-Organization of Hydrogen-Bonding Naphthalene Chromophores into J-type Nanorings and H-type Nanorods: Impact of Regioisomerism.” *Angew. Chem.*, 124(27), 6747–6751.
- Yang, X., Xu, X., and Zhou, G. (2015). “Recent advances of the emitters for high performance deep-blue organic light-emitting diodes.” *J. Mater. Chem. C*, 3(5), 913–944.
- Yelamagad, C. V., Achalkumar, A. S., Rao, D. S. S., and Prasad, S. K. (2007). “The first examples of optically active tris (N-salicylideneaniline)s: manifestation of chirality from molecules to fluid columnar phases.” *J. Mater. Chem.*, 17(42), 4521–4529.
- Yoon, S.-J., Kim, J. H., Kim, K. S., Chung, J. W., Heinrich, B., Mathevet, F., Kim, P., Donnio, B., Attias, A.-J., and Kim, D. (2012). “Mesomorphic Organization and Thermochromic Luminescence of Dicyanodistyrylbenzene-Based Phasmidic Molecular Disks: Uniaxially Aligned Hexagonal Columnar Liquid Crystals at Room Temperature with Enhanced Fluorescence Emission and Semiconductivity.” *Adv. Funct. Mater.*, 22(1), 61–69.
- Yuan, W. Z., Zhang, Y., and Tang, B. Z. (2013). “Crystallization-Induced Phosphorescence for Purely Organic Phosphors at Room Temperature and Liquid Crystals with Aggregation-Induced Emission Characteristics.” *Aggreg.-Induc. Emiss. Fundam. Appl. Vol. 1* 2, 43–60.

Yvon, H. J. (2012). “A guide to recording fluorescence quantum yields.” *HORIBA Jobin Yvon Ltd Stanmore Middx. UK*.

Zhang, Q., Peng, H., Zhang, G., Lu, Q., Chang, J., Dong, Y., Shi, X., and Wei, J. (2014). “Facile bottom-up synthesis of coronene-based 3-fold symmetrical and highly substituted nanographenes from simple aromatics.” *J. Am. Chem. Soc.*, 136(13), 5057–5064.

Zhang, S., Li, W., Yao, L., Pan, Y., Shen, F., Xiao, R., Yang, B., and Ma, Y. (2013). “Enhanced proportion of radiative excitons in non-doped electro-fluorescence generated from an imidazole derivative with an orthogonal donor–acceptor structure.” *Chem. Commun.*, 49(96), 11302–11304.

Zhang, S., Yao, L., Peng, Q., Li, W., Pan, Y., Xiao, R., Gao, Y., Gu, C., Wang, Z., and Lu, P. (2015). “Achieving a Significantly Increased Efficiency in Nondoped Pure Blue Fluorescent OLED: A Quasi-Equivalent Hybridized Excited State.” *Adv. Funct. Mater.*, 25(11), 1755–1762.

Zhao, D. (2016). “Liquid Crystalline AIE Luminogens: Properties and Applications.” *Aggreg.-Induc. Emiss. Mater. Appl. Vol. 2*, ACS Publications, 151–171.

Zheng, H., Xu, B., and Swager, T. M. (1996). “Stabilization of nondiscoid columnar liquid crystals: Studies of unsymmetrical copper bis- β -diketonates.” *Chem. Mater.*, 8(4), 907–911.

Zhu, M., and Yang, C. (2013). “Blue fluorescent emitters: design tactics and applications in organic light-emitting diodes.” *Chem. Soc. Rev.*, 42(12), 4963–4976.

LIST OF PUBLICATIONS**Paper published in international journals**

1. **D. R. Vinayakumara**, Hidayath Ulla, Sandeep Kumar, Anup Pandith, M. N. Satyanarayan, D. S. Shankar Rao, S. Krishna Prasad and Airody Vasudeva Adhikari*. (2018) “Hydrogen bond-driven columnar self-assembly of electroluminescent D–A–D configured cyanopyridones”. *Journal of Materials Chemistry C*, 6, 7385-739.
2. **D. R. Vinayakumara**, Hidayath Ulla, Sandeep Kumar, M. N. Satyanarayan, Airody Vasudeva Adhikari*. (2018) “New fluorescent columnar mesogens derived from phenanthrene-cyanopyridone hybrids for OLED application”. *Materials Chemistry Frontiers*, 2018, 2, 2297-2306.
3. **D. R. Vinayakumara**, K. Swamynathan, Sandeep Kumar and Airody Vasudeva Adhikari*. (2018) “Optoelectronic exploration of novel non-symmetrical star-shaped discotic liquid crystals based on cyanopyridine”. *New Journal of Chemistry*, 42, 16999 -17008.
4. **D. R. Vinayakumara**, Sandeep Kumar and Airody Vasudeva Adhikari*. (2019) “Supramolecular columnar self-assembly of wedge-shaped rhodanine based dyes: synthesis and optoelectronic properties”. *Journal of Molecular Liquids*, 274, 215-222.
5. **D. R. Vinayakumara**, Sandeep Kumar, S. Krishna Prasad and Airody Vasudeva Adhikari.* (2019) “Self-assembly of Taper- and Wedge-Shaped Maleimide Derivatives: Synthesis and Structure-property Relationship” *Journal of Molecular Liquids*. 10.1016/j.molliq.2019.02.054.
6. **D. R. Vinayakumara**, K. Swamynathan, Sandeep Kumar and Airody Vasudeva Adhikari.* “Columnar self-assembly of novel benzylidenehydrazones and their difluoroboron complexes: structure-property correlations” *New Journal of Chemistry*, in press.
7. **D. R. Vinayakumara**, Rajalakshmi K., Sandeep Kumar and Airody Vasudeva Adhikari.* (2019) “Effect of donor strength on the optoelectronic properties of cyanopyridone based unsymmetrical dyad systems.” *Photochemical & Photobiological Sciences*, Revision has been submitted.

RESEARCH PAPERS PRESENTED IN CONFERENCES

1. **D. R. Vinayakumara**, Sandeep Kumar and A.V. Adhikari*. “Hydrogen-bonded stabilized D-A-D configured cyanopyridone based columnar mesogens for OLED applications”. International Conference on Recent trends in material science and technology (ICMST-2018). Indian Institute of Space Science and Technology (IIST), Thiruvananthapuram, Kerala, Indian. October 10-13, 2018.
2. **D. R. Vinayakumara** and Airody Vasudeva Adhikari* “Novel fluorescent nano self-assembled systems for efficient OLEDs”. International conference (Bangalore India nano-2018), Hotel Lalith Ashoka, Bangalore, Karnataka, December 05-07, 2018 (*Won best poster presentation award*).
3. **D. R. Vinayakumara** and Airody Vasudeva Adhikari* “New columnar liquid crystals derived from phenanthrene-cyanopyridone hybrids for OLEDs”. 37th ICC National Conference (37th ICC-2018) Dept. of Chemistry, NITK, Surathkal, Karnataka, December 12-14, 2018.

CIRCULULUM VITE

Present Address

Vinayakumara D. R.
Department of Chemistry
National Institute of Technology Karnataka
Surathkal, Mangalore-575 025
India.
Ph: +91 8971003345
E-mail: vinaykumara.dr@gmail.com

Permanent Address

Vinayakumara D. R.
S/o Revanna D
Kabbala village-577526
Hosadurga Taluk
Chitradurga District
Karnataka, India

Research Experience:

Jan 2015-present:

Ph. D. Research Scholar

Department of Chemistry, NITK-Surathkal
Research area: Design and development of various liquid crystalline materials for optoelectronic applications

Collaborative Ph.D. Research Scholar

SCM group, Raman Research Institute, Bangalore
Research area: Design and development of various liquid crystalline materials for optoelectronic applications

Oct 2013-Oct 2014:

Visiting Research Student

SCM group, Raman Research Institute, Bangalore
Research area: Design and development of various liquid crystalline materials for optoelectronic applications

Education:

Jan 2015-Present:

Ph. D.

Department of Chemistry, NITK-Surathkal
Title: Synthesis and characterization of new heterocycle-based discotic mesogens for optoelectronic applications
Supervisor: Prof. A. Vasudeva Adhikari

June 2011-June 2013:

M.Sc. in Industrial Chemistry

Department of Industrial Chemistry
Kuvempu University, Shankaraghatta, Karnataka, India

List of publications:

1. **D. R. Vinayakumara**, Manish Kumar, P. Sreekanth, Reji Philip and Sandeep Kumar.* (2015) "Synthesis, characterization and nonlinear optical studies of novel blue-light emitting room temperature truxene discotic liquid crystals". *RSC Adv.*, 5, 26596-26603.
2. Prakashaiah, B. G., **D. R. Vinayakumara**, Pandith, A. A., Shetty, A. N.* and Rani, B. A. (2018). "Corrosion inhibition of 2024-T3 aluminium alloy in 3.5% NaCl by thiosemicarbazone derivatives". *Corrosion Science*, 136, 326-338.